Université de Liège

Faculté des Sciences

Année académique 2009-2010

Disordered Tellurides

from Negative Thermal Expansion to Phase-Change Materials

Dissertation présentée par
Céline Otjacques
en vue de l'obtention du grade de
Docteur en Sciences

Résumé

Dans cette thèse, nous étudions l'anomalie de densité observée dans certains alliages liquides à base de tellure ($GeTe_6$, $GeTe_{12}$ et As_2Te_3), à travers leurs propriétés structurales et vibrationnelles. Ces composés subissent en effet une contraction de volume de $\sim 4\%$ en ~ 200 K au-dessus du point de fusion (partiellement dans le liquide sous-refroidi pour $GeTe_{12}$). Cette anomalie est accompagnée d'autres comportements inhabituels, tels qu'un maximum de la chaleur spécifique, un minimum de la vitesse du son et une forte baisse de la compressibilité isotherme [1, 2]. De plus, dans ces alliages liquides covalents, l'anomalie de densité (notée NTE, pour Negative Thermal Expansion) est souvent accompagnée d'une transition semi-conducteur-métal [3, 4]. De nombreuses expériences [5, 6, 7] ou simulations [8, 9, 10] ont été réalisées pour tenter de comprendre les changements structuraux donnant lieu à une NTE dans certains chalcogénides liquides. Malgré ces nombreuses études, aucun mécanisme n'a pu être clairement identifié à ce jour pour expliquer les tendances observées.

Nous commençons par mettre en évidence l'évolution structurale dans les 3 composés par des mesures de diffraction de neutrons, réalisées à plusieurs températures dans la gamme dans laquelle s'étend la NTE. Des simulations de dynamique moléculaire ab initio (DMAB), réalisées dans les mêmes conditions de température et de densité, nous permettent ensuite d'étudier l'évolution de l'ordre atomique local dans le liquide. Dans les structures obtenues par simulations, nous constatons une augmentation des nombres de coordination et une symétrisation de la première couche de voisins autour des atomes quand la température augmente. Pour confirmer ces résultats, nous avons réalisé des expériences de diffusion inélastique de neutrons, et obtenu la densité d'états de vibration (VDOS) le long de la NTE. Nous avons mesuré un changement clair dans la VDOS, consistant en un *red-shift* en température des fréquences les plus élevées. Ces résultats expérimentaux, complétés par les simulation DMAB, nous amènent à proposer un modèle pour l'anomalie de densité observée dans ces systèmes : celle-ci correspond à un changement structural entre un liquide 'basse température' caractérisé par une faible densité et, localement, par une distorsion de type Peierls, et un liquide 'haute température' dans lequel le gain d'entropie de vibration favorise un ordre local toujours octaédrique mais plus symétrique (moins distordu). Finallement, nous comparons l'évolution en température de la conductivité électrique de As_2Te_3, obtenue sur les structures DMAB, avec la transition semi-conducteur-métal mesurée expérimentalement. Nous avons étendu notre étude de la dynamique de ces composés à base de Te aux matériaux dits 'à changement de phase' $Ge_2Sb_2Te_5$ et $Ge_1Sb_2Te_4$.

Les matériaux à changement de phase (noté PCM pour Phase Change Materials), au contraire des matériaux présentés ci-dessus, se dilatent normallement en température dans la phase liquide. Ils exhibent néanmoins une combinaison inhabituelle de propriétés, qui permet leur usage comme mémoires dans des applications commerciales telles que les disque DVD-BlueRay. Les PCM possèdent en effet, en plus de la capacité de passer rapidement (en quelques dizaines de nanosecondes) de la phase amorphe à la phase cristalline (et inversément), un large contraste entre les propriétés optiques et électriques des deux phases [11]. Il est très rare pour un matériau de rassembler ces propriétés physiques, c'est pourquoi, initialement, la plupart des recherches sur les PCM ont été menées dans le but de concevoir l'alliage le mieux adapté aux applications. De nos jours, les composés utilisés dans les mémoires sont générallement à base de tellure, tel que les pseudo-binaires de type $(GeTe)_xSb_2Te_3$ ou les alliages de type Sb_2Te dopés à l'argent ou à l'indium [12, 13]. Le développement des matériaux à changement de phase pour le stockage d'information non-volatile (futures PC-RAM) nécessite une meilleure compréhension théorique de leur structure, de leur stabilité, et de l'origine du large contraste entre les propriétés de leurs phases cristalline et amorphe.

Nous présentons une étude théorique de l'évolution structurale en température des alliages binaires Sb_2Te et Sb_2Te_3, de la phase liquide à la phase amorphe. Ces composés sont considérés comme les composants de base de la plupart des PCM. Nous avons procédé à des simulations DMAB pour obtenir les structures de Sb_2Te et Sb_2Te_3 au-dessus et en-dessous de la température de fusion. Nous décrivons l'ordre local autour des atomes dans les structures liquide et amorphe et comparons celui-ci au cristal. Nos résultats pourraient aider à comprendre la facilité pour ces composés de passer du cristal à l'amorphe, étant donné l'ordre local très fort observé dans l'amorphe. Sur base de simulations DMAB, soigneusement comparées à des expériences, nous étudions également l'ordre local atomique des alliages $Ge_2Sb_2Te_5$ et $Ge_1Sb_2Te_4$, et nous analysons un modèle pour leur structure en phase amorphe. Nous montrons que les structures amorphes subissent une distorsion de type Peierls de l'environnement local, de laquelle résulte l'ouverture d'un gap. Finalement, en reprenant l'ensemble de nos résultats de simulation, nous développons une nouvelle méthode pour l'énumération des contraintes mécaniques en phase amorphe et nous montrons que le diagramme de phase des systèmes $GeSbTe$ peut être séparé en deux zones distinctes, comprenant des compositions ayant des caractères mécaniques bien définis : une phase dite *flexible* riche en tellure, et une phase dite *rigide* qui comprend les matériaux à changement de phase. Ces résultats pourraient ouvrir de nouvelles voies dans la compréhension des PCM et d'autres amorphes complexes, du point de vue de leur rigidité.

Abstract

In this thesis, we study the Negative Thermal Expansion (NTE) in tellurium based liquid alloys ($GeTe_6$, $GeTe_{12}$ and As_2Te_3), through their structural and vibrational properties. These alloys exhibit a volume decrease of $\sim 4\%$ in a ~ 200 K range above the melting temperature (partially in the undercooled liquid for $GeTe_{12}$). The density anomaly is accompagnied by other unusual behaviors, such a maximum in the specific heat, a minimum in the sound velocity and a steep decrease of the isothermal compressibility [1, 2]. Moreover, in these covalent liquid alloys, the NTE often takes place together with a semiconductor to metal (SC-M) transition [3, 4]. Several experiments [5, 6, 7] or calculations [8, 9, 10] were performed to try to understand the structural changes giving rise to a NTE in some liquid chalcogenides. Despite these numerous studies, no driving mechanism could be clearly identified up to now to explain the observed trends.

We evidence the structural evolution by measuring neutron diffraction spectra at several temperatures in the NTE range and perform First Principles Molecular Dynamics (FPMD) simulations at the same temperatures and densities to study the local order evolution in the liquid. The obtained structures show an increase of the coordination numbers and a symmetrization of the first neighbors shell around atoms when the temperature rises. To confirm these results, we performed inelastic neutron scattering (INS) to obtain de vibrational density of state (VDOS) along the NTE. We see a clear change of the VDOS, consisting in a red-shift of the highest frequencies with temperature. These experimental results, in addition to the FPMD simulations of the liquids, lead us to propose a model for the density anomaly observed in some of these tellurium based systems : it corresponds to a structural change between a 'low temperature' liquid, characterized by a low density structure with an octahedral local order distorted locally by a Peierls-like mechanism, and a 'high temperature' liquid in which the vibrational entropy gain favors a more symmetric (less distorted), still octahedral, local order. Finally, electrical conductivity evolution is obtained from the As_2Te_3 simulated structures, to compare with the semi-conductor to metal transition measured in the experiments. We extended our study of the dynamics of these Te-based compounds to the materials, called 'phase-change', $Ge_2Sb_2Te_5$ and $Ge_1Sb_2Te_4$.

The phase-change materials (PCMs), to the contrary of the compounds cited above, exhibit a normal volume expansion in the liquid phase. They possess however an unusual combination of properties, which permits their use as memories in commercial applications, such as Blue-Ray disks. The PCMs show, besides the capacity to switch rapidly (in some

tens of nanoseconds) from the crystal to the amorphous (and reverse), a large contrast between optical or electrical properties of both phases [11]. It is quite rare for a compound to gather these physical properties, and most of the earliest researchs on PCMs were done with the aim to find the most suitable material for applications. Nowadays, the alloys used in memories are generally based on Te, such as the pseudo-binary $(GeTe)_xSb_2Te_3$ or the Ag, In-doped Sb_2Te [12, 13]. The development of PCMs for non volatile data storage (the future PC-RAM) needs a better theoretical understanding of their structure, stability and origin of the large property contrast between crystalline and amorphous phases.

We present a theoretical study on the structural evolution with temperature of the Sb_2Te and Sb_2Te_3 binary alloys, from the liquid to the amorphous phase. These compounds are considered as the basic components of most PCMs. We performed FPMD simulations to obtain Sb_2Te and Sb_2Te_3 structures above and below the melting temperature. We describe the local order around atoms in the liquid and amorphous structures, and compare it to the crystal. Our results could help to understand the ability for those two coumpounds to change from the amorphous to the crystal so easily, because of the strong local order observed in the quench. On the basis of FPMD simulations, carefully assessed by comparison with experimental data, we will also study the atomic local order of the $Ge_2Sb_2Te_5$ and $Ge_1Sb_2Te_4$ phase-change alloys, and analyze a model for their amorphous structure. We show that the amorphous structure undergoes a Peierls-like distortion of the local atomic environment that results in a gap opening. Finally, by analyzing all our FPMD simulations, we develop a new method for enumerating mechanical constraints in the amorphous phase and show that the phase diagram of the $GeSbTe$ system can be split into two compositional regions having a well-defined mechanical character: a Te-rich *flexible* phase, and a *stressed rigid* phase that encompasses the known PCMs. This atomic scale insight should open new avenues for the understanding of PCMs and other complex amorphous materials from the viewpoint of rigidity.

Remerciements

Sept années et de nombreuses personnes à remercier !

Je remercie le Professeur Jean-Pierre Gaspard, qui m'a donné l'opportunité de réaliser cette thèse, pour m'avoir guidée au long de ce travail, avec ses compétences et son enthousiasme scientifique. Je le remercie particulièrement de m'avoir incitée à participer à de nombreuses expériences à l'Institut Laue-Langevin, à Grenoble, travail qui m'a plu énormément. L'ILL, un lieu où la patience règne en maître, au vu du temps consacré aux réglages de précision sur les instruments, à l'attente lors des mesures, au dépouillement minutieux des données. Un lieu d'émerveillement et d'humilité aussi, d'un point de vue technique et surtout humain.

J'ai eu la chance d'avoir non pas un seul mais deux promoteurs[1], et Jean-Yves Raty m'a assurément appris la rigueur et l'autocritique. Je le remercie vivement, pour son aide et ses encouragements quotidiens, mais aussi pour sa bonne humeur.

Ce travail a été jalonné de rencontres, et je tiens à adresser toute ma gratitude à Christophe Bichara, qui en plus d'être un fin connaisseur de la physique a égayé ces années ; Françoise Hippert, pour ses nombreux conseils lors des longues journées (et soirées) passées sur les lignes D4 et IN6 ; Yoshimi Tsuchiya, pour ses indispensables et innombrables données expérimentales ; Gabriel Cuello et Henry Fischer pour leurs patientes explications sur le dépouillement des expériences D4 ; Helmut Schober et Mohammed Sbiri pour leur aide précieuse sur IN6 ; Mark Johnson pour ses conseils couvrant tant les simulations que les expériences ; Vanessa Coulet pour les échantillons préparés avec soin et pour ses encouragements ; René Céolin pour les échantillons souvent demandés en dernière minute ; Brigitte Beuneu, Julia Steiner, Wojtek Welnic, Philipp Merkelbach et Peter Zalden pour les expériences réalisées avec eux à Grenoble.

Je remercie également Mmes Françoise Hippert et Maryse Hoebeke, et Mrs Philippe Ghosez, Riccardo Mazzarello et Matthias Wuttig d'avoir accepté d'être membres de mon jury.

Un grand merci à tous mes collègues du 3ème étage, à Rengin en particulier, pour avoir rendu l'atmosphère de travail agréable.

Enfin, merci à mes amis, à ma famille et à Alban, pas pour m'avoir aidée dans la réalisation de ce travail, mais ... pour tout le reste !

[1] Aussi complémentaires que le sont les expériences de diffusion de neutrons et les simulations ab initio.

Contents

Introduction

Not all materials expand when heated : there are some exceptions to this rule, in solids and even in liquids.

In the solid phase, for example, it is well known that diamond and other zinc-blend semiconductors have a negative thermal expansion (NTE), often referred to as *density anomaly*, at about 100 K [14] : the lattice contracts upon heating. Other types of systems, exhibiting different types of structures and bonding mechanisms, also possess this anomal behavior, as alkali halides with rocksalt structure, or more complex arrangements made of rigid units bonded through bridging atoms [15]. In some cases, the NTE extends over more than 1000 K [16].

Among liquids, the most famous example is certainly given by water, which undergoes a negative thermal expansion in a 4 K range above its melting point [17]. This behavior is also observed in a few liquid chalcogenides (which are compounds based on group VI elements) : $HgTe$ [18], In_2Te_3 [19], Ga_2Te_3 [19] and As_2Te_3 [20] display a NTE in a limited temperature range. The alloys Ge_xTe_{1-x} ($0 \leq x \leq 0.2$) [21] have the same behavior close to the melting point, either in the supercooled liquid or in the thermodynamically stable liquid. These covalent compounds have low coordination numbers N_c (e. g. $2 \leq N_c \leq 4$), both in the crystalline and in the liquid phases, in comparison to the compact structures of the metals and rare gases. The low N_c is the result of a quantum mechanical spontaneous symmetry breaking mechanism, the Peierls distortion. The mechanism has been initially demonstrated for crystal structures [22]; and it has been shown to remain valid in some liquids [23, 24], in which thermal effects restore partly the symmetry and increase the coordination number. The relation between the NTE and the structural evolution, which mainly consists of a modification of the first neighbors shell, has been proved by diffraction experiments [6, 25, 10]. The archetypal example is Te [26], for which the NTE occurs entirely in the undercooled liquid, in a range of about 100 K below the melting temperature $T_m = 723$ K [1]. The thermodynamical changes are accompanied by a marked structural evolution : the Te coordination number increases from 2.4 in the undercooled liquid to about 3 at high temperature [27].

The density anomaly is accompagnied with other unusual behaviors, such a maximum in the specific heat, a minimum in the sound velocity and a steep decrease of the isothermal compressibility [1, 2]. Moreover, in these covalent liquid alloys, the NTE often takes place together with a semiconductor to metal (SC-M) transition [3, 4].

The study of the marginal phenomenon that is the NTE, which concerns only a few chalcogenides compounds, has a wider impact that one might think. This anomaly is restricted to a limited temperature range, but we will see that the effects at the origin of the NTE are actually quite general, the specificity being their thermal evolution and their relative strength. The understanding of the chemical bonding evolution can benefit to the study of other alloys made of the same chemical elements, and thus involving mostly the same kind of bonding, but exhibiting totally different properties. For example, in the so called 'phase-change alloys', that are compounds generally based on tellurium, the structural change giving rise to the interesting properties involves partly the same physical mechanism that the one governing the NTE.

The phase-change materials (PCM), to the contrary of the compounds cited above, exhibit a normal volume expansion in the liquid phase. They possess however an unusual combination of properties, which permits their use as memories in commercial applications, such as in Blue-Ray disks. The PCMs have, besides the capacity to switch rapidly (in some tens of nanoseconds) from the crystal to amorphous state (and reverse), a large contrast between optical or electrical properties of both phases [11]. It is quite rare for a compound to gather these physical properties, and most of the earliest researchs on PCMs were aiming at finding the most suitable materials for applications. Nowadays, the alloys used in memories are generally based on Te, such as the pseudo-binary $(GeTe)_xSb_2Te_3$ or the Ag, In-doped Sb_2Te [12, 13].

The unusual features of the PCMs were the purpose of intense researches these last decades, with a main focus set on the understanding of the structural changes that can lead to such large differences in electrical or optical properties, together with a fast switch, between the amorphous and the crystal.

This thesis is devoted to the study of some tellurides. These ones forming a large variety of alloys, they also possess a wide applications range. Their semi-conductor properties are used in opto-electronical devices as varied as LEDs ($ZnTe$ [28]), radiation detectors ($CdZnTe$ [29]), thermoelectrics (Bi_2Te_3 [30]) or thin film solar cells ($CdTe$ [31]). We will consider two sub-groups of the tellurides, which exhibit very different characteristics. The first sub-group we will study contains alloys that undergo a Negative Thermal Expansion in the liquid state. The other tellurides sub-group we are interested in contains the so-called Phase-Change Materials.

The temperature will be the key parameter all along this thesis, as we will follow the thermal evolution in the liquid state of the first type of compounds, and study the amorphization and the amorphous phase of some PCMs, to compare it with the crystals. We will focus on the structural and dynamical properties of these alloys in these two disordered phases, and will discuss their electronic properties. In condensed matter, bonding plays a crucial role for the understanding of the physical properties and the electronic processes. In the liquid and amorphous states, only a local order is present, to the contrary of the long-range ordering found in the crystals. During this work, we will thus care about the

short, and sometimes more extended, range order present in these structures, by looking at the distances, angles, distortions, chemical order, vibrations, ... at the atomic scale, with the aim to decrypt their influence on the macroscopic properties of the chalcogenides alloys we study.

Several experiments [5, 6, 7] or calculations [8, 9, 10] were performed to try to understand the structural changes giving rise to a NTE in some liquid chalcogenides. Despite these numerous studies, no driving mechanism could be clearly identified up to now to explain the observed trends.

In this thesis, we will focus on two rich-Te $GeTe$ alloys, $GeTe_6$ and $GeTe_{12}$ (in the Chapter 6), and on As_2Te_3 (in the Chapter 8). These compounds have a sharp density anomaly just above the melting point (partly in the undercooled region for $GeTe_{12}$). For example, the volume decreases by $\sim 4\%$ in a 120 K temperature range in $GeTe_6$ [2].

Our task will be to study the thermal evolution of these alloys through their structural and vibrational properties, to understand the *driving force* for the NTE.

First, we will present neutron diffraction experiments that reveal the strong structural evolution with temperature. The information available from a neutron diffraction experiment on a liquid is however quite limited, as we can only access average values for the number of neighbors or interatomic distances. At this point, ab initio computer simulations will be very useful to give a more precise picture of the thermal evolution of the structures at the atomic scale (distances, angles, distorsions and chemical order). Finally, using inelastic neutron scattering, we will be able to relate the structural evolution in the NTE range to noticeable changes in the dynamics of the systems.

On the basis of these experiments and calculations, we will propose a simple model to explain the striking changes observed at the macroscopic scale.

We will complete this work on disordered tellurides by a study of the Sb_2Te and Sb_2Te_3 alloys, which are basic constituants of the widely used PCMs, but are poorly known in their liquid and amorphous phases. Neutron diffraction experiments and computer simulations will give details on the Sb_2Te and Sb_2Te_3 structures above and below (quench) the melting temperature, and we will compare it to the crystals. We will try to understand the ability of these two coumpounds to change from the amorphous to the crystal phase so easily. To achieve this aim, as for the study of the negative thermal expansion, we will concentrate on the local to medium-range order study.

We will also study the atomic local order of the $Ge_2Sb_2Te_5$ and $Ge_1Sb_2Te_4$ phase-change alloys, and analyze a model for their amorphous structures obtained with ab initio molecular dynamics simulations. No NTE is found in these Te-based alloys in liquid phase. There is thus a complete change in the thermal evolution of liquid $GeTe$ compounds when a quantity of Sb is added. In the $Ge_1Sb_2Te_4$ case, one third of the Te is replaced by Sb, compared to $GeTe_6$. To go further in the study of the effects of Sb element on the eutectic $GeTe_6$ behavior, we will investigate two other compounds. First, $GeSb_6$, which can be viewed as the extreme limit case, that is to say, $GeTe_6$ in which Te atoms have been substituted by Sb atoms. Second, $Ge(Sb_{10}Te_{90})_6$, which corresponds to the substitution

of a relatively small quantity of Te by Sb in $GeTe_6$.

In the last chapter, an original way to enumerate the constraints arising from bond-stretching (BS) and bond-bending (BB) interactions will be developped, based on the analysis of atomic scale trajectories obtained from First Principles Molecular Dynamics Simulations (FPMD). Combined with rigidity theory, this will open interesting perspectives to study the amorphous phase change materials in the same way as network glasses. The rigidity theory offers a practical computational scheme using topology, namely the Maxwell counting procedure, and has been central to many contemporary investigations on non-crystalline solids, such as sulphur and selenium based amorphous networks [32, 33]. It has led to the recognition of a rigidity transition [34, 35] which separates *flexible glasses*, having internal degrees of freedom that allow for local deformations, from *stressed rigid glasses* which are 'locked' by their high bond connectivity. What happens with heavier elements such as tellurium which would lead to more complicated local structures, as highlighted both from experiments [36, 37] and simulations [38, 39, 40, 41] ? Does the counting procedure still hold ? Attempts in this direction have been made on the basis of EXAFS measurements [42] but they seem to contrast with experimental findings and observations. A firm ground for the Maxwell constraint counting is therefore very much desirable. We will establish a new method to unambiguously count the constraints in a material and make used of the Maxwell rigidity theory to quantify the $GeSbTe$ amorphous glassy nature via their mechanical properties.

Chapter 1

Overview of phase change materials

In the late sixties, Ovshinsky [43] discovered the rapid and reversible transition between a highly resistive amorphous state and a conductive crystalline state of some chalcogenide alloys. These initial studies were performed on a wide variety of amorphous semiconductors obtained as thin films, such as oxides and boron based glasses, or chalcogenides materials (based on tellurium and/or arsenic) mixed with elements such as silicon or germanium. In this experiment, a voltage was applied across the amorphous alloy and the current was measured with time. A switching was observed, towards a conductive state, which appeared when the applied voltage exceeded a certain treshold. Ovshinsky related this transition to the following characteristics :

- The intensity / voltage curve is symmetrical with respect to the reversal of the applied voltage and current.
- Reversibility : if the current is reduced below a certain value, the material switches back to the high resistivity state.
- This process is repeatable.

With these three points, Ovshinsky actually described the required characteristics for an efficient memory device.

Since this precursor work, the so-called 'phase change alloys' have been studied extensively for decades, either experimentally [44, 45, 46] or with ab initio calculations [39, 47, 48, 41]. The operating principle of the Phase Change Materials (PCM) is based on the easy and reversible switching between the crystalline and amorphous states, each phase possessing very different electrical and optical properties. These materials are nowadays found in commercial applications for optical information storage and dissemination, such as CD-RW, DVD-RW or Blue-Ray disk, and could be used for the achievement of PC-RAM [12, 13].

In the following sections, we will describe first the principle of use of phase change materials, the qualities of a suitable PCM and its possible applications. We will also describe in details the state of the art about the structure of the PCM in the different phases and present the actual knowledge of the relation between structure and properties.

1.1 Principle of use

1.1.1 Recording

Phase change recording is achieved by creating amorphous marks on an initially crystalline support. To do this, spots are locally melted in the crystal and then quenched. This can be realized either by *optical* or *electrical* methods, respectively through the application of a laser or a current pulse of short duration and high intensity. This amorphization is named the SET operation and is represented in Fig. 1.1. The laser (or current) pulse duration has to be short to avoid significant heat dissipation and induce only a local melting of the material. Melting temperatures for typical phase change materials are of the order of 900 K. After the pulse, the temperature decreases so rapidly that the atoms are prevented from going back to their crystalline positions : they get trapped into an amorphous state, the diffusion being almost absent at room temperature. The amorphous (or glassy) state is a metastable solid which does not show any long distance order or periodicity (as in the crystal state). Nevertheless, in amorphous phase, a local order is present between the nearest neighbors, as in the liquid. This local order is generally similar to the one observed in crystalline phase [49]. The structures of these two phases will be discussed in details in section 1.4.

1.1.2 Reading

The large differences between optical (reflectivity) and electrical (conductivity) properties of the amorphous and crystalline phases, depending on the stoichiometry of the compound [11], allow the reading of written information by a laser or by contact electrodes.

1.1.3 Erasing

As the switching from the crystal to the amorphous phase is reversible, it is possible to erase the information written by re-crystallizing of the amorphous marks. This is achieved by heating the amorphous area through a low intensity and long duration laser (or electrical) pulse above the glass transition temperature (named T_g, which is lower than melting temperature, T_m). This heating allows the atoms to move and to reorganize rapidly according to the crystal structure. This is called the RESET operation (see Fig. 1.1). The glass transition temperatures for typical PCM are 130°C for $Ge_2Sb_2Te_5$, 155°C for $AgInSbTe$ or 170°C for $Ge_4Sb_1Te_5$.

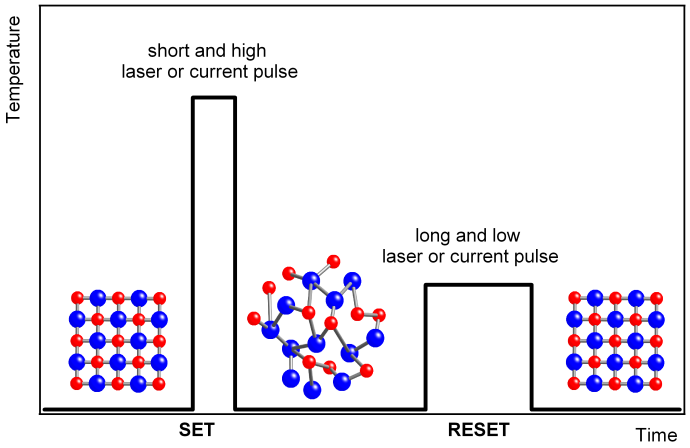

Figure 1.1: Recording and erasing processes in PCM. SET operation: the initially crystalline material is molten and then quenched with a high intensity and short duration laser or electrical pulse. RESET operation: re-crystallization of the amorphous marks is achieved by an heating with a low intensity and long duration laser or electrical pulse up to the glass transition temperature.

The Fig. 1.2 shows a sketch of the recording and erasing processes, called SET and RESET operations respectively, versus temperature and volume.

It is possible to repeat these processes a large number of times, by successive melt-quench-recrystallize operations.

1.2 Characteristics of a 'good' phase change material

Many materials, chalcogenides or not, can be quenched from the liquid to an amorphous phase, if the process is fast enough, and then recrystallized by heating above the glass transition temperature. But the unique property of the materials that are suitable for phase change use is their large contrast in optical and electrical properties between crystalline and amorphous phases. Moreover, phase change materials need to possess additional qualities to make them powerful for applications, such as the fastness of use or the stability.

We can summarize the properties required by a 'good' phase change material as follows [50, 12, 51]:

– Readability. A large contrast between optical and/or electrical properties is mandatory to permit the easy reading of information.

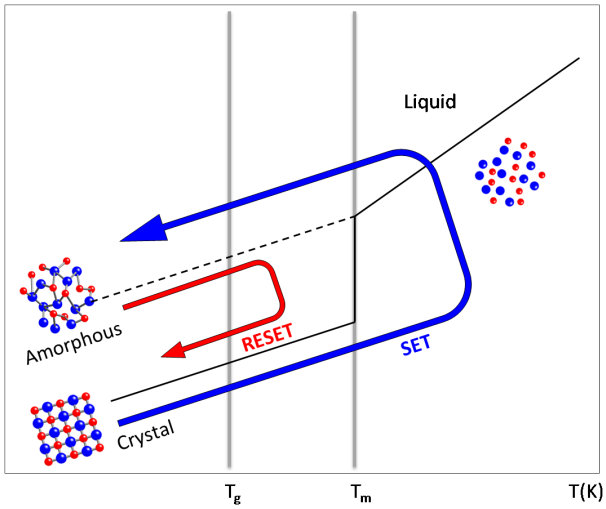

Figure 1.2: Sketch of the recording and erasing processes, called SET and RESET operations respectively, versus temperature and volume. Recording: an initially crystalline material is locally molten ($T > T_m$) and then rapidly quenched to the amorphous phase. Reading of the information is possible thanks to the large differences between optical or electrical properties of both phases. Erasing: the amorphous marks can be switched back to the crystalline state by increasing T above T_g.

- Reversibility. The reversibility of the switching in optical and electrical properties is the basis for a rewritable support, it implies writability and erasability.

- A bad glass forming ability. To switch from the amorphous to the crystal easily (RESET operation).

- Reproducibility of the switching operation.

- A fast switching (typically on the nanosecond scale) between amorphous and crystalline phases.

- Stability with time of the amorphous phase, to insure a durable storage of the information. This requires a high activation energy for the re-crystallization.

- A short recrystallization time, to enable high data-rate recording.

They are also some other required characteristics related to the phase change applications, concerning the process or the fabrication:

- A rapid quenching (typically less than 100 ns). It depends of the process used to realized the amorphization, in case of PCM applications the melt-quench operation is achieved by laser or electrical pulse, which lasts some nanoseconds.

- The ability to allow for a large contrast at reduced sizes, to permit high recording density.

- Low cost constituents and synthesis methods to allow for a wide commercialization.

The qualities that a compound has to gather to be suitable for phase change applications are numerous, this is why the quest for the best material is not yet over, and the processes are still improving.

1.3 Applications

1.3.1 Research of suitable materials

Since the first study of Ovshinsky, several compounds (mostly based on tellurium) were explored. Since many qualities are required together to design the best PCM for applications, the search for suitable compounds needed to explore many compositions of several chemical elements. Because a sufficiently rapid quench allows to obtain an amorphous phase for almost every alloy (provided that the glass transition temperature is high enough to insure the stability with time), the limiting parameter for application was mainly the rapidity of the switching between phases.

The first alloys that gathered all the necessary characteristics for commercial applications were pseudo-binary alloys of type $(GeTe)_x Sb_2Te_3$ [52, 44]. They showed a large contrast in optical properties, which encouraged the research for the development of optical storage devices, on the same format as the CD, commercialized since 1982. Compounds such as $Ge_2Sb_2Te_5$, $Ge_1Sb_2Te_4$ or $Ge_8Sb_2Te_{11}$ are now used in DVD-RW or Blu-ray disks [53].

More recently, a new type of alloys proved to be efficient for PCM applications. They are doped $SbTe$ compounds, as the doped eutectic $Ag_{5.5}In_{6.5}Sb_{59}Te_{29}$ [54]. The Sb-rich $GeSb$ alloys were also studied by experiments and ab initio simulations, and correlations between conductivity, total system energy, and local atomic coordination were revealed [55].

The wide variety of PCM used or promising for applications can be regrouped in a ternary diagram presented by Wuttig and Yamada [56] (see Fig. 1.3). In this diagram, the 3 axis represent Ge, Sb and Te concentrations and three groups of compounds are identified. A first group of phase change materials includes all the pseudo-binary alloys built like $(GeTe)_x(Sb_2Te_3)$, such as $Ge_2Sb_2Te_5$ and $Ge_1Sb_2Te_4$. The second group contains PCM which are doped $SbTe$ alloys (in particular the eutectic $Sb_{70}Te_{30}$). A third group contains the Sb-based PCM (such as $GeSb_6$).

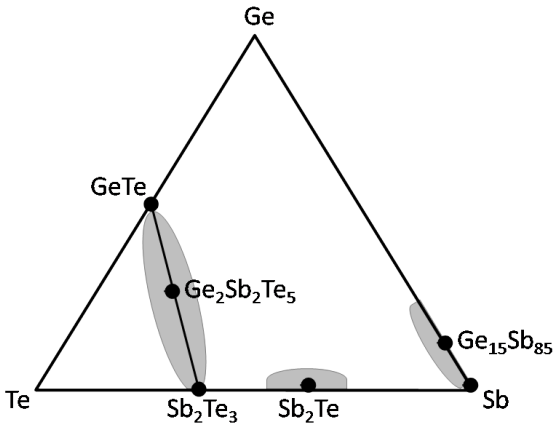

Figure 1.3: Ternary diagram regrouping the PCM used or promising for applications. Reproduced from [56].

1.3.2 Applications using optical recording

An optical storage system consists of an optical drive (made of a laser, characterized by its wavelength, a set of optical elements to shape and focus the laser beam, a disk driving to house the disk and a signal detection system) and a corresponding optical medium (the disk) [53].

The disk consists of two layers of substrate (usually polycarbonate), with, in between, one or two very thin layers of phase change material, initially crystalline. The thickness of the phase-change layer is typically comprised between 5 and 30 nm (depending on the application), for a the total disk thickness equal to 1.2 mm. The writing, reading and erasing operations are accomplished by a nanosecond laser pulse, of wavelength depending on the kind of disk. The data are represented by small amorphous marks written on a track which forms a concentric spiral on the disk. These marks have a lower reflectivity than the surrounding crystal layer, and represent a sequence of bits 1 on a 0 matrix. To read the information, the intensity of the laser beam reflected by the disk is detected and a subsequent conversion from digital to analogical signal is done [53].

The typical parameters of optical PCM commercial applications, such as the laser wavelength or the diameter of the amorphous marks, are reported in Table 1.1 [53, 56].

Parameter	CD-RW	DVD-RW	BD-RW (single)	BD-RW (dual)
Year of commercialization	1997	2000	2003	2004
Recording density (GB)	0.65	4.7	25.0	50.0
Laser wavelength (nm)	780 (IR)	650 (R)	405 (B)	405 (B)
Spot size (nm)	900	550	238	238

Table 1.1: Typical parameters of optical PCM commercial applications [53, 56].

1.3.3 Non-volatile electronic memories (PC-RAM)

The contrast in electrical properties (conductivity) between the amorphous and crystalline phases of PCM can reach more than 3 orders of magnitude [43]. This property may be used in future PC-RAM, as the crystallization process in the lately discovered PCM alloys is now fast enough, and permits high storage densities, to compete with the flash memory or with the dynamic RAM [56]. In a PC-RAM, the writing and erasing operations are achieved by a nanosecond electrical pulse instead of a laser pulse as in the optical PCM. A PC-RAM is made of two electrodes to write, read or erase information by voltage differences, on an active region made of PCM. The intensity of current versus voltage in a PC-RAM is plotted in Fig. 1.4 [50]. The reading operation is performed at low current intensity. The switching (for example from the amorphous to crystalline phase) is realized by increasing the voltage up to a treshold value, at which the amorphous phase becomes less resistive. This permits to a much larger current to flow through the amorphous region of the cell, and dissipates enough heat to crystallize the active region.

1.4 Structure of phase change alloys

If the structures of phase change materials are reasonably well known in the crystalline and, more recently, liquid phases, questions remain concerning the amorphous phase.

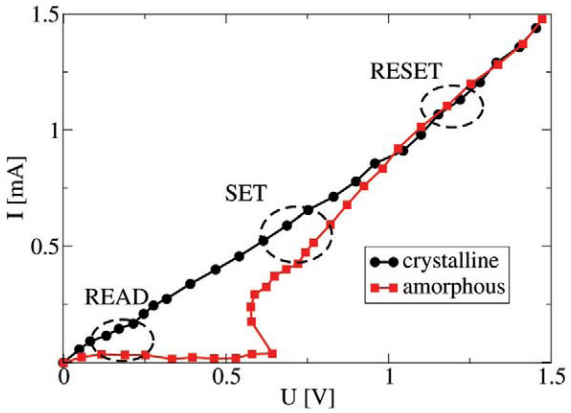

Figure 1.4: Current voltage curve for a phase-change memory cell. SET and RESET denote the switching regions. READ denotes the region of readout. Reproduced from [57].

1.4.1 Crystalline phase

Building-blocks: Sb_2Te, Sb_2Te_3, GeTe

The building compounds of a wide number of PCM are the Sb_2Te, Sb_2Te_3 and $GeTe$ alloys. The crystalline structure of these compounds results from the Peierls distortion instability, its nature depending on the number of p-electrons [58] (see Chapter 2 for further details). Their space group and cell parameters are given in Table 1.5.

The Sb_2Te and Sb_2Te_3 compounds crystallize in layered structures, with trigonal or rhombohedral symmetries. The crystal of Sb_2Te consists of nine layers stacked along the c-axis of an hexagonal supercell [59], containing only one kind of atom each.

The crystalline Sb_2Te_3 can also be described in an hexagonal supercell, consisting in 15 layers [60] either made of Sb or Te. It can also be viewed as a stacking of 5 'Sb_2Te_3' layers.

The $GeTe$ crystallizes at room temperature in a rhombohedral structure of type $R3m$, which can be viewed as a distorted $NaCl$-type structure. It is the binary analogue of the grey arsenic structure [61, 62].

In these three structures, the atomic environment is octahedral with some distortions depending on the site. The three structures are plotted in Fig. 1.5.

Pseudo-binary alloys $(GeTe)_xSb_2Te_3$

The PCM lying along the pseudo-binary $(GeTe)_xSb_2Te_3$ line are observed in a stable and a metastable crystalline phase, the latter being the one used in phase change applications.

Compound	Space group	a (Å)	c (Å)	α	u
Sb_2Te	$P\bar{3}m1$	4.272	17.633		
Sb_2Te_3	$R\bar{3}m$	4.274	30.47		
$\alpha - GeTe$	$R3m$	5.988		88°15'	0.238

Table 1.2: Cell parameters of the PCM building components, at room temperature and pressure. In $\alpha - GeTe$, atoms are present at (u, u, u) and $(-u, -u, -u)$.

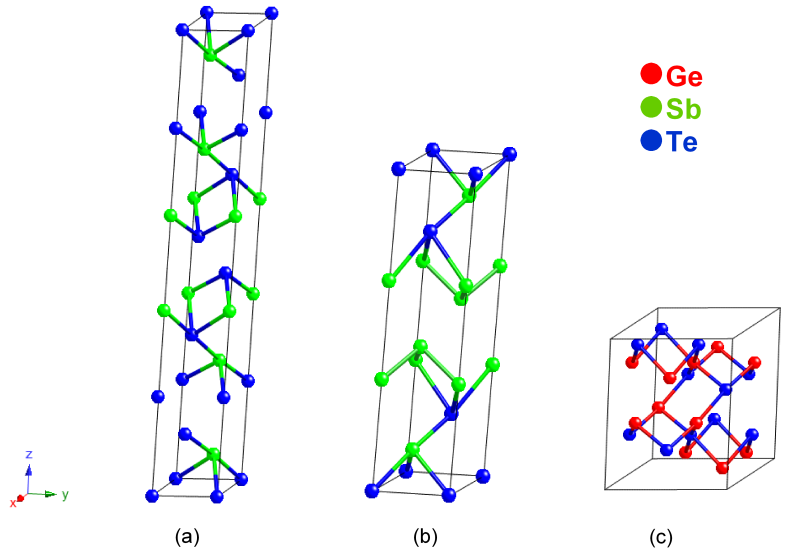

Figure 1.5: Crystalline phase of (a) Sb_2Te_3 [60], (b) Sb_2Te [59] and (c) $GeTe$ [61].

When the crystal is grown in thin layer by laser irradiation, as in phase change applications (see sections 1.3.2 and 1.3.3), a metastable phase is obtained. It belongs to the $Fm\bar{3}m$ space group, and consists of a close packed cubic structure of $NaCl$ type. The Te atoms occupy 100 % of the 4(a) sites, while Ge and Sb atoms are generally supposed to randomly occupy the 4(b) sites. This corresponds to a succession of 6 layers of Te or Ge/Sb atoms alternatively. The Ge/Sb layers are not filled with atoms, leaving vacancies depending of the compound stoichiometry. For example in $Ge_2Sb_2Te_5$ (illustrated in Fig. 1.6 (a)), 20 % of the sites are empty [63, 64].

When the metastable phase is heated above temperatures of around 500 K (depending of the compound), it transforms into a stable phase [65]. This latter consists of a complicated structure, with close packed stacking, the periodicity of which depending on the compound. For example, $Ge_2Sb_2Te_5$ has a nine layers structure ($P\bar{3}m1$) [66], containing either Te or Ge/Sb (randomly placed) atoms. The difference between the stable and metastable phases, besides the fact that no vacancies are observed in the first one, is that pairs of adjacent Te layers are presents in the stable crystal [63]. This phase is illustrated in Fig. 1.6 (b) for $Ge_2Sb_2Te_5$.

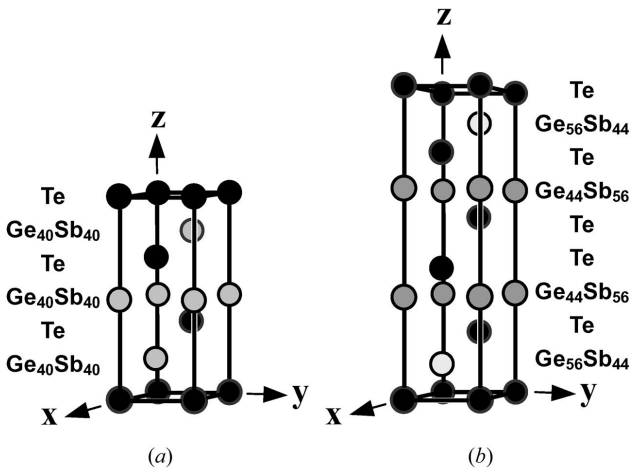

Figure 1.6: Crystal structures of (a) metastable and (b) stable $Ge_2Sb_2Te_5$, shown schematically in perspective, and depicted in hexagonal unit cell. Black circles show the atomic positions for Te. Gray circles show those for Ge or Sb. Reproduced from [63].

Shamoto et al. [67] studied the $NaCl$ type (metastable) crystal structure of $Ge_2Sb_2Te_5$ by atomic pair distribution function analysis of pulsed neutron powder diffraction data. Large displacements of Ge atoms were found in the structure, suggesting a large degree of disorder in the $GeSb$ sub-lattice (see Fig. 1.7).

Luo and Wuttig [68] listed all the known PCM that show good properties for data

storage applications. They noted that their crystalline structure is rocksalt (compared to some 'unsuccesful' samples, all of them crystallizing in chalcopyrite structure) and that their number of s and p electrons is always larger than 4, and usually comprised between 4.3 and 5.

Wuttig et al. studied vacancies present in the meta-stable crystalline phase of $GeSbTe$ alloys by density-functional theory calculations [37]. They started from a $Ge_2Sb_2Te_4$ alloy (0 % vacancies) with a rock-salt structure in which the Te atoms occupy one sublattice and the Ge/Sb atoms occupy randomly the other. They compared the vacancies formation energies by varying the vacancies concentration up to 30 % in the $GeSbTe$ structures. They found that the removal of either Ge or Sb atoms from $Ge_2Sb_2Te_4$ is energetically favorable. On top of the vacancies, relaxation of the Ge atoms from the perfect rock-salt like lattice positions was shown to further stabilize the structure.

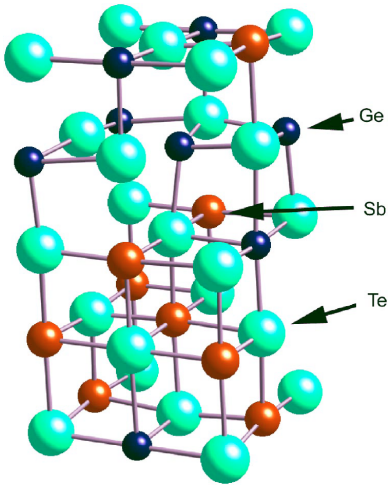

Figure 1.7: Schematic of the large displacements of Ge atoms found in $Ge_2Sb_2Te_5$. Reproduced from [67].

Up to now, studies on the crystalline phase of phase change alloys have shown that they possess either a rocksalt (cubic-like) sructure, often accompanied with vacancies and/or distorsions [63, 67, 56, 65, 37].

1.4.2 Liquid phase

The writing operation implies a short period during which the system is in the liquid state before rapid cooling and amorphization. The melting temperatures are typically around 900 K. Despite the fact that the local order present in the liquid phase could give a good idea of what will be the local order after a rapid quench, the study of the PCM in liquid phase has been largely neglected.

In a recent neutron diffraction study [69], it was shown that it is possible to sort Te-based PCM from other Te-based alloys (including alloys of the type $CuInTe$, $AgSbTe$, etc.) by measuring the ratio of the heights $S(q_1)$ and $S(q_2)$ of the two first peaks of the structure factor. It was shown that the Te-based PCM have ratios higher than unity, which correspond to a predominantly octahedral local order, while most of the non-PCM studied are predominantly tetrahedrally bonded (ratio smaller than unity). It was also observed that the compounds which exhibit octahedral order both in liquid and crystalline states (see section 1.4.1) possess very similar liquid and amorphous densities, smaller that the crystal one. This fact suggests that the liquid phase could be a useful starting-point to study the amorphous phase, this latter being much more difficult to synthesize in large quantity. Furthermore, the fact that all the liquid PCM studied possess an octahedral structure together with densities similar to the amorphous phase indicates that local order in liquid and amorphous phases could be very similar, this octahedral order being already found in the crystal.

Since this neutron diffraction experiment, first principles molecular dynamic simulations studies were performed on various phase-change compounds or components ($Ge_1Sb_2Te_4$, $AgInSbTe$, Sb_2Te_3) in liquid phase (and amorphous phase, see further section) [41, 48, 70]. These three studies confirmed the picture of an octahedral local order in the liquid phase.

1.4.3 Amorphous phase

The amorphous phase is obtained by a rapid cooling from the liquid. Because of the fastness of this quench, the long range order observed in a crystal does not have time to settle, and only a short or medium range order is found in the amorphous state. The amorphous structure of the PCM is still controversial as no explanation is unanimously accepted.

In 2004, Kolobov et al. [36] reported large structural differences between the crystalline and amorphous phases of $Ge_2Sb_2Te_5$. They performed Extended X-Ray Absorption Fine Structure (EXAFS) and X-ray Absorption Near Edge Structure (XANES) experiments on crystalline and laser-amorphized samples and analyzed the Fourier transform of the spectra at the Ge, Sb and Te edges. They also simulated EXAFS spectra by using a rock-salt model as the starting structure for the crystal. By looking at the crystal structure obtained from the fit, they found, as previously shown in [67], that the Ge and Sb atoms are shifted from the $NaCl$ sites, giving rise to shorter and longer distances for bonds between nearest neighbors. In the amorphous phase, they found smaller distances, which was confirmed by Raman scattering experiments, the measured Raman modes being found more rigid. They showed that the best agreement with the XANES experiment was obtained for tetrahedrally bonded Ge atoms. They suggested the following mechanism : the intense laser pulse applied on the crystalline material induces a breaking of the weaker (longer) bonds in the crystal, and the Ge atoms flip to the tetrahedral positions. The authors called this structural change while going from the crystal to the amorphous phase *umbrella flip*

(see Fig. 1.8). This model cannot, obviously, apply for PC materials without Ge, such as the $SbTe$ family.

The model of Kolobov was studied on the $Ge_1Sb_2Te_4$ material by ab initio ground state calculations [71]. Studying different crystal configurations, Welnic and co-workers demonstrated that the octahedral environment for Ge atoms was more stable than the tetrahedral one (in the so-called *spinel* phase, all the Ge atoms are tetrahedrally coordinated with Te atoms, which is locally identical to the Kolobov's model). These two structures exhibiting a sufficient optical contrast, the authors attributed the octahedral structure to crystal and the spinel one to amorphous.

In 2006, Kohara et al. performed reverse Monte-Carlo fits to synchrotron radiation X-ray measurements [72] of amorphous $Ge_2Sb_2Te_5$. They found that the amorphous is made of even-numbered (4-fould and 6-fold) ring structures and present angles distributions well peaked on 90°, as in the crystal phase. They compared with the ring statistic for amorphous $GeTe$ and found rings of various sizes (both odd and even) in the structure, due to numerous $GeGe$ homopolar bonds. They concluded that the unusual ring statistic of amorphous $Ge_2Sb_2Te_5$ is the key parameter for rapid phase transition between amorphous and crystalline phases.

Baker et al. [42] published another EXAFS study of amorphous $Ge_2Sb_2Te_5$, in which they identified unambiguously the presence of $GeGe$ bonds (14 % of the Ge bonds), while $TeTe$, $SbSb$ and $SbGe$ bonds were shown to be absent. For the first time, they postulated the important role of homopolar bonds for the PCM properties. They found coordination numbers equal to 3.9±0.8 for Ge, 2.8±0.5 for Sb and 2.4±0.6 for Te. Jovari et al. [73] used reverse Monte-Carlo simulation technique to generate models of structure compatible with $Ge_1Sb_2Te_4$ and $Ge_2Sb_2Te_5$ X-ray diffraction and EXAFS data. In their RMC structures, they also found a significant homopolar bonding ($GeGe$ and $GeSb$), with a mostly tetrahedral environment for Ge atoms in $Ge_2Sb_2Te_5$, while no $TeTe$ and $SbSb$ bonds were detected. The majority of the atoms in their structures satisfy the $8-N$ octet rule (90 %−95 % of Ge, Sb and Te atoms having four, three and two neighbors respectively).

Another experimental study of $Ge_1Sb_2Te_4$ material in crystalline and amorphous phases, by high-resolution X-ray and UV-photoelectron spectroscopy, was published by Klein and co-workers [45], showing the coexistence of two environments (octahedral and tetrahedral) for Ge and Sb in the amorphous phase.

In these contrasted results, various amounts of tetrahedrally bonded Ge atoms have been reported for the amorphous phase (from 30 % to 100 %). Recent FPMD studies on different $(GeTe)_x(Sb_2Te_3)$-type PCM in the amorphous phase highlighted the small but non-negligible quantity of tetrahedrally coordinated Ge in the structures (34-38 %), compared to the octahedral Ge, together with homopolar $GeGe$, $SbSb$ or $GeSb$ bonds [40, 39, 74, 47, 75].

Caravati et al [40] found that, in amorphous $Ge_2Sb_2Te_5$, most of the Ge and Sb atoms in the structure are fourfold-coordinated, while Te is mostly threefold-coordinated in defective octahedral sites which recall the local environment of the crystal. They found a proportion of 22 % of tetrahedrally coordinated Ge atoms in the structure, favored by the presence of $GeGe$ and $GeSb$ bonds. For the authors, this coexistence of two environment for Ge atoms (octahedral and tetrahedral) might be the key parameter to understand the strong optical contrast between the crystalline and amorphous phases of PCM and the fastness of the switching.

Akola and Jones [39] used larger sets of atoms (460) and longer quenching times to obtain a model for the amorphous $Ge_2Sb_2Te_5$. They concluded to a mostly octahedral order around Ge and Sb, the Ge atoms being mostly four-coordinated with one third of them being tetrahedrally coordinated. They also found a long-range order on the Te atoms, together with an $ABAB$ square structural pattern ($A = Ge$ or Sb and $B = Te$). They attributed the rapid switching from the amorphous to the crystal to a reorientation of disordered $ABAB$ squares to form an ordered lattice. They also evidenced the presence of cavities, or vacancies, mainly surrounded by Te atoms. Akola and Jones also studied the pseudo-binary alloy $Ge_8Sb_2Te_{11}$, which is used in the Blu-Ray disks [47]. This compound was found to show many structural similarities with $Ge_2Sb_2Te_5$ (a mostly octahedral order was found, with 42 % of Ge atoms in tetrahedral coordination, the $GeGe$ bonds being more present in this case).

Recently, an alternative description to the Kolobov's model was presented. First, Shportko et al. investigated the dielectric function of the crystalline and amorphous phases of different PCM by infrared spectroscopy and spectroscopic ellipsometry [76]. They found an electronic dielectric constant up to 200 % larger for the crystal than for the amorphous, and stronger that expected for non-PCM covalent alloys. They attributed it to the fact that crystalline PCM are all based on distorted cubic structures and possess resonant bonding, due to the alignement of the p-orbitals. Resonant bonding requires a longer-range order than the conventional electron pair bond of the 8-N rule (i. e. the second and higher neighbours need to be aligned). In the amorphous state, this high level of ordering is not possible, and so the structure reverts to a simple 8-N rule structure, which requires a lower level of ordering (on the nearest neighbours only). They thus concluded that the different dielectric constant values between the amorphous and crystalline phases of PCM can be taken as clear evidence that the medium range order needed for resonant bonding is absent in the amorphous PCM, and that this change in bonding is as significant as the lowering of the Ge coordination to four, or the formation of $GeGe$ bonds. After this experimental study, Huang and Robertson [77] postulated that, during the transition from the crystalline to the amorphous phase, the Ge atoms are displaced along the (110) direction rather than along the (111) (see in Fig 1.8) and retain the coordination number of the crystal. As said in [76], they made the assumption that, moreover the change in the local order around Ge atoms, the medium range order is totally lost in the amorphous structure (no medium range order at the second-neighbor level) [78]. With calculations

on model periodic structures, they evidenced a large difference in the optical properties of the crystalline and amorphous phases of different compounds (Se, Te and $GeTe$). They attributed this optical contrast to the loss of medium-range order and resonant bonding in the amorphous phase.

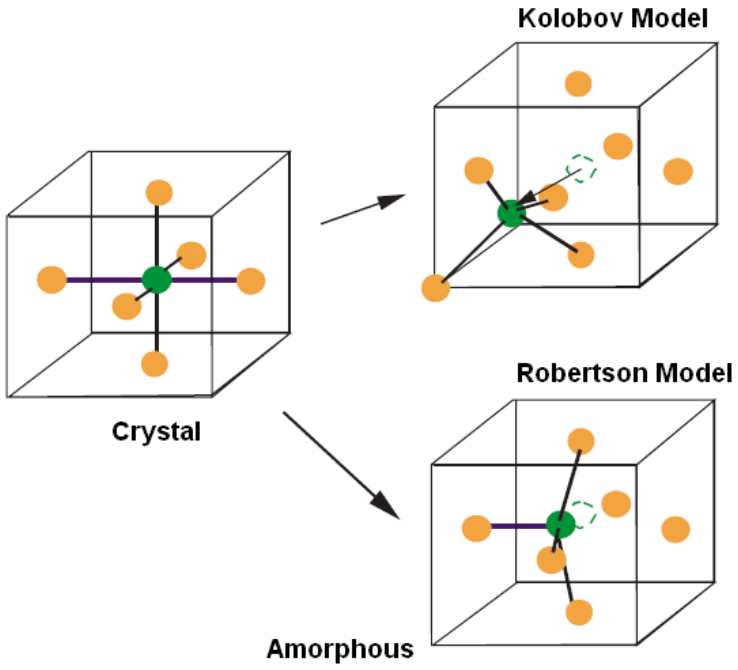

Figure 1.8: Umbrella flipping model presented by Kolobov [36] for the switching between the crystalline and amorphous phases in the PCM, together with the resonant bonding model presented by Huang and Robertson. Reproduced from [77].

Chapter 2

The Peierls distortion

In this work, we study compounds made of columns IV, V and VI elements of the periodic table, in liquid and amorphous phases. In this chapter, we will review the physics principles that govern the covalent structures of these elements and alloys. In the crystalline phase, many of them are subject to a periodic distortion (or symmetry breaking) of the simple cubic structure. This effect originates from an electronic instability that, via the electron-phonon coupling, results in the so called *Peierls distortion*. The stability of these structures depends on the coordination number N_c (the number of closest neighbors around one atom in the structure), which is given by the *octet rule*. This distortion is also sometimes observed, albeit locally, in disordered phases.

2.1 Theoretical model for interactions: the Tight-Binding model

For simplicity and in order to get analytical results (see the next sections), we resort to a tight-binding description of the electronic states. The tight-binding method has been widely used, for its simplicity and because it allows the understanding of several mechanisms [79]. It can be applied to all the systems in which the electrons are localized in the neighborhood of the atoms, this is the case of the s and p valence electrons of the covalent alloys.

This method is based on the following approximations:

- The *monoelectronic approximation*, which supposes that each electron is moving in the average field of the other electrons and ions.

- The *LCAO approximation* (Linear Combination of Atomic Orbitals), which consists of the development of the eigen states ψ_n of the system (molecular orbitals) on the basis of the atomic orbitals ϕ_i (i representing the different orbitals s, p, d, ...) : $\psi_n = \sum_{\mathbf{R},i} a^n_{\mathbf{R},i} \phi_i(\mathbf{r} - \mathbf{R})$, $\mathbf{R}$ being the atomic positions.

To obtain the eigen values and eigen states of the Schrödinger equation of the system,

$$H\psi_n = \left[-\frac{\hbar^2}{2m}\nabla^2 + V(\mathbf{r})\right]\psi_n = E_n\psi_n \tag{2.1}$$

where $V(\mathbf{r})$ is the sum of the atomic potentials $v_{\mathbf{R}}(\mathbf{r}-\mathbf{R})$, one has to solve

$$det\left|H_{\mathbf{R}i,\mathbf{R}'i'} - E_n S_{\mathbf{R}i,\mathbf{R}'i'}\right| = 0 \tag{2.2}$$

where we defined

$$S_{\mathbf{R}i,\mathbf{R}'i'} = \left\langle \phi_i(\mathbf{r}-\mathbf{R})|\phi_{i'}(\mathbf{r}-\mathbf{R}')\right\rangle \tag{2.3}$$

and

$$H_{\mathbf{R}i,\mathbf{R}'i'} = \left\langle \phi_i(\mathbf{r}-\mathbf{R})\,|H|\,\phi_{i'}(\mathbf{r}-\mathbf{R}')\right\rangle \tag{2.4}$$

In the tight-binding approximation, the integrals 2.3 are neglected when different atomic sites ($\mathbf{R} \neq \mathbf{R}'$) are considered. Moreover, the atomic orbitals being normalized on the same site, we have

$$S_{\mathbf{R}i,\mathbf{R}'i'} = \delta_{\mathbf{R}\mathbf{R}'}\delta_{ii'} \tag{2.5}$$

The diagonal term ($\mathbf{R} = \mathbf{R}'$) of the integrals 2.4 involving orbitals centered on the same site,

$$\langle \phi_i(\mathbf{r}-\mathbf{R})\,|H|\,\phi_{i'}(\mathbf{r}-\mathbf{R})\rangle \tag{2.6}$$

can be separated in two terms :

$$E^0_{\mathbf{R}i} = \left\langle \phi_i(\mathbf{r}-\mathbf{R})\left|-\frac{\hbar^2}{2m}\nabla^2 + v(\mathbf{r}-\mathbf{R})\right|\phi_i(\mathbf{r}-\mathbf{R})\right\rangle \tag{2.7}$$

and

$$\alpha^{\mathbf{R}}_{ii'} = \left\langle \phi_i(\mathbf{r}-\mathbf{R})\left|\sum_{\mathbf{R}'\neq\mathbf{R}} v_{\mathbf{R}'}(\mathbf{r}-\mathbf{R}')\right|\phi_{i'}(\mathbf{r}-\mathbf{R})\right\rangle \tag{2.8}$$

being called *crystalline field* integral. In the $\mathbf{R} \neq \mathbf{R}'$ term of 2.6, we keep only the integrals involving orbitals centered on sites that are *first* neighbors,

$$\beta^{\mathbf{R}\mathbf{R}'}_{ii'} = \left\langle \phi_i(\mathbf{r}-\mathbf{R})\left|v_{\mathbf{R}'}(\mathbf{r}-\mathbf{R}')\right|\phi_{i'}(\mathbf{r}-\mathbf{R}')\right\rangle \tag{2.9}$$

These are called *resonance integrals*. We suppose hereafter that all resonance integrals β (< 0) decrease with the distance r as:

$$\beta(r) = \beta_0 r^{-q} \tag{2.10}$$

2.2 The Bloch wavefunctions

In the case of a crystal made of N atoms, and if we consider the s and p electrons only, the obtention of the eigen states of Eq. 2.1 requires the diagonalization of a $4N * 4N$ matrix. For an infinite crystal, the ionic potential is periodic and the Bloch theorem simplify these calculations. It gives for the solutions of Eq. 2.1

$$\Phi_{\mathbf{k}i}(\mathbf{r}) = \frac{1}{\sqrt{N}} \sum_{\mathbf{R}} e^{i\mathbf{k}\cdot\mathbf{R}} \phi_i(\mathbf{r} - \mathbf{R}) \tag{2.11}$$

Following this, we have

$$\Phi_{\mathbf{k}i}(\mathbf{r} + \mathbf{a}) = e^{i\mathbf{k}\cdot\mathbf{a}} \Phi_{\mathbf{k}i}(\mathbf{r}) \tag{2.12}$$

where $\mathbf{a}$ is a fundamental vector of the crystal lattice and $\mathbf{k}$ is the wave vector. The elements of the Hamiltonian matrix have non-zero values only if the corresponding wave vectors are identical, which simplifies the problem as only the diagonalization of a $4 * 4$ matrix is required for each of the N wavevectors of the first Brillouin zone.

2.3 Cohesive energy

The cohesive energy of the system, E_{coh}, is the sum of an attractive term due to the resonance between the orbitals and a repulsive term:

$$E_{coh} = E_{att} + E_{rep} \tag{2.13}$$

2.3.1 Attractive interactions

In quantum mechanics, the attractive energy E_{att} is due to the partial filling, up to the Fermi level, of the electronic density of states, $n(E)$.

Electronic instability of the linear chain with a half-filled band The simplest example to illustrate the Peierls distortion is to compare two one-dimensional structures made of H atoms (half-filled s-band) : a periodic linear chain (1) and a dimerized chain (2) (see in Fig. 2.1).

The linear chain (1) is defined by a unit cell parameter a (see Fig. 2.1). All interatomic distances, r, being equal, the resonance integrals $\beta(r)$ between neihboring H atoms are also equal. The dimerized chain (2) shows an alternation of short and long distances, r_s and r_l, characterized by resonance integrals β_s and β_l respectively (with $|\beta_s| > |\beta_l|$). The unit cell parameter is now equal to $2a$ (the width of the Brillouin zone is then divided by 2). If we take the atomic level shifted by α as the reference energy ($E^0 - \alpha = 0$), the dispersion relation is :

$$E(k) = -2|\beta| \cos(ka) \tag{2.14}$$

for the linear chain (1) and :

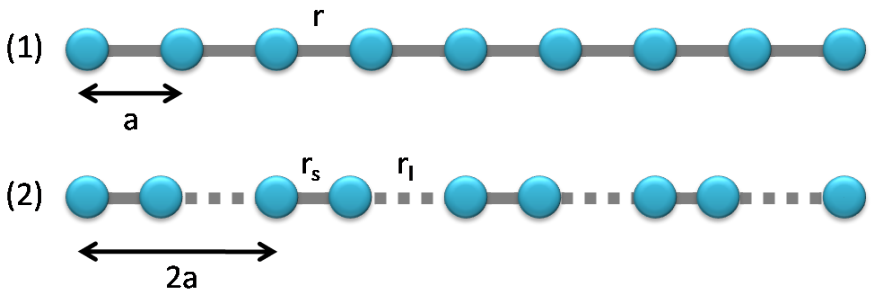

Figure 2.1: Linear (1) and dimerized (2) chains.

$$E(k) = \pm\sqrt{(\beta_l - \beta_s)^2 + 4\beta_l\beta_s \cos^2(ka)} \tag{2.15}$$

for the dimerized chain (2). Peierls observed [22] that the dispersion curves for the dimerized chain lead to the opening of a gap (i. e. forbidden energy values), in comparison with the continuous spectrum for the linear chain (see in Fig. 2.2). This gap is symmetric with respect to the reference energy $E^0 - \alpha$ and its width E_g at the border of the first Brillouin zone ($k = \pm\pi/2a$) is equal to

$$E_g = 2|\beta_l - \beta_s| \tag{2.16}$$

In the case of a half-filled band, the occupied states close to the Fermi level in the undistorted structure are shifted to lower energies by the opening of the gap in the dimerized chain. Consequently, the total electronic energy of the system, given by:

$$E_{att} = \int_0^{k_F} 4E(k)n(k)dk = \int_{-\beta_s-\beta_l}^{E_F} 2En(E)dE \tag{2.17}$$

is lower than for the undistorted chain. This mechanism is called the Peierls distortion [22]. The density of electronic states, $n(E)$, is obtained from the dispersion relations 2.14 and 2.15 and is plotted for the undistorted and distorted chains in Fig. 2.2.

To determine if the most stable structure for a linear chain made of H atoms is the (1) or the (2) chain, it is mandatory to include a repulsive term and compute the cohesive energy.

2.3.2 Repulsive interactions

The repulsive term has for origin the repulsion between the ions and between the electrons (Pauli principle) and is impossible to compute exactly. Let us consider a 2 body repulsive potential of the form:

$$E_{rep} = \frac{1}{2}\sum_{i,j\neq i} V(r_{ij}) \tag{2.18}$$

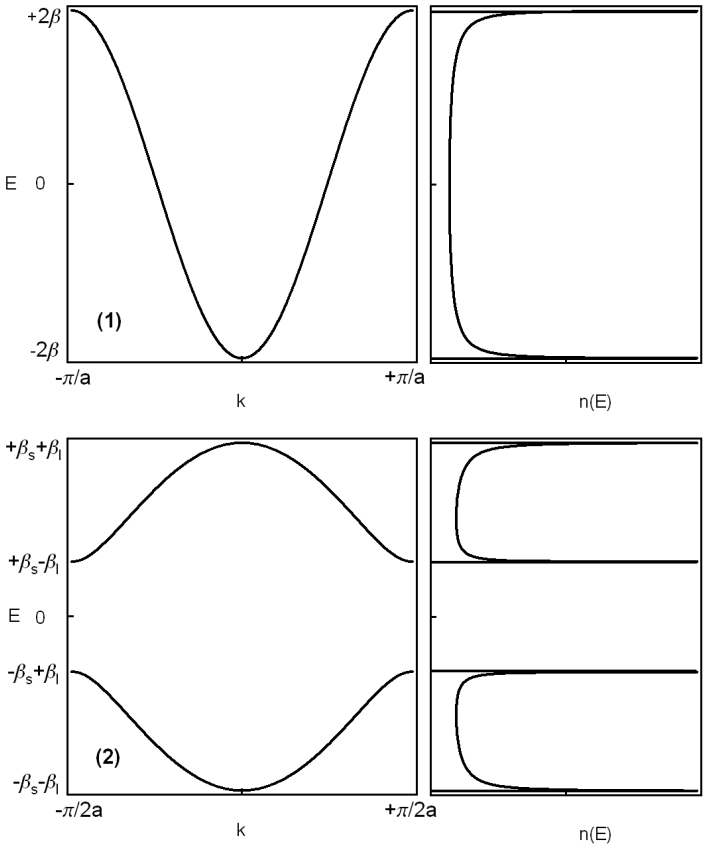

Figure 2.2: Dispersion curves (left panels) and density of electronic states (right panels) for the undistorted (top) and dimerized (bottom) chains.

in which $V(r_{ij})$ possesses a form in inverse power of the interatomic distance[1] r_{ij}:

$$V(r_{ij}) = V_0 r_{ij}^{-p} \tag{2.19}$$

The parameter p is a measure of the repulsion : the larger p, the stronger the repulsive potential. This term diverges in $r = 0$ (unphysically small interatomic distances are prevented).

To insure the stability of the structures, the parameter p has to be larger than q.

The value of the p parameter (calculated for different chemical elements in [80]) in the repulsive part of the cohesive energy is important because it determines if the Peierls distortion appears or not in the structure. For a given density, a low p/q ratio will favor the Peierls distortion, while a high ratio will destroy it (see the simple case studied in the next section).

Density is the second important parameter for the Peierls distortion : a weak density will favor the distortion while a high density tends to annihilate it.

2.4 Relative stability of the structures

If the structure only involves one distance parameter r (between the first neighbors), the cohesive energy can be specified as [24]:

$$E_{coh} = -Ar^{-q} + Br^{-p} \tag{2.20}$$

where A and B are positive coefficients for the attractive and repulsive part, respectively. The bond term coefficient A depends on the atomic structure, on the band filling and on the level of approximation used in the calculation of the density of states. The repulsive energy coefficient B is proportional to the number of nearest neighbors, N_c (see Eq. 2.18). The equilibrium interatomic distance, r_{eq}, is found by imposing a minimum in the cohesive energy $\left.\frac{\partial E_{coh}}{\partial r}\right|_{r=r_{eq}} = 0$ and is given by

$$r_{eq} = \left(\frac{pB}{qA}\right)^{\frac{1}{p-q}} \tag{2.21}$$

Using 2.21 in Eq. 2.20, we obtain the following expression for the cohesive energy at the equilibrium:

$$E_{coh}^{eq} = \frac{A^{\frac{p}{p-q}}}{B^{\frac{q}{p-q}}} \left(\frac{q}{p}\right)^{\frac{p}{p-q}} \left(1 - \frac{p}{q}\right) \tag{2.22}$$

[1] It is also possible to take an exponential form for the attractive and repulsive parts of the total energy.

If we compare the energies at equilibrium for two different structures (1) and (2), for fixed p and q parameters, we obtain:

$$\frac{E^{(1)}}{E^{(2)}} = \left(\frac{A^{(1)}}{A^{(2)}}\right)^{\frac{p}{p-q}} \left(\frac{B^{(2)}}{B^{(1)}}\right)^{\frac{q}{p-q}} \tag{2.23}$$

in which $p-q$ is a positive quantity, as the stabilty of the structures imposes $p > q$. The equality of the energies $E^{(1)}$ and $E^{(2)}$ induces the existence of a critical p/q ratio:

$$\left(\frac{p}{q}\right)_{crit} = \frac{\ln\left(B^{(1)}/B^{(2)}\right)}{\ln\left(A^{(1)}/A^{(2)}\right)} \tag{2.24}$$

It is then possible to determine the more stable structure by comparing the energies of all the competing structures, for given values of the p and q parameters.

Thanks to this simple model, we can understand the mechanism of the symmetry breaking (Peierls distortion) and define a condition for its occurence.

As an example, we can consider the one-dimensional structures in Fig. 2.1 : an undistorted chain (1) and a dimerized chain (2).

If we consider only the first neighbors, it can be shown that the coefficient $A \sim \sqrt{N_c}$ ($N_c = 2$ for the undistorted chain and 1 in the dimerized chain). For the critical p/q ratio we obtain (B being $\sim N_c$) :

$$\left(\frac{p}{q}\right)_{crit} = 2 \tag{2.25}$$

and thus[2] :

- if $p < 2q$ a distortion is present (low-coordination structures are favoured) ;
- if $p > 2q$ no distortion is present (compact structures are more stable).

The dimer is thus stable only if the repulsive term is weak enough (wich is the case for the H atoms), to the contrary of, for example, the Lennard-Jones potential ($p = 12$) used to describe the rare gases. Note that the p parameter increases with the period number of the chemical element considered, which is reflected by the occurence of more compact structures (as, for example, the simple cubic structure of the Po). The value of the parameter q of the attractive term is generally close to 2 or 3 [81].

The comparison of simple one-dimensional structures has been generalized to m-merized (repeated pattern made of one short bond and m long bonds) one-dimensional chains in [24].

[2]More generally, if the attractive part of the cohesion energy is proportional to $N_c^{1/\gamma}$, the critical p/q ratio will be equal to γ.

2.5 Peierls distortion in crystals

Most of the crystalline structures of columns V, VI and VII pure elements and their compounds (with some notable exceptions such as Oxygen or Polonium) can be understood in terms of the Peierls distortion [23]. Indeed, in these systems where bonding is essentially due to the p orbitals (to the contrary of the group IV elements, in which the bonding involves a strong sp-hybridization), the simple cubic structure is naturally favored, because it maximizes the resonance between the directional p orbitals. If only the $pp\sigma$ integrals are considered in the tight-binding approach, the three-dimensional problem is decoupled along the three spatial directions. As in the one dimensional case, the p-band being only partly filled, the undistorted structure is unstable against a *distorted simple cubic* structure, exhibiting short r_s and long r_l bonds, in which the coordination number differs from 6. The *octet rule* [82] :

$$N_c = 8 - N_{sp} \tag{2.26}$$

that links the number of nearest neighbors N_c (or number of short bonds) and the number of s and p valence electrons, N_{sp}, is verified. This expression is valid for pure elements. As the p-band filling ratio varies, different distortion patterns, that open a gap at the Fermi level, are responsible for the structures of the different groups of the periodic table. Due to the distortions, the 90° bond angles of the simple cubic structure are also altered.

2.5.1 Group V

The group V elements possess an s^2p^3 electronic configuration (filled s-band and half-filled p-band). A Peierls distortion, which doubles the elementary cell dimensions in the three directions, produces the 'short-long-short-long' bonds alternation (see Fig. 2.3 (a) and (b)) in the P, As, Sb and Bi crystal structures[3]. According to the octet rule, group V crystalline elements are 3-coordinated (3 short bonds), which actually corresponds to a Peierls distortion of a 6-coordinated structure. The periodicity doubling in each direction of space associated to this distortion (compared to the simple cubic structure, see Fig. 2.3 (c)) causes to the opening of a gap at the Fermi level : group V crystalline elements are semi-conductors or semi-metals.

2.5.2 Group VI

Group VI elements have an s^2p^4 electronic configuration (the p band is 2/3 filled). A threefold multiplication of the elementary cell lenght is observed, together with a sequence of type *long-long-short* distances in the three directions (see Fig. 2.3 (d)) for S, Se and Te elements[4]. These elements possess consequently 2 first neighbors, in agreement with the octet rule. Oxygen (which forms diatomic molecules) and Polonium (which crystallizes in a simple cubic lattice) are two exceptions to this rule.

[3] In P, As, Sb and Bi, the parameter r_l/r_s of the distortion is equal to 1.68, 1.25, 1.17 and 1.12 respectively.

[4] In S, Se and Te, the ratio r_l/r_s is equal to 1.8, 1.5 and 1.31 respectively.

2.5.3 Group VII

Elements from group VII have an s^2p^5 electronic configuration (the p band is 5/6 filled). For all these elements, the crystalline structure consists of an arrangement of diatomic molecules (see Fig. 2.3 (e)).

2.5.4 Alloys

More generally, the octet rule is also valid for alloys. In the case of compounds made of heavy elements, an average coordination number $\overline{N}_c$ is taken into account, as well as an *average* number of electrons $\overline{N}_{sp}$. It has been shown by Gaspard et al. [24] that the periodicity of the distortion is simply imposed by the number of electrons per atom ratio: if the averaged p band filling is equal to n/m (where n and m are prime numbers one for each other), the structure will experience a multiplication of the elementary cell by a factor m. The coordination number will follow the Octet rule (using an average valence $s+p$ electrons number) and the resulting structures are Peierls-distorted. This rule has been verified for numerous chalcogenide compounds (composed of groups IV, V and VI elements), up to very large m values [58] :

- the lightest IV-VI compounds, such as SnS, $SnSe$ and GeS (group $Pbnm$), in which the local order consists of a distorted octahedron with 3 shortest and three longest distances [58] ;
- $\alpha - GeTe$, an heavier IV-VI compound, which is, at room temperature, the binary analogue of the As (A7 rhombohedral phase consisting of a stack of corrugated planes of alternating atoms with $N_c = 3$) [83] ;
- some V-VI compounds, such as As_2Te_3 [84] or Sb_2Te_3 [60] (in which the average p-band filling is equal to 3/5 and the structure consist of a stacking of 5 layers of Sb_2Te_3 units) and Sb_2Te [59].

All these compounds are semi-conductors [85]. The space groups and cell parameter of the $GeTe$, Sb_2Te_3 and Sb_2Te compounds are given in the Chapter 1 section 1.4.1.

The case of $GeTe$ is particular as, at $T = 703$ K, this compound undergoes a crystalline phase transition to a $NaCl$-type structure, called $\beta - GeTe$ ($N_c = 6$) [83].

The bonding properties described here also provide an explanation for the instability of the undistorted rocksalt structure of the $(GeTe)_x(Sb_2Te_3)_y$ pseudo-binary alloys (in metastable phase) against the Peierls distortion (see Chapter 1).

2.6 Peierls distortion in liquids

The initial description of the Peierls distortion was only valid for crystalline solids. Nevertheless, some experiments have shown that it was also present, locally, in some liquids

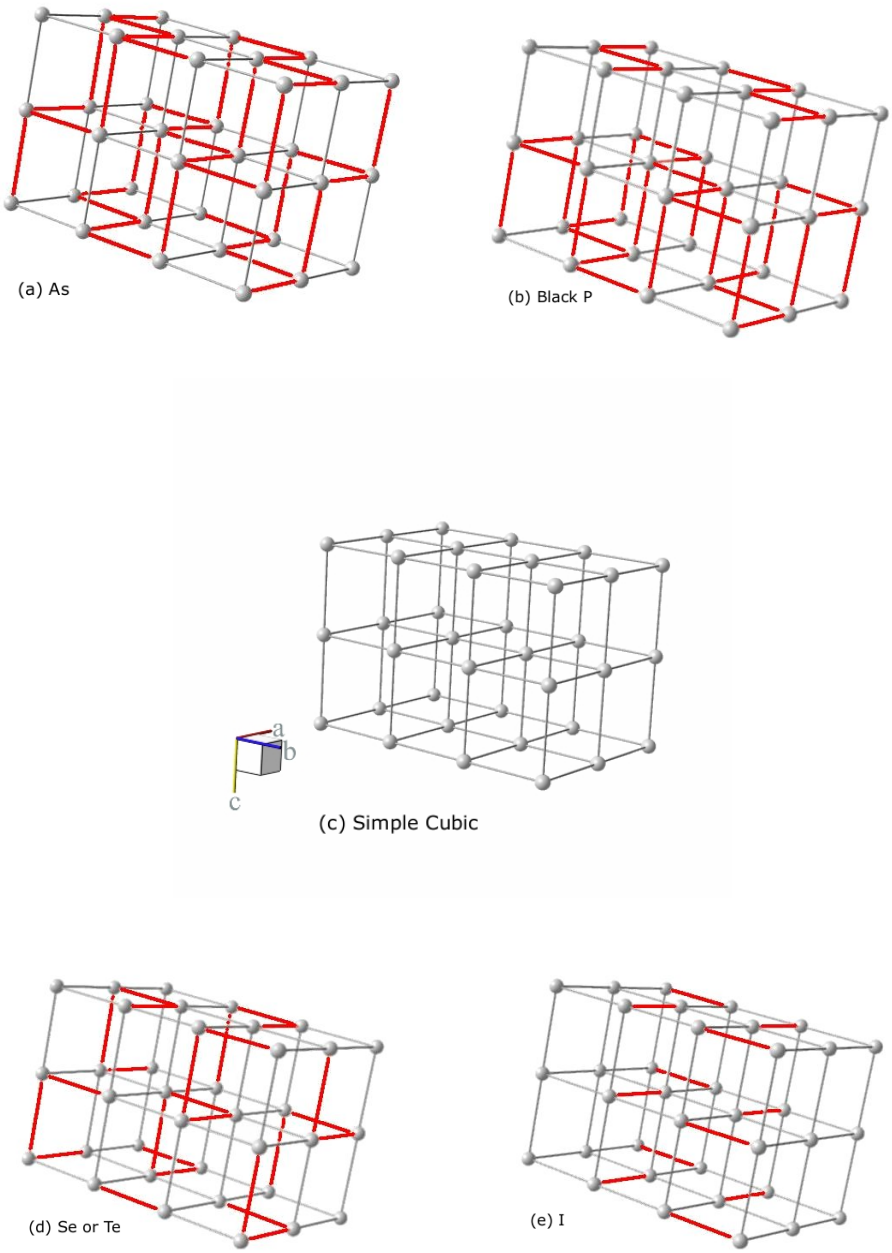

Figure 2.3: Schematic representation on a regular cubic lattice of the As (a), black P (b), Te (d) and I (e) structures, compared to the simple cubic lattice (c). Shorter interatomic distances are indicated in red. In As and P the Peierls distortion produces corrugated planes of threefold bonded atoms ($N_c = 3$). In Se and Te the Peierls distortion produces helicoidal chains of atoms ($N_c = 2$). In I it results in diatomic molecules.

or amorphous systems [86, 23, 87], such as As, Se or Te, as long as the temperature is not too high. The case of pure liquid elements is briefly presented hereafter, and will be detailed in Chapter 3. The Peierls distortion can also be present in liquid compounds, as we will show in Chapter 8 for As_2Te_3 just above the melting point.

2.6.1 Group V

The fact that the Peierls distortion is maintained upon melting depends on the nature of the element (see Chapter NTE for further details). Two cases are observed:

- For the lighter elements, such as P or As, the coordination number remains close to 3 upon melting [23].
- For heavier elements, such as Sb and Bi, N_c increases strongly upon melting [87]. In this case, the thermal energy is higher than the distortion energy and the distortion is destroyed.

Recently, Chiba et al. evidenced, by X-ray diffraction experiments, the suppression of the Peierls distorsion in liquid As and GeX ($X = S, Se, Te$) under pressure [88].

2.6.2 Group VI

Upon melting, the coordination number remains equal to 2 for S and Se. In Te, it increases to 2.7 (see Chapter 3). It can be shown that these compounds keep locally a Peierls distorted arrangement in the liquid.

2.6.3 Liquid IV-VI semi-conductors

Neutron scattering experiments performed on a series of liquid IV-VI compounds [89] showed that they exhibit different structural modifications upon melting. The Peierls distortion is still present in liquid SnS, $SnSe$ and $SnTe$, and modified for GeS and $GeSe$ (inducing a coordination number $\sim 3 + 1$).

In $GeTe$ ($T_m = 1000$ K), an unusual evolution of the coordination number upon melting is observed, as N_c decreases from $Z = 6$ in the solid to $Z \sim 3$ in the liquid (similar to what found in the low temperature crystalline form). This decrease of N_c is combined with the persistence of a semiconducting behavior in the liquid. When T increases in the liquid phase, $GeTe$ gradually evolves to a metallic state (and N_c increases accordingly).

2.6.4 Liquid Phase Change-Materials

Phase-Change materials of type $(GeTe)_x(Sb_2Te_3)_y$ were found (by neutron diffraction) to exhibit an octahedral local order in the liquid phase [69], which can become distorted through a volume expansion (showed by FPMD simulations on $Ge_1Sb_2Te_4$ [41]). An

octahedral local order with distorsion was also evidenced (by FPMD simulations) in liquid $SnSe_2$ [90], at variance with the other IV-VI alloys, such as $GeSe_2$, that display a tetrahedral ordering in the liquid phase.

Chapter 3

Negative thermal expansion in liquids

A part of this thesis is dedicated to the investigation, with different methods, of the negative thermal expansion in some liquid covalent compounds. The aim is to follow the structural and dynamical evolution of these alloys with temperature, and to understand which phenomena are responsible for this thermodynamical anomaly.

In the present chapter, after a brief theoretical review of the normal behavior of liquids with temperature, we will describe the anomal behavior observed in some pure elements and compounds in liquid phase.

We will also define some important parameters for the discussion of the negative thermal expansion (for example, thermal expansion coefficient or compressibility).

3.1 Behavior of liquids with temperature

It is well kown that most materials increase their volume, both in solid and liquid phase, when temperature increases. This phenomenon comes from the anharmonicity of the interatomic potential, as we will see in the next paragraph. The liquid phase is a condensed phase, as the solid, but the lack of the simplifications due to the translation symmetry found in the crystals makes it difficult to study. The liquid phase presents a short range order but no long range order (> 10 Å), which allows only for a local study of the atomic environment. However, the chemical bonding is essentially local, and does not generally evolve much upon melting. The local order in the liquid phase is also, for most compounds, similar to that found in the solid.

Thermal expansion Interatomic potentials are, in first approximation, harmonic (and thus spherically symmetric, see the red curve in Fig. 3.1). A system which possesses such a quadratic form (or more generally a symmetric form) for its energy versus the atomic displacements (relatively to the equilibrium positions) cannot undergo any volume variation when temperature increases : no thermal expansion occurs. To account for the

thermal expansion, we have to consider, for a classic oscillator, the effect of anharmonic terms in the potential energy (which is related to the average distance between a pair of atoms).

Let us suppose that the potential energy of atoms displaced by x from their equilibrium position at 0 K obeys the following expression :

$$U(x) = ax^2 - bx^3 + cx^4 \tag{3.1}$$

with a, b and $c > 0$. For small oscillations around the minimum $x = 0$, this expression gives a correct representation of the interatomic potential. The average displacement (calculated using the Boltzmann distribution which weights the possible x values by their thermodynamical probability) is equal to

$$\langle x \rangle = \frac{\int_{-\infty}^{\infty} x \mathrm{e}^{-U(x)/k_B T} dx}{\int_{-\infty}^{\infty} \mathrm{e}^{-U(x)/k_B T} dx} \tag{3.2}$$

For displacements such that the anharmonic terms in Eq. 3.1 are small compared to $k_B T$, we can make a series expansion of the exponential in Eq. 3.2, which finally gives for the average displacement :

$$\langle x \rangle = \frac{3b}{4a^2} k_B T \tag{3.3}$$

The expansion is thus proportional to T, as seen in Fig. 3.1. In this figure, the green dotted line represents, in the anharmonic case, the average displacement compared to the equilibrium position. It increases when the vibrational amplitude increases, which corresponds to a *positive* thermal expansion with temperature.

Thermal expansion coefficient The thermal expansion coefficient, α_P, is defined by the relative volume variation with temperature:

$$\alpha_P = \frac{1}{3V} \left(\frac{\partial V}{\partial T} \right)_P \tag{3.4}$$

Bulk modulus Another important parameter for the study of the volume evolution with temperature is the bulk (or incompressibility) modulus[1], B, defined as:

$$B^{-1} = -\frac{1}{V} \left(\frac{\partial V}{\partial P} \right)_T \tag{3.5}$$

3.2 Some examples of anomalous liquids

3.2.1 Water

Water presents numerous anomalies, among which some are also reported in covalent systems. Water is characterized by an unusual thermodynamical behavior, whose origin

[1]For example, the incompressibility modulus of As at zero pressure is equal to ~ 40 GPa.

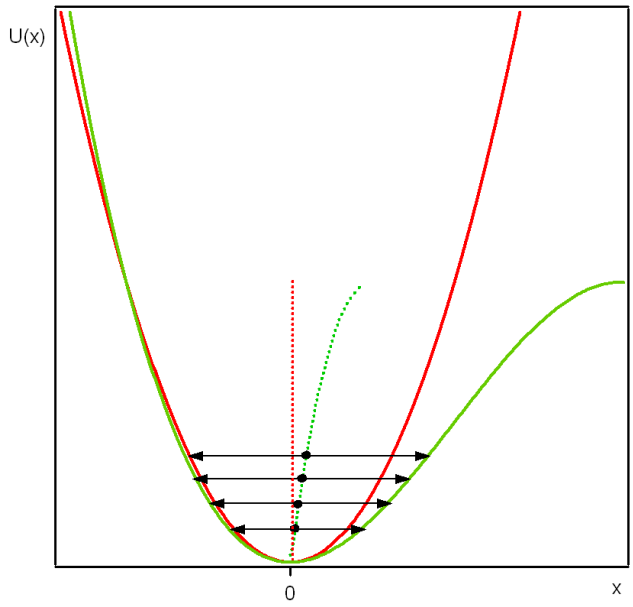

Figure 3.1: Potential energy $U(x)$. The minimum is located in the equilibrium position (here $x_0 = 0$). The red curve represents a quadratic form of the potential energy, the green curve represents the energy including the anharmonic terms (see Eq. 3.1). Dotted lines indicate the average atomic displacement evolution with T. This average displacement is 0 in case of the harmonic potential and increases with vibrational amplitude increase in the case of an anharmonic potential, corresponding to a thermal expansion.

is not totally understood yet. Water is exceptional for several reasons. In particular, it has a thermal expansion coefficient α_P (defined in Eq. 3.4) three times smaller than that of a typical liquid and, with temperature decrease, this anomaly becomes stronger. At 4°C, a density maximum is observed (if temperature gets lower, the volume increases, to the contrary of the usual behavior). Fig. 3.2 shows the water density evolution with temperature, between −40°C (undercooled water) and 100°C.

It is generally accepted that the observed anomalies in water come partly from the unusual characteristics of the hydrogen bonding [91, 92] and, thus, if the effects are similar to those observed in some covalent liquid alloys, their origin is different.

3.2.2 Group Va: *As*

In Arsenic ($T_m = 1090$ K), the coordination number, N_c, does not change upon melting [23, 87], compared to its value in the solid (where $N_c = 3$, according to the Octet rule, see Chapter 2). The coordination number was found slightly higher ($N_c = 3.5$) by numerical tight-binding simulations [94], with bonding occuring mostly at an angle of 90°. At highest

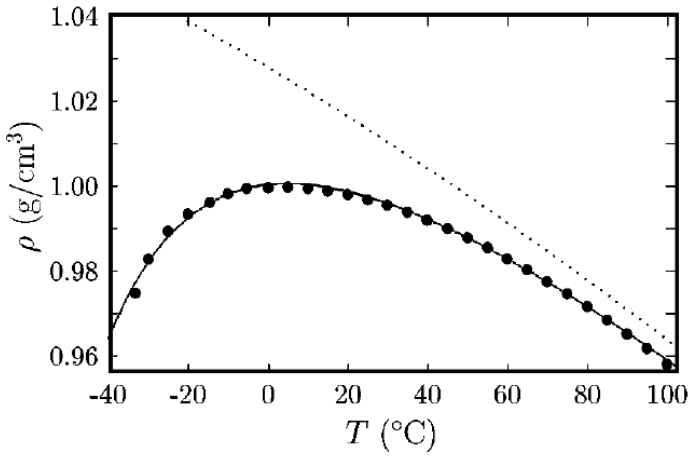

Figure 3.2: Water density evolution with temperature [93, 92]. We observe the unusual increase of the density up to a maximum located at 4°C. The dotted line corresponds to a normal expansion.

temperature, N_c could reach 6, as in the simple cubic [95], but this is still hypothetical as experimental data are lacking up to now. Molten As is a semi-conductor, to the contrary of antimony or bismuth which possess a metallic character [19, 96] and a higher N_c.

Sound velocity measurements with temperature in some liquid group V elements (As, Sb and Bi) and alloys ($AsSb$ and $AsBi$) have been performed by Tsuchiya [97, 98]. Sound velocity v_s, which depends on the interatomic potential, can be a very sensitive tool to evidence the existence of structural changes in liquids. It was measured by Tsuchiya as followed : piezoelectric ceramics are used to produce and detect a sound pulse, which permits to measure the time for sound to travel between one delay-line and a reflector. Note that the measurements on pure liquid As are made in a limited T range because of its high vapor pressure and its toxicity. Sound velocity measurements with temperature for As, Sb and Bi are shown in Fig. 3.3, together with results for a wide variety of pure liquid elements [97, 98, 99]. An unusual dependence of v_s with T is observed in liquid and undercooled liquid As : it increases very sharply when T rises, to the contrary of most metallic liquids, such as Sb or Bi, in which v_s decreases slowly and almost linearly. Among all molten elements, such a behavior of v_s has, up to now, only been observed in pure tellurium, whose v_s evolution with temperature is also plotted in Fig. 3.3.

From the sound velocity measurements in As shown in Fig. 3.3, Tsuchiya calculated the adiabatic compressibility, K_s :

$$K_s = \rho^{-1} v_{sound}^{-2} \tag{3.6}$$

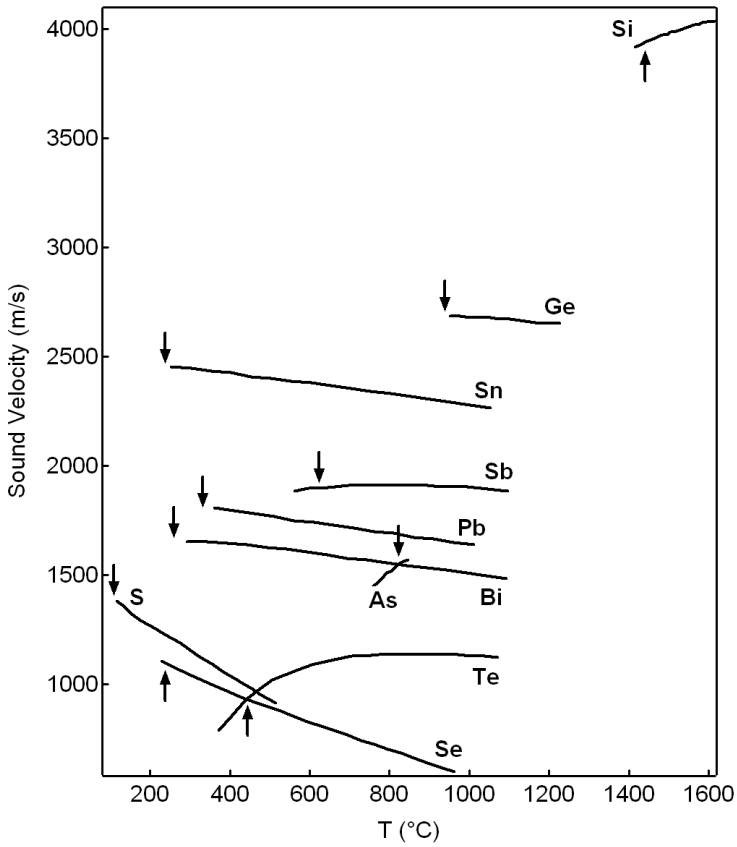

Figure 3.3: Sound velocity evolution with temperature for selected liquid or undercooled liquid pure elements. Melting temperatures are indicated by vertical arrows [1, 97, 98, 99].

where ρ is the density, that Tsuchiya estimated from a linear extrapolation of the results of McGonial and Grosse [100] (see Fig. 3.10). As we can see in Fig. 3.4, the As compressibility is about twice as large as that of Sb or Bi. This is related to the fact that, the local structure of liquid As being close to the solid structure ($N_c \sim 3$), its bonding is different from that of Sb and Bi, for which the coordination number is much larger [23]. The structure of liquid As can be viewed as Peierls distorted, as in the crystalline phase : around one atom in liquid As, besides the $3-4$ closest neighbors, there are $2-3$ other neighbors with longer interatomic distances [94]. These longer distances can be shortened more easily than the shortest ones, the repulsive term of the interatomic potential being less important. This explains the strong compressibility measured. We also see in Fig. 3.4 the strong dependency with temperature of the As compressibility, which implies that the As structure should vary rapidly around the melting temperature. According to Tsuchiya, the undercooled As compressibility could have a maximum (as observed in Te, see section 3.2.3) in a temperature range lower than the one reached in this experiment.

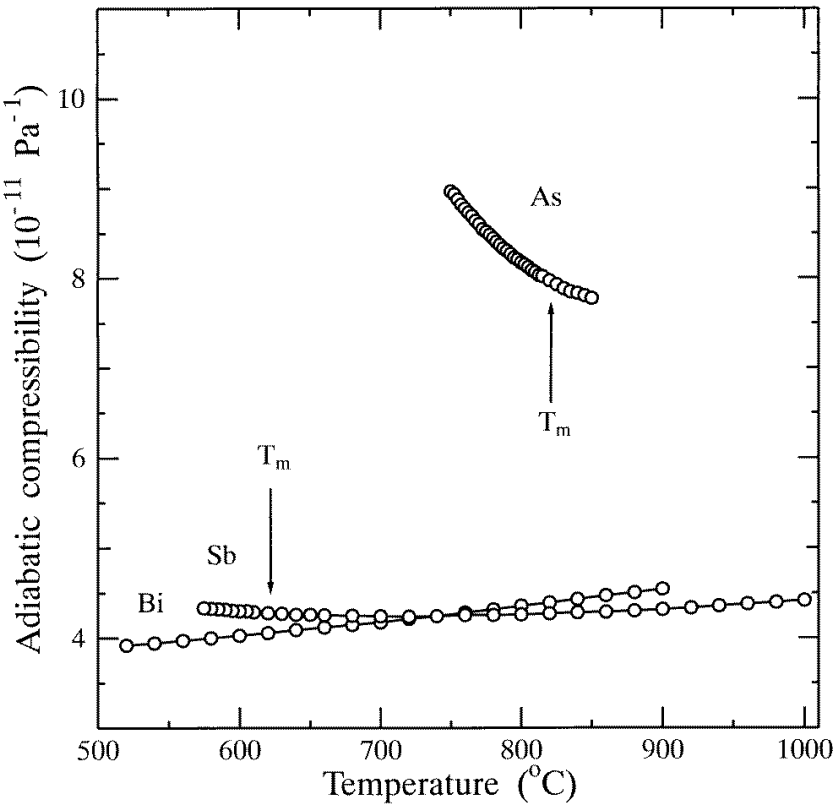

Figure 3.4: Adiabatic compressibility K_s for liquid As, Sb and Bi [97]. Melting temperatures are indicated with vertical arrows.

Sb, Bi Upon melting, the Sb and Bi coordination numbers N_c increase strongly, to the contrary of the situation encountered in As. Indeed, they go from $N_c = 3$ in the solid state (according to the Octet rule, see Chapter 2) to $N_c = 8.7$ for Sb ($T_m = 904$ K) and to $N_c = 8.8$ for Bi ($T_m = 544$ K). Molten Sb and Bi elements are metallic [101].

We have seen in Fig. 3.3 that the sound velocity evolution with temperature of Sb or Bi in the liquid phase does not show any anomaly. Pure Sb and Bi do not undergo any negative thermal expansion [98].

3.2.3 Group VIa: *Te*

The anomalous behavior of sound velocity in undercooled liquid Te is shown in Fig. 3.3, by comparison with a wide variety of liquid and undercooled pure elements. As observed in Fig. 3.6, this is correlated with a pronounced negative thermal expansion (NTE) in the undercooled region, just below the melting point. Within a 160 K range, the molar volume decreases by ~ 4 %, which is very unusual. This NTE is also accompanied by a maximum in the specific heat C_p, as shown in Fig. 3.7 [1].

These thermal anomalies have been correlated with the temperature evolution of the coordination number N_c by neutron diffraction measurements [102, 103, 27]. The Te coordination number N_c, which is equal to 2 in the solid (see Chapter 2), increases up to ~ 2.7 upon melting ($T_m = 723$ K), and reaches ~ 3 at higher T (50 K above T_m). When pure liquid Te is undercooled, N_c decreases, and a structure with $N_c \sim 2.4$ is observed, which is closer to the crystalline coordination number. To the contrary of Se, which remains semi-conductor up to high temperatures, Te becomes metallic upon melting [104].

S, Se Liquid S and Se elements, on the other hand, do not exhibit any NTE.

The liquid sulphur at temperatures close to the melting point ($T_m = 386$ K) consists of annular S_8 molecules (ring), as in the solid. The coordination number is thus equal to 2, according to the octet rule, both in the solid and in the liquid phases (see Chapter 2). At $T = 432$ K, liquid S shows a second order transition to a polymeric structure. With this transition, its viscosity increases strongly, the coordination number N_c remaining equal to 2 [105]. Sulphur is an insulator.

The liquid Se has a chain-like structure above the melting temperature ($T_m = 392$ K), as in the solid (see Chapter 2, solid Se, as well as Te, consists of helicoïdal chains, resulting from a Peierls distortion of the simple cubic structure). Its coordination number remains close to 2. This structure persists above 1300 K and transforms, around 1800 K and under high pressure, in a denser structure of interconnected chain segments [106]. In the same range of temperature and pressure, the conductivity increases strongly and Se, which was semi-conductor, becomes metallic.

3.2.4 Alloys

Liquid As and Te are not the only liquids to exhibit an unusual evolution with temperature as many alloys based on these elements also show thermodynamical anomalies (in sound velocity, molar volume, specific heat, ...) in the undercooled liquid and/or in the regular liquid state. These anomalies are observed on a variable temperature range, depending on the compound. Fig. 3.5 shows the sound velocity evolution with T of a variety of Te-based binary alloys [107, 108, 2, 98, 20]. We observe that, if some alloys have a normal dependence of v_s with T (Ag_2Te, $SnTe$ or $CdTe$ for example), other show an anomaly (As_2Te_3, In_2Te_3 and Ga_2Te_3).

We report hereafter some experimental results obtained by Tsuchiya for $GeTe$ [2] and $AsTe$ [98] compounds, and for some phase-change materials alloys [20]. Some of these compounds are investigated in this work (see next chapters) either by neutron diffraction and inelastic scattering experiments, or by computer simulations, to establish their structural and dynamical evolution with temperature.

GeTe alloys

The molar volume evolution with temperature of the rich-Te $GeTe$ system is plotted in Fig. 3.6. In each compound, except $GeTe$, a negative thermal expansion is observed, either in the liquid or in the undercooled liquid region.

This volume anomaly is correlated with anomalous behavior of other thermodynamical properties, as shown in Fig. 3.7 for the specific heat C_p evolution with temperature. A peak is observed for all $GeTe$ alloys with Ge concentration ranging from 0 % to 20 %.

The case of the eutectic $Ge_{15}Te_{85}$, for which the anomaly occurs entirely above the melting point (because of its lower melting temperature), will be discussed in Chapter 6.

AsTe alloys

The molar volume evolution with temperature for $AsTe$ compounds is plotted in Fig. 3.8 [98]. The NTE observed in undercooled liquid Te shifts to higher temperatures when the As concentration increases in the $AsTe$ alloy. The corresponding thermal expansion coefficients α_P are plotted with respect to T in Fig. 3.9. On each curve, a negative minimum is observed, which coincides with the volume decrease in Fig. 3.8.

Analogy between *As* and *Te* Experimental results for $AsTe$ systems suggested structural changes similar to the ones observed in pure Te, for As concentrations going up to 70 % [98]. In all cases, see Fig. 3.8, a negative thermal expansion is observed. Such a behavior is expected if molten As undergoes structural changes upon heating, as does pure Te [1]. The molar volume evolution with temperature of undercooled liquid As is plotted in Fig. 3.10. It has been obtained by Tsuchiya from extrapolation of $AsSb$ and

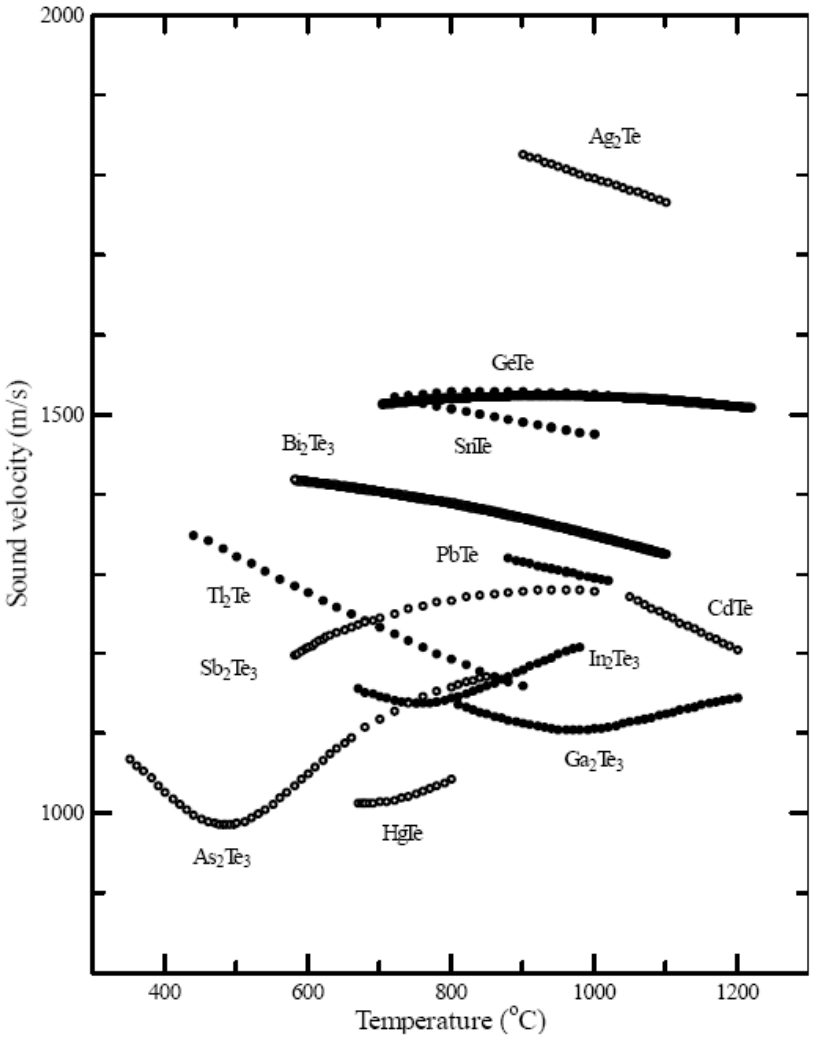

Figure 3.5: Sound velocity evolution with temperature for liquid or undercooled binary alloys based on Te [107, 108, 2, 98, 20].

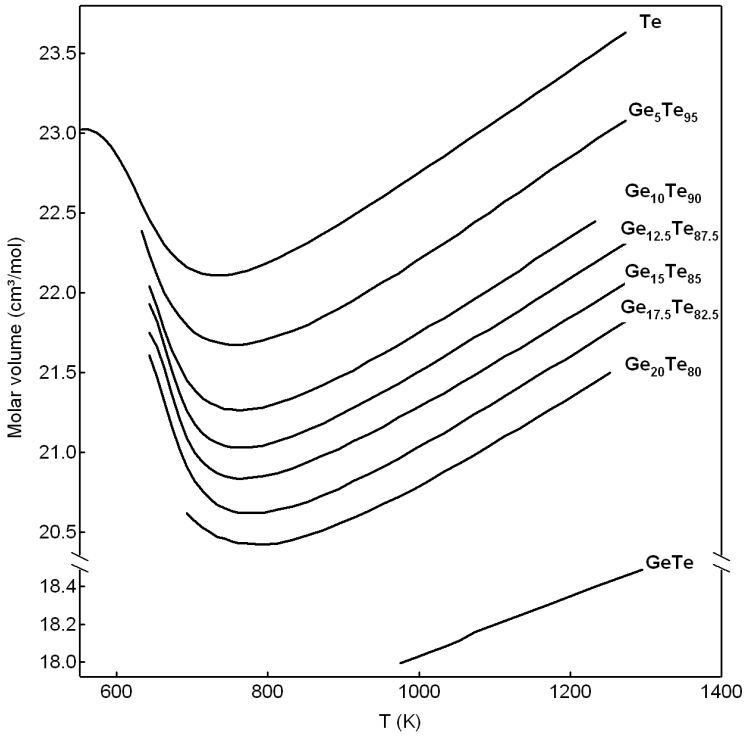

Figure 3.6: Molar volume evolution with temperature for liquid $GeTe$ binary alloys [2].

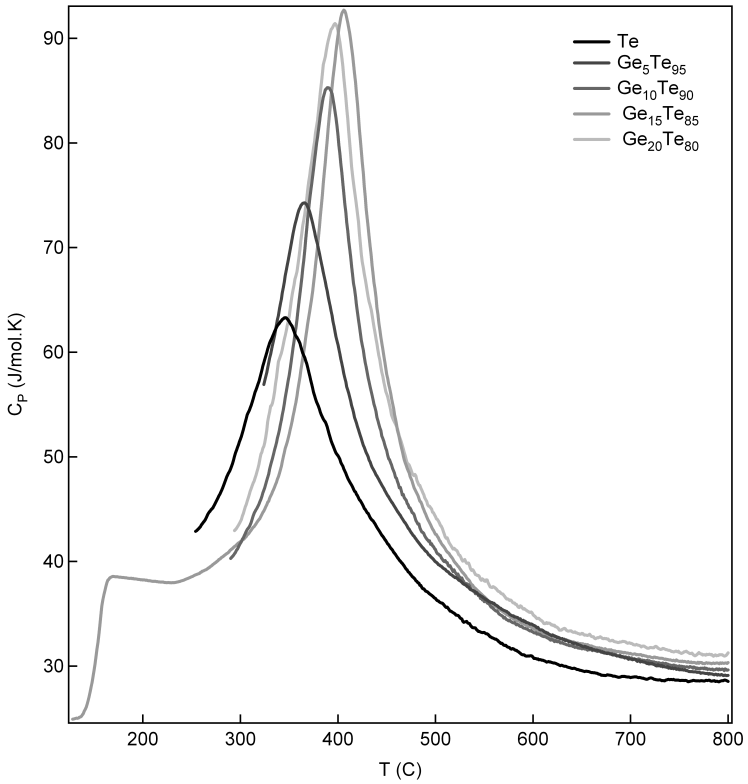

Figure 3.7: Specific heat, C_p, evolution with temperature for liquid $GeTe$ binary alloys [2].

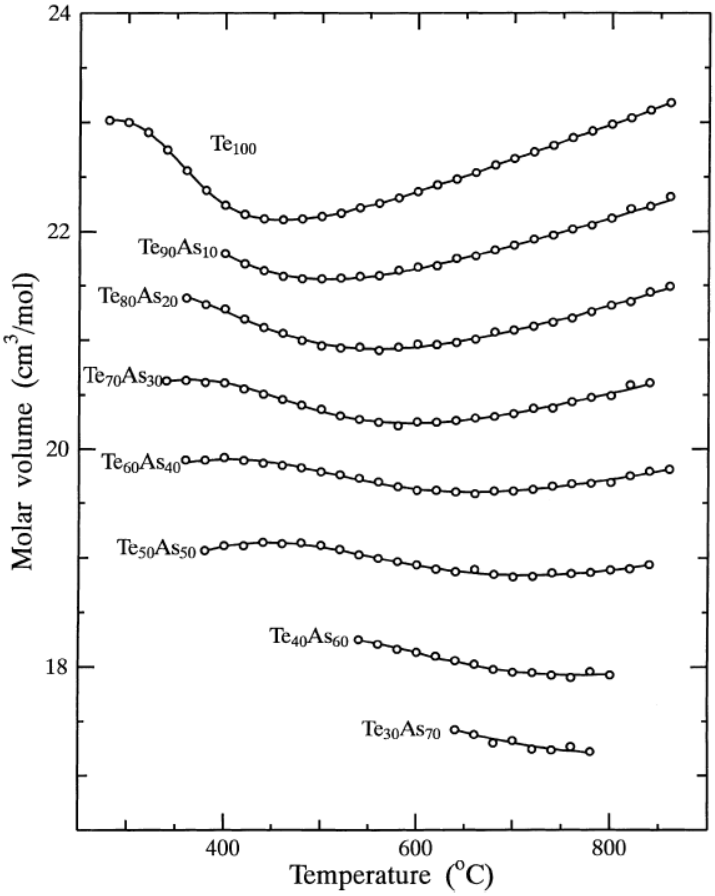

Figure 3.8: Molar volume evolution with temperature for $AsTe$ compounds. Solid lines are non-linear fits, from which the thermal expansion coefficients in Fig. 3.9 were calculated. For each compound a NTE is observed. Reproduced from [98]. ($T_m^{Te} = 723$ K and $T_m^{As} = 1090$ K).

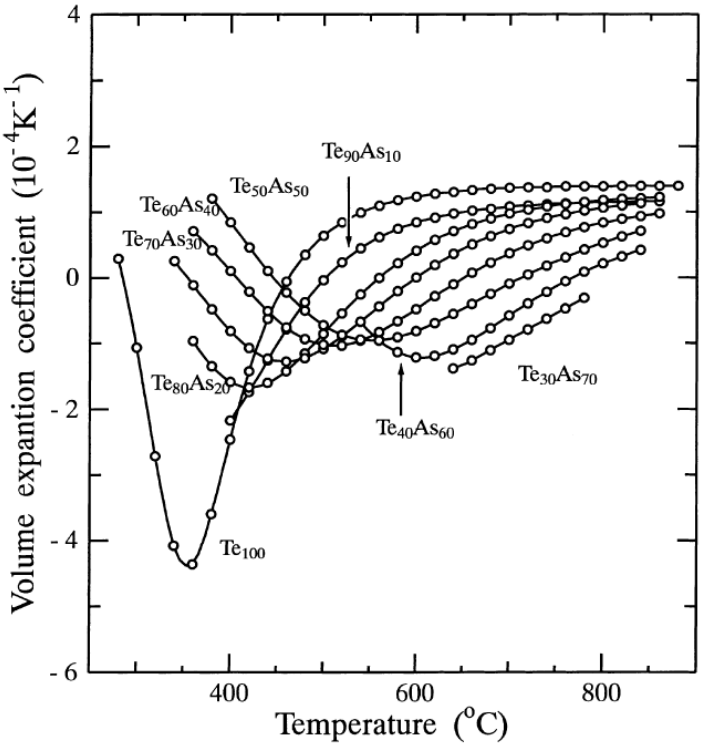

Figure 3.9: Thermal expansion coefficient evolution with temperature for $AsTe$ compounds. On each curve, a negative minimum is observed, which coincides with the volume inflexion point in Fig. 3.8. Reproduced from [98]. ($T_m^{Te} = 723$ K and $T_m^{As} = 1090$ K).

$AsBi$ compounds molar volume measurements [98]. We observe that the molar volume reaches a minimum just below the melting point, and increases with further undercooling. Consequently, the thermal expansion coefficient reaches a negative minimum in the same region, around 1013 K. It was suggested that the situation in the liquid As at the melting point is similar to that of liquid Te.

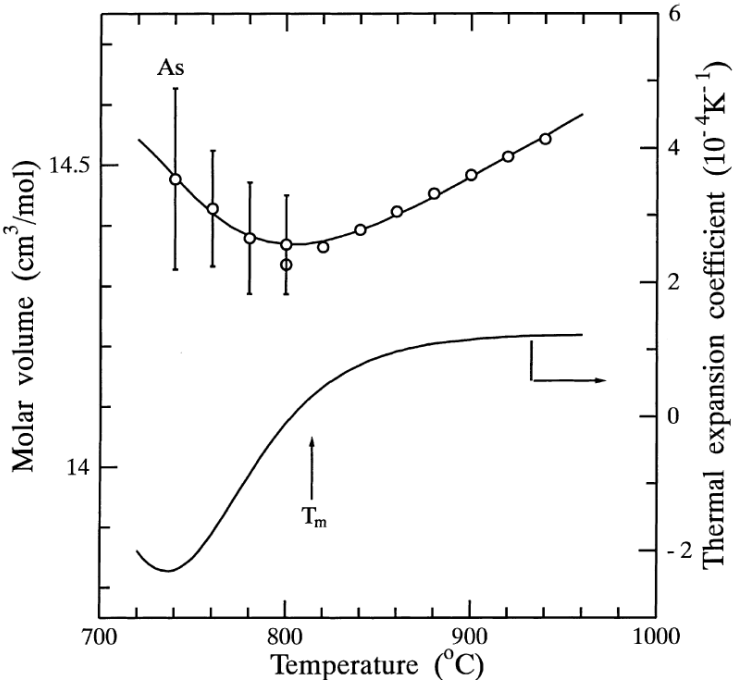

Figure 3.10: Molar volume (upper curve) and thermal expansion coefficient (lower curve) for liquid Arsenic. Reproduced from [98].

GeSbTe phase-change alloys

Tsuchiya and coworkers also studied the behavior with temperature of some liquid alloys used as phase-change materials, such as the pseudo-binary alloys of type $(GeTe)_xSb_2Te_3$ and $(GeTe)_xSb$. The sound velocity evolution with temperature for a variety of compounds is plotted in Fig. 3.11 [20]. All these curves have a maximum and a more or less pronounced tendency to fall down when temperature decreases (especially in the Te-rich alloys), but no minimum is observed (contrary to the undercooled Te).

No anomaly is found in the molar volume evolution of $GeSbTe$ phase-change materials in liquid phase (see Fig. 3.12).

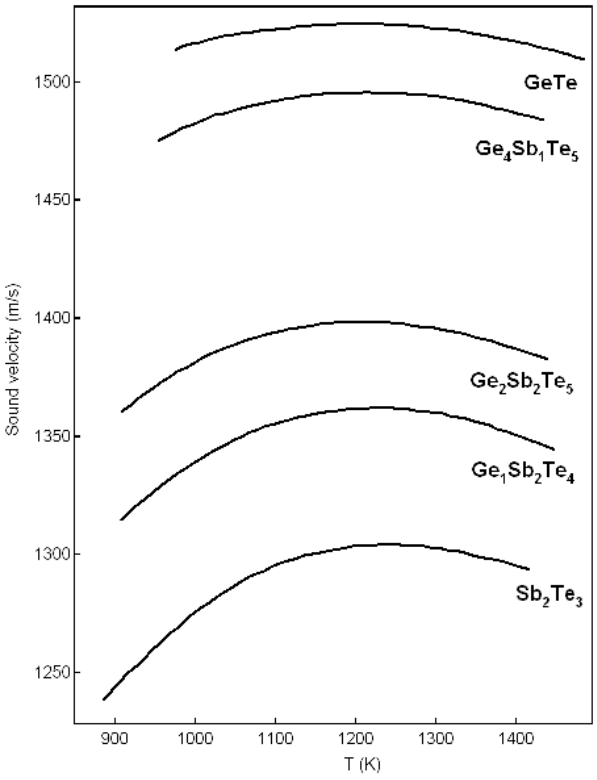

Figure 3.11: Sound velocity evolution with temperature for liquid binary or ternary $GeSbTe$ alloys [20].

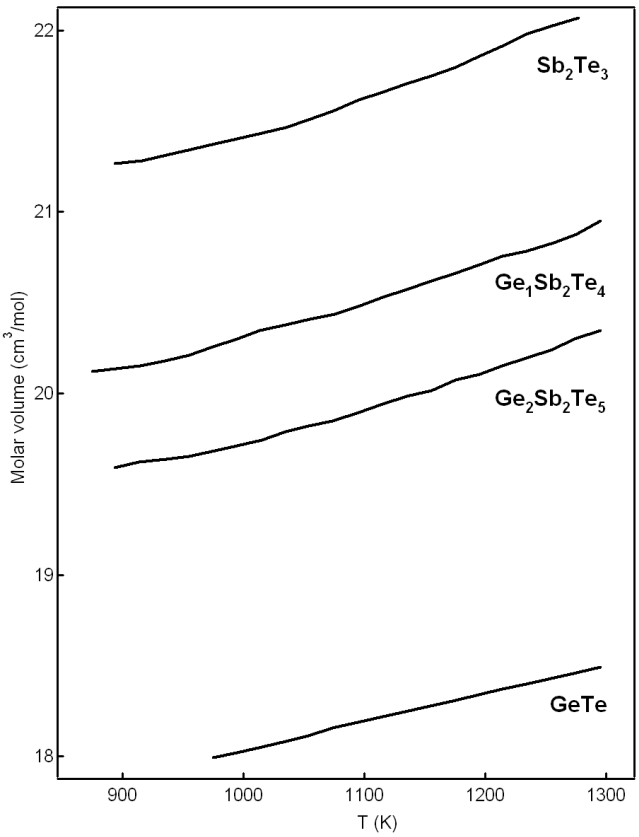

Figure 3.12: Molar volume evolution with temperature for liquid binary or ternary $GeSbTe$ alloys [20].

Chapter 4

Neutron diffraction and inelastic scattering

The study of condensed matter at the atomic scale can be achieved by various methods such as high resolution electron microscopy, tunneling microscopy, X-ray absorption spectroscopy, and neutron or X-ray scattering experiments. We performed neutron diffraction experiments on liquid and amorphous covalent compounds in order to analyze their structure. The liquids and glasses possess a short range order but lack any long distance order, compared to crystals. This specificity imposes that we describe the structure with probabilistic atomic distribution functions, to the contrary of crystals, where periodicity allows a description of a macroscopic structure with a few parameters (unit cell and fractional coordinates). In addition, we did inelastic neutron scattering experiments to obtain some information on the dynamical properties of the materials we study.

We performed five experiments on the two-axis diffractometer D4, devoted to disordered materials, at the Institut Laue-Langevin (ILL), in Grenoble, to study the structure of, among others, As_2Te_3, $GeSb_6$, $SnSe_4$ and Sb_2Te compounds in the liquid phase, and some phase-change materials (in particular $Ge_1Sb_2Te_4$ and $Ge_2Sb_2Te_5$) in the amorphous phase. We also performed three inelastic scattering experiments on the time-of-flight spectrometer IN6, also at the ILL, in order to study the vibrational properties of alloys that exhibit a negative thermal expansion in the liquid phase (Te-rich $GeTe$ alloys and As_2Te_3) and their temperature evolution.

In this chapter, after a short summary of the general theory of neutron scattering, we will recall the basic theory of neutron diffraction by liquid and glassy materials, the data treatment of diffraction experiments and the presentation of the D4 instrument. The remaining sections are devoted to a brief theory of inelastic neutron scattering and a presentation of the IN6 instrument.

4.1 Neutron properties

In the nuclear reactor core, the neutrons are produced from the U^{235} isotope fission. The neutrons are cooled down (slowed down) to about room temperature. The neutron wavelengths are distributed around an average value given by the formula

$$\lambda(\text{Å}) = \frac{30.8}{\sqrt{T(\text{K})}} \tag{4.1}$$

The thermal neutrons ($T = 300$ K) possess an energy of about 25 meV and a wavelength of about 1.8 Å (corresponding to a velocity $v = 2200$ m/s). The *cold* or *hot sources*[1] thermalize the neutron at 25 K and 2000 K respectively : they thus allow to obtain longer (about 6 Å) or shorter (about 0.7 Å) wavelengths.

4.2 Generalities on neutron scattering

According to van Hove [109] the scattered intensity is given by the double differential scattering cross-section, $d^2\sigma/d\Omega dE$, which is the probability density for a neutron with an incident energy E_0 impinging on a sample of N scatterers, with scattering lenghts b_i and located at the i sites, to be scattered with a wavevector $\mathbf{k}_f$ and a final energy comprised between E and $E + d(\hbar\omega)$, in a solid angle element $d\Omega$. It is written :

$$\frac{d^2\sigma}{d\Omega d\omega} = \frac{k_f}{k_0}\frac{1}{N}\sum_{i,j}\overline{b_i b_j}\frac{1}{2\pi}\int_{-\infty}^{\infty}\left\langle e^{-i\mathbf{q}\cdot\mathbf{r}_i(0)}e^{i\mathbf{q}\cdot\mathbf{r}_j(t)}\right\rangle e^{-i\omega t}dt \tag{4.2}$$

where the i, j sum is over the different isotopes and species in the sample. The brackets $\langle\rangle$ denote the thermal average of scattering centers positions $\mathbf{r}_i(0)$ and $\mathbf{r}_j(t)$ and the horizontal bars indicate the average on all the i sites by the scattering length distribution of each atomic species. For neutrons, this distribution of b_i has two possible origins : the spins and the isotopic distribution for one species in the sample.

The series 4.2 can be split into two subseries : a *coherent* term ($i \neq j$) and an *incoherent* term ($i = j$) :

$$\frac{d^2\sigma}{d\Omega d\omega} = \frac{1}{4\pi}\frac{k_f}{k_0}\left[\sigma_{coh}S(\mathbf{q},\omega) + \sigma_{incoh}S_{incoh}(\mathbf{q},\omega)\right] \tag{4.3}$$

Coherent term The coherent term depends on the relative positions of the scattering centers and involves the so called *dynamic structure factor*, $S(\mathbf{q},\omega)$. It is the time-Fourier transform of the intermediate scattering function $F(\mathbf{q},t)$, defined as :

[1] The cold and hot sources are respectively made of a tank of liquid deuterium at 25 K and a block of graphite at 2000 K.

$$F(\mathbf{q},t) = \frac{1}{N}\sum_{i,j\neq i}^{N}\left\langle e^{-i\mathbf{q}\cdot\mathbf{r}_i(0)}e^{i\mathbf{q}\cdot\mathbf{r}_j(t)}\right\rangle \tag{4.4}$$

and thus

$$S(\mathbf{q},\omega) = \frac{1}{2\pi}\int_{-\infty}^{\infty}F(\mathbf{q},t)e^{-i\omega t}dt \tag{4.5}$$

Incoherent term The incoherent dynamic structure factor is the time-Fourier transform of the incoherent intermediate scattering function $F_{inc}(\mathbf{q},t)$, defined as:

$$F_{inc}(\mathbf{q},t) = \frac{1}{N}\sum_{i=1}^{N}\left\langle e^{-i\mathbf{q}\cdot\mathbf{r}_i(0)}e^{i\mathbf{q}\cdot\mathbf{r}_i(t)}\right\rangle \tag{4.6}$$

where the same scatterer appears at times 0 and t, and thus

$$S_{inc}(\mathbf{q},\omega) = \frac{1}{2\pi}\int_{-\infty}^{\infty}F_{inc}(\mathbf{q},t)e^{-i\omega t}dt \tag{4.7}$$

Coherent and incoherent scattering lengths In Eq. 4.3, we have introduced the *coherent* and *incoherent* scattering cross sections $\sigma_{coh} = 4\pi b_{coh}^2$ and $\sigma_{incoh} = 4\pi b_{incoh}^2$, in which the *coherent* and *incoherent* scattering lengths are used. Assuming that two b_i on different sites are uncorrelated, one has for the average of the products of $b_i b_j$ in the case of a monoatomic system[2] :

$$\overline{b_i b_j} = \overline{b_i b_i} = \overline{b^2} \qquad i = j \qquad \text{(same site)} \tag{4.8}$$

$$\overline{b_i b_j} = \overline{b}_i\overline{b}_j = \overline{b}^2 \qquad i \neq j \qquad \text{(different sites)} \tag{4.9}$$

and we can define the coherent

$$b_{coh} = \overline{b} \tag{4.10}$$

and incoherent

$$b_{incoh} = \sqrt{\overline{b^2} - \overline{b}^2} = \overline{|b - \overline{b}|} \tag{4.11}$$

scattering lengths, which are respectively the average value of the b in the sample and the standard-deviation of the scattering lengths distribution.

4.3 Neutron diffraction by liquids and glasses

The following theoretical developments are mainly inspired from the review paper of H. Fisher, A. Barnes and Ph. Salmon: *Neutron and X-ray diffraction studies of liquids and glasses* [110].

[2]This can be generalized for a polyatomic system.

The study of liquid and amorphous materials started with X-ray sources but the low penetration depth of the X-rays does not fit well with the complex sample environment of liquids at high temperature. The advent of neutron sources boosted the field of scattering by liquid matter as it is easier to cope with the container and the furnace, because of the larger penetration depth of neutron. The third generation of synchrotron sources, producing high energy, penetrating, X-rays, are now available and the X-ray scattering by liquid and amorphous matter started a new life. However, the X-ray atomic form factor decreases rapidly with q and this remains a difficulty.

The basic formalism summarized in this section starts with a system of point-like scattering centers, and can be generalized by superimposing extended scattering centers or atoms on each point. This formalism can be either applied to neutron or X-rays diffraction, but here we will focus on neutron scattering.

4.3.1 Differential scattering cross-section for neutron diffraction

In a neutron diffraction experiment, the *differential cross section*, $d\sigma/d\Omega$ (i. e. the fraction of neutrons scattered in an elemental solid angle $d\Omega$, in steradians), is measured, without post-sample energy analysis. In practice, $d\sigma/d\Omega$ is the integration on all possible energy transfer of the double differential cross section $d^2\sigma/d\Omega dE$ (see Eq. 4.2). To simplify the treatment, we consider here only the almost elastic scattering by atoms which have fixed positions, that is to say, the *static approximation* (see further for details). The differential cross section (in barns/steradians, where a barn equals 10^{-24} cm^2), for the diffraction of a beam of neutron by a sample of N atoms located at i sites and having neutron scattering lengths b_i, is given by

$$\frac{d\sigma}{d\Omega} = \overline{\left\langle \left| \sum_i^N b_i e^{i\mathbf{q}\cdot\mathbf{r}_i} \right|^2 \right\rangle} = \left\langle \sum_{i,j}^N \overline{b_i b_j} e^{i\mathbf{q}\cdot\mathbf{r}_{ij}} \right\rangle \tag{4.12}$$

where the $\mathbf{r}_{ij} = \mathbf{r}_i - \mathbf{r}_j$ vector represents the i and j atomic sites relative positions and the $\mathbf{q} = \mathbf{k}_0 - \mathbf{k}_f$ vector is the momentum transfer (see Fig. 4.1). This equation expresses that the scattering atom at site i emits spherical waves with amplitude b_i which interfer with the other waves coming from the other sites[3]. The $\langle\rangle$ brackets denote the thermal average of scattering centers positions (which are not fixed, because of the thermal diffusion), on all the possible states for the system, while the horizontal bars indicate the average on all the i sites by the scattering length distribution of each atomic species. Note that the distribution of neutron scattering lengths gives rise to incoherent scattering (see Section 4.3.2). Following Eq. 4.12, $d\sigma/d\Omega$ is a function of the $\mathbf{q}$ vector only.

Static approximation (sa) This is useful to make the *static approximation*, stating that the energy exchange, $\hbar\omega$, is considered to be very small compared with the incident energy, $\hbar\omega_0$. It is important to note that the scattered quanta in a diffraction experiment

[3]This equation is valid for all sorts of samples, crystalline, powder, liquid, glass, etc.

are counted by the detector regardless of their energy exchange with the sample. The measurement thus results in an integration of the double differential scattering cross-section, $d^2\sigma/d\Omega dE$ (see Eq. 4.2), at constant detector angle 2θ and over all possible energy exchanges[4]:

$$\left(\frac{d\sigma}{d\Omega}\right)_{meas} = \int_{-\infty}^{+\hbar\omega_0} d(\hbar\omega)\frac{d^2\sigma}{d\Omega dE} \tag{4.13}$$

where $E = \hbar\omega = E_0 - E_f$ is the energy loss of the quanta (i. e. the difference between its initial and final energies, E_0 and E_f respectively), all having incident energy $E_0 = \hbar\omega_0$. For neutrons, $\hbar\omega = (\hbar^2/2m_n)(k_0^2 - k_f^2)$. Within the static approximation, $E_0 = \hbar\omega_0 \gg \hbar\omega$, so that the upper limit in the integration can be extended to infinity. It can also be shown that the integration over $\hbar\omega$ occurs at constant $\mathbf{q}$ [111], so that Eq. 4.13 reduces to:

$$\left(\frac{d\sigma}{d\Omega}\right)_{meas}^{sa} = \int_{-\infty}^{+\infty} d(\hbar\omega)\left(\frac{d^2\sigma}{d\Omega dE}\right)_{\mathbf{q}} = \frac{d\sigma}{d\Omega}(\mathbf{q}) \tag{4.14}$$

The static approximation thus leads well to the Eq. 4.12. Moreover, the structure is supposed to be relatively static during the time the incident quantum wavepacket travels from one atom to the next in the sample. The scattering event thus results in a relatively instantaneous 'snapshot' of the local structure, validating the use of time-independent positions $\mathbf{r}_i$ for the scattering centers in Eq. 4.12. Correction terms for inelasticity can be taken into account later in the treatment (see Section 4.4).

Scattered intensity The intensity $I(\mathbf{q})$, i. e. the number of counts per second measured by a detector of solid angle $d\Omega$, is given by:

$$I(\mathbf{q}) = \Phi\frac{d\sigma}{d\Omega}d\Omega \tag{4.15}$$

It is proportional to the incident flux of particles on the sample, Φ (in $\mathrm{s^{-1}cm^{-2}}$), measured by the monitor. We assume here a perfect efficiency of the detection. The intensity $I(\mathbf{q})$ is also a function of $\mathbf{q}$ vector, which, for a quantum of incident wavelength λ_0, is related to the scattering angle 2θ via

$$q = |\mathbf{q}| = \frac{4\pi}{\lambda_0}\sin\theta \tag{4.16}$$

This equation follows from the scattering triangle in Fig. 4.1 and is valid for $k_f = k_0$ (elastic scattering) and for $k_f \approx k_0$ (the static approximation). For an isotropic sample (such as a polycrystalline powder, glass or liquid), the scattering is not dependent of the azimuthal angle ϕ of the scattered quanta, but only of the diffraction angle 2θ, the diffraction pattern having a conical symmetry (Debye-Scherrer diffraction).

[4]For simplicity, we did not take into account the detector efficiency in this expression.

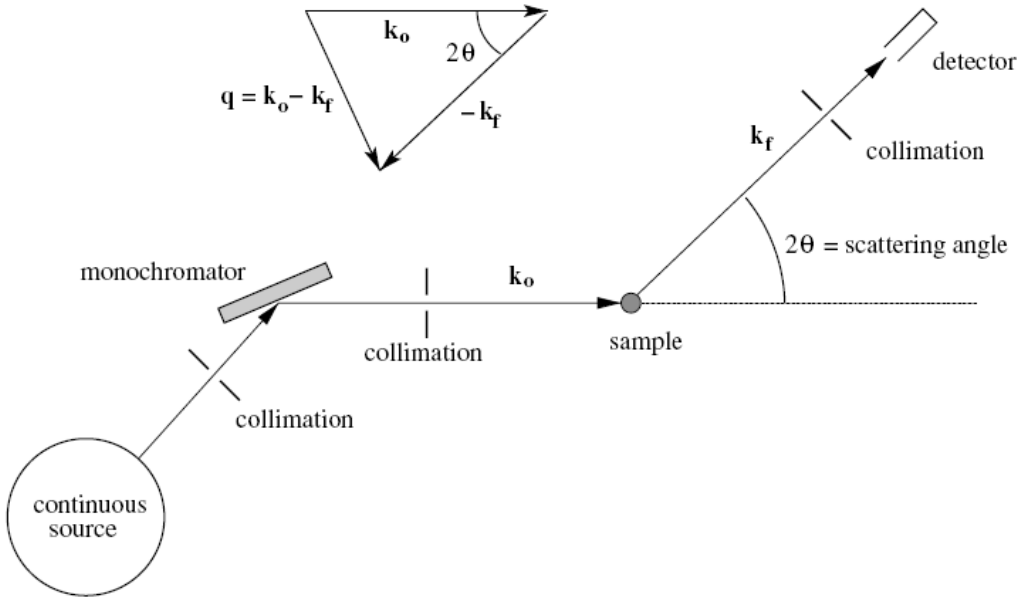

Figure 4.1: Schematic view of a diffraction experiment from a continuous source of neutrons, reproduced from [110]. The scattering triangle of wavevectors is shown at the top. Details concerning the D4 diffractometer in particular are given in section 4.5.

A diffractogram of a liquid or a glass can therefore be obtained by varying either 2θ (reactor sources, such as at the ILL) or λ_0 (pulsed sources, not used in this study) or both. While *scattering* describes a process either elastic or inelastic, *diffraction* stands for the cases where there is no selection in energy transfer between neutron and sample, but an integration.

In the following, the treatment of a diffraction spectra is given in the case of a monoatomic sample (one unique atomic species) and polyatomic sample (for which partial structure factors have to be considered).

4.3.2 The case of a monoatomic system

In the static approximation, the differential scattering cross-section per atom for a monoatomic sample can be written as follows

$$\begin{aligned}\frac{1}{N}\left[\frac{d\sigma}{d\Omega}(\mathbf{q})\right] &= \frac{1}{N}\left[\frac{d\sigma}{d\Omega}(\mathbf{q})\right]^{coh} + \frac{1}{N}\left[\frac{d\sigma}{d\Omega}(\mathbf{q})\right]^{incoh} \\ &= \overline{b}^2 S(\mathbf{q}) + \left(\overline{b^2} - \overline{b}^2\right) \\ &= b_{coh}^2 S(\mathbf{q}) + b_{incoh}^2 \end{aligned} \tag{4.17}$$

where the coherent b_{coh} and incoherent b_{incoh} scattering lengths are given by Eq. 4.10 and 4.11 respectively. In Eq. 4.17, we introduced the *static structure factor*, $S(q)$, defined as

$$S(\mathbf{q}) = \frac{1}{N}\left\langle \sum_{i,j}^{N} e^{i\mathbf{q}\cdot\mathbf{r}_{ij}} \right\rangle \tag{4.18}$$

which is dimensionless and converges to 1 for $\mathbf{q} \to \infty$.

The coherent part of $d\sigma/d\Omega$ has a $\mathbf{q}$ dependency and is relative to the diffraction by correlated points, while the incoherent part is isotropic and relative to the diffraction by non-correlated points. The static structure factor $S(\mathbf{q})$, which carries all the structural information, does not, logically, appear in the incoherent part. Fig. 4.2 shows the differential scattering cross-section per atom for a typical monoatomic liquid or glass.

Total cross-section For neutrons, the scattering lengths are almost independent of $\mathbf{q}$ and we can integrate $d\sigma/d\Omega$ directly to obtain the total sample cross-section which is the sum of two terms:

$$\sigma = \int_{4\pi} \frac{d\sigma}{d\Omega} d\Omega = \sigma_{coh} + \sigma_{incoh} = 4\pi b_{coh}^2 + 4\pi b_{incoh}^2 = 4\pi\overline{b^2} \tag{4.19}$$

where $d\Omega = 2\sin(2\theta)d\theta d\phi = (\lambda/2\pi)^2 q(dq)d\phi$ and the integral for the coherent part is accurate only for wavelengths λ that are small compared to the interatomic distance. The coherent part σ_{coh} tends to $4\pi N\overline{b}^2$ for $\mathbf{q} \to \infty$. The b_{coh} and b_{incoh} (generally expressed

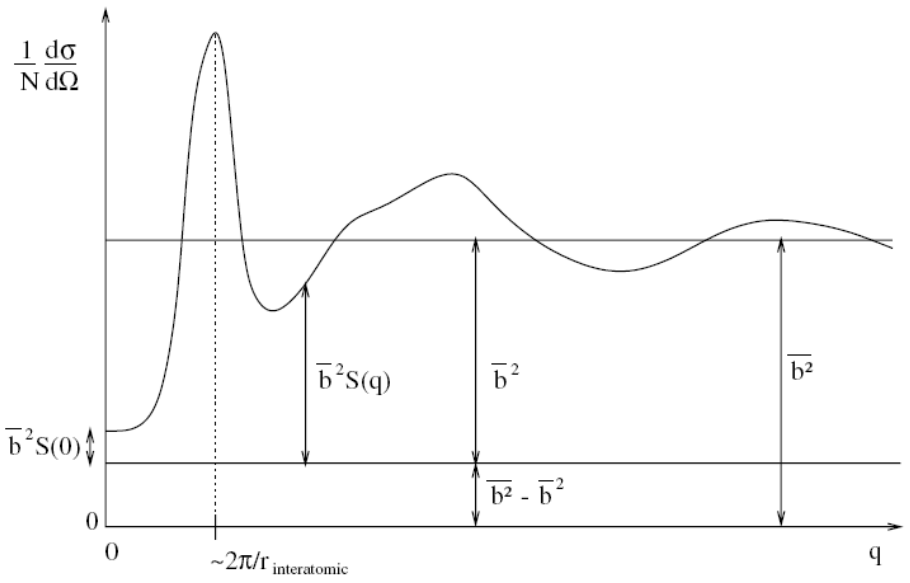

Figure 4.2: Differential scattering cross-section per atom $(1/N)d\sigma/d\Omega = \bar{b}^2 S(\mathbf{q}) + (\overline{b^2} - \bar{b}^2) = b_{coh}^2 S(\mathbf{q}) + b_{incoh}^2$ for a typical monoatomic liquid or glass. The position of the first peak is inversely proportional to the interatomic distances. Reproduced from [110].

in fm) and σ_{coh} and σ_{incoh} (in barns, with 1 barn = 100 fm^2) are tabulated in [112]. In Table 4.1, a few examples of values are given for elements constitutive of the compounds studied in this thesis.

Element	Z	$b_{coh}(fm)$	σ_{coh} (barns)	σ_{incoh} (barns)
Ge	32	8.185	8.42	0.18
As	33	6.58	5.44	0.06
Sb	51	5.57	3.90	0.007
Te	52	5.80	4.23	0.09

Table 4.1: Coherent b_{coh} scattering length (in fm), and coherent σ_{coh} and incoherent σ_{incoh} scattering cross-sections (in barns) for element of Z atomic number (values corresponding to thermal neutrons).

Interference function It is often more convenient to decompose $d\sigma/d\Omega$ in a slightly different way: a *distinct* contribution (relative to the interference between atoms) and a *self* contribution (relative to the isolated atoms) :

$$\frac{1}{N}\left[\frac{d\sigma}{d\Omega}(\mathbf{q})\right] = \frac{1}{N}\left[\frac{d\sigma}{d\Omega}(\mathbf{q})\right]^{distinct} + \frac{1}{N}\left[\frac{d\sigma}{d\Omega}(\mathbf{q})\right]^{self}$$
$$= \bar{b}^2 F(\mathbf{q}) + \overline{b^2} \tag{4.20}$$

where

$$F(\mathbf{q}) = \frac{1}{N}\left\langle \sum_{i,j\neq i}^{N} e^{i\mathbf{q}\cdot\mathbf{r}_{ij}} \right\rangle = S(\mathbf{q}) - 1 \tag{4.21}$$

is the *interference function* (i.e. for different atomic sites). The limit value of $F(\mathbf{q} \to \infty) = 0$ and, to the contrary of $S(\mathbf{q})$, $F(\mathbf{q})$ can have negative values.

Pair correlation function *g(r)* A monoatomic sample structure can be described in real space in terms of the pair correlation function $g(r)$, which is related to the probability of finding an atom at a position r in space relatively to a reference atom taken as the origin. The functions $S(\mathbf{q})$ and $g(r)$ are related to each other by the Fourier transforms:

$$S(\mathbf{q}) - 1 = \rho_0 \int (g(\mathbf{r}) - 1)\, e^{i\mathbf{q}\cdot\mathbf{r}} d\mathbf{r} \tag{4.22}$$

and

$$g(\mathbf{r}) - 1 = \frac{1}{\rho_0 (2\pi)^2} \int (S(\mathbf{q}) - 1)\, e^{-i\mathbf{q}\cdot\mathbf{r}} d\mathbf{q} \tag{4.23}$$

where ρ_0 is the atomic number density. As for $S(\mathbf{q})$, $g(\mathbf{r})$ is dimensionless. In the case of liquid or glassy samples, for which the average structure is isotropic, only the norms $r = |\mathbf{r}|$ and $q = |\mathbf{q}|$ have to be taken into account and the exponential factors $e^{\pm i\mathbf{q}\cdot\mathbf{r}}$ can be replaced by $\sin(qr)/qr$, which simplifies the expression for the static structure factor:

$$S(q) = 1 + \frac{1}{N}\left\langle \sum_{i,j\neq i}^{N} \frac{\sin(qr_{ij})}{qr_{ij}} \right\rangle \tag{4.24}$$

and the expressions of the Fourier transforms:

$$S(q) - 1 = \frac{4\pi\rho_0}{q} \int_0^\infty r\,(g(r) - 1)\sin(qr) dr \tag{4.25}$$

and

$$g(r) - 1 = \frac{1}{2\pi^2 r \rho_0} \int_0^\infty q\,(S(q) - 1)\sin(qr) dq \tag{4.26}$$

whence $S(q \to \infty) = 1$ and $g(r \to \infty) = 1$. Fig. 4.3 shows the pair distribution function $g(r)$ for a typical monoatomic liquid or glass.

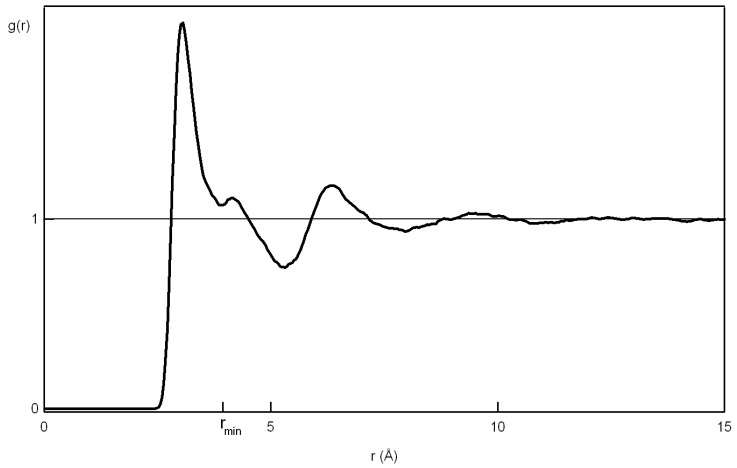

Figure 4.3: Pair distribution function $g(r)$ for a typical monoatomic liquid or glass.

The coordination number $\mathbf{N_c}$ The *Radial Distribution Function* RDF(r), defined by

$$RDF(r) = 4\pi r^2 \rho_0 g(r) \tag{4.27}$$

can be integrated to obtain the *average* number of neighbouring atoms in a coordination shell:

$$\overline{n} = \int_{r_1}^{r_2} RDF(r)dr = 4\pi\rho_0 \int_{r_1}^{r_2} g(r)r^2 dr \tag{4.28}$$

where r_1 and r_2 are the distances corresponding, for example, to consecutive minima in $g(r)$. The averaged number of atoms in the *first shell* is often called the *coordination number*, N_c. It should be noted that this coordination number is an *average* (every atom in the structure does not have this same number of atoms around it) and that the definition of the r_1 and r_2 limits is somewhat arbitrary (various methods are used). In this work, we will consider that the first coordination shell extends from $r = 0$ to the first minimum of $g(r)$, r_{min} (see Fig. 4.3).

In practice, the finite maximum q-value that is accessible in diffraction experiments (see Section 4.5) leads to peak broadening in real space after the Fourier transform, as well as to non-physical oscillations in $g(r)$ (*truncature* oscillations, which can be reduced by a prudent use of damping functions before the Fourier transform).

4.3.3 The case of a polyatomic system

In a polyatomic system, the different chemical properties of the different atomic species give rise to correlations between scattering lengths and atomic positions. This imposes to

use *partial* structure factors, which take into account the different atomic species present in the sample, to describe the chemical order of the structure in details.

Total and partial interference functions The generalization of Eq. 4.20 to an isotropic system including n chemical species is direct and is also decomposed in *distinct* and *self* parts:

$$\frac{1}{N}\left[\frac{d\sigma}{d\Omega}(q)\right] = \overline{b}^2 F_T(q) + \sum_{\alpha}^{n} c_\alpha \overline{b_\alpha^2} \tag{4.29}$$

where the total interference function $F_T(q)$ between all the atoms is given by a weighted sum of the partial interference functions $F_{\alpha\beta}(q)$ between atoms of type α and atoms of type β

$$F_T(q) = \sum_{\alpha,\beta}^{n} c_\alpha c_\beta \overline{b}_\alpha \overline{b}_\beta F_{\alpha\beta}(q) \tag{4.30}$$

in which c_α is the concentration of type α atoms and $\sum_\alpha^n c_\alpha = 1$. We see that the partial interference function $F_{\alpha\beta}(q)$ are dimensionless but $F_T(q)$ has the same dimensions as $d\sigma/d\Omega$ (barns/str). As in the monoatomic case, the partial interference function $F_{\alpha\beta}(q)$ represents the sum of the scattering amplitudes products from distinct i sites (among the type α atoms) and j sites (among the type β atoms).

Partial structure factors $\mathbf{S}_{\alpha\beta}(\mathbf{q})$ By analogy with the monoatomic system, see Eq. 4.21, we can define the *partial structure factors*, $S_{\alpha\beta}(q)$, by decomposing $F_T(q)$ as follows:

$$F_T(q) = \frac{1}{\overline{b}^2} \sum_{\alpha,\beta}^{n} c_\alpha c_\beta \overline{b}_\alpha \overline{b}_\beta \left[S_{\alpha\beta}(q) - 1\right] \tag{4.31}$$

where each $S_{\alpha\beta}(q)$ is a function that depends only on the distribution of α atoms around β atoms (or inversely). By analogy with Eq. 4.24, the partial structure factor $S_{\alpha\beta}(q)$ for an isotropic system can be written as

$$S_{\alpha\beta}(q) = 1 + \frac{1}{c_\alpha c_\beta N} \left\langle \sum_{i,j\neq i}^{N_\alpha, N_\beta} \frac{\sin(q r_{ij})}{q r_{ij}} \right\rangle \tag{4.32}$$

where $N_\alpha = c_\alpha N$ is the number of α atoms and i and j refer to sites among the α and β atoms, respectively.

Partial pair distribution functions Fourier transformation of the $S_{\alpha\beta}(q)$ leads to the *partial pair distribution functions*, $g_{\alpha\beta}(r)$:

$$S_{\alpha\beta}(q) - 1 = \frac{4\pi\rho_0}{q} \int_0^\infty r\left(g_{\alpha\beta}(r) - 1\right) \sin(qr) dr \tag{4.33}$$

and

$$g_{\alpha\beta}(r) - 1 = \frac{1}{2\pi^2 r \rho_0} \int_0^\infty q \left(S_{\alpha\beta}(q) - 1\right) \sin(qr) dq \tag{4.34}$$

where ρ_0 is still the total number density of atoms. The partial structure factors $S_{\alpha\beta}(q \to \infty) = 1$ for all α, β in analogy to the $S(q)$ of a monoatomic system. The partial pair-distribution functions $g_{\alpha\beta}(r)$ are the probability densities of finding a β atom at a given distance r from an α atom.

Average partial coordination number The *partial coordination numbers* $\overline{n}_\alpha^\beta$ (or the average number of β atoms in a spherical shell around an α atom) are found by integration of a partial radial distribution function:

$$\overline{n}_\alpha^\beta = 4\pi\rho_0 c_\beta \int_{r_1}^{r_2} g_{\alpha\beta}(r) r^2 dr \tag{4.35}$$

Total structure factor The *total structure factor* $S_T(q)$, defined as

$$S_T(q) = \sum_{\alpha,\beta}^{n} c_\alpha c_\beta \overline{b}_\alpha \overline{b}_\beta S_{\alpha\beta}(q) = F_T(q) + \sum_{\alpha,\beta}^{n} c_\alpha c_\beta \overline{b}_\alpha \overline{b}_\beta \tag{4.36}$$

converges to $\sum_{\alpha,\beta}^{n} c_\alpha c_\beta \overline{b}_\alpha \overline{b}_\beta = \left|\sum_\alpha^n c_\alpha \overline{b_\alpha}\right|^2$ for $q \to \infty$. Given that

$$\left|\sum_\alpha^n c_\alpha \overline{b_\alpha}\right|^2 = \overline{b}^2 \quad \text{and} \quad \sum_\alpha^n c_\alpha \overline{b_\alpha^2} = \overline{b^2} \tag{4.37}$$

are still the averages on the sample, we can write for a polyatomic sample:

$$\begin{aligned} \frac{1}{N}\left[\frac{d\sigma}{d\Omega}(q)\right] &= S_T(q) + \left(\overline{b^2} - \overline{b}^2\right) \\ &= F_T(q) + \overline{b^2} \end{aligned} \tag{4.38}$$

We see that the incoherent contribution still represents the total standard-deviation of the b distribution, as in Eq. 4.17.

In this work, we performed neutron diffraction experiments on alloys and obtained the total structure factor $S_T(q)$. The experimental determination of partial $S_{\alpha\beta}(q)$ structure factors requires other techniques, such as isotopic substitution, that we did not use. We nevertheless got access to $S_{\alpha\beta}(q)$ using computer simulations, as we will see in the following chapters, and compared their weighted sum (see Eq. 4.36) with the experimental $S_T(q)$.

4.4 Data treatment of a neutron diffraction experiment

Subtraction of the different external contributions to the diffracted intensity
When a neutron experiment is performed, they are several external contributions to subtract to obtain $d\sigma/d\Omega$ of the sample only. It is mandatory to subtract, from the total detected signal, the diffracted intensities coming from:

- the sample container (in our case, it consists of a quartz tube) ;
- the sample environment (such as the furnace in our experiments on liquids) ;
- the background.

To do this, it is necessary to obtain diffracted intensities from the sample in its container and environment, the empty container (with sample environment), the sample environment and the background (see Fig. 4.4 for an example of scattered intensities from the different contributions).

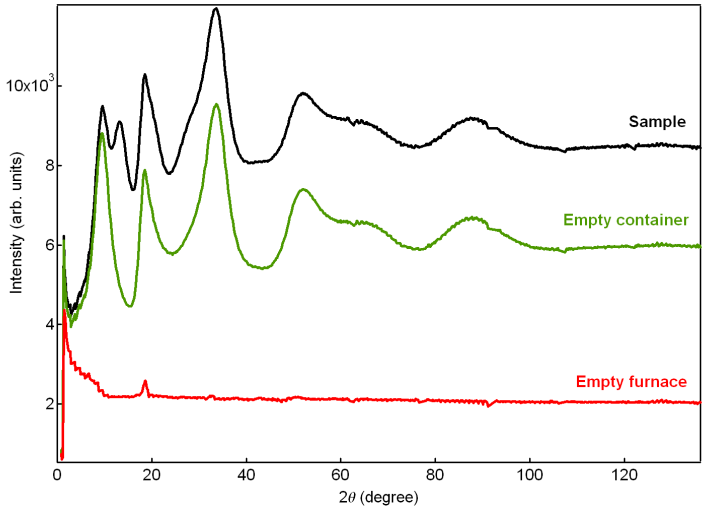

Figure 4.4: Scattered intensities for the empty furnace (red line), the empty container inside the furnace (green line) and the sample in its container inside the furnace (black line). The sample is Sb_2Te at 923 K, see Chapter 9.

The subtraction of these intensities from the total diffracted intensity cannot be made roughly. It is necessary to take into account angular attenuation coefficients (because of the absorption and scattering, see next paragraph) and the multiple scattering, by the sample itself and by its environment.

Attenuation corrections The attenuation corrections resulting from absorption and scattering have been described by Paalman and Pings [113] in the case of a completely and uniformly illuminated sample of cylindrical geometry in an annular container, this simple configuration being the most commonly used. They provided coefficients (which depend on the scattering angles) that permit the proper subtraction of the empty container diffractogram taking into account the attenuation of the sample and its container. Their method however ignores the multiple scattering, supposing that a neutron is scattered only once. Complicated corrections can take into account the multiple scattering, assuming that the neutron actually undergoes one or more scattering event in the sample (each individual scattering event being elastic and isotropic) [114].

Normalization of the sample intensity To follow the treatment detailed in the previous sections to obtain the pair correlation functions, the scattered intensity (after the subtraction of contributions that do not arise from the sample) has to be normalized to an absolute cross-section. It can be done by comparing with the measured intensity of a reference sample of known scattering cross-section and volume. The reference sample for normalization is generally vanadium, because its cross-section is almost completely incoherent and therefore isotropic and easily measured. Note that if the diffracted intensity by a reference sample has not been measured, a 'self-normalization' is still possible, by aligning the $d\sigma/d\Omega$ with the theoretical value for the sample composition.

Inelasticity correction The inelasticity correction has been described by Placzek [115]. An inelasticity correction becomes necessary when the energy exchange, $\hbar\omega$, between the neutron and the sample, becomes comparable to the incident energy E_0, making the static approximation no longer valid. Another consequence is that, for a given λ_0, the scattering angle depends not only on q but also on $\hbar\omega$. The integration in Eq. 4.14 is no longer performed at constant q, as required by the static approximation. In general, only the *self* part of the differential scattering cross-section is affected by inelasticity. Practically, inelasticity gives rise to a 'fall down' of the self scattering with increasing q. Except for the lightest atoms, the corrections for reactor sources can be expressed in the form

$$\left[\frac{d\sigma}{d\Omega}(q)\right]^{self}_{measured} = \left[\frac{d\sigma}{d\Omega}(q)\right]^{self}_{corrected} [1 + P(q)] \tag{4.39}$$

where $P(q)$ is a polynomial expansion in powers of q^2.

4.5 D4 diffractometer

A schematic top-view of the disordered-material diffractometer D4 at the ILL is given in Fig. 4.5. The D4 instrument is a two-axis diffractometer, dedicated to the determination of pair distribution functions in isotropic systems. The D4 diffractometer is supplied with neutrons from the hot source, which means that the neutrons are thermalized by a graphite block at 2000 K, corresponding to short wavelengths (0.3 - 0.8 Å). This permits scattered intensity measurements up to high q values (in our case, up to 23 Å^{-1}).

Monochromator The first axis of D4 is the rotating axis of the monochromator (20 cm x 20 cm), which is made of 9 Cu monocrystals cut parallel to the (220) planes.

Monitor Placed between the monochromator and the sample, a monitor counts the number of incident neutrons on the sample. This permits to compare measurements on the basis of a constant incident neutrons number.

Slits The beam is then delimited by two slits (horizontal and vertical) made in isotopically enriched $^{10}B_4C$, which has a strong absorption cross section for thermal and hot neutrons. They are placed depending of the sample size.

Sample The second axis of D4 (reference axis for the 2θ angle) goes trough the sample. When the sample is studied at room temperature, it is placed in a cylindrical bell jar (diameter of 46 cm) equipped with two Aluminium windows: one for the beam entrance and one which covers the 0 - 140° angular field in 2θ. When measurements are performed at low or high temperatures, a cryostat or a furnace can be placed around the sample, inside the bell jar. In our experiments, we used a furnace made of cylindrical foils of vanadium (chosen because of its isotropic scattering). The sample are placed at the center and heat is produced by Joule effect in the vanadium foils.

Detector The multidetector is constituted of nine elements: each detector covers an 8° angle in 2θ and they are spaced by 7°. These nine elements contain a gas of ^3He. The neutrons are converted in charged particules by decomposition of the ^3He atoms of the gas. These particules are accelerated by a high voltage between the detector entrance and the detectors cells. In every detector element, 64 cells detect these electrical impulses. The cells are situated at 1.15 m of the sample and spaced of 2.5 mm. They permit the scattered intensity measurement by steps of 0.125° in 2θ. Note that, because of the 7° empty zone between each element, the detector has to be moved to cover the 2θ range from 0 to 140°. This large array of detectors provides not only a high counting rate but also a very good counting-rate stability.

4.6 Inelastic neutron scattering by liquids and glasses

Cold or thermal neutrons have energies that correspond to diffusive and vibrational motions of the atoms in a liquid or a glass. The interaction of incident neutrons with the sample by inelastic scattering is thus an ideal tool to study the dynamical properties of matter.

In an inelastic scattering experiment, the scattered intensity is measured versus scattering vector $\mathbf{q}$ (difference between neutron final and initial wavevectors, $\mathbf{k}_f$ and $\mathbf{k}_0$ respectively) and $\hbar\omega$ (difference between final and initial neutron energies, E_f and E_0 respectively) [117]. Fig. 4.6 summarizes the different possibilities for these values. The neutron energy can

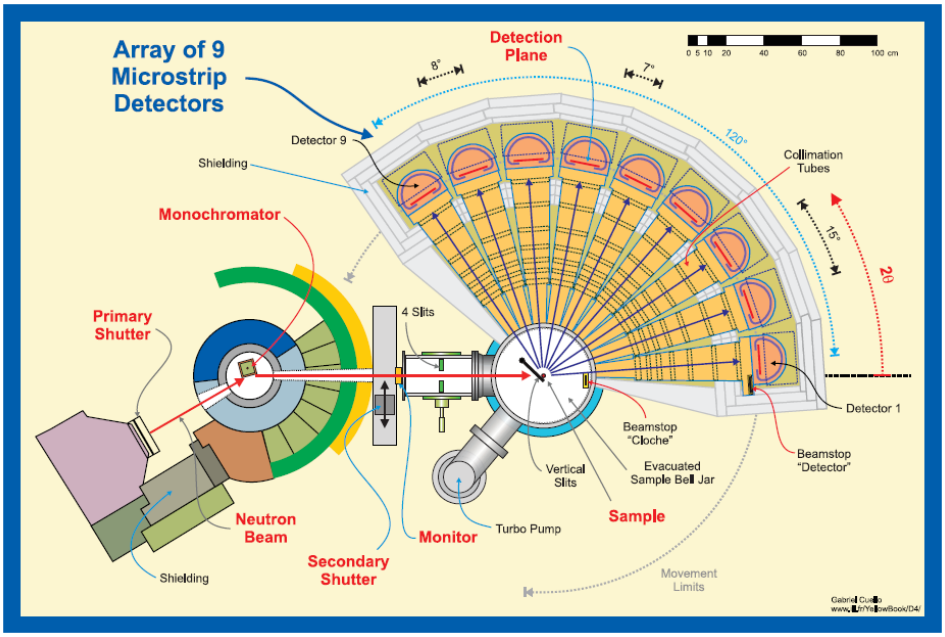

Figure 4.5: Schematic top-view of D4, showing the arrangement of the 9 detectors and their collimation tubes. Reproduced from [116].

- decrease : $E_f = E_1 < E_0$ (inelastic scattering case 1, the neutron gives some energy to the sample) ;
- remain constant : $E_f = E_0$ (elastic scattering) ;
- increase : $E_f = E_2 > E_0$ (inelastic scattering case 2, the neutron absorbs some energy from the sample).

In an inelastic scattering experiment, the double differential scattering cross-section, $d^2\sigma/d\Omega dE$, is taking into account (see Eq. 4.2), to the contrary of a diffraction experiment in which it is integrated over the energy to give $d\sigma/d\Omega$.

Time-of-flight spectrometer The time-of-flight (TOF) spectrometers are made to record simultaneously the scattered neutrons in a large wavevector and energy transfer range. They are used to measure the dynamic structure factor $S(\mathbf{q}, \omega)$ (see Eq. 4.5) for disordered samples. The continuous neutrons flow is cut in short pulses to determine the starting time of the neutrons' flight. Hundreds of detectors are placed to record simultaneously the scattered neutrons for several wavevector values. The inelastic scattering of neutrons makes that they gain or lose energy and, thus, their velocity changes. The part

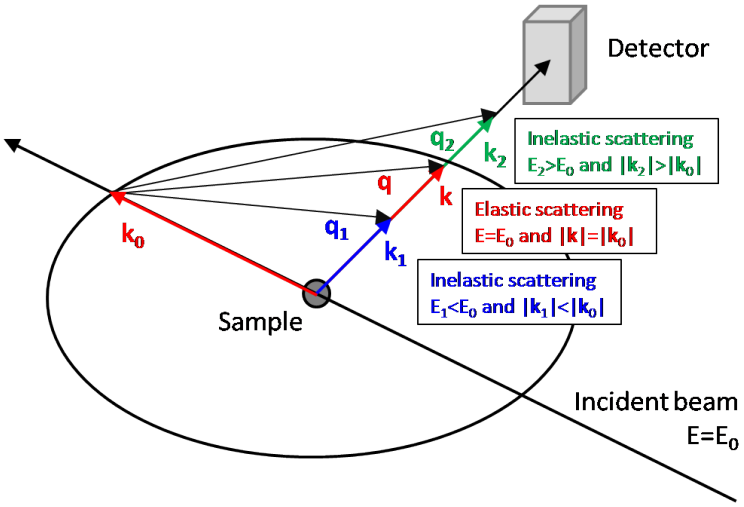

Figure 4.6: Schematic of an inelastic scattering experiment.

of the spectrum corresponding to a given energy loss will be selected by the time interval between two pulses.

4.7 IN6 experimental setup

The IN6 instrument is a time-of-flight spectrometer designed for quasielastic and inelastic scattering. It is supplied with neutrons from the cold source, which means that the neutrons are thermalised at 25 K, corresponding to longer wavelengths than on the D4 instrument. On IN6, the incident wavelengths are in the range of 4 to 6 Å. A schematic top-view of the IN6 instrument is given in Fig. 4.7.

Monochromator An intense beam is extracted from a neutron guide by a vertically focussing monochromator array. It is made of three composite pyrolityc graphite monochromators using the full heigh (20 cm) of the guide and focussing the beam at the sample position. This monochromator can deliver four wavelengths: 4.1 (the one we used), 4.6, 5.1 and 5.9 Å.

Fermi chopper To achieve the time-focussing condition, the beam is pulsed by a Fermi chopper. The normal distance between the chopper and the sample is 38 cm. To prevent frame-overlap when the chopper is rotating faster than 7500 rpm, a supressor chopper is placed before the Fermi chopper and rotates in phase with the latter.

Sample The sample is placed in a cylindrical bell jar to avoid the interaction between neutrons and H contained in air, which is a strong scatterer. If the measurement is made

at low or high temperature, a cryostat or a furnace can be placed around the sample, inside the bell jar.

Detector The detector bank is entirely covered with detector boxes, thus avoiding the inconvenience of moving the counters, as in D4 (see section 4.5).

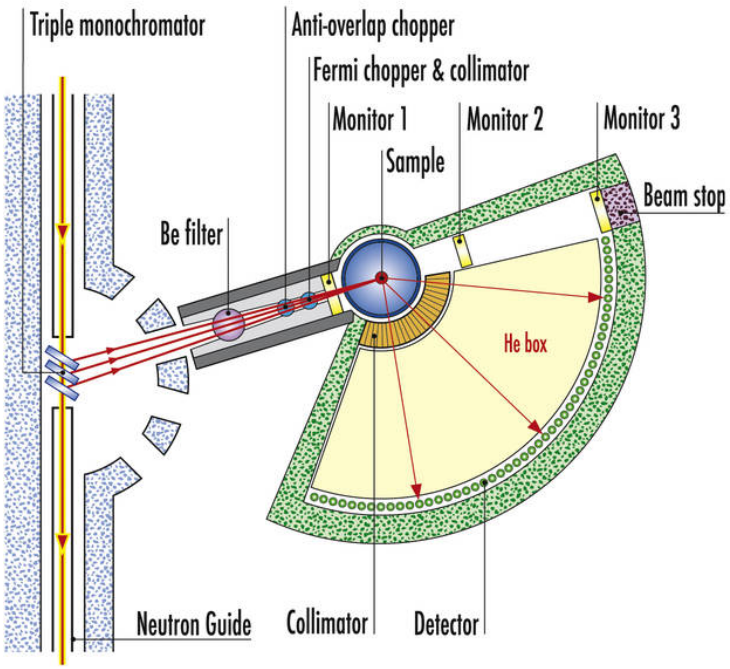

Figure 4.7: Schematic top-view of IN6. Reproduced from [118].

Chapter 5

Simulation techniques

Ab initio computer simulations are performed with the hope to understand the structural or interactions properties of atoms assemblies. This can be a test of theoretical predictions, a complement to classical experiments, or a tool to access to supplementary information, impossible to obtain in other ways. Some guesses are mandatory about the interactions between atoms but it is possible to reproduce exactly some macroscopic properties.

5.1 Density Functional Theory

A solid is made of a huge number of atoms, i. e. electrons and nuclei, interacting with each other. The exact resolution of the Schrödinger equation of such a system is impossible without the use of some approximations. In the *Born–Oppenheimer approximation*, the electrons are supposed to adapt instantaneously to the ionic potential and, consequently, the electron-phonon coupling is neglected. This approximation gives excellent results for many purposes [119]. The Density Functional Theory (DFT) was developed by Hohenberg, Kohn and Sham [120, 121] to calculate the electronic states of complex systems in their ground state. It has rapidly become an unavoidable tool for theoretical physicists and chemists. Its basic idea is to deal with the total electronic density, $n(\mathbf{r})$, instead of considering the many-body wavefunction appearing in the Schrödinger equation for a system of N interacting electrons. This will reduce the system of interacting electrons into an auxiliary system of N non-interacting electrons with the same density as the interacting system. This huge simplification has the great interest to lead to exact single-particle equations (the simplifications being introduced afterward), compared to the Hartree-Fock approximation [122, 123].

5.1.1 The Kohn-Sham equations

It can be shown [120] that the electronic density is uniquely defined given an external potential $V^{ext}(\mathbf{r})$ for the electrons (the ionic potential). There is thus a one-to-one correspondence between this external potential and $n(\mathbf{r})$. The external potential determining the wavefunction ϕ, this latter must be a unique functional of the density as well. The

other terms in the hamiltonian (kinetic energy T and electron-electron interactions W) depending only of the electronic density, the total energy of the system is a functional of the density.

The DFT ground state of a system is found by solving the Kohn-Sham equations [121] for single-particles self-consistently

$$\left[-\frac{\hbar^2}{2m_0}\nabla^2_{\mathbf{r}} + V^{eff}(\mathbf{r}, n(\mathbf{r}))\right]\phi_i = \epsilon_i\phi_i \tag{5.1}$$

where the first term is the kinetic energy operator T. The V^{eff} term contains three contributions: the total external potential due to the ions, V^{ext}, the Coulombic potential due to the electronic system,

$$e^2\int\frac{n(\mathbf{r}')}{|\mathbf{r}-\mathbf{r}'|}d\mathbf{r}', \tag{5.2}$$

and the exchange-correlation term, which accounts for the exchange and correlation effects of the electrons. This latter term is the derivative of the exchange-correlation energy functional $E^{xc}[n(\mathbf{r})]$,

$$\frac{\delta E^{xc}[n(\mathbf{r})]}{\delta n(\mathbf{r})}. \tag{5.3}$$

It includes all the effects of the many-body character of the true electronic system. The charge density

$$n(\mathbf{r}) = \sum_i |\phi_i(\mathbf{r})|^2 \tag{5.4}$$

is expressed in terms of the single-particles orbitals ϕ_i (called Kohn-Sham orbitals), which are solutions of Eq. 5.1. The orthonormality constraints $\langle\phi_i|\phi_j\rangle = \delta_{ij}$.

Single-particles The single-particle states do not correspond to electrons : they represent fictitious fermionic particles with the only requirement that their density is identical to the density of real electrons. These particles can be considered as *non-interacting* : this is very important as the resolution will be considerably simplified. Within the DFT scheme, the system of interacting particles in an external potential V^{ext} is now replaced by a system of non-interacting particles in an effective potential V^{eff}.

Self-consistency Since the effective potential is a function of the density, which is obtained from the Eq. 5.4, and hence depends on all the single-particles states, it is necessary to solve these equations by iterations until self-consistency is reached. The only issue of this problem is the exact form of $E^{xc}[n(\mathbf{r})]$, which is unknown and cannot be determined exactly for a complex, inhomogeneous system (the widely used approximations for E^{xc} will be presented in the next subsection).

Starting from some guess of the input charge density $n^{in}(\mathbf{r})$, the following sequence of operations is performed:

$$n^{in} \rightarrow \left(T + V^{eff}\right)(n^{in}) \rightarrow \text{solve KS equations} \rightarrow \phi_i(\mathbf{r}) \rightarrow n^{out}(\mathbf{r}) = \sum_i |\phi_i(\mathbf{r})|^2 . \quad (5.5)$$

This iterative process converges with a judicious choice of new density in terms of the density found at the previous steps, as for exemple with a simple *linear mixing* algorithm of type :

$$n^{new} = \alpha n^{out} + (1-\alpha) n^{in}, \quad (5.6)$$

with $0 < \alpha < 1$, which guarantees convergence if α is small enough. More sophisticated algorithms (as for example Anderson [124] or Broyden [125]) use the input and output of several preceding steps to determine the next optimal input combination.

Once the self-consistency in reached, many output quantities can be computed (total energy, forces, stresses, ...).

5.1.2 Exchange-correlation potential

The approximations arise in the Density Functional Theory because the exchange-correlation energy E^{xc} is unknown for an inhomogeneous system. The two models presented briefly in the following are the most widely used approximations.

The Local Density Approximation (LDA) The simplest approximation proposed by Kohn and Sham is the Local Density Approximation (LDA) [121]. It supposes the use of the exchange-correlation energy of the homogeneous electron gas, which can be calculated [126]. The spatial dependence of $n(\mathbf{r})$ is then neglected. The exchange-correlation energy at $\mathbf{r}$ is replaced by the corresponding energy of the homogeneous electron gas with density n. The exchange-correlation energy of the free, homogeneous electron gas, can be written

$$E^{xc}_{hom} = n\epsilon^{xc}_{hom}. \quad (5.7)$$

where n is the density of the gas and ϵ^{xc}_{hom} is a spatially constant energy per electron. For an inhomogeneous system, in the LDA approximation, the exchange-correlation energy per atom at each point $\mathbf{r}$ is assumed to be the same as in the homogeneous electron gas with that density:

$$\epsilon^{xc}_{LDA}(\mathbf{r}) = \epsilon^{xc}_{hom}(n(\mathbf{r})). \quad (5.8)$$

And thus, the exchange-correlation energy is given by

$$E^{xc}_{LDA}[n(\mathbf{r})] = \int n(\mathbf{r})\epsilon^{xc}_{LDA}(\mathbf{r})d\mathbf{r} \quad (5.9)$$

The General Gradient Approximation (GGA) An extension of the LDA is the General Gradient Approximation (GGA) which describes the exchange-correlation energy not only as a function of the local density but also of its variation. The exchange-correlation energy is slightly more complex to calculate

$$E^{xc}_{GGA}(n\mathbf{r})) = \int n(\mathbf{r})\epsilon^{xc}_{LDA}(\mathbf{r}, \nabla\mathbf{r})d\mathbf{r} \tag{5.10}$$

Among these GGA's parametrizations, in this thesis we will use the one of Perdew and Wang [127, 128].

5.1.3 Diagonalization of the Kohn-Sham Hamiltonian

The basic step of a DFT calculation is the evaluation of the Kohn-Sham Hamiltonian H_{KS} and its diagonalization. To solve the Eq. 5.1, it is necessary to expand the Kohn-Sham wave functions ϕ in some suitable basis set $\{\varphi_i\}$ as

$$\phi(\mathbf{r}) = \sum_i c_i\varphi_i(\mathbf{r}) \tag{5.11}$$

For an orthonormal basis set, the problem reduces to solve

$$\sum_j (H_{ij} - \epsilon\delta_{ij})c_j = 0, \tag{5.12}$$

where the matrix element $H_{ij} = \langle\phi_i|H|\phi_j\rangle$. In the case of a non-orthonormal basis-set, the following equation has to be solved :

$$\sum_j (H_{ij} - \epsilon S_{ij})c_j = 0, \tag{5.13}$$

where $S_{ij} = \langle\phi_i|\phi_j\rangle$ is the overlap matrix.

They are several choice for the basis set [129]. In this thesis, we used the method involving a set of plane waves.

5.1.4 The plane waves expansion

A standard approach in DFT calculations is to expand the Kohn-Sham wave functions in an appropriate basis set and diagonalize the KS-Hamiltonian, H_{KS}. Different types of basis sets are possible: *Localized* basis sets, *Delocalized* basis sets, or *Mixed*. In our calculations, we used a *Plane Waves* (PW) delocalized basis set for states of wave vector $\mathbf{k}$, as this method is simple and reasonably accurate for structural optimization and the determination of the electronic ground state and the total electronic energy of the materials we study.

In the plane wave expansion, using the fact that any periodic function can be expanded in the complete set of Fourier components, the KS wave functions are represented in the following Bloch form :

$$\phi_i(\mathbf{r}) = \frac{1}{\sqrt{\Omega}} \sum_{\mathbf{G}} c_{i,\mathbf{k}+\mathbf{G}} e^{i(\mathbf{k}+\mathbf{G})\cdot\mathbf{r}}, \tag{5.14}$$

where $\mathbf{k}$ is a point in reciprocal space, $\mathbf{G}$ a reciprocal lattice vector and Ω the volume of the crystalline unit cell. The $c_{i,\mathbf{k}+\mathbf{G}}$ are the expansion coefficients of the wavefunction in the basis of orthonormal plane waves $|\mathbf{k}+\mathbf{G}>$ satisfying

$$\langle \mathbf{k}+\mathbf{G}'|\mathbf{k}+\mathbf{G}\rangle \equiv \frac{1}{\Omega}\int e^{-i(\mathbf{k}+\mathbf{G}')\cdot\mathbf{r}} e^{i(\mathbf{k}+\mathbf{G})\cdot\mathbf{r}} = \delta_{\mathbf{k}+\mathbf{G}',\mathbf{k}+\mathbf{G}}. \tag{5.15}$$

The solution of Eq. 5.1 in Fourier space :

$$\sum_{\mathbf{G}} (\langle \mathbf{k}+\mathbf{G}'|T+V_{eff}|\mathbf{k}+\mathbf{G}\rangle - \epsilon_i \delta_{\mathbf{k}+\mathbf{G}',\mathbf{k}+\mathbf{G}}) c_{i,\mathbf{k}+\mathbf{G}} = 0, \tag{5.16}$$

requires the diagonalization of the matrix $H_{KS} = T + V_{eff}$, whose matrix elements are :

$$\langle \mathbf{k}+\mathbf{G}'|H_{KS}|\mathbf{k}+\mathbf{G}\rangle \tag{5.17}$$

The inconvenients of a Plane Waves basis set (compared to localized ones) are the slow convergence with respect to basis set size (many more Plane Waves than localized functions are needed), and the requirement for supercells and vacuum layers in the case of finite systems. The advantages are that it is easy to evaluate the convergence quality (just by increasing the cutoff energy, which is the maximal possible value for the kinetic energy in the calculation), they are easy to use (based on Fourier transforms) and it is possible to easily calculate forces, using the Hellmann-Feynman theorem [130, 131].

Non periodic systems To the contrary of crystals, amorphous materials, liquids or molecules for example, does not have perfect periodicity. The cell must be 'large enough' to give a reasonable description of physical properties.

5.1.5 The ionic potential

A huge number of PW is needed for the highly localized core electrons, which are difficult to expand in a plane wave basis set. This justifies the use of *pseudo-potentials* (PP), that are smooth effective potentials that reproduce the effect of the nucleus plus core electrons on the valence electrons [132]. As the core electrons are not important to describe physical properties like the bonding in a solid, only the valence electrons which take part in the bonding have to be treated explicitly in the calculation. This is achieved by replacing the coulombic nuclear potential by a weaker potential (pseudopotential), which represents the combined effect of the core electrons and the nuclear potential. In a Coulomb potential the core wave functions exhibit strong oscillations and, due to the orthogonality between core and valence states, the valence wave functions also strongly oscillate in the core region.

However, one can show that it is possible to construct a pseudopotential operator which yields pseudo eigenstates, which are nodeless within the core and which have the same energy as the true valence states.

They are different kinds of pseudo-potentials (empirical, atomic, norm-conserving). The pseudo-potentials we use in this thesis are ultra-soft PP [133].

5.2 Ab initio Molecular Dynamics

Ab initio (or First Principles) Molecular Dynamics (FPMD) simulations, in which at each step the interatomic forces are obtained from a ground state DFT calculation, are used to follow the time evolution of a system at finite temperature, starting from an initial configuration with N ions in a volume V. The dynamical evolution can be obtained by integrating the classical equation of motion, $\ddot{\mathbf{x}}_i(t) = \mathbf{F}_i(t)/m_i$, related to every atom of mass m_i in the structure. It is then mandatory to calculate the forces acting on the N ions. Forces are derived from the potential energy $U(\mathbf{r}_1, \mathbf{r}_2, \ldots, \mathbf{r}_N)$ which depends on the atomic positions $\mathbf{r}_1, \mathbf{r}_2, \ldots, \mathbf{r}_N$.

Once the forces acting on the ions have been computed, the integration of motion equations to obtain atomic trajectories with time is usually made with the so-called *Verlet algorithm* :

$$\mathbf{x}(t + \delta t) = 2\mathbf{x}(t) - \mathbf{x}(t - \delta t) + \delta t^2 \ddot{\mathbf{x}}(t) \tag{5.18}$$

where δt is the *time-step* of the MD run.

Forces can also be used to determine the lowest energy equilibrium structure (structural optimization).

5.3 Our simulations

We used Density Functional Theory as implemented in the VASP software package [134] to compute the electronic structure of the systems. The valence s and p electrons were treated explicitely, while core electrons are represented by ultrasoft pseudopotentials [133]. We used the exchange-correlation functional PW91 in a general gradient approximation (GGA) [128]. In the VASP code, the electronic wavefunctions are represented on a plane waves basis, with a cutoff depending on the compound studied (from 175 to 250 eV). This level of accuracy allows for relatively fast calculations, while still reproducing the $GeTe$, Sb_2Te_3 and As_2Te_3 crystal properties satisfactorily (the cell parameters and first neighbors distances are reproduced with 3% and 0.3%, respectively, for $GeTe$, 1.8% and 1.1% for Sb_2Te_3 and 1.9% and 2.0% for As_2Te_3). For each alloy studied, the electronic calculations were performed at the Γ point only.

The molecular dynamics simulations were performed in the constant NVT (canonical) ensemble using a Nosé thermostat [135] and the equations of movements were integrated using a 3.6 fs time step. The systems studied contain between 162 and 216 atoms (depending on the compound) in a cell whose size is adapted to the measured experimental densities. The compounds were studied either in liquid or amorphous phase.

For each compound, we started from a cubic supercell containing the atoms in a $NaCl$ arrangement at the experimental density. The following procedure was identical for all the systems studied. The systems were heated for more than 10 ps at 3000 K, followed by a 10-20 ps equilibration at the desired temperatures in liquid phase. Some of them were then quenched down to 300 K in $\sim$ 25 ps. Statistics over the structural quantities in the amorphous state were finally accumulated over 20-40 ps.

The characteristics of the calculations on the different compounds studied in this thesis will be given in the following chapters.

Chapter 6

Structure and dynamics of the negative thermal expansion in the Te-rich liquid Ge_xTe_{1-x} alloys

Not all materials expand when heated, as seen in the Chapter 3. The rich-Te Ge_xTe_{1-x} alloys ($0 \leq x \leq 0.2$) [21] undergo a NTE close to the melting point, either in the supercooled liquid (e. g. pure tellurium [26, 1]) or in the thermodynamically stable liquid.

In this chapter, we analyze the NTE in two rich-Te based liquid alloys, $GeTe_6$ and $GeTe_{12}$, through the structural and vibrational atomic properties.

In the case of Ge_xTe_{1-x}, the NTE is most prominent around the eutectic concentration, $Ge_{15}Te_{85}$ (referred to here as $GeTe_6$), between 633 K and 733 K (see Chapter 3, Fig. 3.6). This particular composition has been extensively studied by thermodynamic (density [21], specific heat [2]), and electrical resistivity measurements [136]. These anomalous variations in macroscopic properties have been related to structural changes, experimentally [6] [7], or by First Principles Molecular Dynamics (FPMD) [9]. These studies led to a picture of a p-bonded liquid in which atoms have an octahedral environment. This octahedral local structure is distorted at low temperature by a Peierls-like mechanism, leading to a larger atomic volume. At higher temperature, a more symmetric structure is recovered, together with a smaller volume because the longer bonds are more easily shortened than the shorter ones are elongated. This proposed mechanism displays some analogy with the $\alpha \rightleftharpoons \beta$ transition of the crystalline $GeTe$ compound [137] that results from the disappearance of the Peierls distortion that stabilizes the low temperature $\alpha - GeTe$ phase. However, no driving force for this gradual structural change in the liquid state could be clearly identified up to now and the goal of the present work is to investigate this NTE via an analysis of the dynamical properties of liquid $GeTe_6$ and $GeTe_{12}$.

The particularity of eutectic $GeTe_6$ is that the NTE region lies almost entirely above T_m, the melting temperature being lower than in the other Ge_xTe_{1-x} alloys. On the contrary, in $GeTe_{12}$ ($T_m = 694$ K), the NTE is almost entirely comprised in the undercooled liquid temperature range, as in pure Te ($T_m = 723$ K) [138]. The experimental study of the NTE in $GeTe_6$ is thus facilitated compared to the $GeTe_{12}$ case, but the latter is a good point of comparison between eutectic Ge_xTe_{1-x} compound and pure Te behaviors.

First, we will present a diffraction experiment perfomed on the D4 diffractometer (at the Institut Laue-Langevin, Grenoble), which demonstrates a strong structural evolution with temperature, for both alloys.

Second, using inelastic neutron scattering, we relate this structural evolution in the NTE range to noticeable changes in the vibrational density of states. We will show that the structural evolution resulting in the NTE is due to a gain of vibrational entropy that cancels out the Peierls distortion.

Finally, we present First Principles Molecular Dynamics simulations, results that further emphasize the role of the temperature dependence of the Ge atomic environment in this mechanism.

We will extend our study to the dynamical structure of $Ge_2Sb_2Te_5$ and $Ge_1Sb_2Te_4$ liquid alloys for comparison. These are typical materials that form the active layer of Phase Change (PC) non volatile data storage devices (see Chapter 1). They do not exhibit any NTE in the stable liquid state (see Fig. 3.12 in Chapter 3), but adopt, like $GeTe_6$, a mostly octahedral local order, as evidenced by FPMD [41] and an extensive set of neutron scattering measurements performed at various temperatures [69].

6.1 Neutron diffraction experiment

6.1.1 Experimental setup

We performed neutron diffraction experiments on the two-axis D4 diffractometer, on $GeTe_6$ ($T_m = 648$ K [138]) and $GeTe_{12}$ ($T_m = 694$ K [138]) in liquid phase at the temperatures[1] indicated in Table 6.1. These temperatures are also indicated in Fig. 6.1 together with the temperature dependence of the molar volume.

The samples were prepared, from the pure elements, by R. Céolin, from the Faculté des Sciences Pharmaceutiques et Biologiques, at the Université Paris Descartes. They were molten, homogenized and then sealed under vacuum in quartz tubes of 6 mm internal/8 mm external diameter. Special care was set to limit the empty volume inside the container as Te high vapor pressure could cause sensible variations in composition with temperature. The total scattered intensity was measured as a function of the scattering angle 2θ for an incident neutron wavelenght $\lambda = 0.6956$ Å. The 2θ angular range extended from 0.750° up to 138.5° with a 2θ step equal to 0.125° which corresponds to neutron scattering vectors

[1] Note that we tried to reach $T = 643$ K for $GeTe_{12}$ but the sample recrystallized.

$GeTe_6$		$GeTe_{12}$	
T (K)	ρ (at/Å^{-3})	T (K)	ρ (at/Å^{-3})
623	0.02755	673	0.02771
643	0.02769	693	0.02792
653	0.02780	723	0.02809
685	0.02839	758	0.02814
796	0.02888	813	0.02808

Table 6.1: Experimental densities from [21] at temperatures studied by neutron diffraction for $GeTe_6$ and $GeTe_{12}$.

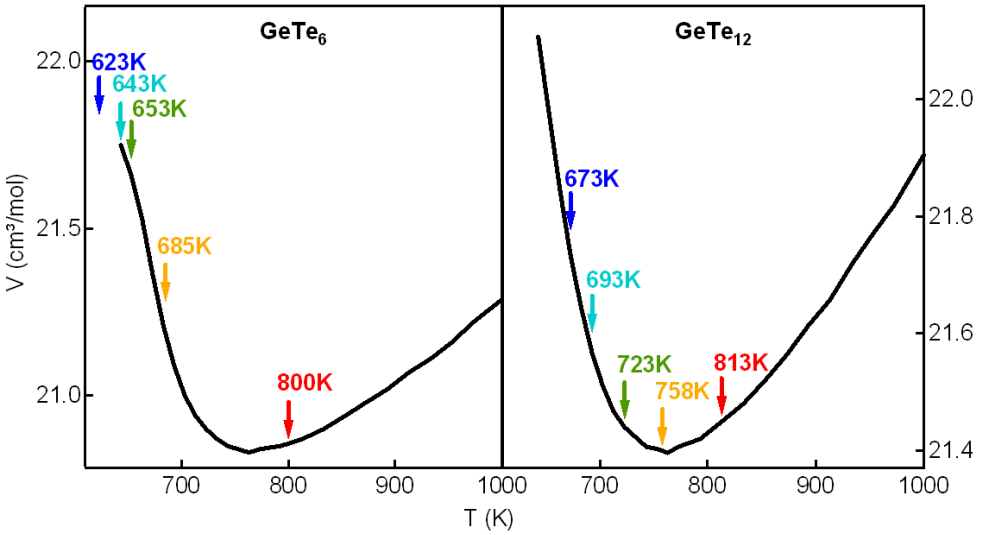

Figure 6.1: Molar volume evolution with temperature for liquid $GeTe_6$ (T_m = 648 K), measured by Tsuchiya [21] and $GeTe_{12}$ (T_m = 694 K), extrapolated from the Tsuchiya measurements on liquid Ge_5Te_{95} and $Ge_{10}Te_{90}$ (left and right panel respectively). Temperatures measured in the neutron diffraction experiment are indicated with vertical arrows.

$q = 4\pi \sin\theta/\lambda$ in the range 0.118 to 16.893 Å^{-1}. We measured the signal from the sample for 5 hours at each temperature. We measured the empty quartz (cut from the same original tube) signal at two temperatures, with the same recording time as for the samples, and performed linear interpolation to build the data at the intermediate temperatures needed. These counting times correspond to total numbers of neutrons detected equal to $\sim$ 14000000 for the container+sample signal and $\sim$ 9500000 for the empty container, which gives a ratio of the container+sample / empty container signals equal to $\sim$ 1.5. In order to obtain the scattered intensity from the samples, the contribution of the empty quartz cell (see Fig. 6.2) was substracted following the method of Paalman and Pings [113]. The multiple scattering was removed and Plazeck corrections [115] for inelastic scattering were carried out. The origin of these corrections has been briefly explained in Chapter 4 section 4.4. We also measured a vanadium sample with a cylindrical geometry identical to that of the samples, in order to get an absolute normalization of the cross sections.

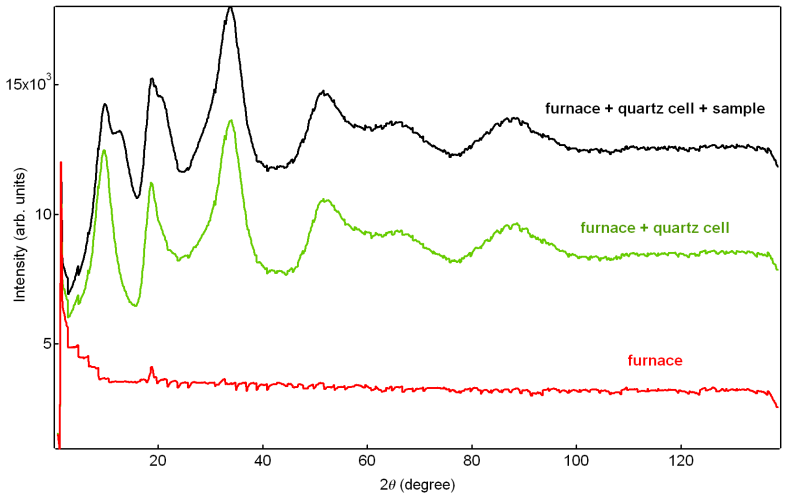

Figure 6.2: Scattered intensities for the empty furnace at room T (red line), the empty container inside the furnace (green line) and the sample of $GeTe_6$ in its container inside the furnace (black line) at $T = 653$ K.

6.1.2 Structure factors S(q)

The structure factors of $GeTe_6$ and $GeTe_{12}$ are presented in Fig. 6.3 and 6.4 respectively, up to the maximal q value of 16 Å^{-1}. We can see, in both cases, well resolved oscillations. The changes with T are the most noticeable in the case of $GeTe_6$: a strong evolution of the entire $S(q)$ is observed, with a decrease of second and third peak heights. These evolutions and the peak positions are in agreement with the results reported in [6]. In $GeTe_{12}$, the same tendency is observed, to a lesser extent, the measurements having been made at higher T compared to the NTE range (because of the experimental impossibility

to reach lower T). The changes in height and position of the three first peaks of $S(q)$, between lowest and highest T, for both compounds, are reported in Table 6.2. We see that the largest evolution, in both compounds, is the decrease of second peak height with T. In $GeTe_6$, we also observe a decrease of the third peak height and an increase of the first peak height, while in $GeTe_{12}$ both remain more or less constant. The peak's positions are evolving with T, specially in $GeTe_6$, where the first peak is moving to larger q while the second and third are moving to smaller q.

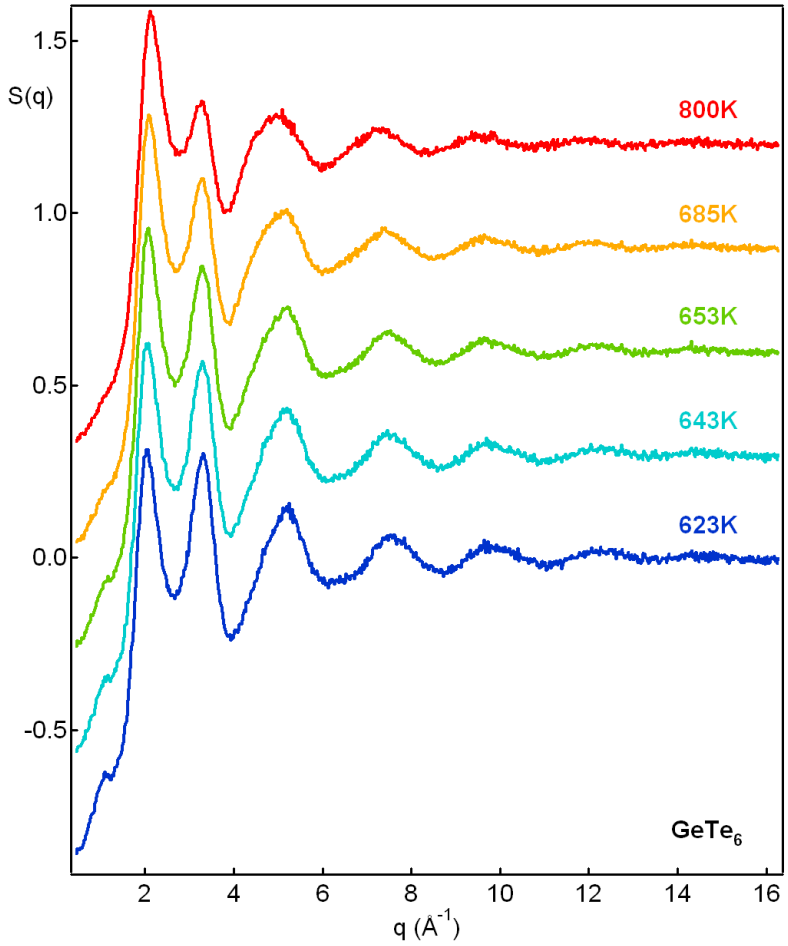

Figure 6.3: Evolution of the structure factors $S(q)$ with temperature for $GeTe_6$, obtained on D4.

The thermal evolution of the structure factor $S(q)$ for liquid $GeTe_6$ is similar to that measured by neutron diffraction on pure Te by Menelle et al. [27] (see Fig. 6.5).

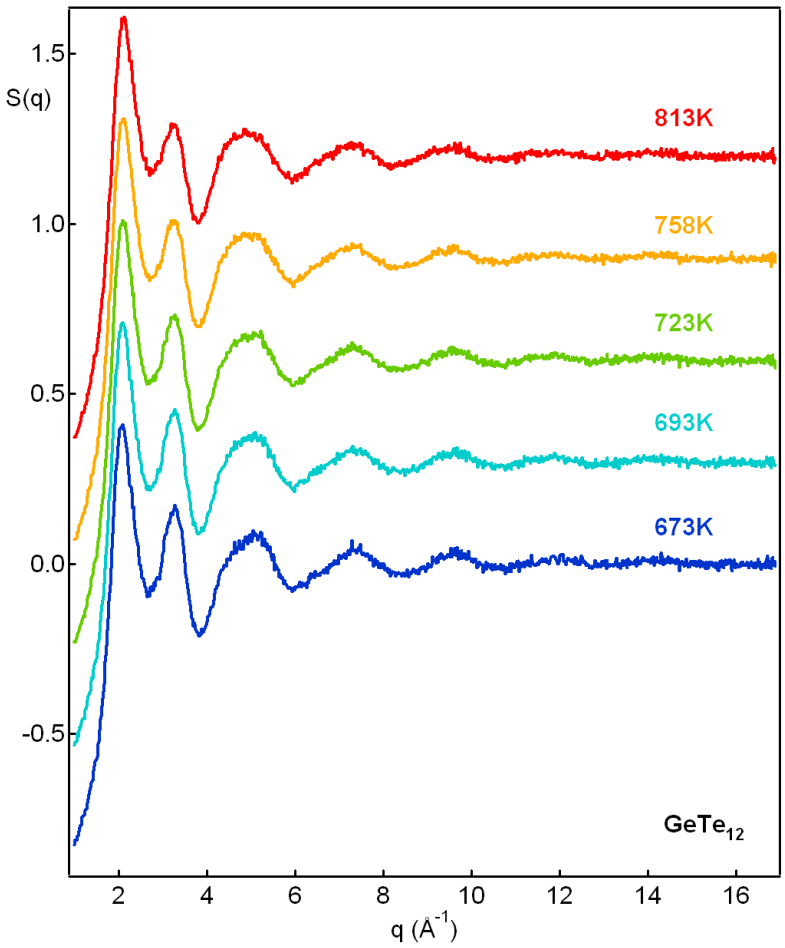

Figure 6.4: Evolution of the structure factors $S(q)$ with temperature for $GeTe_{12}$, obtained on D4.

Compound	peak 1		peak 2		peak 3	
	H	q	H	q	H	q
$GeTe_6$	+6.1%	+4.4%	-13%	-1.2%	-6%	-5.3%
$GeTe_{12}$	+0.7%	+1.9%	-6.8%	-1.1%	+0.9%	-2.4%

Table 6.2: Changes (in %) in height (H) and position (q, in $Å^{-1}$) of the three first peaks of $S(q)$, between lowest and highest T, for $GeTe_6$ and $GeTe_{12}$.

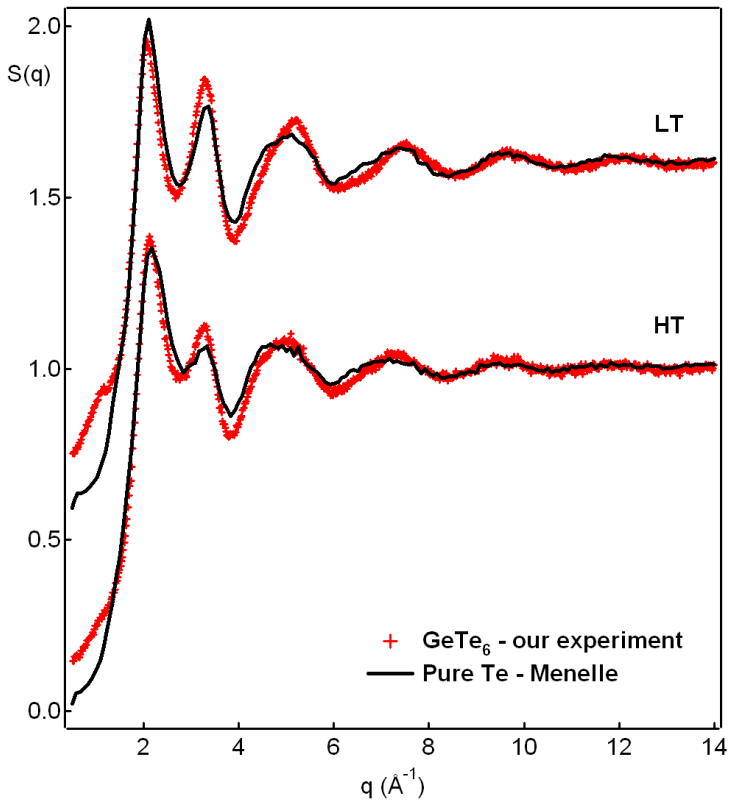

Figure 6.5: Thermal evolution of the structure factors $S(q)$ for $GeTe_6$ (at 653 K and 800 K), obtained on D4, compared with the results from [27] obtained on pure Te (at 623 K and 923 K).

6.1.3 Pair correlation function g(r)

The pair correlation functions, $g(r)$, presented in Fig. 6.6, were obtained by a Fourier transform of the total experimental $S(q)$ (Eq. 4.26 in Chapter 4), without the use of a damping function. The results are satisfactory, as the oscillations (mostly evidenced for r below ~ 2 Å) due to the truncation are not too strong. Three peaks are present in the $g(r)$, both for $GeTe_6$ and $GeTe_{12}$. Above the third shell of neighbors the atoms are randomly disributed, no subsequent structure being found in the $g(r)$. When temperature increases, the position of the first peak slighly shifts to higher r values while the positions of the following peaks remain more or less constant (see Table 6.3), and their heights decrease. Between the lowest and highest temperatures, the coordination numbers calculated from the first peak area up to a distance r_{cut} (see Eq. 4.28 in Chapter 4) evolve from 2.4(6) to 2.9(5) in $GeTe_6$ ($r_{cut} = 3.10$ and 3.24 Å) and from 2.3(8) to 2.6(4) in $GeTe_{12}$ ($r_{cut} = 3.16$ and 3.22 Å). These coordination numbers are in agreement with the results in [6] for liquid $GeTe_6$.

Compound	T (K)	peak 1	peak 2	peak 3
$GeTe_6$	623	2.69	4.14	6.16
	796	2.81	4.16	6.18
$GeTe_6$ [6]	633	2.68	4.12	6.17
	943	2.86	4.12	6.26
$GeTe_{12}$	673	2.79	4.17	6.18
	813	2.83	4.18	6.20

Table 6.3: Position, in Å, of the three first peaks of $g(r)$, at lowest and highest T, for $GeTe_6$ and $GeTe_{12}$.

From these results, it is clear that both $GeTe_6$ and $GeTe_{12}$ undergo strong structural changes during the NTE temperatures range. These results confirm the neutron diffraction experiment published previously for $GeTe_6$ [6].

6.2 Inelastic scattering experiment

The noticeable structural changes observed in the NTE range suggest that a dynamic thermal evolution could also be measured, and inelastic neutron scattering is the method of choice to follow the interatomic force constants as a function of the temperature.

For comparison, we also performed experiments on two Te-based phase-change materials, these alloys presenting a normal behavior with temperature (positive thermal expansion).

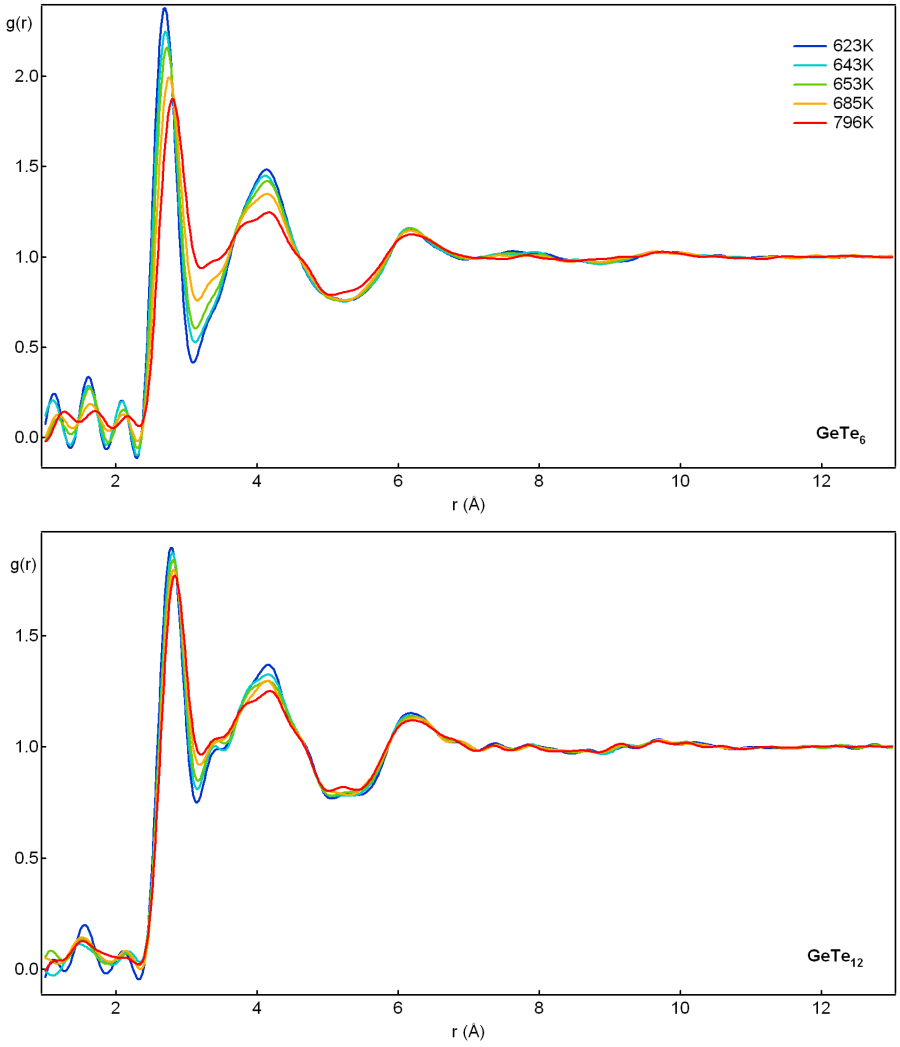

Figure 6.6: Pair correlation function evolution with temperature for $GeTe_6$ (top) and $GeTe_{12}$ (bottom).

6.2.1 Experimental set-up

We performed measurements of the vibrational densities of states (VDOS) of $GeTe_6$, $GeTe_{12}$, $Ge_1Sb_2Te_4$ and $Ge_2Sb_2Te_5$ at various temperatures by inelastic neutron scattering on the IN6 time-of-fligth spectrometer at the ILL in Grenoble (see section 4.7 in Chapter 4 for details about this instrument). For $GeTe_6$, measurements were performed at 673, 773 and 873 K. For $GeTe_{12}$ they were made at 643, 683, 693, 703, 763 and 873 K. For $Ge_1Sb_2Te_4$ and $Ge_2Sb_2Te_5$ the temperatures were 973, 1073 and 1173 K.

The samples were conditioned in the same way as those of the D4 experiment, with diameters 8 mm (internal) / 10 mm (external). We used a wavelength $\lambda = 4.1$ Å, which, together with a 2θ range going from 10 to 115°, gives access to a q range of 0.3 to 2.6 $Å^{-1}$. We recorded the signal scattered by the sample for 6 hours at each temperature. Because of the dominant scattering from the container, rather long counting times (minimum 5 hours) are required in order to obtain reasonable statistics on the final spectra. The quartz contribution to the signal was subtracted using a reference empty quartz tube, measured at the same temperatures and with the same aquisition time as the samples.These counting times correspond to total numbers of neutrons detected equal to $\sim$ 29000000 for the container+sample signal. The ratio of the container+sample / empty container signals is equal $\sim$ 1.35. We normalized the spectra to the reference spectrum of a 6 mm diameter vanadium cylinder. The data were corrected for the energy dependent detector efficiency and time-independent background.

The time-of-flight (TOF) data were converted into a dynamical structure factor $S(2\theta, \omega)$. An integration of $S(2\theta, \omega)$ over the 2θ range accessible to the experiment (10° to 115°) was performed in order to obtain the vibrational density of states VDOS, $n(\omega)$ [139]. Finally, the experimental VDOS was normalized to unity. As the q-range available to the experiment is finite and correlated with the ω range, the $n(\omega)$ density is incomplete and slightly distorted. However, since the (q, ω) range is the same for all measurements, comparisons of $n(\omega)$ are meaningful.

6.2.2 Experimental VDOS

The measured VDOS's are presented in Fig. 6.7. The overall shapes are quite similar for the four systems studied, with noticeable contributions up to $\sim$ 40 meV and a main broad peak around $10 - 20$ meV. Close to zero energy transfer, the full contribution of the quasielastic neutron scattering (QENS) due to diffusion in the liquid could be removed, while it still contributes at higher energies. For this reason, the VDOS increase steeply (almost linearly) at low energies. This effect is stronger at higher temperature for $GeTe_x$ and independent of T for PC materials. This indicates a strong variation in the diffusion coefficient in $GeTe_x$ with the NTE and no significant variation in GST. Accordingly, in the scattering function $S(q, \omega)$ or in its integral over q, $S(\omega)$ (plotted in Fig. 6.8), in which the QENS signal is most evident, $GeTe_x$ materials show a significant temperature dependence of the width of the QENS signal, whereas the QENS signal of PC materials is essentially temperature independent.

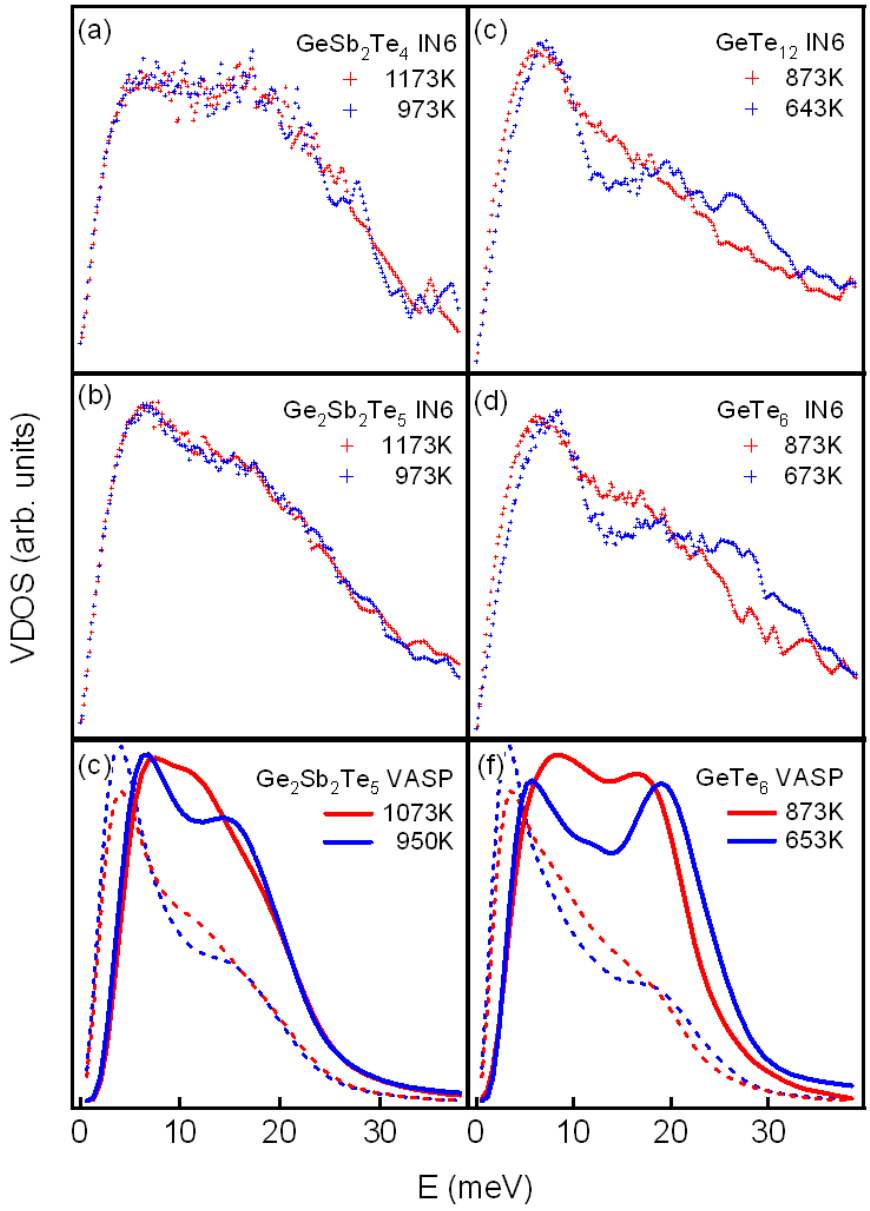

Figure 6.7: Evolution with temperature of the VDOS for $Ge_1Sb_2Te_4$ (a), $Ge_2Sb_2Te_5$ (b), $GeTe_{12}$ (c) and $GeTe_6$ (d), obtained on IN6. Total VDOS obtained from $S(q,\omega)$ calculated on FPMD simulated $Ge_2Sb_2Te_5$ and $GeTe_6$ structures are plotted on (c) and (f) (dotted lines), jointly with the differences between VDOS and VDOS_{sum_p}, see Eq. 6.7 (plain lines).

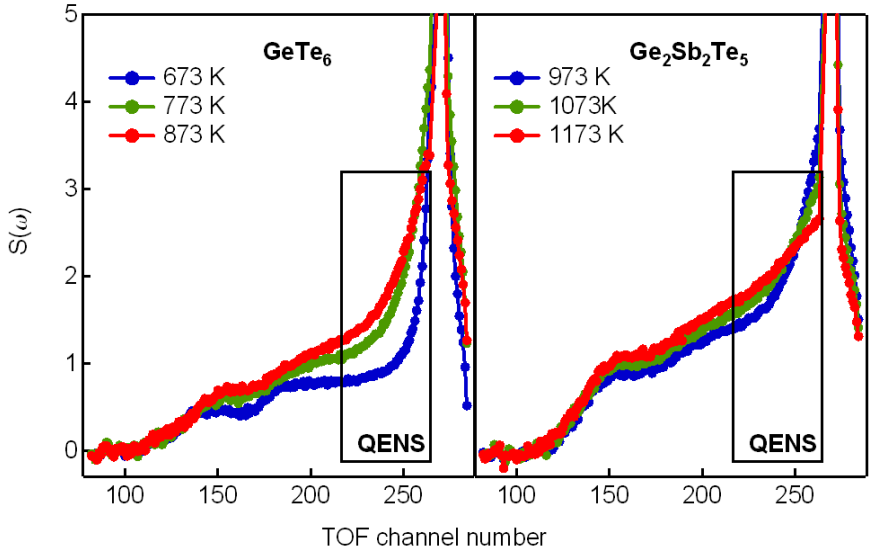

Figure 6.8: Evolution with temperature of the $S(\omega)$ for $GeTe_6$ (left panel) and $Ge_2Sb_2Te_5$ (right panel), versus TOF channel number.

Moreover, these measurements produce contrasted results concerning the temperature dependence of the VDOS. The $Ge_1Sb_2Te_4$ and $Ge_2Sb_2Te_5$ VDOS's remain essentially unchanged in the 200 K range spanned. On the contrary, $GeTe_6$ and $GeTe_{12}$ VDOS's evolve significantly with temperature. Between 18 and 35 meV, the vibrational modes are shifted towards lower energies (or frequencies) when temperature is increased within the range of the NTE. This *red shift* is thus related to the structural changes that are associated to the density anomaly. Since it appears in the medium to high frequency side of the VDOS, we may assume that it concerns mostly $GeTe$ bonds (involving the lightest atoms, Ge). To quantify the shift of the vibrational modes to lower energies, we fitted the spectra with a sum of two Lorentzian functions $A/((x-x_0)^2+B)$ (see in Fig. 6.9), whose centers x_0 are indicated in Table 6.4.

Looking at the first Lorentzian centers obtained (Table 6.4), we can see that the low energy part of the spectra remains roughly stable, for all the compounds, in the experimental temperature range. The center of the second Lorentzian, at higher energy, remains almost constant with temperature, within the accuracy of the experiments, in $Ge_2Sb_2Te_5$ and $Ge_1Sb_2Te_4$. On the contrary, in $GeTe_{12}$ and $GeTe_6$, the change of the vibrational modes is rather sharp : the second peak center shifts respectively by -23 % and -24 % while increasing temperature.

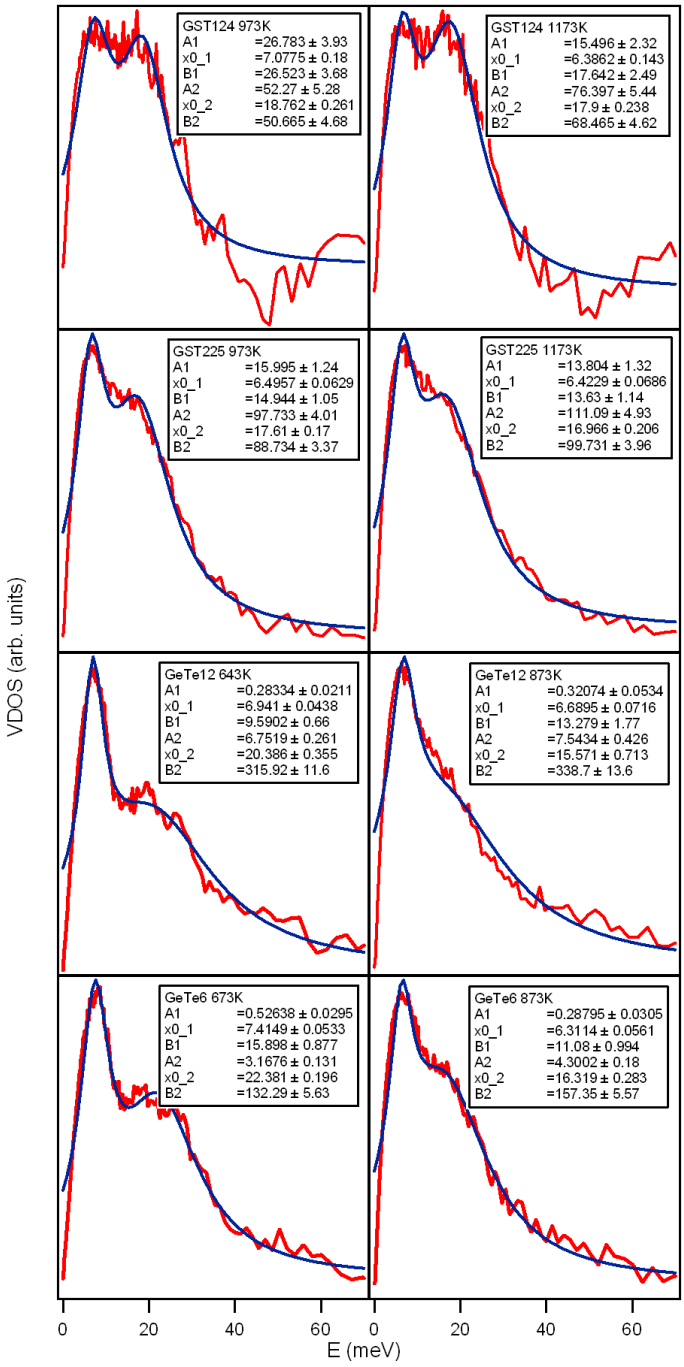

Figure 6.9: Results of the fit of the experimental densities of vibrational states with a sum of two Lorentzian curves $A/((x-x_0)^2+B)$. The fitting parameters obtained are indicated in insets.

	$Ge_1Sb_2Te_4$		$Ge_2Sb_2Te_5$		$GeTe_{12}$		$GeTe_6$	
T (K)	973	1173	973	1173	643	873	673	873
Peak 1	7.1(2)	6.4(1)	6.5(1)	6.4(1)	6.9(1)	6.7(1)	7.4(1)	6.3(1)
Peak 2	18.8(3)	17.9(2)	17.6(2)	17.0(2)	20.4(4)	15.6(7)	22.4(2)	16.3(3)

Table 6.4: Centers (in meV) of the two peaks obtained by a fit of the experimental density of vibrational states with a sum of two Lorentzian curves (and the standard deviations), for every compound, at the different temperatures.

6.3 First Principles Molecular Dynamics study

First Principle Molecular Dynamics (FPMD) simulations allow to obtain the evolution with time of the positions and velocities of an ensemble of atoms. Different structural, dynamical, electrical, ... properties can be computed from these runs.

In this thesis, we will always begin the analysis of the FPMD results by comparing it with the experimental data (i. e. $S(q)$ and $g(r)$). From the FPMD simulations, we obtain directly the partial pair correlation functions, $g_{\alpha\beta}^{fpmd}$ for the α and β chemical species, vs the interatomic distance r, by computing the number of β neighbors of one central α atom in a spherical shell of radius r and thickness dr, divided by $4\pi r^2\rho$ (averaged on all the atoms in the simulation box and over the duration of the simulation run). For a comparison with the experimental $g(r)$, it is necessary to compute the sum of these partial pair correlation functions, weighted by the neutron scattering lenghts b_α and b_β of the chemical species :

$$g^{fpmd}(r) = \frac{\sum_{\alpha\beta} c_\alpha c_\beta b_\alpha b_\beta g_{\alpha\beta}(r)}{\sum_{\alpha\beta} c_\alpha c_\beta b_\alpha b_\beta} \tag{6.1}$$

where c_α and c_β are the concentrations of the α and β chemical species. The structure factor, $S^{fpmd}(q)$, is then obtained by a Fourier transform of the $g^{fpmd}(r)$ (see Eq. 4.25 in Chaper 4).

In this section, we will see that the analysis of experimental VDOS is consistent with the study of the VDOS's of liquid $GeTe_6$ and $Ge_2Sb_2Te_5$ calculated on FPMD atomic trajectories.

Concerning the structural results obtained from the FPMD simulations, we will focus on the $GeTe_6$ alloy only.

6.3.1 Simulations parameters

For $GeTe_6$, we performed FPMD simulations to obtain atomic trajectories on a 216 atoms box (31 Ge and 185 Te) at the experimental liquid densities [107] (ρ = 0.02780 Å^{-3} at 653 K and ρ = 0.02871 Å^{-3} at 873 K). The liquid $Ge_2Sb_2Te_5$ corresponds to calculations on a 162 atoms box (36 Ge, 36 Sb, 90 Te) at the experimental liquid density (ρ = 0.0305 Å^{-3}). We first heated the liquid at 3000 K for 10 ps and then thermalized

it at the desired temperatures and densities for at least 10 ps each. We used the PW91 exchange correlation functional [128], ultrasoft pseudopotentials [133], Ge ($4s$ and $4p$) and Sb and Te ($5s$ and $5p$) valence electrons and a planewave cutoff energy of 175 eV. Calculations were performed at the Γ point only.

6.3.2 Structure factors

The calculated structure factors, $S(q)$, from the MD runs are presented in Fig. 6.10, together with the experimental results in similar temperature conditions. At high q, the overall shape of experimental $S(q)$ is well reproduced by the simulations. At lower q, the evolution of the two first peaks is similar to the experiment : the height of first peak increases with T while for the second peak it decreases. Nevertheless, the calculated $S(q)$ peaks are positioned at lower q values than the experimental ones, which leads to a distance overestimate in the calculated $g(r)$, and to an underestimate of vibrational frequencies (see next section). This has been observed previously for pure Te [104] or rich Te-based compounds [9] and is due to the GGA approximation which slightly overestimates the $TeTe$ bond lengths. The $S(q)$ shape at low temperature is similar to the FPMD simulations on $GeTe_6$ (at 680 K) published by Akola and Jones [140] (see Fig. 6.11).

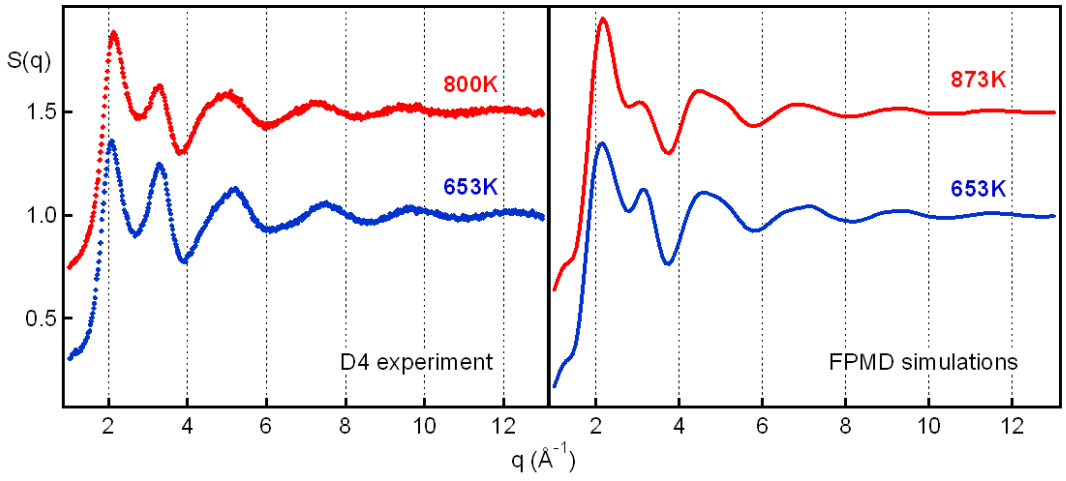

Figure 6.10: Evolution with temperature of liquid $GeTe_6$ structure factor, experimental (left panel) and FPMD results (right panel). The high temperature curves are shifted by 0.5 upwards for clarity.

A recent study by Akola et al. [141] compares the results obtained by FPMD on liquid pure Te, using two different approximations for the exchange-correlation energy : the PBE [142] and the TPSS [143]. The TPSS, which is a hybrid functional that includes some Hartree-Fock exchange, is found to yield slightly better results. If we compare their

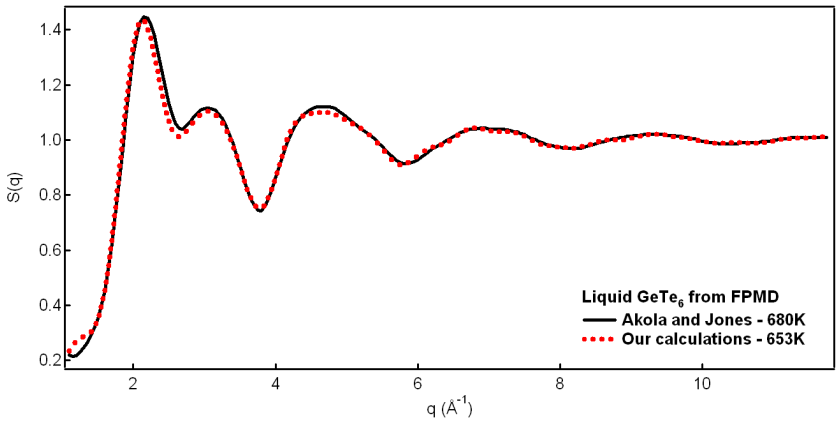

Figure 6.11: Comparison between $S(q)$ of liquid $GeTe_6$ from this thesis and the calculations of Akola and Jones [140].

calculated $S(q)$ to ours (on $GeTe_6$) and to the experimental results by Menelle et al. [27], at low and high temperatures, we see that the two FPMD curves are similar in phase at high q-value, the only (small) decrepencies appearing on the two first peaks (see Fig. 6.12).

6.3.3 Pair correlation functions

The total and partial pair correlation functions were calculated at low and high temperature (see Fig. 6.13 and 6.14 respectively). As expected from the structure factors, the distances are slightly overestimated compared to the experiment (by $\sim$ 0.13 Å on the first $g(r)$ peak). The partial coordination numbers (see Table 6.5) indicate that the heteropolar bonds are favored around Ge, and homopolar ones around Te (which is due to the large concentration of Te atoms). At low temperature, the average coordination numbers equal 4.6 for Ge and 3.3 for Te. The number of neighbors around each type of atoms are increasing with temperature. This increase is similar to the results found by Reverse Monte-Carlo fit in [7]. The partial coordination numbers are also in agreement with the results of Akola and Jones [140] at 680 K, except for the N_{GeTe} which is found higher by 0.6 in our simulations.

6.3.4 Interatomic distances in the FPMD structures

Distance distributions For each type of central atom 0 in the FPMD structures, the six first neighbors i are selected and sorted according to their bond length (see Fig. 6.18). The first bond length contributes to the distribution $d_1(r)$, the second to $d_2(r)$, etc. These six distances are averaged over all the atoms in the structure and over the duration of the run, to produce the distances ditributions of Fig. 6.15 and 6.16 (for central Ge and Te respectively) at 653 and 873 K. By this procedure, the third neighbor distance for one

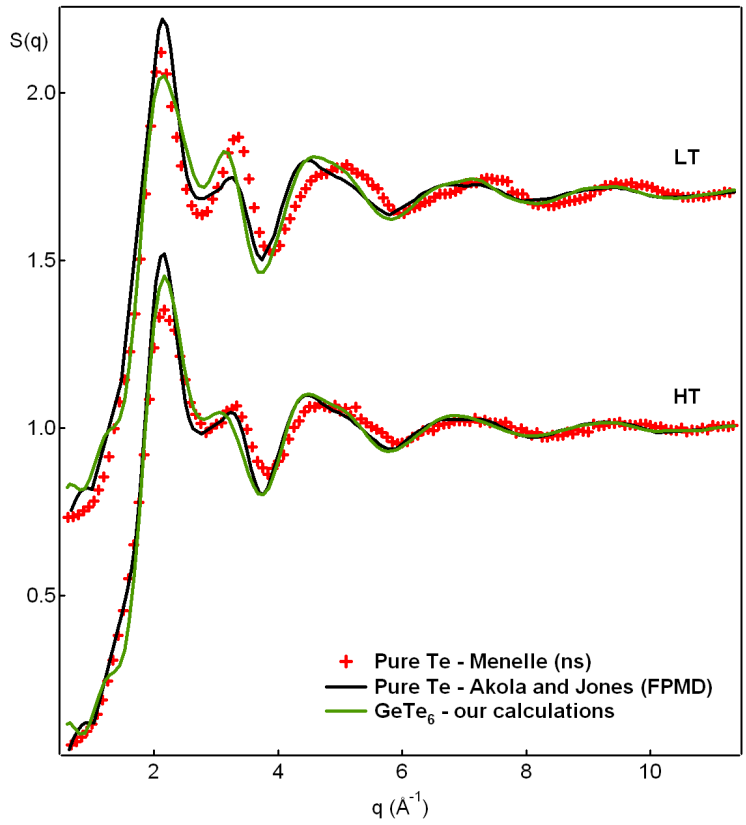

Figure 6.12: Comparison between $S(q)$ of liquid $GeTe_6$ from this thesis (at 653 K and 873 K) and the calculations of Akola and Jones on pure Te (at 625 K and 970 K) [140]. Neutron diffraction results on pure Te (at 623 K and 973 K), from [27], are also shown.

T (K)	r_{min}^{fpmd}	N_c^{GeGe}	N_c^{GeTe}	N_c^{TeGe}	N_c^{TeTe}	N_c^{Ge}	N_c^{Te}
653	3.40	0.2(3)	4.3(6)	0.7(3)	2.5(8)	4.5(9)	3.3(1)
873	3.56	0.3(7)	4.9(9)	0.8(3)	3.4(4)	5.3(6)	4.2(7)
680 [140]	3.46	0.2	3.6	0.6	2.5	3.8	3.1

Table 6.5: Positions of the first minimum r_{min}^{fpmd} (taken as the cutoff distance for integration) in total pair correlation functions, $g(r)$ (from FPMD), partial coordination numbers from partial pair correlation functions, $g_{\alpha\beta}(r)$, and total coordination numbers for Ge and Te atoms. The second decimal is indicated in parentheses. The results [140] are from Akola and Jones. All distances are given in Å.

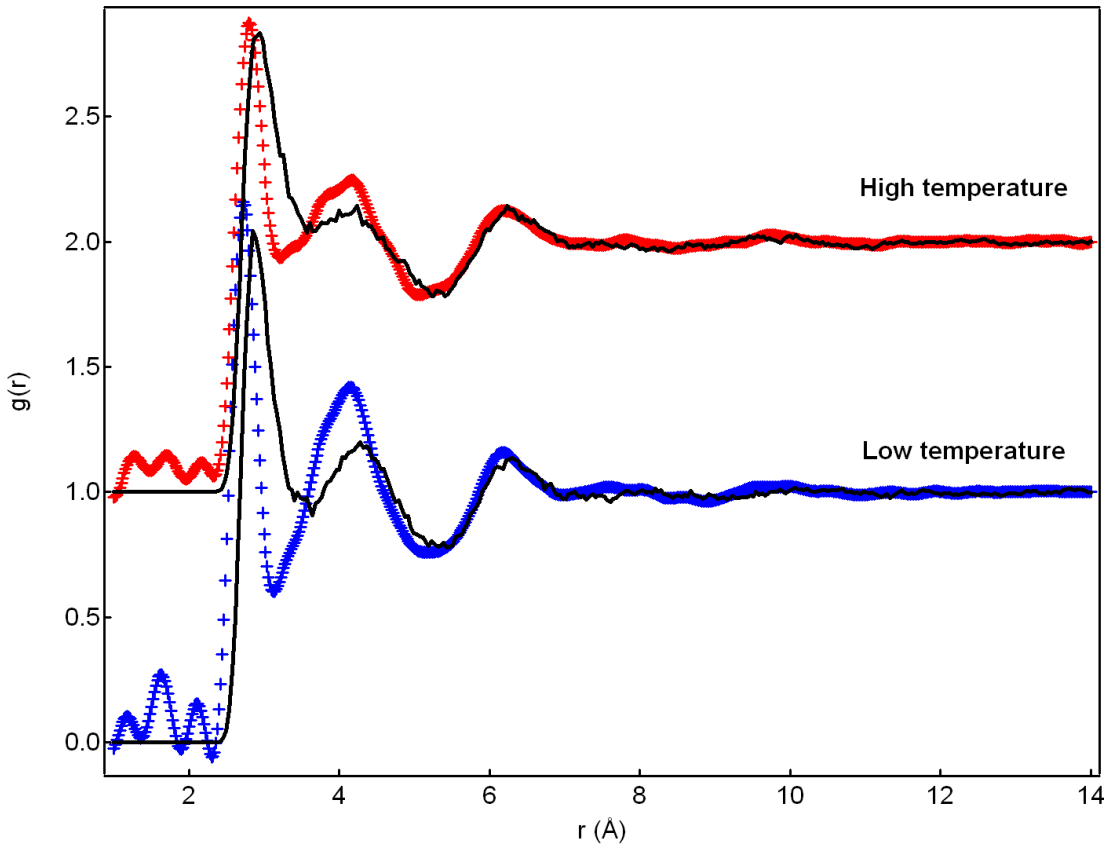

Figure 6.13: Pair correlation functions of liquid $GeTe_6$ at high (800 K in the experiment, 873 K in FPMD simulations) and low temperatures (653 K), from experiment (markers) and FPMD (black lines). The high temperature curves are vertically shifted by 1 for clarity.

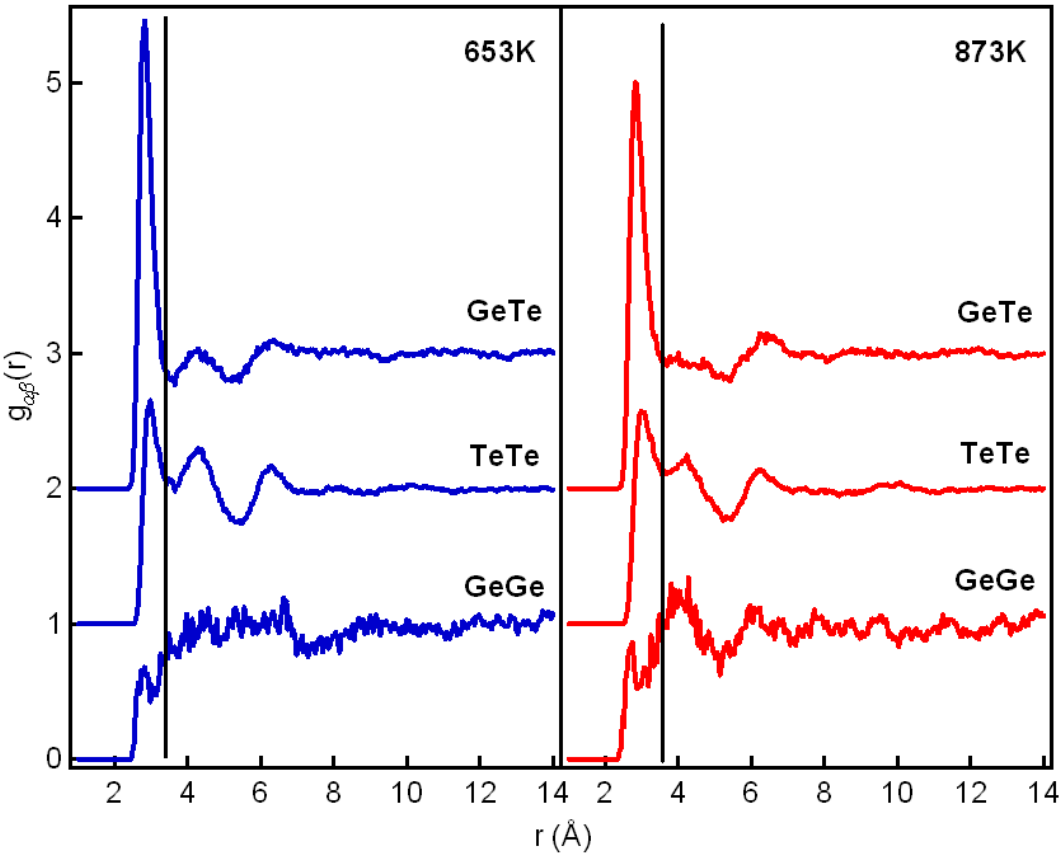

Figure 6.14: Partial pair correlation functions of liquid $GeTe_6$ at high and low temperatures. The vertical black lines indicate the cutoff distances taken to compute the coordination numbers.

given atom can be shorter than the second neighbor distance for another atom : that is the reason why the distributions overlap significantly. The sum of these 6 distributions is also represented. In both graphs, we positioned vertical black lines at the average distances, to view more easily the evolution upon heating. At high temperature, the total distances distribution does not show any particular profile, except a thermal widening (broad peak). When going from the high to the low temperature, we clearly see, either around Ge or Te atoms, that the longer distances are increasing. At low temperature, around each element, two peaks begin to appear, separating the shorter and longer distances of the first neighbor shell, in agreement with the coordination number evolution found previously.

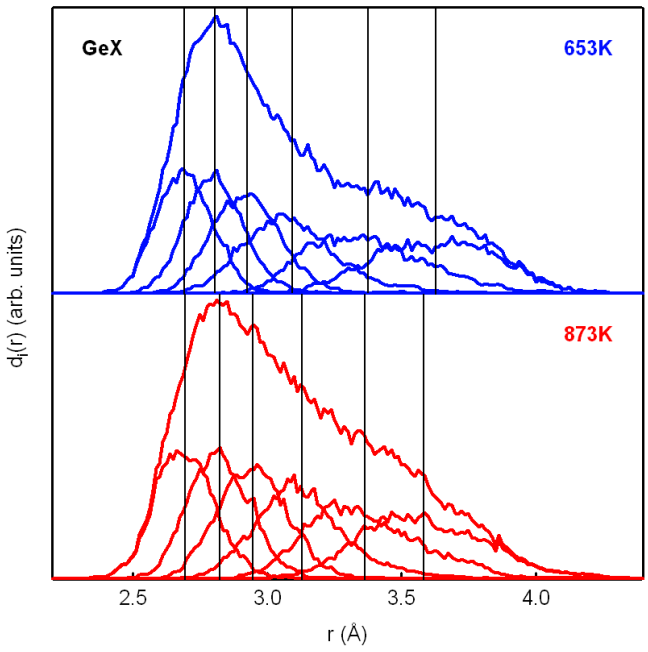

Figure 6.15: Evolution with temperature of the distributions of distances around Ge atoms in liquid $GeTe_6$. The vertical black lines are positioned at the average distances.

Average distances In Fig. 6.17, we plotted the average distances around Ge (left panel) and Te (right panel) (calculated from the distance distributions), and their standard-deviation at 653 and 873 K. In addition to the shortening of longer distances with temperature, the shorter distances (the first 4 in the Ge case and the first 2 in the Te case) are elongating. We also note that the standard deviations are increasing with the identity i of the neighbor.

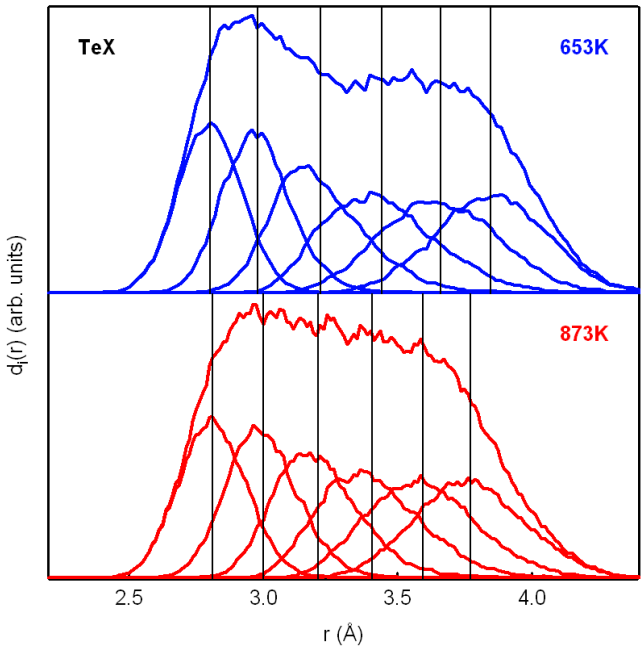

Figure 6.16: Evolution with temperature of the distances distributions around Te atoms in liquid $GeTe_6$. The vertical black lines are positioned at the average distances at low temperature.

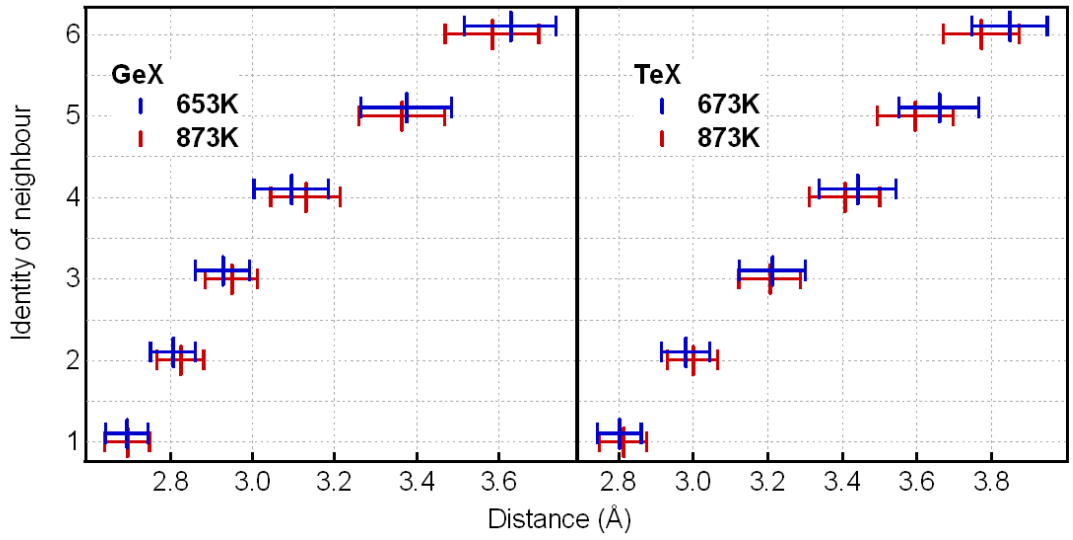

Figure 6.17: Average distances around Ge (left panel) and Te (right panel) (calculated from the distances distributions) and their standard deviations, at 653 and 873 K. The blue markers are vertically shifted by 0.1 for clarity.

6.3.5 Angle distributions

We analyze the partial bond angle distributions (PBADs), $P(\theta_{ij})$, of the 15 angles $\widehat{i0j}$ defined between a central atom 0 and the i^{th} and j^{th} neighbors with $i = 1, \ldots, 5$ and $j = 2, \ldots, 6$ (see Fig. 6.18), that is to say 102, 103, 203, etc[2] (see Fig. 6.19). The sum of these partial distributions give the total bond angle distributions (see Fig. 6.20). The total bond angle distributions clearly indicate that the local order around each chemical species is essentially octahedral (peaks around 90 and 180°) in liquid $GeTe_6$. If we detail the partial angles (see Fig. 6.19), we see that the angle distributions between the four closest neighbors are sharply peaked in comparison with the broadness of the other angle distributions. This agrees with the previous results of RMC [7] and FPMD simulations [9]. This is however in contradiction with [140], in which Ge atoms are found to be tetrahedrally bounded.

[2]Note that the choice of looking up to $i = 6$ is motivated by the fact that, in telluride systems, octahedral local structures with six neighbors around a central atom are expected [41]. The reduction to a lower number of possible neighbor/angles in, for example, the case of purely tetrahedral systems, is straightforward.

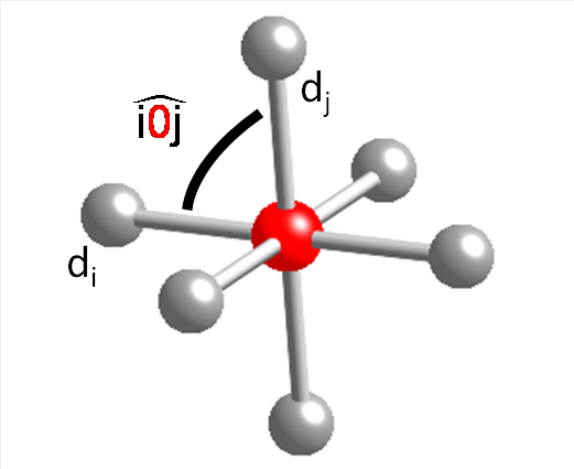

Figure 6.18: Partial bond angle distributions $P(\theta_{ij})$ are obtained by averaging, over all the atoms in the structure and over the duration of the run, the angles $\widehat{i0j}$ between a central atom 0 and the i^{th} and j^{th} neighbors with $i = 1, \ldots, 5$ and $j = 2, \ldots, 6$.

6.3.6 Dynamics

Diffusion

An useful parameter to quantify the atomic dynamics is the diffusion coefficient, D. It can be directly extracted from the atomic displacements as a function of time t :

$$D = \lim_{t \to +\infty} \frac{\langle |\vec{r}_i(t) - \vec{r}_i(0)|^2 \rangle}{6t} \tag{6.2}$$

where the brackets denote the average over all particles i and the vectors $\vec{r}_i$ are the atomic positions. In Fig. 6.21, we plotted the temperature dependence of the mean square displacement of the Ge and Te atoms as a function of time. The calculated atomic mean square displacements has a linear time dependence. The partial atomic diffusion coefficients (see Table 6.6) increase with temperature, as in normal liquid, especially for the Ge atoms : while the Te atoms are more mobile than the Ge atoms at 653 K, it is the contrary at high T.

We can use the Stokes-Einstein [144] relation to obtain a rough estimate of the viscosity, η, from the average diffusion coefficient :

$$\eta = \frac{k_B T}{6\pi r_0 D} \tag{6.3}$$

where r_0 is the radius of an atomic sphere [145]. It is reasonable to take $r_0 = \rho^{-1/3}/2$, where ρ is the liquid density. The results we obtain for the thermal evolution of the viscosity are indicated in Table 6.6 (with $r_0 = 1.7$ at 653 K and 1.6 at 873 K). The

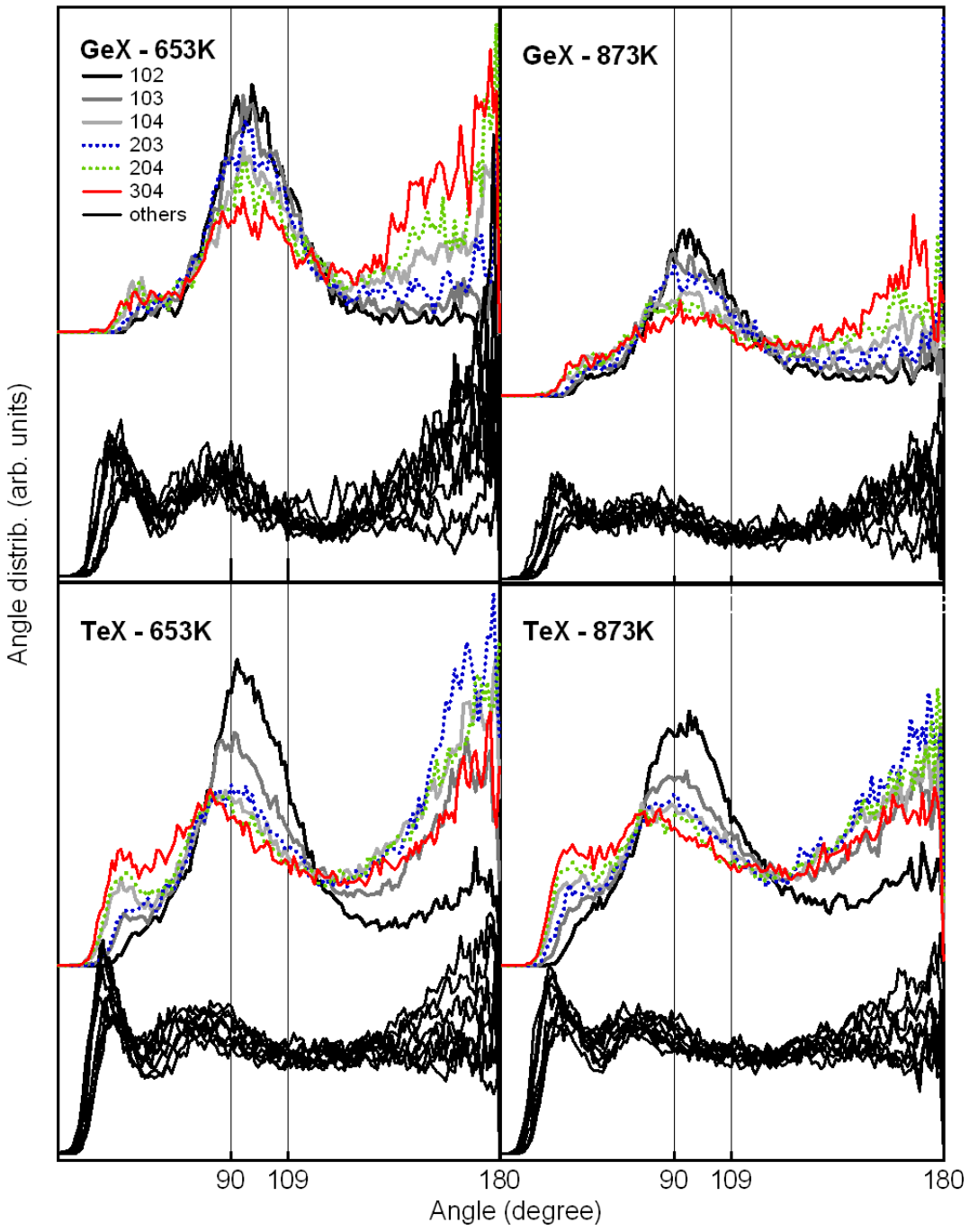

Figure 6.19: Partial bond angle distributions $P(\theta_{ij})$ around Ge and Te atoms in liquid $GeTe_6$, at low and high temperatures.

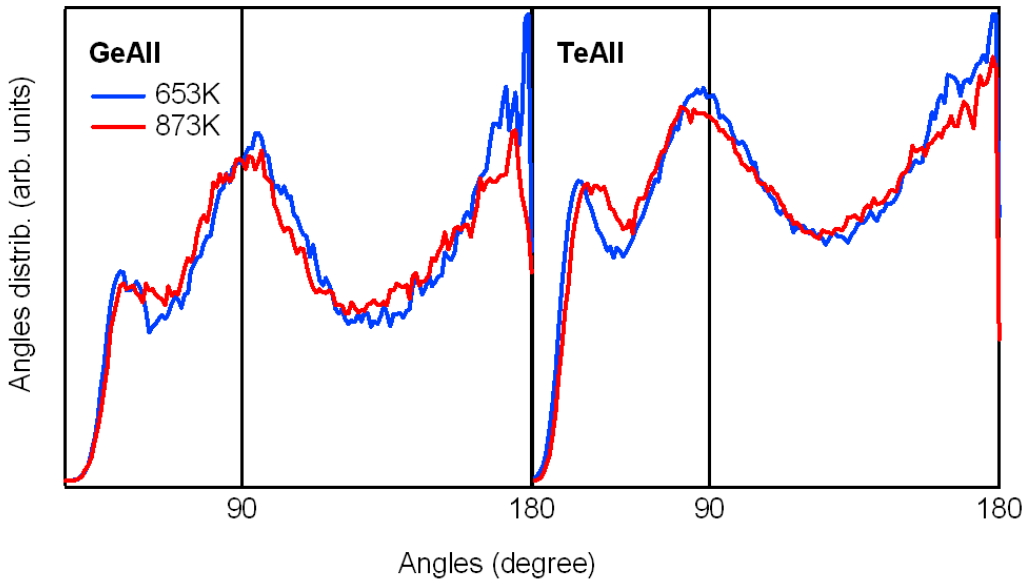

Figure 6.20: Total bond angle distributions around Ge and Te atoms in liquid $GeTe_6$, at low and high temperatures.

liquid $GeTe_6$ becomes less visquous when temperature increases, as in normal liquids. For comparison, the viscosity of the $Ge_2Sb_2Te_5$ obtained by FPMD evolves from 0.8 to 1.1 cP between 950 and 1073 K (calculated with $r_0 = 1.6$ Å). This is in agreement with the results obtained by Akola et al. with FPMD simulations on pure Te [141].

We are not able to reproduced the strong evolution of the experimental viscosity when temperatures decreases (experimentally, η goes from 1.7 cP at 873 K to 25.9 at 673 K [146]). It is due to both the box size, which is too small to allow for the accurate calculation of such properties, and the limited simulation time.

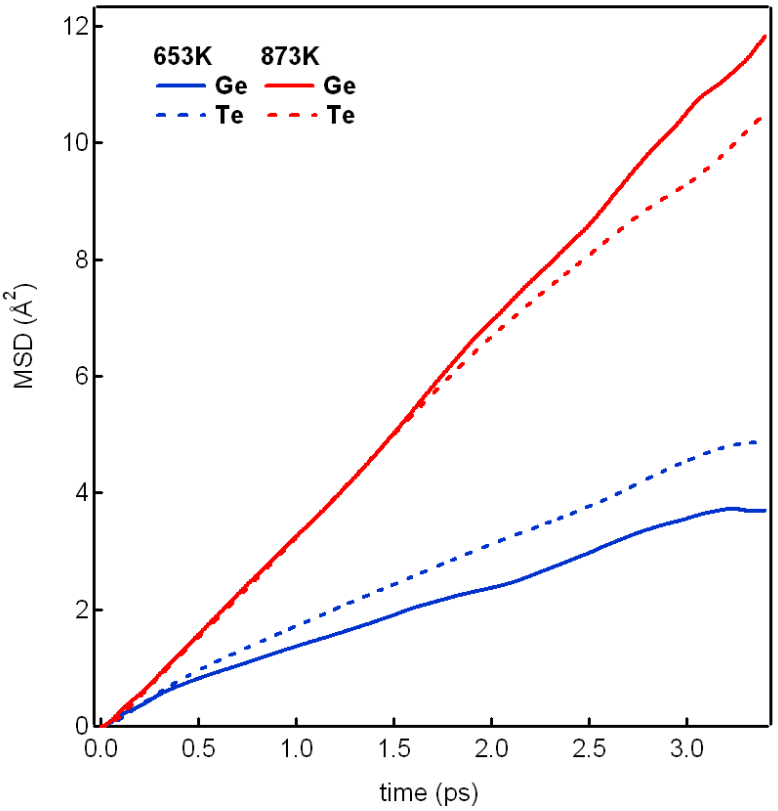

Figure 6.21: Evolution with temperature of the Mean Square Displacement (MSD) of Ge and Te atoms in liquid $GeTe_6$.

Vibrational Density of States

We computed the total dynamical structure factor $S(q,\omega)$ and the partial dynamical structure factors $S_p(q,\omega)$ (for each type of element) on the molecular dynamic trajectories obtained for $GeTe_6$ and $Ge_2Sb_2Te_5$, using the *nMoldyn* code [147]. We integrated the total and partial structure factors obtained from simulations over the same q range as

T (K)	D		η
	Ge	Te	
653	2.0	2.5	1.2
873	5.8	5.3	0.8

Table 6.6: Evolution with temperature of the diffusion coefficient D (in 10^{-5} cm^2/s) and the viscosity η (in cP), from FPMD simulations on liquid $GeTe_6$.

that accessible to the IN6 experiment, to obtain the total and partial vibrational densities of states :

$$S(q,\omega) \rightarrow \text{VDOS} \tag{6.4}$$

$$S_p(q,\omega) \rightarrow \text{VDOS}_p \text{ for Ge, Sb or Te atoms} \tag{6.5}$$

The total VDOS are plotted (dashed lines) in Fig. 6.7 (c) and (f). The FPMD results are in qualitative agreement with the experimental trends : in the case of $GeTe_6$, we see a shift of the high frequency tail (which ranges from 18 to 30 meV) towards lower energies with increasing temperature and no evolution of this part of the spectra in the case of $Ge_2Sb_2Te_5$.

Nevertheless, in the simulations, the vibrational frequencies are about 30 % lower than in the experiment, meaning that the calculated vibrational modes are too soft (as already discussed in the previous subsection). This is in line with the observation that the computed local structure [9] is not distorted enough, leading to a too broad first neighbors peak in the pair correlation function and a too low second peak in the static structure factor as compared to the experiments [6]. However, the trends are reproduced and further analysis of the simulation results confirms that the high energy modes that appear between 18 and 30 meV in $GeTe_6$ at low temperature involve Ge atoms.

The partial VDOS (for each element) are plotted in Fig. 6.22. In the energy range where the red-shift is observed in experimental $GeTe_6$ VDOS, the only curve which evolves with T is the VDOS$_p$ corresponding to Ge in $GeTe_6$. This confirms that the changes evidenced in the experimental VDOS for $GeTe_6$, along the NTE, involve mostly the Ge atoms.

Because of the general underestimate of the vibrational frequencies in comparison with the experiment, the contribution of the diffusion to the spectra (which arises at low energy) dominates and partly obscures the expected frequency shift in total VDOS. To remove the contribution of diffusion to the spectra, we proceeded as follows. We summed the partial VDOS$_p$ obtained in equation 6.5, weighted by the concentration c of each element (Ge, Sb or Te), and obtained, for $GeTe_6$ and $Ge_2Sb_2Te_5$, a VDOS$_{sum_p}$ that contains all the homopolar vibrational information, as well as the full diffusive part of the spectra :

$$\text{VDOS}_{sum_p} = \sum_{el=Ge,Sb,Te} c(el)\text{VDOS}_p(el) \tag{6.6}$$

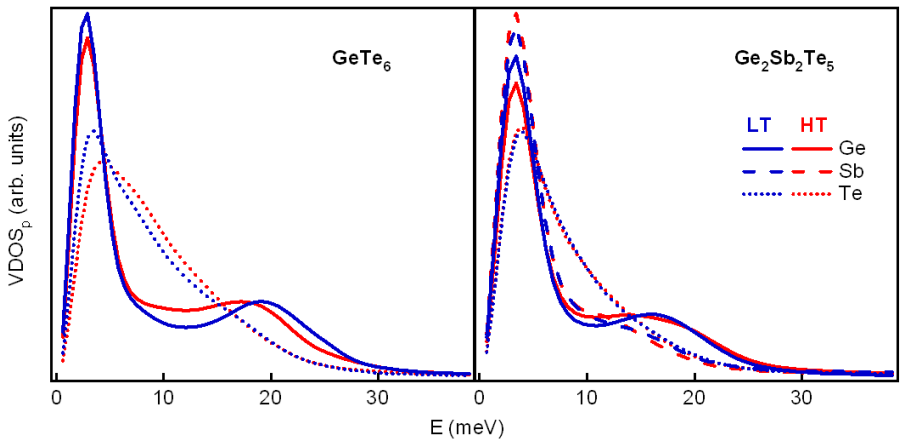

Figure 6.22: Evolution with temperature of liquid $GeTe_6$ (left panel) and $Ge_2Sb_2Te_5$ (right panel) partial VDOS, for each chemical element. Blue lines : low temperature. Red lines : high temperature.

The differences between the VDOS obtained from total $S(q,\omega)$ and the VDOS_{sum_p} give VDOS_{dif} , which contains all interactions except the homopolar ones, and without the atomic diffusion :

$$\text{VDOS}_{dif} = \text{VDOS} - \text{VDOS}_{sum_p} \tag{6.7}$$

Finally, those differences, plotted in Fig. 6.7 for $Ge_2Sb_2Te_5$ (c) and $GeTe_6$ (f), were normalized to unity. This decomposition emphasizes the temperature evolution of the highest frequency modes in $GeTe_6$, which are mostly attributed to the $GeTe$ vibrations.

6.4 Distorted octahedral liquid model

The observed red-shift of the VDOS correlated with the volume contraction induced by a temperature increase in $Ge_xTe_{(1-x)}$ alloys ($0 \leq x \leq 0.20$) can be easily interpreted within the distorted octahedral liquid model briefly sketched in the introduction of this chapter.

Since the liquid is essentially chemically ordered in the temperature range of the NTE, Ge atoms reside inside distorted octahedral cages with six Te neighbors. Because of the Peierls instability, that has been shown to remain active also in disordered structures [23], the local environment is distorted at low temperatures : one Ge atom is more strongly bonded to some Te atoms (typically three or four) and more loosely bonded to the remaining ones. The shorter and stronger $GeTe$ bonds correspond to higher vibrational frequencies. When temperature increases, as shown by combining neutron elastic scattering and EXAFS [148, 7], the Ge and Te average coordination number *increases* (at

variance with usual liquids) while the volume shrinks as sketched in Fig. 6.27 (a) and (b). There is nevertheless an apparent paradox : the volume of the cage surrounding a Ge atom shrinks but at the same time the nearest neighbor distances elongate.

This is also observed in the $\alpha \rightarrow \beta$ transition of the crystalline $GeTe$ compound, and in pure Se and Te [149] alike. In $GeTe$ the volume shrinks by $\simeq$ 1 % at the $\alpha \rightarrow \beta$ transition but at the same time the short interatomic distances increase by +2.4% (and simultaneously the long distances decrease by -2.8%)[83].

Our FPMD simulations on $GeTe_6$, performed at two different densities for low and high temperatures, reproduce this behavior.

Three Body Correlations function An interesting way to visualize the rate of distorsion in disordered structures, if the local order is quasi-octahedral, is to plot, with respect to distances, the probability for one central atom (either Ge or Te) to have two almost aligned neighbors at distances r_1 and r_2 (as in [150]). Only bonds that are aligned within a cone of 30° of apperture are taken into account (see Fig. 6.23). This probability is called 'Three Body Correlation function' (TBC).

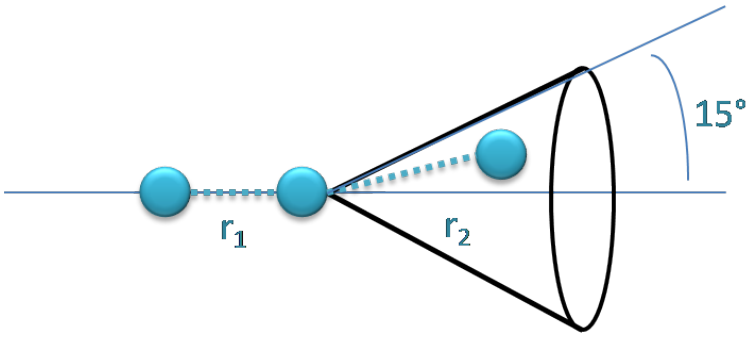

Figure 6.23: To study the local distortions in our FPMD structures, we check the probability for one central atom to have two almost aligned neighbors at distances r_1 and r_2.

The TBC for almost aligned triplets of atoms centered on Ge or Te (bonds aligned within 15°) in $GeTe_6$, at 653 and 873K, are plotted in Fig. 6.24 and 6.25 respectively. In the Ge case, the two distinct maxima observed at 653 K clearly indicate a tendency to alternate short r_s (average value $\sim$ 2.87 Å) and long r_l (average value $\sim$ 3.18 Å) almost aligned bonds, which is coherent with the distortion scheme presented in Fig. 6.27 (a) at low temperature. At 873 K, the volume is smaller and the probability for short and long bonds alternation around Ge atoms becomes much smaller, consistent with the symmetrization depicted in Fig. 6.27 (b).

Around Te atoms, at low temperature, a distorsion is hardly evidenced : the two peaks are very close to the diagonal, almost merged. We can compare it to the TBC obtained on an octahedral crystal at finite temperature[3], plotted in the Fig. 6.26. With temperature, the intensity of the peaks becomes smaller but their positions do not evolve as in the Ge case. The Ge atoms thus clearly play a different role than the Te ones, as already evidenced from the analysis of the experimental VDOS evolution with temperature.

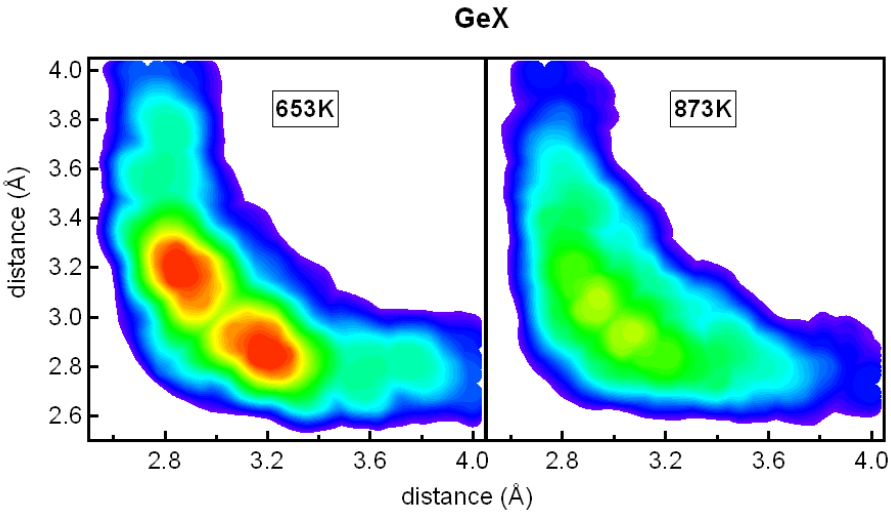

Figure 6.24: Three body correlation functions for almost aligned triplets of atoms, centered on Ge atoms, calculated on simulated $GeTe_6$ structures, at 653 K (left panel) and 873 K (right panel). Almost aligned means that the bond angle between the two bonds is larger than 165°. Contours are drawn between 35 % of the maximum value and maximum value of normalized correlation at 653 K (from blue to red).

The behavior is totally different for the PC-materials. Their structure factors $S(q)$ [151] and their VDOS are nearly independent of T above the melting temperature. From that we deduce that both the structure and the force constants are roughly temperature insensitive. This is related to the normal evolution of the atomic volume with respect to temperature (see Chapter 3 Fig. 3.12).

6.5 Vibrational entropy

We can use the experimental VDOS to estimate the vibrational entropy of the system, S_{vib}, along the NTE [152]. In order to quantify its variation, ΔS_{vib}, for $GeTe_6$ between

[3]This crystal was simply modeled by allowing movements of 10 % of the interatomic distances at equilibrium for atoms positioned on the nodes of a $NaCl$-type lattice.

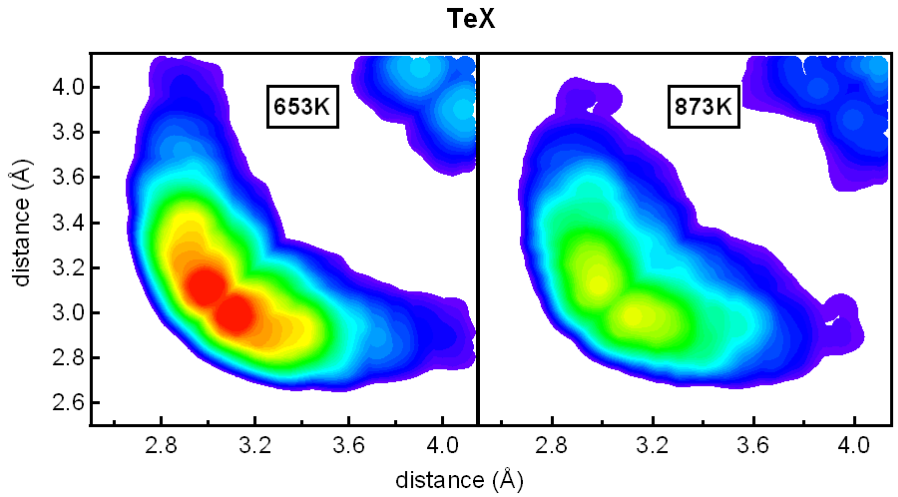

Figure 6.25: Three body correlation functions for almost aligned triplets of atoms, centered on Te atoms, at 653 K (left panel) and 873 K (right panel). Almost aligned means that the bond angle between the two bonds is larger than 165°. Contours are drawn between 35 % of the maximum value and maximum value of normalized correlation at 653 K (from blue to red).

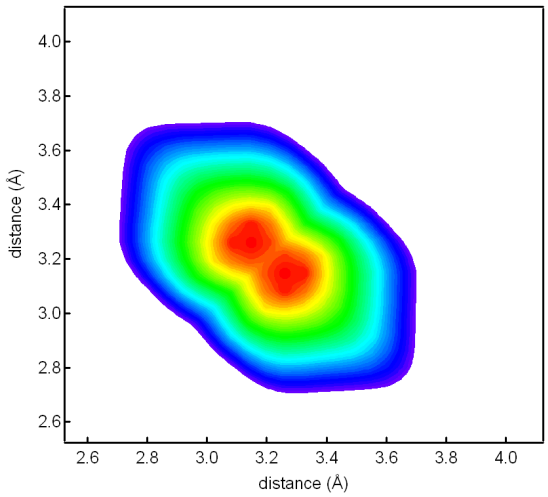

Figure 6.26: Three body correlation functions for almost aligned triplets of atoms in an octahedral crystal at finite temperature. This crystal was simply modeled by allowing movements of 10 % of the interatomic distances at equilibrium for atoms positioned on the nodes of a $NaCl$-type lattice. Same conventions as Fig. 6.24 and 6.25.

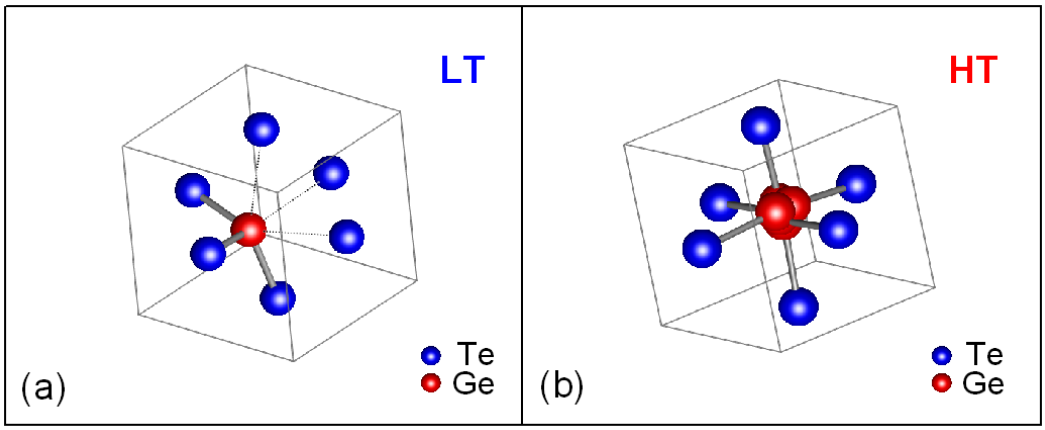

Figure 6.27: (a) Sketch of the low temperature structure with a Ge atom in a larger volume distorted octahedral environment. (b) At higher temperature, the local environment of Ge atom inside the octahedral cage becomes more symmetric because of the larger vibrational entropy.

673K and 873K, we can approximate the contribution of the VDOS redshift to the vibrational entropy using [153] :

$$S_{vib}(T) = 3R \int n(\omega)[\{(\hbar\omega/2kT)\coth(\hbar\omega/2kT)\} - \ln\{2\sinh(\hbar\omega/2kT)\}]d\omega \qquad (6.8)$$

Taking the value at 673 K as the reference, the additional vibrational entropy contribution between 673 K and 873 K, ΔS_{vib}, can be estimated to 8.9 J/mol.K. In comparison, the total entropy change between both temperatures, ΔS, calculated by integrating the experimental C_p/T data from Tsuchiya measurements [2], is equal to 14.3 J/mol.K (see Chapter 3 Fig. 3.7 for $C_p(T)$ curves). We can see in Fig. 6.28 that the ΔS_{vib} calculated from the vibrational densities of states obtained on IN6 thus represents the largest part (62 %) of the total variation of S between both temperatures. This fact is especially striking in comparison with the 'normal liquid' case [152], in which the non-vibrational part of the entropy has the fastest increase with T, and thus provides the dominant contribution to total entropy increase ($\sim$ 70 % in liquid Se at 600 K [152]).

It should be noted that Eq. 6.8 is in principle not valid in our case, because it takes into account the harmonic normal modes only, and thus neglects the temperature dependence of the VDOS and of the underlying effective potential. It is however clear that the contribution of the vibrational entropy is truly dominating in the case of $GeTe_6$. The chemical ordering is strong and similar in $GeTe_6$ (and $GeTe_{12}$) and the GST's. In the latter's case, our experiment shows that there is no additional vibrational entropy change with temperature compared to the 'normal liquid' case. However, in the $GeTe_6$ (and $GeTe_{12}$) case, the change in effective potential along the negative thermal expansion obviously results in important anharmonic terms. Actually, from our INS experiment, we

can estimate the variation in S due to the inclusion of terms resulting from $\Delta n(\omega)/\Delta T$ by the differentiation with T of the Helmholtz free energy :

$$F(T) = 3RT \int n(\omega, T) \left[\ln \left\{2 \sinh(\hbar\omega/2kT)\right\}\right] d\omega \tag{6.9}$$

in which we consider the $\Delta n(\omega)/\Delta T$ obtained from experiment. This would give an additional contribution to S_{vib} of 1.0 J/mol.K (see Fig. 6.28).

In summary, the $GeTe_6$ increase in vibrational entropy computed from the experimental VDOS thus reaches approximately 69 % of the total entropy increase (see Fig. 6.28). The ΔS is thus largely due to the vibrational contribution, that overcompensates the internal energy loss in the Gibbs energy balance.

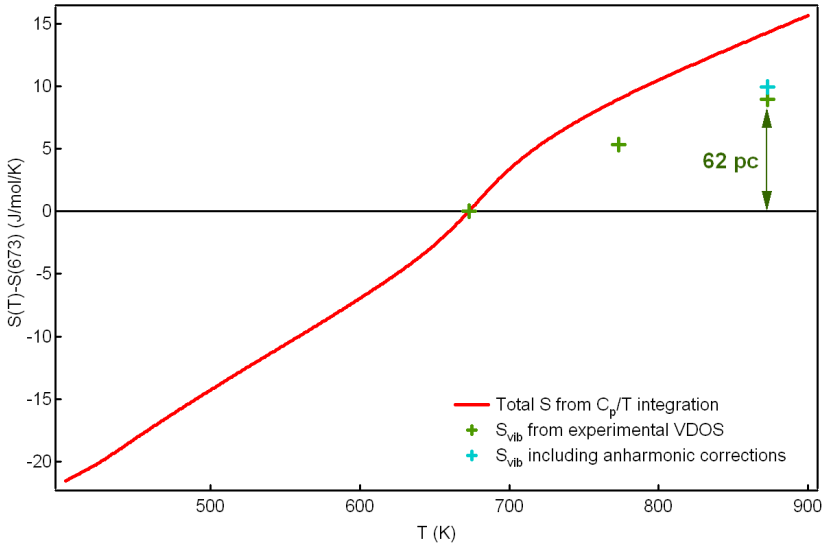

Figure 6.28: Total entropy (red line) obtained from C_p measurements on $GeTe_6$ performed by Y. Tsuchiya [2] compared with the vibrational entropy (green markers) calculated from the vibrational densities of states obtained on IN6, with Eq. 6.8, between 673 K and 873 K. The relative variation of S_{vib} between both extreme temperatures represents 62 % of the variation of total entropy (69 % if we include the contribution that occurs from $\Delta n(\omega)/\Delta T$). We also represented the additional S_{vib} from anharmonic therms in the derivation of (2) (light blue marker). We estimate the error bar on S_{vib} to ~ 0.2 J/mol.K (obtained by varying the coefficient of the QENS background to the $S(q, \omega)$ spectra).

6.6 Conclusion

With these experiments and computer simulations, we identified the driving force for the NTE in rich-Te Ge_xTe_{1-x} alloys and demonstrated the role of the vibrational entropy

evolution with temperature.

Depending on the relative magnitude of the energy gained by the Peierls-like distortion (ΔE) and the vibrational entropy gained ($T\Delta S_{vib}$) when the local symmetry is recovered, the NTE domain could theoretically extend up to T such that $T\Delta S_{vib} \approx \Delta E$. It has been shown the heavier the p-bonded elements, the lower the Peierls distortion energy [24]. For pure Te, the NTE occurs below the melting temperature (in the undercooled liquid). An addition of Ge increases the Peierls distortion energy and a NTE is observed above the melting point because the melting temperature is lower.

In conclusion, we have shown that, in rich-Te alloys, the gain of vibrational entropy is the driving force for the observed NTE [154]. We may expect this mechanism to apply to all Peierls distorted p-bonded elements and alloys, provided that the melting temperature is smaller than the distortion energy.

Chapter 7

Effects of antimony addition in Te-rich Ge_xTe_{1-x} alloys

In the previous chapter, we presented inelastic neutron scattering experiments and FPMD simulations performed to understand the driving force for the negative thermal expansion measured in the rich-Te Ge_xTe_{1-x} alloys in the liquid phase. We concluded that the large gain in vibrational entropy observed during the NTE overcomes the Peierls distortion present at low temperatures, and leads to a more symmetric, denser, structure.

We have also studied the behavior of two alloys known for their phase change properties: $Ge_1Sb_2Te_4$ and $Ge_2Sb_2Te_5$. These compounds are also based on Te (as most of the phase change alloys, see Chapter 1), and include a third chemical element, Sb. No NTE is found in these alloys in liquid phase, and we did not measure any change in the vibrational density of states neither. There is thus a complete change in the thermal evolution of liquid $GeTe$ compounds when a quantity of Sb is added. In the $Ge_1Sb_2Te_4$ case, one third of the Te was replaced by Sb, compared to $GeTe_6$. To go further in the study of the effects of the Sb element on the eutectic $GeTe_6$ behavior, we performed measurements and simulations on the following compounds :

- $GeSb_6$: it can be viewed as the extreme limit case, that is to say, $GeTe_6$ in which all the Te has been substituted by Sb.
- $Ge(Sb_{10}Te_{90})_6$: which corresponds to the substitution of a relatively small quantity of Te by Sb in $GeTe_6$.

7.1 Sound velocity measurements

The sound velocities, v_s, evolution with temperature for alloys whose stoechiometry goes from $GeTe_6$ to $GeSb_6$ have been measured by Tsuchiya [21, 20] and are presented in Fig. 7.1. Note that no $V(T)$ data are available up to now for these compounds (except for $GeTe_6$). In Fig. 7.1, we can still observe a minimum in the sound velocity when only

5 % of Te is substituted by Sb in $GeTe_6$. As soon as 10 % of Te is substituted by Sb, no minimum in the sound velocity is found anymore. Following the parallelism between v_s and the molar volume evolution with T described in Chapter 3, a NTE, if it exists, will not take place in the liquid phase in this case (or at least, not entirely). Nevertheless, for $Ge(Sb_{10}Te_{90})_6$, $Ge_1Sb_2Te_4$ and $GeSb_6$, the behavior of v_s with T does not correspond to what is observed for 'normal liquids' neither (see for exemple $v_s(T)$ for Sn or Pb in Chapter 3 Fig. 3.3).

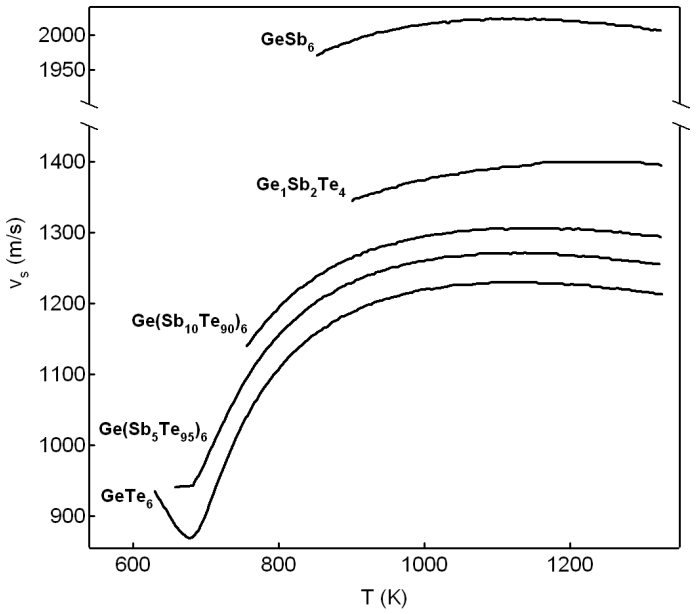

Figure 7.1: Sound velocity evolution with temperature for alloys whose stoechiometry goes from $GeTe_6$ to $GeSb_6$. Reproduced from [21, 20].

7.2 Neutron diffraction experiment

7.2.1 Experimental set-up

The neutron diffraction experiment on $GeSb_6$ was carried out on the two-axis diffractometer D4 at the ILL (Grenoble), for $Ge(Sb_{10}Te_{90})_6$ it was on the two-axis diffractometer 7C2 at the LLB (Saclay). The samples were put in quartz tube of 6 mm internal/8 mm external diameter ($GeSb_6$) and 8 mm/10 mm ($Ge(Sb_{10}Te_{90})_6$) and sealed under vacuum. We used an incident neutron wavelength $\lambda = 0.6950$ Å for $GeSb_6$, 0.7240 Å for $Ge(Sb_{10}Te_{90})_6$, together with a 2θ angular range going from 0.875° to 136.125° (3.6° to 140.0°) with a 2θ step equal to 0.125°(0.02°), on D4 (7C2) respectively. This corresponds to neutron scattering vectors in the range 0.138 to 16.772 $Å^{-1}$ (0.54 to 15.44 $Å^{-1}$).

Measurements on $GeSb_6$ were performed at 840 K, T_m = 870 K, 923 K and 1023 K, and the empty quartz cell signal was measured at 830 K, 880 K, 930 K and 1023 K.

For $Ge(Sb_{10}Te_{90})_6$ the temperatures of measurement were 1070 K, 970 K, 907 K, 847 K and 770 K and the empty quartz cell signal was measured at 1070 K, 970 K and 830 K (and obtained by interpolation for the non-measured temperatures).

7.2.2 Structure factors and pair correlation function

$\mathbf{GeSb_6}$

The experimental structure factor, $S(q)$, for the $GeSb_6$ compound at 923 K is presented in Fig. 7.2. Well resolved oscillations are observed up to $q \sim 13$ Å^{-1}. The first peak (which possesses a shoulder on the high q side) is the highest, followed by peaks of decreasing height. The $S(q)$ at all temperatures are similar, as shown in Fig. 7.3 for 840 K and 923 K. The pair correlation function, $g(r)$, obtained by Fourier transform of structure factor (see Chapter 4 Eq. 4.26), is presented in Fig. 7.4. The position r_1 of first maximum is equal to 2.96 Å and the coordination number N_c is equal to 5.9(5). This is an estimation from experiment and only the detailed study of partial $g_{\alpha\beta}(r)$ (obtained, in this thesis, by FPMD simulations, see next sections) can yield actual coordination numbers, without the bias due to the neutron scattering lengths.

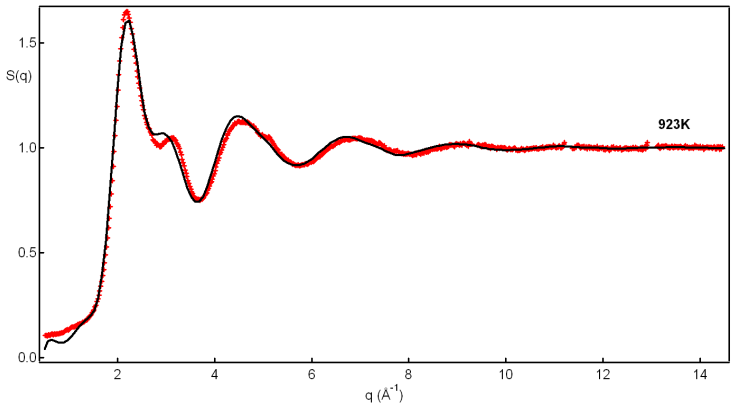

Figure 7.2: Structure factor $S(q)$ of $GeSb_6$ (T_m = 870 K) at 923 K, measured on D4 (red markers), together with FPMD result (black line).

$\mathbf{Ge(Sb_{10}Te_{90})_6}$

To the contrary of $GeSb_6$, an evolution of the $S(q)$ with temperature is observed in $Ge(Sb_{10}Te_{90})_6$ (see Fig. 7.5). It can be compared to the $GeTe_6$ case : when the temperature decreases, the first peak height remains stable while the intensity of the second peak is increasing. A slight evolution of the third peak can also be noticed. Nevertheless, these changes are less drastic than in $GeTe_6$. The quantity of Sb added here does not

completely cancel out the striking evolution with T observed in $GeTe_6$, to the contrary of the $Ge_1Sb_2Te_4$ case. Despite the fact that no minimum of the sound velocity is measured for liquid $Ge(Sb_{10}Te_{90})_6$ (see Fig. 7.1), the $S(q)$ behavior indicates that we are probably not so far from this minimum (which would then probably be situated in the undercooled liquid phase). No measurements of the density evolution with temperature being available, we cannot directly relate the $S(q)$ changes (and the sound velocity anomal behavior) to a possible NTE, but our measurements suggest that the changes observed could stand on the high temperature side of the NTE.

We can see in Fig. 7.6 the evolution of the pair correlation function obtained by Fourier Transform of the structure factors.

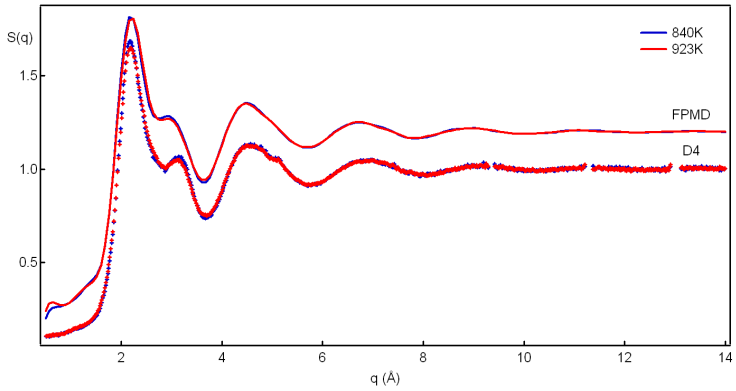

Figure 7.3: Structure factor $S(q)$ of $GeSb_6$ ($T_m = 870$) at 923 K and 840 K, measured on D4 (red and blue markers), together with FPMD simulations result (red and blue lines, shifted by 0.2 for clarity).

7.3 Inelastic neutron scattering experiment

7.3.1 Experimental setup

The inelastic neutron scattering experiment was performed on the IN6 time-of-flight spectrometer at the ILL for both compounds, using a wavelenght $\lambda = 4.14$ Å. Samples were put in cylindrical quartz cells of diameter 8 mm (internal)/10 mm (external). For $GeSb_6$, measurements were performed at 840 K (undercooled liquid), 870 K (T_m), 920 K and 970 K. For $Ge(Sb_{10}Te_{90})_6$, temperatures were 640 K (undercooled liquid), 670 K (T_m), 740 K, 770 K, 870 K and 970 K.

Concerning the $Ge(Sb_{10}Te_{90})_6$, it should be noted that during this experiment we tried to reach lower temperatures than for the diffraction experiment. We cooled the sample and reached T as low as 640 K (below this T, the sample re-crystallized). At these lowest temperatures (from 690 K to 640 K), the $S(q)$ signal obtained from the inelastic scattering

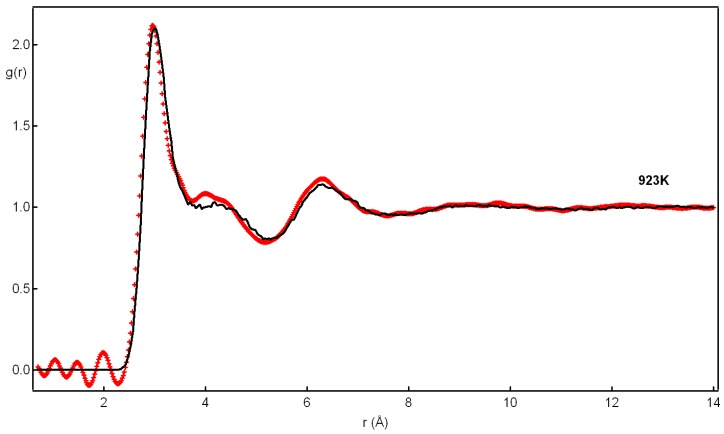

Figure 7.4: Pair correlation function $g(r)$ of $GeSb_6$ at 923 K, measured on D4 (red markers), together with FPMD simulations result (black line).

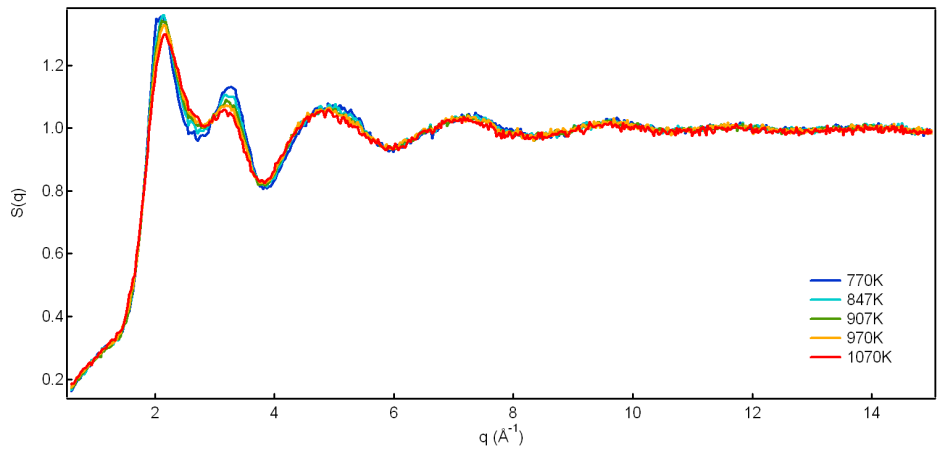

Figure 7.5: Thermal evolution of the $Ge(Sb_{10}Te_{90})_6$ structure factor, measured on 7C2.

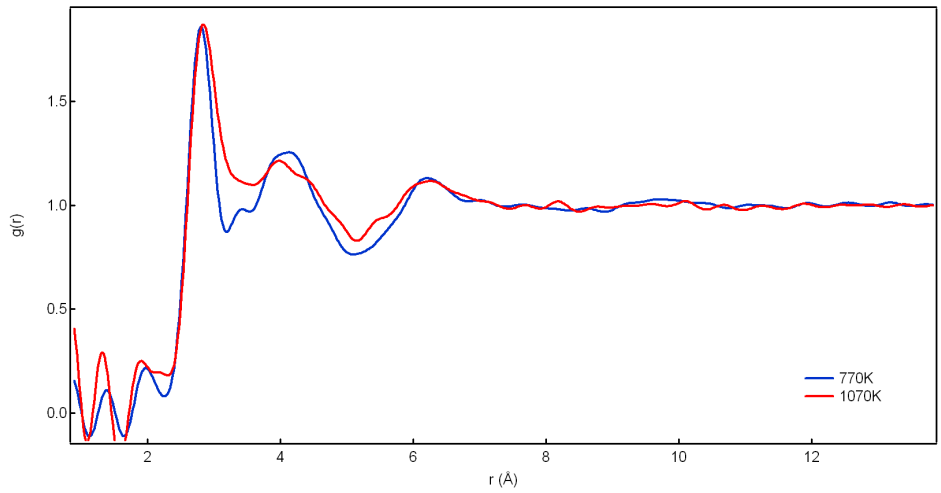

Figure 7.6: Pair correlation function $g(r)$ of $Ge(Sb_{10}Te_{90})_6$ at the lowest and highest temperatures measured on 7C2.

experiment started to decrease strongly in intensity (which can be explained by a strong variation of the density). Consequently, it is possible that the three lowest temperatures presented hereafter correspond to a pure (undercooled) molten state, or to a mixture of melt-crystallites, which would create Bragg peaks outside of the q range available with the inelastic scattering experiment (limited to low q values of 2.56 $Å^{-1}$), and thus, not oberved.

7.3.2 Vibrational densities of states

The VDOS evolution with temperature, for $GeSb_6$ and $Ge(Sb_{10}Te_{90})_6$, is plotted in Fig. 7.7. These compounds behave differently with temperature :

- For $GeSb_6$, the VDOS shape consists of two peaks, around 6 and 12 meV. As in the structure factors (see the previous sections), no T evolution is observed.

- For $Ge(Sb_{10}Te_{90})_6$, at the lowest T, the VDOS is also made of two peaks, located around 8 and 16 meV respectively. The second is smaller than the first one, to the contrary of $GeSb_6$ VDOS in which the two peaks are equally high. The VDOS shape changes with temperature : when T increases, the two peaks shift to slightly lower energies, and they almost merge. However, we do not see any evolution of the VDOS highest energy part, as evidenced in $GeTe_6$ (see Chapter 6 Fig. 6.7). The largest evolution comes from the low-energy range of the spectra (quasi-elastic part), which changes from a slightly concave to a slightly convex slope.

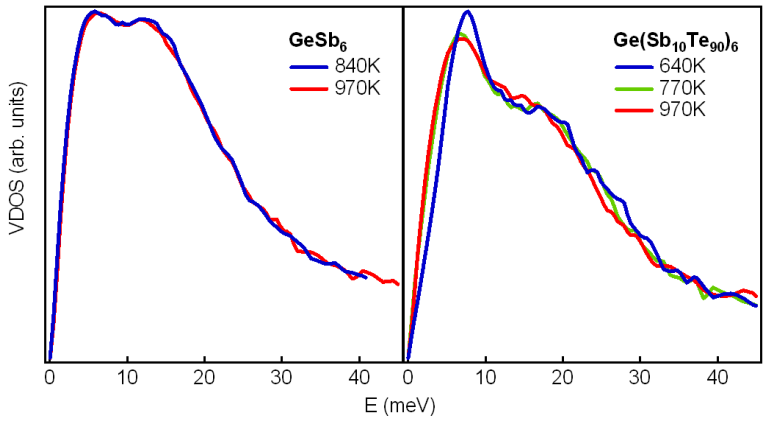

Figure 7.7: VDOS evolution with temperature for $GeSb_6$ and $Ge(Sb_{10}Te_{90})_6$.

In Fig. 7.8, we plotted jointly the VDOS for the 'limit' compounds ($GeTe_6$ and $GeSb_6$) and for $Ge(Sb_{10}Te_{90})_6$. At low T, the $Ge(Sb_{10}Te_{90})_6$ VDOS looks more like the $GeTe_6$ one (the two peaks are still distinct), but we can see that this small addition of Sb has already caused a noticeable change in the VDOS shape. At high T, the $Ge(Sb_{10}Te_{90})_6$ VDOS is almost identical to the $GeTe_6$ one. Moreover, the quasi-elastic part of the spectra is identical for the three compounds (which is not the case at low T).

The changes in the $Ge(Sb_{10}Te_{90})_6$ VDOS are significantly smaller in comparison with $GeTe_6$ and $GeTe_{12}$. This is coherent with the fact that the sound velocity evolution of this compound is not regular. But, since no minimum of the sound velocity is observed, the thermal evolution of the VDOS can be expected to be lower than for $GeTe_6$.

7.3.3 Evolution with T of the quasi-elastic part of the spectra

The low-energy part of the $Ge(Sb_{10}Te_{90})_6$ VDOS spectra is plotted in Fig. 7.9. We can see the continuous evolution with temperature of the curvature from concave to convex. This is related to the modification of the quasi-elastic scattering. This can be further studied using the $q-$integrated $S(q,\omega)$, which is plotted in Fig. 7.10. We observe a thermal broadening of the quasi-elastic peak, in agreement with the increase of the VDOS with T for these energies. The $S(\omega)$ can also be represented at given q vector values, as in Fig. 7.11. We observe, for each q, the significant thermal broadening of the quasi-elastic peak, together with the variation in q of the peak's position. This evolution should probably be related to an important evolution of the diffusion constant.

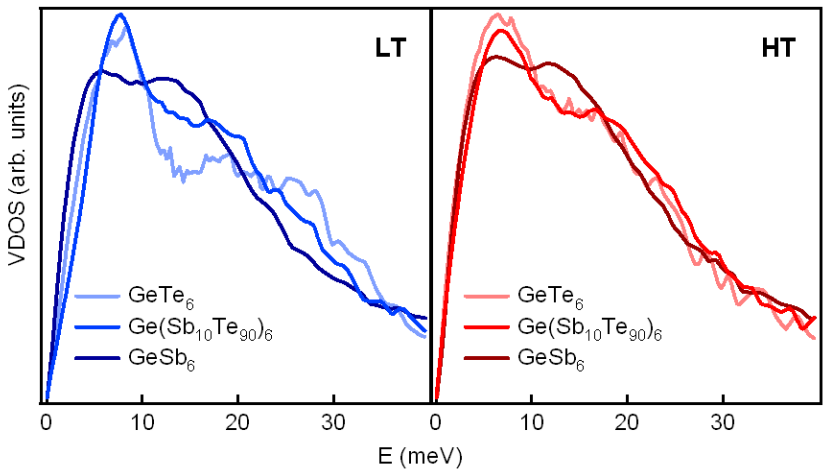

Figure 7.8: VDOS for the 'limit' compounds ($GeTe_6$ and $GeSb_6$) and for $Ge(Sb_{10}Te_{90})_6$, at lowest (left panel) and highest T (right panel).

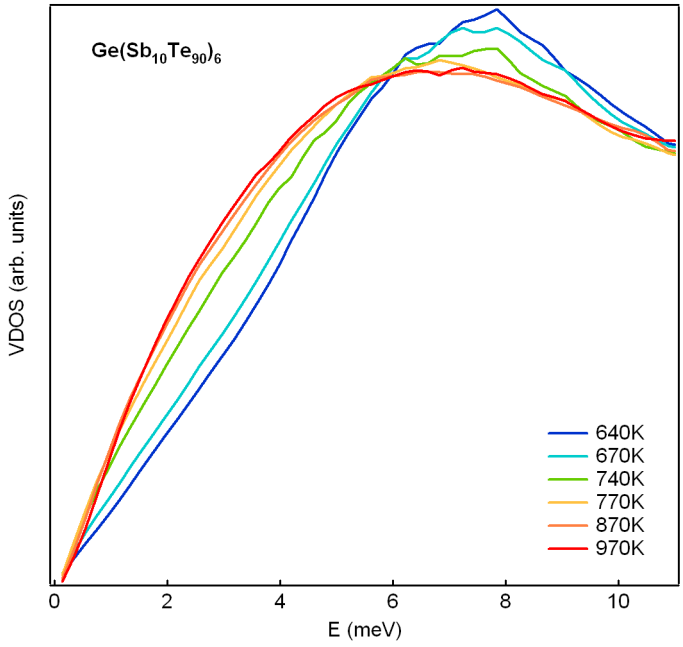

Figure 7.9: Low-energy part of the $Ge(Sb_{10}Te_{90})_6$ VDOS spectra.

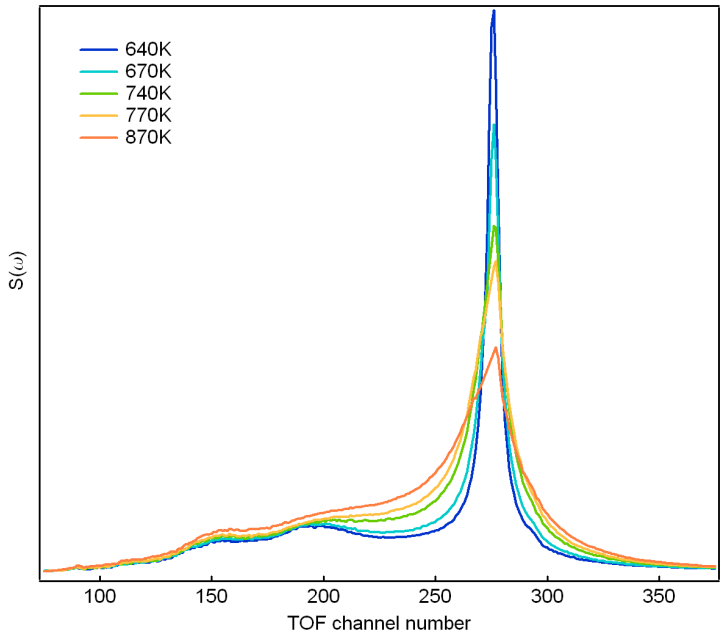

Figure 7.10: $S(\omega)$ evolution with T for $Ge(Sb_{10}Te_{90})_6$, versus TOF channel number.

7.4 $GeSb_6$ FPMD simulations

We performed FPMD simulations of $GeSb_6$ to obtain atomic trajectories for a 216 atoms system (31 Ge and 185 Sb) at the experimental liquid density [20] ($\rho = 0.0322$ Å^{-3}). We first heated the liquid at 3000 K for 10 ps and then thermalised it at 840 K (T_m) and 923 K for 15 ps each. We used Ge ($4s$ and $4p$) and Sb ($5s$ and $5p$) valence electrons and a 175 eV planewave cutoff energy. In this section, we present the structural and dynamical results calculated on the structures obtained, and compared it to the experiments detailed in the previous sections.

7.4.1 Structures

Structure factor

The calculated structure factor, $S(q)$, at 923 K, is presented in Fig. 7.2, together with the experimental results. We see that the experimental $S(q)$ is almost perfectly reproduced by FPMD simulations. The $S(q)$ from FPMD at 923 K and 840 K are similar, as the experimental $S(q)$ are (see Fig. 7.3).

Pair correlation functions and partial coordination numbers

The computed pair correlation function, $g(r)$, at 923 K, is presented in Fig. 7.4, together with the experimental results. As the structure factor, the experimental $g(r)$ is quite well

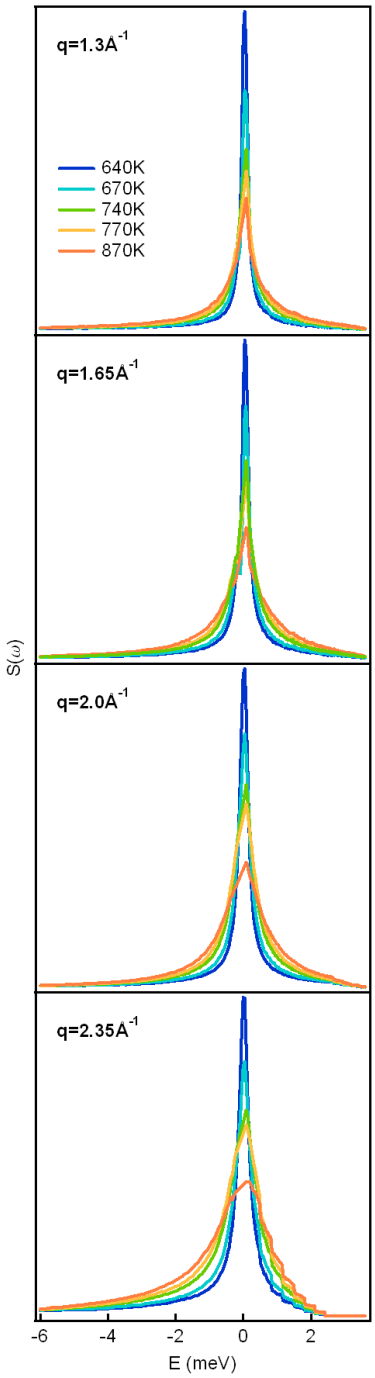

Figure 7.11: $S(\omega)$ evolution with T for $Ge(Sb_{10}Te_{90})_6$, for different values of the q vector.

reproduced by FPMD simulations.

From the FPMD partial pair correlation functions, $g_{\alpha\beta}(r)$, that are plotted in Fig. 7.12, we obtain the following partial coordination numbers : $N_{GeGe} = 0.9(7)$, $N_{GeSb} = 5.5(2)$, $N_{SbGe} = 0.9(2)$ and $N_{SbSb} = 5.0(5)$, and thus $N_{Ge} = 6.4(9)$ and $N_{Sb} = 5.9(7)$, which is close to the estimation from the experimental $g(r)$. The heteropolar bonds are favoured around *Ge*, and homopolar ones around *Sb*. This chemical order is similar to what is found in the liquid $GeTe_6$.

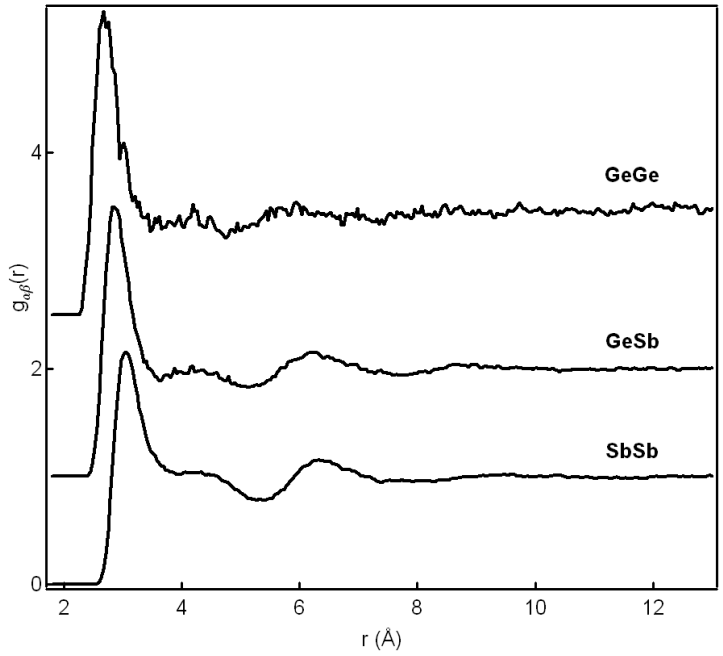

Figure 7.12: Partial pair correlation functions, $g_{\alpha\beta}(r)$, from FPMD simulations of $GeSb_6$ at 923 K.

Distance distributions

The distances distributions around *Ge* and *Sb* atoms are plotted in Fig. 7.13. The sum of the 6 first neighbors distributions makes a broad peak (which is the main contribution to $g(r)'s$ first peak). The distances distributions are found similar at 840 K. At variance with the liquid $GeTe_6$ (see Fig. 6.17 in Chapter 6), we do not see any evolution of the first neighbor shell with temperature.

Total and partial bond angles distributions

In the liquid $GeSb_6$, the total bond angles distribution are peaked on 90 and 180° around both elements (see Fig. 7.14), which indicates a predominantly octahedral local

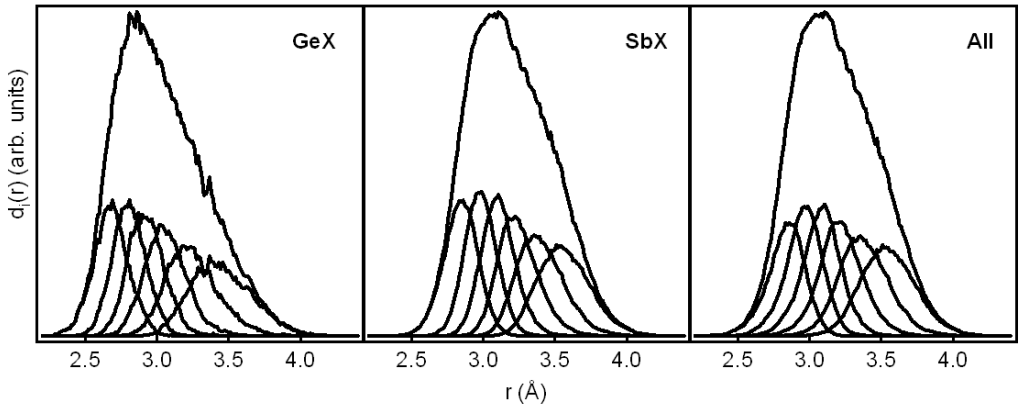

Figure 7.13: Distribution of distances around Ge or Sb atoms, and total in the liquid $GeSb_6$ at 923 K.

order around atoms in the structures, as in liquid $GeTe_6$.

The partial bond angles distributions $P(\theta_{ij})$ (see previous chapter for a definition) are well peaked for the angles between the closest neighbors, typically when i and j are ≤ 4, while for the other angles they are flatter (see Fig. 7.15). Around Sb atoms, the $P(\theta_{ij})$ for i and $j \leq 4$ are clearly peaked around 90° while around Ge they are peaked around $\sim 98°$ on average.

Three Body correlations functions

To compare the situation in liquid $GeSb_6$ with the distorsion encountered in liquid $GeTe_6$ at low temperature, we calculated the Three Body Correlations functions at 923 K, plotted in Fig. 7.16 (see definition of the TBC in the previous chapter, in Fig. 6.23). Two peaks (they could be viewed as a single broad peak) are situated along the diagonal and almost merged, meaning that no distorsion is present. This situation can be compared to the case of Ge at high temperature, or to the case of Te, in $GeTe_6$. This can also be compared to the case of an octahedral crystal at finite temperature (vibrations giving rise to similar TBC with slightly off-diagonal main peaks) plotted in Fig. 6.26 in the previous chapter.

7.4.2 Dynamics and density of vibrational states

To compare with experimental result, we calculated the total dynamical structure factor $S(q, \omega)$ on the molecular dynamic trajectories obtained for $GeSb_6$. We integrated it over the same q range as accessible on the IN6 experiment, to obtain the total vibrational densities of states (see Fig. 7.17).

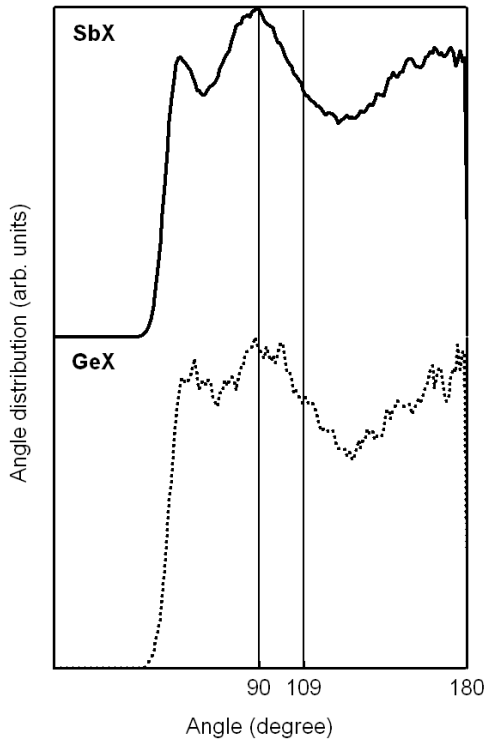

Figure 7.14: Total bond angle distributions around *Ge* and *Sb* atoms in the liquid $GeSb_6$ at 923 K.

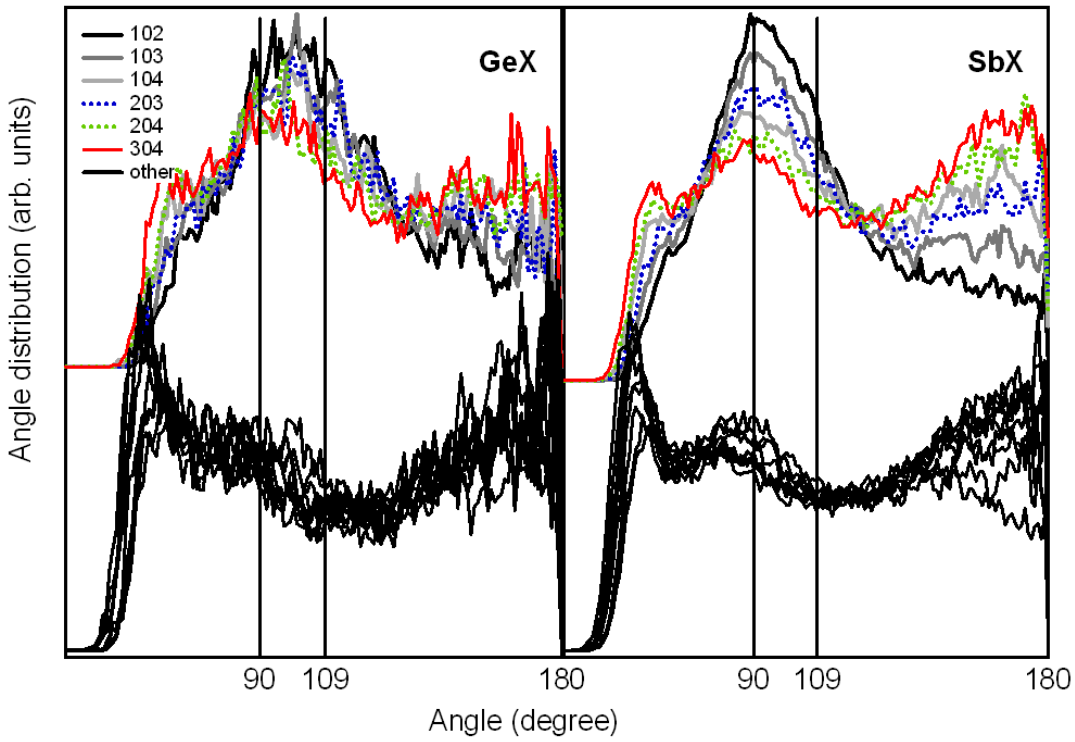

Figure 7.15: Partial bond angle distributions $P(\theta_{ij})$ around Ge and Sb atoms in the liquid $GeSb_6$ at 923 K.

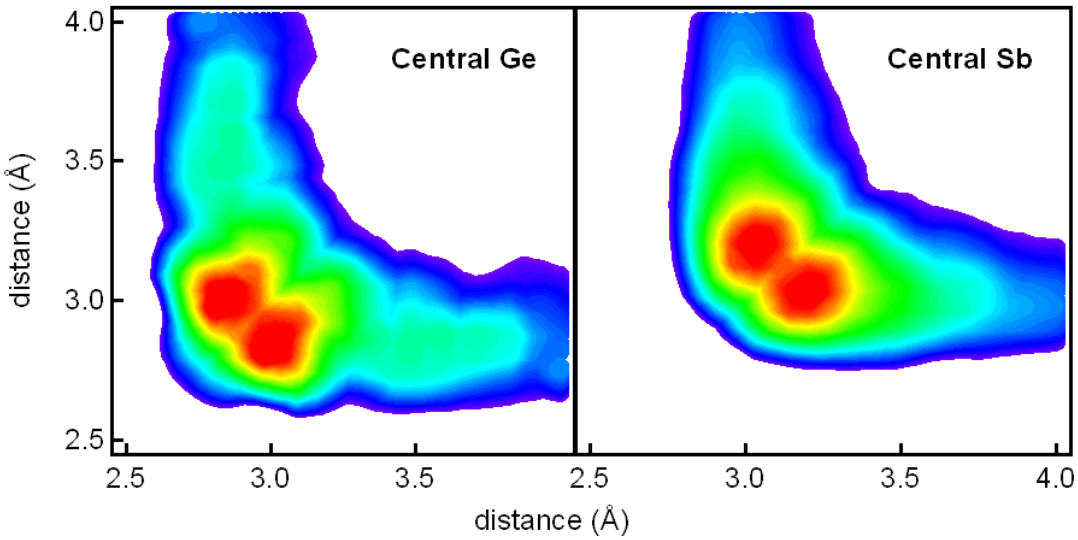

Figure 7.16: Three body correlation functions around Ge and Sb in liquid $GeSb_6$. The bond angle between the two bonds is limited to more than 165°. Contours are drawn between 35 % of the maximum value and the maximum value of the normalized correlation (from blue to red).

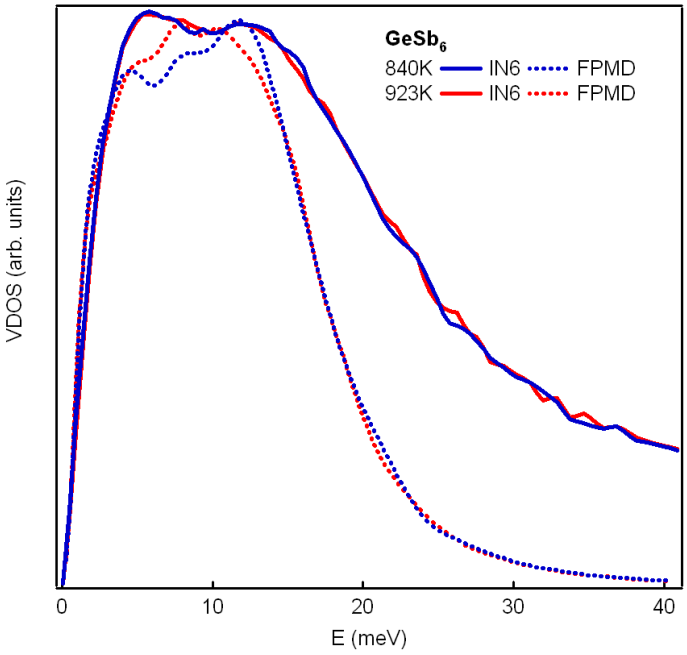

Figure 7.17:

As in the experiment, the calculated VDOS is similar at low and high temperatures, to the contrary of what is found in liquid $GeTe_6$ (see Fig. 6.7 in Chapter 6). This is coherent with the absence of structural thermal evolution. We have a good agreement with experiment up to 13 meV, but a much faster decrease of the intensity of the VDOS at highest energies.

7.5 Conclusion

Despite some similarities found between $GeTe_6$ and $GeSb_6$ (in the chemical order for exemple), we see that both compounds exhibit totally different behaviors with temperature. It was expected from the sound velocity measurements that $GeSb_6$ would behave as a 'normal' liquid with temperature, and we actually found it to have a thermal behavior identical to the other phase-change materials ($Ge_1Sb_2Te_4$ and $Ge_2Sb_2Te_5$) studied in the liquid phase in the previous chapter. The results we obtained by FPMD simulations are in excellent agreement with the diffraction and inelastic scattering experiments, and allow for a detailed description of liquid $GeSb_6$.

We have also shown that even the substitution of a small quantity (10 %) of Te by Sb in $GeTe_6$ has striking effects on the structural and dynamical characteristics of the compound :

- The structure factor still shows a small thermal evolution of the second peak, but the effects are reduced by the addition of Sb. The observation of the thermal evolution is difficult because of the melting temperature which is now higher (compared to the possible NTE range) than in the $GeTe_6$ eutectic compound.
- The VDOS shape is obviously closer to $GeTe_6$ than $GeSb_6$ but the red-shift with T of the high energy part is no longer observed in $Ge(Sb_{10}Te_{90})_6$.

Nevertheless, the effects depend on the degree of Te substitution by Sb : in $Ge_1Sb_2Te_4$ (one third of the Te replaced by Sb compared to $GeTe_6$), the evolution of the VDOS (as well as that of $S(q)$) is totally canceled out, while in $Ge(Sb_{10}Te_{90})_6$ a change of the quasi-elastic part of the spectra is still observed, as in $GeTe_6$. It would be interesting to run FPMD calculations for this compound, but this would require long calculation times and/or larger number of atoms because of the small quantity of Sb. The intermediate compound between $GeTe_6$ and $Ge(Sb_{10}Te_{90})_6$, that is to say $Ge(Sb_5Te_{95})_6$, could also be studied experimentally to have a complete map of these alloys. From its sound velocity evolution with temperature, we anticipate that its behavior would be very close to that of $GeTe_6$.

Chapter 8

Structural and vibrational study of the negative thermal expansion in liquid As_2Te_3

In this chapter, we present an experimental and theoretical study of the liquid As_2Te_3 which, as $GeTe_6$ does, exhibits a negative thermal expansion just above the melting temperature. It is interesting to test the generality of the structural and dynamical evolutions we found for $GeTe_6$ along the NTE (see chapter 6).

Tsuchiya measured the thermal evolution of the molar volume and found a contraction above T_m in As_xTe_{1-x} compounds (x varying from 10 to 70) [98]. These measurements were presented in chapter 3 Fig. 3.8. For As_2Te_3, this NTE (presented in Fig. 8.1) extends over 250 K above $T_m = 654$ K [155]. Electronic transport studies [5, 4, 8] show the presence of a semi-conductor-metal (SC-M) transition in As_2Te_3 in the NTE temperature range. The dc conductivity increases from $\sim 30\ \Omega^{-1}cm^{-1}$ to $\sim 1700\ \Omega^{-1}cm^{-1}$ between 673 K and 973 K [8]. Many experimental and theoretical studies have been devoted to the structure of liquid As_xTe_{1-x} alloys with contradictory results. Neutron diffraction studies on liquid As_2Te_3 were performed by Uemura [156] at 697 K and 925 K and, more recently, by Maruyama et al. [157] in the entire NTE temperature range. In the first study, no temperature evolution was reported between 697 K and 925 K. On the contrary, Maruyama et al. observed a strong evolution of the measured spectra between 673 K and 1073 K. Endo and Ikemoto [4, 8] performed EXAFS experiments at the As and Te K-edges as a function of temperature for different As_xTe_{1-x} compositions in the liquid state and related the SC-M transition to structural changes. In As_2Te_3, they concluded that the atomic distances are nearly independent of temperature in a 150 K range above the melting point, while coordination numbers around As and Te atoms are decreasing. They interpreted this evolution by a structural transformation from a network structure to a chain structure and associated it with the SC-M transition. They also found a non negligible proportion of homopolar bonds.

A first-principle molecular dynamic (FPMD) study of As_2Te_3 indicated structural and electronic density of states (EDOS) changes with temperature [158, 159]. Unlike the results of the EXAFS experiments, no clear tendency of transformation from a network to a chain-like structure above the melting point was reported, while an increase of the partial EDOS at the Fermi level, larger for Te than for As, was observed. It was concluded that the electronic states around Te atoms play an important role in the SC-M transition when increasing temperature.

Recently, another FPMD study of liquid As_xTe_{1-x} alloys has been published [160], in which the authors compare structural, dynamical and electronic properties for $x = 0.2, 0.3, 0.4, 0.5$ and 0.6 at fixed T (= 800 K). They found that the total coordination number of Te atoms, N_c^{Te}, slightly increases with As concentration, while N_c^{As} remains constant. Combining the structural information available from EXAFS analysis [8], the molecular dynamics simulations results of Shimojo [159], and neutron diffraction spectra between 673 K and 1073 K, Maruyama et al. [157] conclude that the SC-M transition is associated with the transformation to a denser configuration composed of shortened chain molecules.

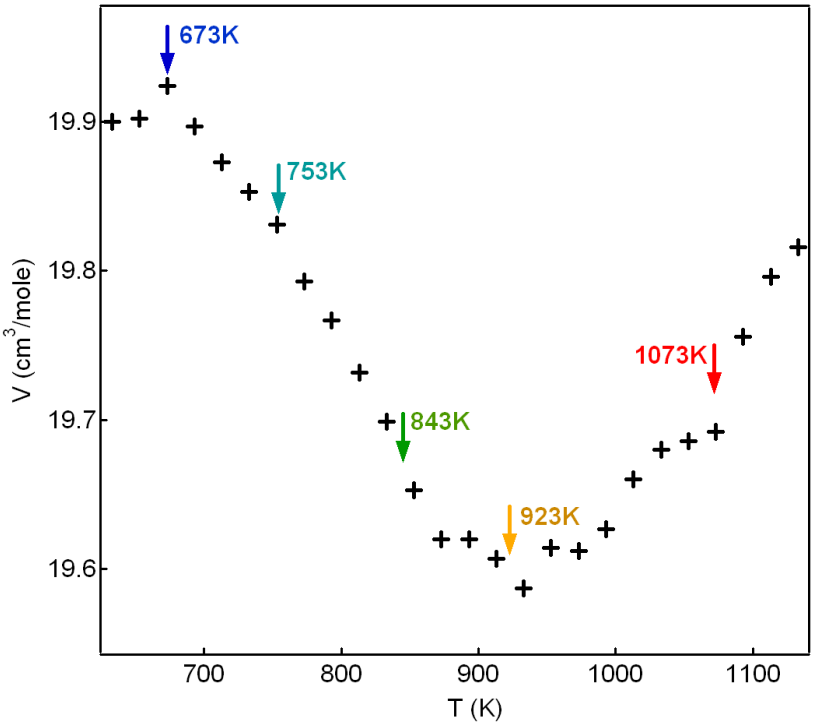

Figure 8.1: Molar volume evolution with temperature for liquid As_2Te_3 (T_m = 654 K), measured by Tsuchiya [98] (markers). Temperatures considered in this study are indicated with arrows.

The aim of the present work is to obtain more information on the structural and dynamical evolution of As_2Te_3 in the NTE temperature range by combining neutron diffraction and inelastic scattering experiments with ab initio simulations.

We evidence the changes in As_2Te_3 structure by measuring neutron diffraction spectra at five temperatures in the NTE range and perform first principles molecular dynamics (FPMD) simulations at the same temperatures and densities to study the local order evolution in the liquid. Our calculated structures show an increase of the coordination numbers and a symmetrization of the first neighbor shell around atoms when the temperature rises. To confirm these results, we perform inelastic neutron scattering (INS) to obtain the vibrational density of state (VDOS) evolution along the NTE. We see a clear change of the VDOS, consisting in a red-shift of the highest frequencies with temperature, as already evidenced in $GeTe_6$.

Finally, the electrical conductivity evolution is obtained from the simulated structures, to compare with the semi-conductor to metal transition measured in experimental studies.

8.1 Techniques

8.1.1 Diffraction experiment

The neutron diffraction experiment was carried out on the two-axis diffractometer D4 at the ILL (Grenoble).

The total scattered intensity was measured as a function of the scattering angle 2θ for an incident neutron wavelength $\lambda = 0.6970$Å. The 2θ angular range extended from 1.750° up to 138.375° with a 2θ step equal to 0.125°, which corresponds to neutron scattering vectors $q = 4\pi \sin\theta/\lambda$ in the range 0.275 to 16.853 Å^{-1}. The samples were prepared[1] from the pure elements, molten, homogenized and then sealed under vacuum in quartz tubes of 8 mm internal/10 mm external diameter.

Measurements were performed at 673 K, 753 K, 843 K, 923 K and 1073 K, *i. e.* in and above the NTE temperature range. These temperatures are indicated in Fig. 8.1 together with the temperature dependence of the molar volume measured by Tsuchiya [98]. The empty quartz cell signal was measured at 673 K, 923 K and 1073 K. The obtained differential cross section (per atom), $d\sigma/d\Omega$, at large q coincides with the expected value ($4\pi\overline{b^2} = 4.713$ barns) within a few percent, which validates the data treatment. The neutron scattering lengths are 6.58 fm As and 5.80 fm for and Te [112].

8.1.2 Inelastic scattering experiment

The inelastic neutron scattering experiment was performed on the IN6 time-of-flight spectrometer at the ILL, using a wavelength $\lambda = 4.14$ Å. Measurements were performed

[1] By R. Céolin, from the Faculté des Sciences Pharmaceutiques et Biologiques, at the Université Paris Descartes.

at 673 K, 803 K, 923 K and 1073 K.

8.1.3 First Principles Molecular Dynamics simulations

We performed FPMD simulations to obtain atomic trajectories on a 210 atom box (84 *As* and 126 *Te*) at the experimental liquid densities [98] (indicated in Table 8.1). We first heated the liquid at 3000 K for 5 ps and then cooled it down to desired temperatures in 20 ps. We then thermalized the liquid for 16 ps. We used the VASP package with the PW91 exchange correlation functional [128], ultrasoft pseudopotentials [133], As (*4s* and *4p*) and Te (*5s* and *5p*) valence electrons and a planewave cutoff energy of 250 eV. Electronic calculations were performed at the Γ point only.

8.2 Structural evolution with temperature : experimental $S(q)$ and $g(r)$

The structure factors $S(q)$ at the different measurement temperatures are presented in Fig. 8.2 (solid lines). They exhibit strong oscillations which are significantly evolving with temperature. The dominant effect is the decrease of the second and third peak heights by respectively 12 % and 7 % between the lowest temperature (673 K) and the highest one (1073 K) while the first peak height only decreases by 5 %. We also observe, at highest temperature, the annihilation of the pre-peak located at 1.16 $Å^{-1}$. Between 673 K and 1073 K the peak's position shifts slightly to higher q for the first peak (from 2.14 $Å^{-1}$ to 2.20 $Å^{-1}$) and to smaller q for the second peak (from 3.42 $Å^{-1}$ to 3.34 $Å^{-1}$). The third peak maximum position remains almost constant, but a shoulder develops on its low q side. This evolution of structure factor in the NTE temperature range is similar to the results of Maruyama et al. [157].

We performed Fourier transforms of the experimental structure factors to obtain the pair correlation functions $g(r)$, represented in Fig. 8.3 (a) (solid lines). We observe a strong decrease of the first and second peak heights with temperature, by 25 % and 15 % respectively. Positions of the first and second maximum r_1^{exp} and r_2^{exp} and first minimum r_{min}^{exp} in $g(r)$ and coordination numbers n_c^{exp} obtained from the first peak area are reported in Table 8.1. For each temperature, the coordination number was calculated by integrating $4\pi r^2 \rho g(r)$ from a fixed distance $r = 1.6$ Å to a cutoff distance taken equal to r_{min}^{exp}. The distances r_1^{exp} and r_{min}^{exp} are slightly increasing with temperature, while r_2^{exp} is slightly decreasing. The coordination number is increasing from 2.4(8) at 673 K to 2.8(6) at 1073 K.

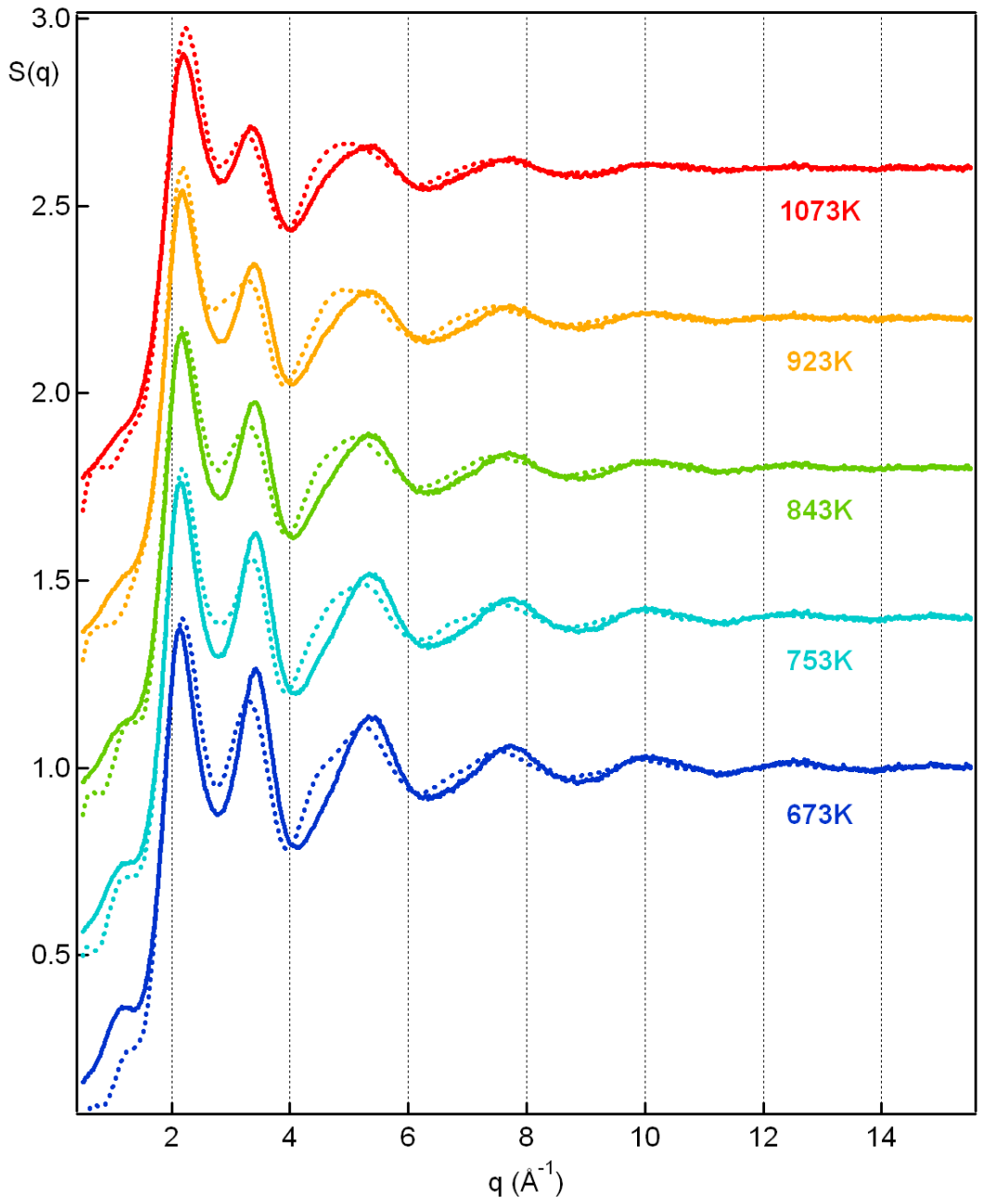

Figure 8.2: Evolution with temperature of liquid As_2Te_3 structure factor, experiment (solid lines) and FPMD results (dotted lines). The curves are vertically offset by 0.4 each for clarity.

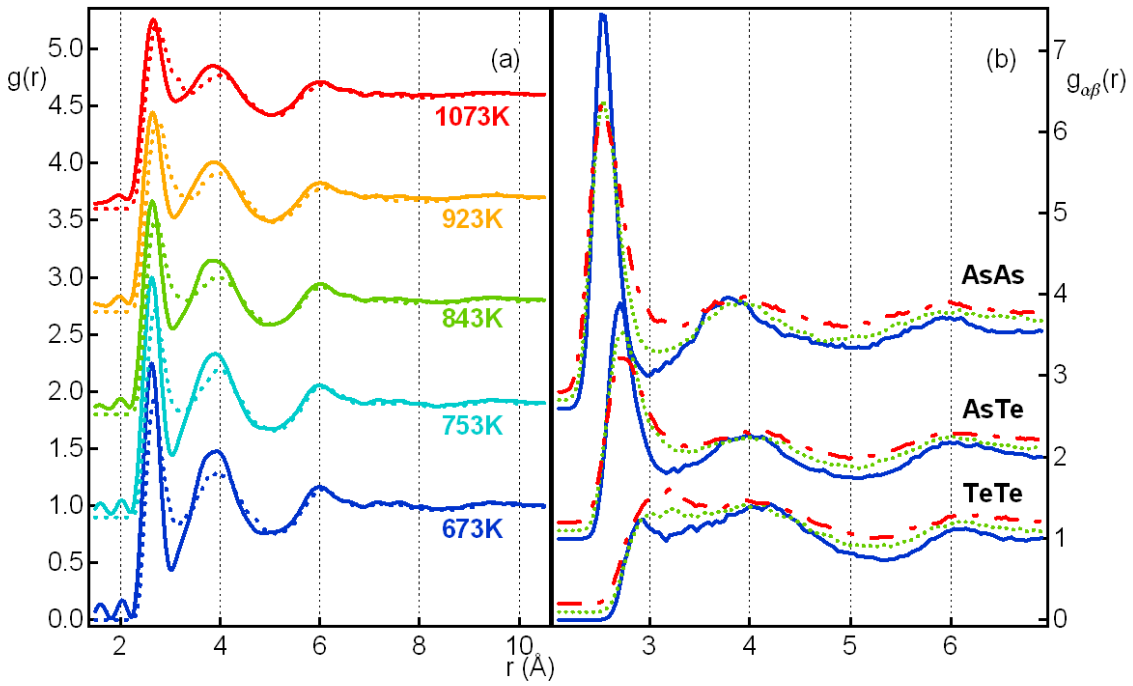

Figure 8.3: (a) Temperature evolution of the experimental pair correlation functions for As_2Te_3 (solid lines). Comparison with FPMD results (dotted lines). The curves are vertically offset by 0.9 each for clarity. (b) Partial pair correlation functions $g_{\alpha\beta}(r)$ versus temperature, from FPMD, at 673 K (solid blue lines), 843 K (dotted green lines) and 1073 K (dashed-dot red lines). The curves for each kind of atomic pair are vertically offset by 1.0 each, and by 0.1 between the different temperatures.

T (K)	ρ (Å^{-3})	r_1^{exp}	r_{min}^{exp}	r_2^{exp}	n_c^{exp}
673 K	0.0302	2.62	3.02	3.92	2.4(8)
753 K	0.0304	2.64	3.04	3.90	2.5(3)
843 K	0.0306	2.64	3.08	3.84	2.6(2)
923 K	0.0307	2.66	3.10	3.88	2.6(9)
1073 K	0.0305	2.66	3.14	3.86	2.8(6)

Table 8.1: Temperatures (in K), experimental liquid densities [98], positions of the first maximum r_1^{exp} and minimum r_{min}^{exp} in experimental g(r) and coordination numbers n_c^{exp}. The second decimal is indicated between parentheses. All distances are given in Å.

T (K)	r_1^{fpmd}	r_{min}^{fpmd}	n_c^{AsAs}	n_c^{AsTe}	n_c^{TeAs}	n_c^{TeTe}	n_{tot}^{As}	n_{tot}^{Te}
673 K	2.68	3.13	1.5(1)	1.9(0)	1.2(7)	0.8(9)	3.4(1)	2.1(6)
753 K	2.68	3.17	1.4(9)	2.1(1)	1.4(0)	0.9(4)	3.6(0)	2.3(4)
843 K	2.72	3.17	1.5(6)	2.0(9)	1.3(9)	0.9(9)	3.6(5)	2.3(8)
923 K	2.73	3.19	1.6(2)	2.1(4)	1.4(3)	1.0(6)	3.7(6)	2.4(9)
1073 K	2.74	3.24	1.9(2)	2.0(9)	1.3(9)	1.3(4)	4.0(1)	2.7(3)

Table 8.2: Temperatures (in K), positions of the first maximum r_1^{fpmd} and minimum r_{min}^{fpmd} in total g(r) from FPMD, coordination numbers n_c^{AB} (A being the central atom) from partial pair correlation functions and total coordination numbers for As and Te. The second decimal is indicated between parentheses. All distances are given in Å.

8.3 Calculated structure factors and pair correlation functions

In Fig. 8.2, we also present, together with the experimental curves for comparison, the calculated $S(q)$ obtained from FPMD simulations at the same T conditions. The overall $S(q)$ shape is in qualitative agreement with experiment, at each temperature, up to the highest q values. More importantly, the characteristic features of the $S(q)$ thermal evolution are well reproduced by the FPMD results. The decrease of the second and third peak heights with temperature is similar for the experimental and FPMD results, while the first peak height is found roughly constant in both cases. Finally, the position of the first peak of the calculated $S(q)$ agrees well with experiment, the positions of the second and third peaks being slightly shorter than the observed ones, which will lead to a distance overestimate in the calculated $g(r)$. A similar effect has been observed previously for $GeTe_6$ [9] and is due to the GGA approximation which slightly overestimates the $TeTe$ bond lengths.

In Fig 8.3 (a), we present the total pair correlation functions obtained by the sum of the partial pair correlation functions from FPMD, weighted by the neutron scattering lengths. The agreement with the experiment at the two highest temperatures is good for the whole r range, while the two first peaks are slightly too small at the other temperatures.

In Fig. 8.3 (b), the calculated partial pair correlation functions $g_{\alpha\beta}(r)$ at 673 K, 843 K and 1073 K for the $AsAs$, $AsTe$ and $TeTe$ atomic pairs are shown. The $AsAs$ and $AsTe$ curves possess a prominent first peak for all temperatures, slightly decreasing and broadening when T increases. The first peak of the $TeTe$ partial pair correlation function is very small at all temperatures and it moves to higher r and broadens upon heating.

Coordination numbers The positions of the first maximum r_1^{fpmd} and minimum r_{min}^{fpmd} in total $g(r)$ from FPMD, partial coordination numbers n_c^{AB} (A being the central atom) obtained from the partial pair correlation function and total coordination numbers for As and Te are reported in Table 8.2. Coordination numbers were calculated with a cutoff

distance equal to r_{min}^{fpmd} for each temperature. We observe that r_1^{fpmd} and r_{min}^{fpmd} are slightly larger (by ~ 0.08 Å in average) than in the experimental $g(r)$, as expected from the GGA approximation. As in the experiment, the coordination numbers from FPMD are increasing with temperature : the total coordination number for As is increasing from 3.4 to 4.0 between 673 K and 1073 K and for Te it rises from about 2.2 to 2.7. This is surprisingly close to the n_c evolution in pure molten Te along the NTE temperature range [27].

	T (K)	$AsAs$ (Å)	$AsTe$ (Å)	$TeTe$ (Å)
This study	673	2.5(1)	2.7(0)	2.9(4)
	843	2.5(1)	2.7(4)	3.0(0)
	1073	2.5(1)	2.7(4)	3.2(0)
Endo[8]	673	2.48	2.62	2.72
	773	2.47	2.63	2.72
Shimojo[159]	700	2.53	2.72	2.94
Zhu [160]	800	2.55	2.72	2.88

Table 8.3: First maxima of partial $g_{\alpha\beta}(r)$ from this study, compared to bond lengths obtained from EXAFS experiment [8] and other FPMD studies [159, 160]. The second decimal is indicated between parentheses.

8.4 Analysis of the FPMD structures

Total bond angle distributions Total angle distributions around As and Te are plotted in Fig. 8.4 (a) and (b) respectively. They remain peaked around 90° and 180° when heating, around both types of atom, with a small broadening at high temperature. This indicates that the local order in liquid As_2Te_3 is very much octahedral in the temperature range studied (as most of the sites of the crystalline phase [84]).

Distance distributions We show in Fig. 8.5 the evolution with temperature of the 6 shortest distances distributions (over all the atoms in the simulation boxes) around As and Te atoms.

At low temperature, the neighborhood of As and Te atoms consists of two distinct shells of 'shorter' and 'longer' interatomic distances. In the case of As, the first shell contains exactly three neighbors, in the Te case it contains only two.

When the temperature increases, the short and long distance distributions spread and become less distinct. Those two sub-shells of neighbors are merging in a unique, wide, peak at high temperature in the Te case, while we can still distinguish them in the As case.

Average distances evolution with temperature To see more clearly the first neighbors shell evolution, we plotted in Fig. 8.6 the average value of the 6 first distance

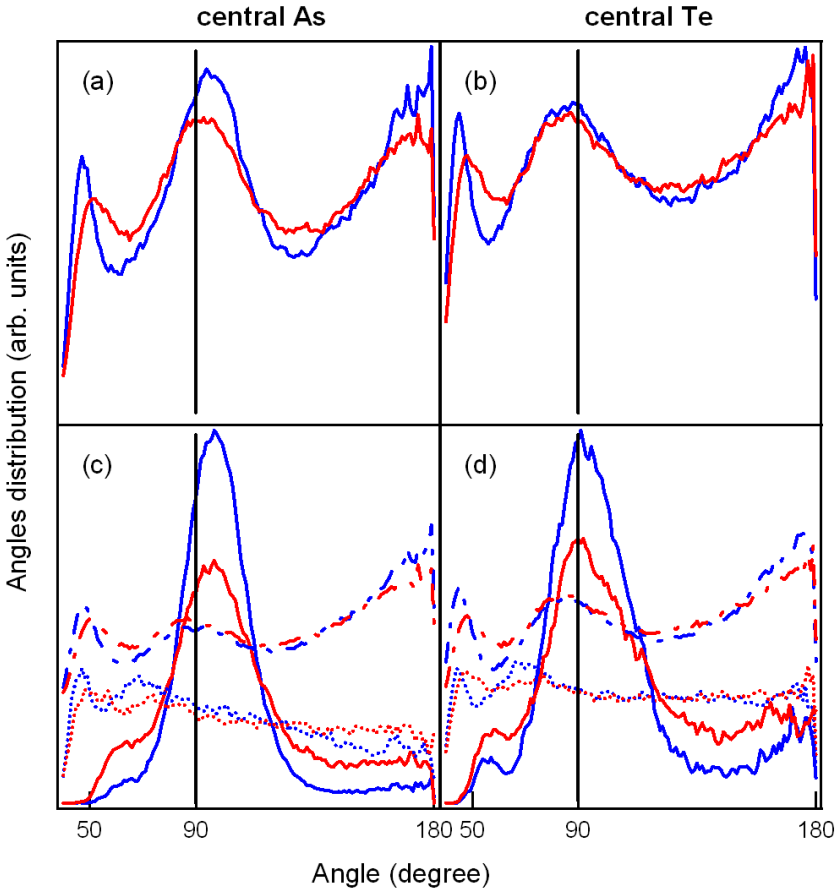

Figure 8.4: Evolution of the angle distributions with temperature. (a) and (b) Total angle distributions around As and Te atoms. (c) and (d) Partial angle distributions around As and Te. Solid lines: Distributions of angle between the 3 (2) first neighbors around As (Te) atoms. Dotted lines: Distributions of angle between the 4^{th} to 6^{th} (3^{th} to 6^{th}) neighbors around As (Te) atoms. Dashed-dotted line: remaining angles, between the shortest and longest bonds (vertically shifted for clarity). Blue lines 673 K, red lines 1073 K.

distributions around As and Te atoms versus temperature.

This figure confirms that the low temperature first neighbors shell, separated in 3+3 distances around As and in 2+4 distances around Te, is evolving when heating, in both cases, towards 6 almost regularly distributed distances. This indicates a symmetrization of the local order around both As and Te atoms. Around As, the first distance is constant when increasing temperature, the second and third distances are slightly increasing and the three largest are decreasing. Around Te, the two first distances are slightly increasing while the four largest are decreasing with T. The largest distances decrease faster than the shortest ones elongate, this fact explaining why the volume is shrinking with T.

These observations agree with the increase of partial coordination numbers with temperature, around As and Te atoms, obtained from partial pair correlation functions.

Partial bond angle distributions We also analyzed the bond angle distributions and calculated all the partial angle distributions a_{ij} between bonds i and j ($i, j = 1, 6$, $i \neq j$) around As and Te atoms. In the case of As, we observed a 3+3 distance distribution at low T, so we chose to compare the sum of angle distributions a_{12}, a_{13} and a_{23} (between the shortest bonds) to the sum of angle distributions a_{45}, a_{46} and a_{56} (between the longest bonds). For Te, the distance distributions were of type 2+4 at low T, we thus compare the angle distribution a_{12} to the sum of angle distributions a_{ij} with $i, j = 3, 4, 5, 6$. Results are respectively presented in Fig. 8.4 (c) and (d).

One observes that the angles between the shortest bonds are peaked between 90 and 100° for As and around 90° for Te at each T. The angle distributions are remarkably peaked for a liquid. We also observe a broadening of the main peak when T increases. We do not observe any peak around 180°, which suggests that the 3 (As case) or two (Te case) first distances are not aligned. The angles distributions between the longest bonds are very flat, indicating their softness, compared to the angles between the shortest bonds. The remaining angles (between a short and a long bond), plotted with dashed-dotted lines in Fig. 8.4 (c) and (d), are peaked around 90° and 180°, indicating that the shortest and longest bonds preferentially face each other.

Chemical order In reference [158], the sharp SC-M transition observed with temperature in liquid As_2Te_3 was attributed to a significant loss of chemical order. To quantify the chemical order around atoms in liquid As_2Te_3, the Warren-Cowley [161, 162] short range order parameter, $\alpha^{(i)}$, is very useful and easy to obtain from the FPMD structures. It is defined by

$$\alpha^{(i)} = 1 - \frac{P_{ij}}{c_j} \quad (j \neq i = 1, 2) \tag{8.1}$$

where c_j is the concentration of $j-$type atoms and P_{ij} is the probability for one i type atom to have a j type atom neighbor within a sphere of radius R. For a random distribution of particles $\alpha^{(i)} = 0$, while a positive (negative) value indicates a tendency to homocoordination (heterocoordination).

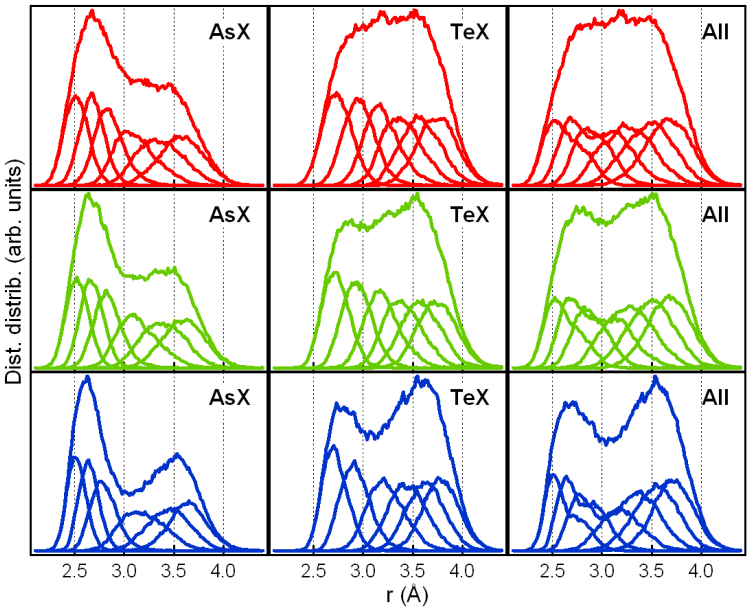

Figure 8.5: Evolution with temperature of distances distributions around *As* and *Te* atoms, and average on both (top 1073 K, middle 843 K, bottom 673 K). The 6 first distances distributions are represented separately and summed.

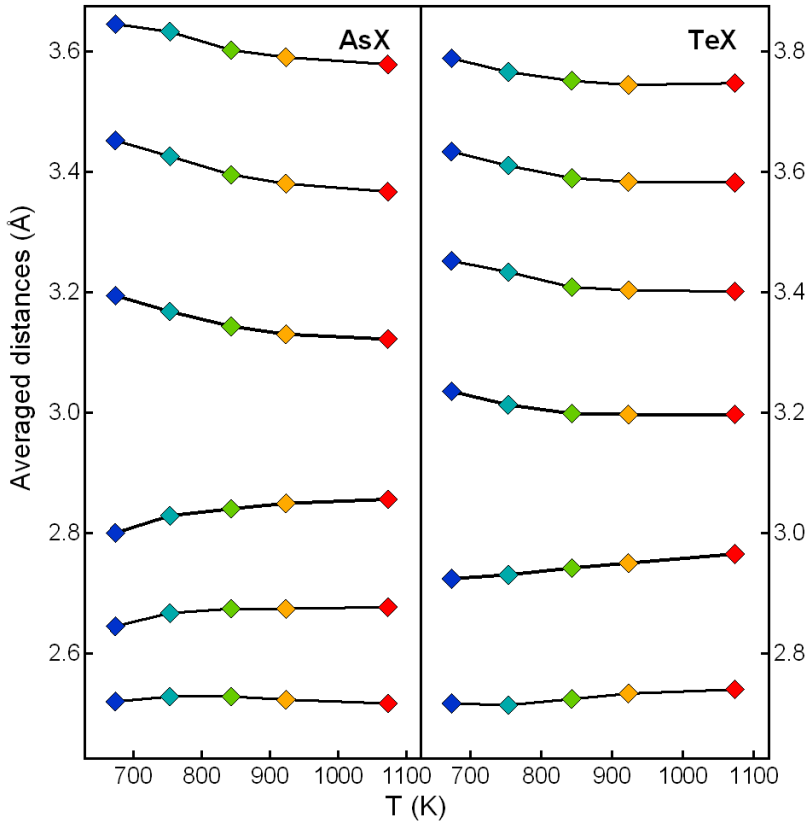

Figure 8.6: Evolution with temperature of the 6 average distances (from distance distributions, see Fig. 8.5) around As (left panel) and Te (right panel) atoms.

We averaged $\alpha^{(i)}$ on all the As or Te atoms in the FPMD structures at the different temperatures. We chose the radius R in two different ways : limiting the total number of neighbors to 6 (first neighbors shell) and to 3 (2) in the case of As (Te). Results are plotted in Fig. 8.7.

For As, the short range order parameter suggests a mostly disordered neighborhood, $\alpha^{(i)}$ being close to 0 for the different T.

For Te, there is a tendency to maximize the number of As among the 2 first neighbors. Our results for the Warren-Cowley parameter are in line with the EXAFS study made by Enddo et al [8], where they demonstrated the presence of chemical disorder in liquid As_2Te_3. It is however interesting to note that, if little variation is observed between 673 K and 923 K (the NTE temperature range), at highest temperatures there is a clear tendency to form more $AsAs$ and $TeTe$ bonds inside the structure.

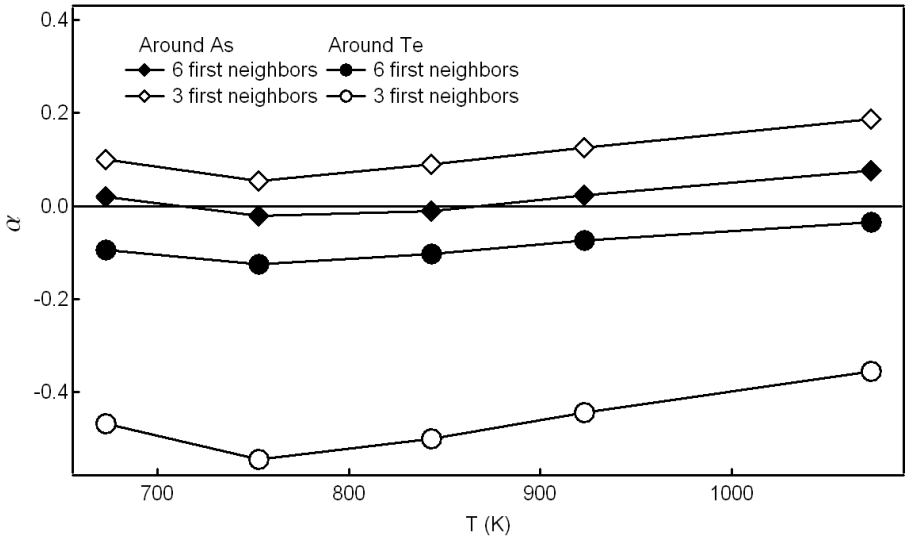

Figure 8.7: Evolution with temperature of the Warren-Cowley parameter $\alpha^{(i)}$ (see Eq. 8.1) for As (diamonds) and Te (circles) atoms.

8.5 Dynamical evolution with temperature

At low energies (up to 10 meV) the VDOS (see Fig. 8.8 a) follows an almost linear slope, that doesn't evolve with T. For the higher frequencies, we see a change of the VDOS shape with temperature. At low temperature, the VDOS clearly has two broad peaks, at low and high energies. When temperature increases, the high energy peak moves towards lower frequencies, ultimately merging with the low energy peak, and leaving only one wide peak. The largest change occurs between 673 K and 923 K, thus in the NTE

region. This temperature evolution in the measured VDOS shape is very well reproduced by the VDOS obtained from FPMD simulations, also shown in Fig. 8.8 (b), although the FPMD frequencies appear to be systematically underestimated by $\sim$ 15 %. We can also obtain partial VDOS from the FPMD trajectories, calculated on As or Te atoms separately, see Fig. 8.9. The high energy part of the total spectra is mainly due to the As atoms. In the discussion, we will relate the evolution in VDOS to the local order changes observed in the simulated structure.

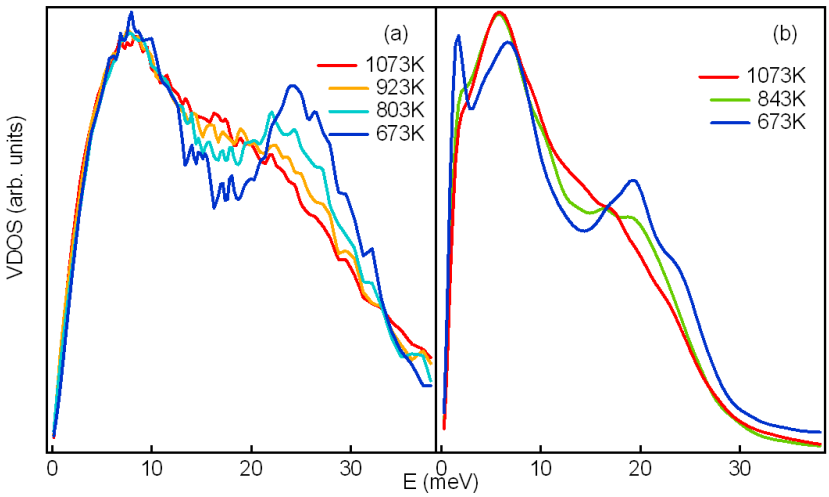

Figure 8.8: Evolution with temperature of the density of vibrational states from INS experiment (a) and from FPMD trajectories (b).

8.6 The semi-conductor to metal transition with temperature

In the literature, liquid As_2Te_3 was mostly investigated because of its pronounced semi-conductor to metal (SC-M) transition over a small T range [5, 4, 8].

8.6.1 Partial EDOS evolution from FPMD simulations

We calculated the partial EDOS, for s-states and p-states of As and Te atoms, from the simulated structures at 673, 753, 843, 923 and 1073 K. Results are shown on Fig. 8.10 for selected temperatures. For both elements, the partial densities of p-states (solid lines) exhibit a marked evolution with temperature. They present a deep minimum at the Fermi level E_F at the lowest temperature 673 K. When T increases from 673 K to 1073 K, the p-state EDOS at E_F increases by $\sim$ 50 % for both kinds of atoms. We thus observe that

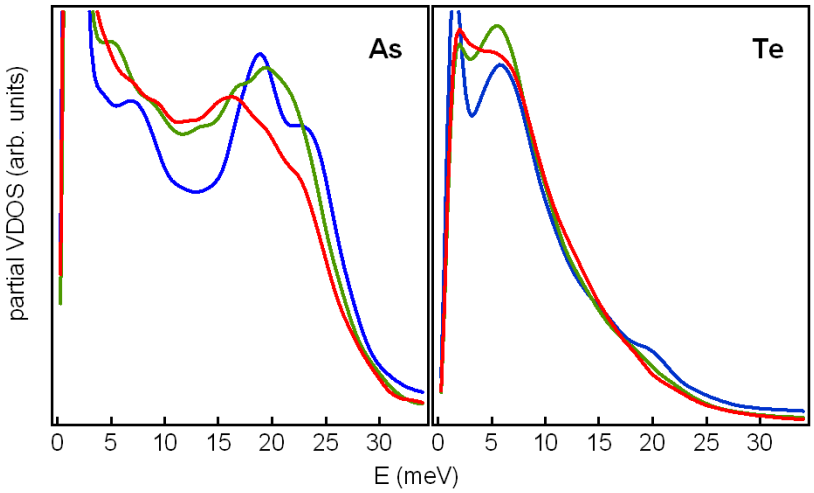

Figure 8.9: Evolution with temperature of the partial densities of vibrational states of As (left panel) and Te (right panel) on our calculated structures (blue lines 673 K, green lines 843 K, red lines 1073 K).

$p-$states from both As and Te atoms contribute almost equally to the metallization of the system.

8.6.2 Conductivity evolution with temperature

Finally, we calculated the optical conductivities from our simulated structures using the Kubo-Greenwood formula [163, 164]. Results are plotted in Fig. 8.11. By linear extrapolation (applied between 0.5 eV and 1.0 eV, see Fig. 8.11) to zero energy we obtain the electrical conductivity evolution with temperature, given in the Table 8.4 together with experimental values [5, 8]. These evidence a semi-conductor to metal transition with temperature in the NTE range. The measured electrical conductivity at high T is well reproduced by our FPMD simulations, while at low T the calculated values are significantly higher that the experimental ones. This can be explained by the too high value of the electronic density of states at the Fermi level found in simulated structure at low temperatures, which is caused by the well-known underestimate of the electronic gap of semi-conductors within the DFT-GGA approximation. We nevertheless observe a steep increase of the calculated dc conductivity, which almost triples between 673 K and 1073 K, giving the same trend as in the experimental observations.

8.7 Discussion

From our experimental $g(r)$ and our calculated $g_{\alpha\beta}(r)$, we evidence an increase of the coordination numbers with temperature. These results are at variance with the evolution

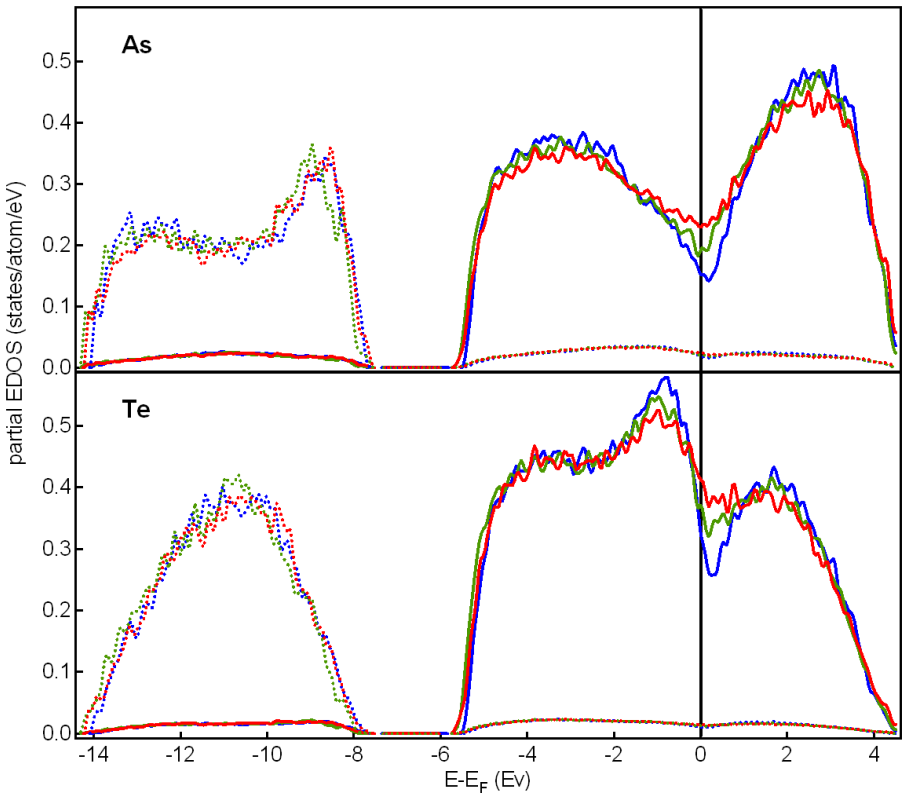

Figure 8.10: Evolution with temperature of the calculated partial densities of electronic states (in states/atom/eV) of As (top) and Te (bottom). Blue lines 673 K, green lines 843 K, red lines 1073 K. Origin of the energies is taken at the Fermi level E_F. Solid lines: p-states. Dotted lines: s-states.

T	σ [5]	T	σ [8]	T	σ (this study)
673	28	676	30	673	684
750	12	756	192	753	981
838	531	832	658	843	1290
933	1391	901	1137	923	1376
973	1717			1073	1666

Table 8.4: Evolution of electrical conductivity σ (in $\Omega^{-1}cm^{-1}$) with T (in K). Experimental results are from Oberafo [5] and Endo [8].

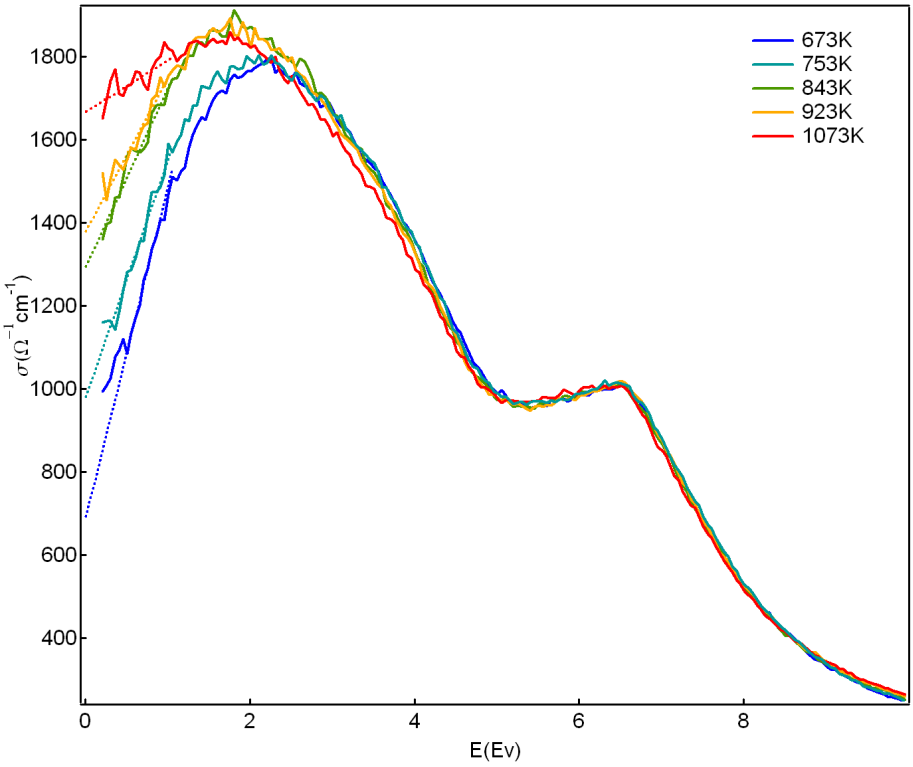

Figure 8.11: Evolution with temperature of the optical conductivities on our calculated structures (solid lines) and linear extrapolation to zero energy to obtain dc conductivities (dotted lines).

found with EXAFS experiment by Endo et al [8], despite the good agreement between first maxima of partial $g_{\alpha\beta}(r)$ from our FPMD calculations and bond lengths estimated from EXAFS analysis, reported in Table 8.3. In this table, interatomic distances from other FPMD studies [159, 160] are also indicated. These are in excellent agreement with the present results. In reference [8], authors evidenced a decrease of n_c with T, both around As and Te atoms. For As, they found that N_c, equal to 2.6 at the melting point, drops to 2 around 773 K. Around Te, they found that N_c is decreasing from around 1.5 to 1.2 in the same T range. They interpreted this decrease of partial coordination numbers by a transformation of the 3 dimensional network structure into a chain structure composed of twofold coordinated As atoms and onefold coordinated Te atoms (*network-chain transformation*). The difference between their results and N_c evolution with T from this study may probably be attributed to the larger effective error bars on the EXAFS coordination numbers. It is actually very difficult to extract accurate coordination numbers from EXAFS experiments performed on strongly disordered, high temperature, systems, as this implies including, among others, anharmonic terms and asymmetric distances distributions[2]. This is supported by the fact that the interatomic distances reported in [8] agree with the ones obtained in our experiment ($r_1 \sim 2.64$ Å).

Besides the thermal evolution consisting of an increase of the number of neighbors around each type of atom in the structure (see Table 8.2), we evidence a symmetrization of the local environment along the NTE (see Fig. 8.5 and Fig. 8.12). This effect implies (see Fig. 8.6) the shortening of longest bonds together with the increase of shortest bonds around atoms. The volume shrinks with T because the largest distances decrease more than the shortest ones elongate. This is similar to what was observed around the Ge atoms in $GeTe_6$ [165]. The increase of the shortest distances with T is correlated with the softening of vibrational modes, which explains the redshift observed in the VDOS with T (see Fig. 8.8).

Three Body Correlation functions The TBC (see Chapter 6 Fig. 6.23) are presented in Fig. 8.12, for central As or Te. At low temperature, for both elements, we observe two distinct maxima in the TBC graphs, corresponding to two inequivalent distances. This expresses the presence of a distorsion in the local order around atoms in the structure and confirms that longer and shorter bonds are not distributed randomly between neighbors but preferentially face each other, as revealed by the partial angle distributions. Upon heating, the two peaks in As and Te TBC graphs are decreasing in intensity and tend to merge within a single peak, and thus, equivalent distances. We observe that the distorsion, pronounced at low temperature, almost disappears when heating, either in the case of central As or Te. This agrees with the observations made for the distances distribution evolution with T, showing the symmetrization of the first neighbors shell.

[2]Therefore the comparison with diffraction experiments is generally useful.

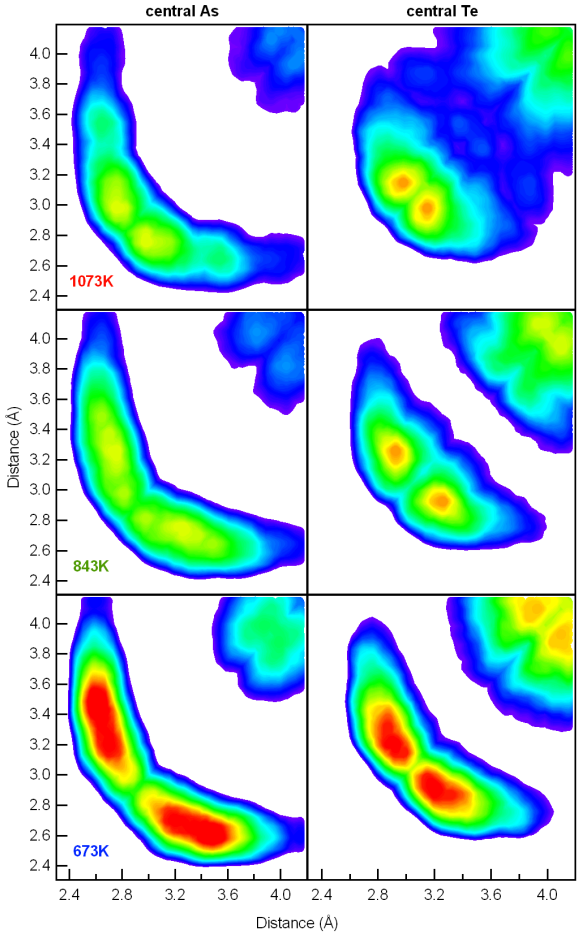

Figure 8.12: Evolution with temperature of three body correlation functions around central *As* (left panel) or *Te* (right panel) atom. The three atoms considered are aligned with angle larger than 165°. Colors go from blue (40 % of the maximum) to red (maximum).

8.8 Conclusion

In summary, we have performed a joined experimental and theoretical study of liquid As_2Te_3. The structure of the liquid evolves from a Peierls-distorted local order to a less distorted, but still octahedral, order, during the Negative Thermal Expansion. Inelastic neutron scattering measurements indicate that the structural changes are due to a drastic change in vibrational density of states and that the NTE is of entropic origin. This driving mechanism is similar to what was concluded previously from the study of the liquid $GeTe_6$ evolution with temperature.

In parallel, the alteration of the local Peierls distorsion is responsible for the large increase in conductivity along the SC-M transition without indication of changes in chemical order or Te chain formation.

Chapter 9

Structure and dynamics of liquid and amorphous Sb_2Te and Sb_2Te_3

The Sb_2Te and Sb_2Te_3 compounds are considered as the root components of most Phase Change Materials (PCMs), which are used for commercial applications of information storage. Despite the great interest for PCMs, studies on the behavior of their building blocks with temperature (a key parameter for the understanding of phase change properties) are not numerous.

In this chapter, we present a combined experimental and theoretical study on the structural evolution with temperature of the Sb_2Te and Sb_2Te_3 binary alloys, from the liquid to the amorphous phase.

We performed diffraction experiments on both compounds in liquid phase and on Sb_2Te in amorphous phase, on the D4 diffractometer at the ILL.

We also performed FPMD simulations to obtain detailed Sb_2Te and Sb_2Te_3 structures above and below (quench) the melting temperature. Compared to the work described in the previous chapters, in which only the liquid phase was considered, here we had to quench the liquid FPMD structures. Even if the mechanism of the switching in PCM is still under debate (see Chapter 1), experimentally, the usual way to get a compound in the amorphous phase is to melt it and then to rapidly decrease the temperature below the melting point. If the quench is fast enough, the atoms do not have time to go back to their crystalline positions and only a local order is recovered (as in the liquid state). Depending of the cooling method, the quench lasts some microseconds down to few nanoseconds inside the phase-change devices. However, the longest simulation times we can hope for now are well shorter, and reach at most a few tens of picoseconds. This limitation could appear as an insuperable difficulty for the obtention of an amorphous phase by FPMD. We would at least have to assume that the amorphous structure remains very close in chemical order to the liquid phase. Actually, the limited numbers of atoms that can be studied with ab initio techniques imply a system of nanometer size, and the size/time ratio (∼nm / ns)

is thus close to the one found experimentally, with macroscopic systems ($\sim$ μm / μs). The obtention of the amorphous state through ab initio MD simulations is thus sound and we will see in this chapter that the experimental structural evolution from liquid to amorphous is reproduced.

We will describe the local order around atoms in the liquid and amorphous phases, and compare the latter to the crystal. We will also present structural and dynamical properties related to the medium-range order ($\sim$ 10 Å) present in the quenched FPMD structures. Our results could help to understand the ability for these two coumpounds to change from amorphous phase to crystal phase so easily, because of the strong ordering observed in the quenched phase. We also describe electronic properties computed on the FPMD structures.

9.1 Sb_2Te and Sb_2Te_3 as building components of Phase-Change materials

In literature, the binary compounds Sb_2Te and Sb_2Te_3 are systematically cited as the basic components of a large number of ternary or quaternary mixtures, which are known for their phase change properties [166]. They are the roots of the ternary phase diagram introduced by Wuttig and Yamada [56] (see Chapter 1 Fig. 1.3) to depict the different types of phase change alloys. In this diagram, the 3 axes represent Ge, Sb or Te concentrations and several groups of compounds are identified :

- The first group of PCMs is based on Sb_2Te_3, and includes all the pseudo-binary alloys built like $(GeTe)_x(Sb_2Te_3)$, such as $Ge_2Sb_2Te_5$ and $Ge_1Sb_2Te_4$.
- The second group contains the PCMs which are doped eutectic $Sb_{70}Te_{30}$, such as the compound $Ag_{5.5}In_{6.5}Sb_{59}Te_{29}$.
- The third group includes the Sb-based PCM, as $GeSb_6$. This compound will be treated in the Chapter 11.

The phase change alloys based on Sb_2Te or Sb_2Te_3 have been studied extensively for decades, either experimentally [44, 45, 46] or with ab initio calculations [39, 47, 48]. These materials are already used for commercial applications, such as DVD-RW or Blue-Ray disks (see Chapter 1).

9.1.1 PCM structures in the different phases

As detailed in Chapter 1, the atomic structures of phase change materials that are suitable for applications begin to be known, in the different phases, but the explanation of their unusual properties is still unclear.

In the liquid state, neutron diffraction study on a wide variety of PCM indicates that they all possess a octahedral local order [69]. In the crystal, they adopt cubic-like structures, often accompanied with vacancies and/or distorsions [63, 67, 56, 37].

The situation in the amorphous phase is less clear, as no explanation is unanimously accepted. All the proposed models stand for a transition from a sixfold (crystal) to a fourfold (amorphous) coordination for the Ge atoms in the structure. While a previous model was supposed a switching from an octahedral to a tetrahedral local order around the Ge atoms [36], Huang and Robertson recently suggested that the Ge environment could remain octahedral in the amorphous [77] (see Chapter 1).

9.1.2 Sb_2Te and Sb_2Te_3 as PCM components

The structural evolutions appearing with phase transitions in PCM are difficult to relate to optical or electrical contrast. That is why the study of structural, dynamical and electrical properties of the key components Sb_2Te and Sb_2Te_3 in different phases is probably the best starting point to gain understanding of more complex systems. In spite of this, specific studies on Sb_2Te and Sb_2Te_3 are not numerous, except miscellaneous experimental studies reported on crystalline Sb_2Te_3 because of its thermo-electrical properties [167].

These compounds crystallize in layered structures, with trigonal or rhombohedral symmetry. Their space group and cell parameters are given in Chapter 1. These crystalline structures are stabilized by Peierls distortions (see Chapter 2) and can be viewed as a stacking of distorted cubes, with angles close to 90° between the 3 closest neighbors and smaller between the 3 others (see Fig. 9.1).

Concerning the liquid and amorphous phases of Sb_2Te, neither experimental nor theoretical studies were published up to now, to our knowledge. Nevertheless, the liquid structure of a rich-Sb $SbTe$ alloy, doped with Ag and In ($Ag_{3.5}In_{3.8}Sb_{75.0}Te_{17.7}$) was studied recently by FPMD simulations [47]. A medium range order ($\sim$ 8 Å) was found, with very few $TeTe$ bonds, and preference for Ag and In atoms to be near Te atoms rather than Sb. Concerning the Sb_2Te_3 alloy, Park et al. measured optical properties (dielectric functions, optical gap) on crystalline and amorphous thin films [168] (they measured an optical band gap of 0.52 eV in the amorphous). Another First Principles study has been published recently [70], in which the liquid Sb_2Te_3 was obtained at 1003 K and then quenched to 300 K to model the amorphous phase. In this paper, authors report that local environments around Sb and Te atoms are similar to those reported in $Ge_2Sb_2Te_5$ and $GeTe$ phase change materials, i. e. octahedral around Sb and Te atoms, with respectively about 4 and 3 neighbors. They found a non-negligible part of homopolar bonds in their structures.

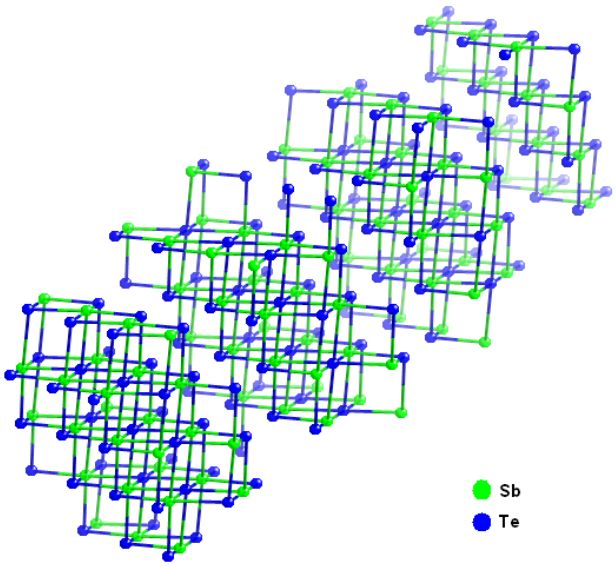

Figure 9.1: The crystalline structures of Sb_2Te and Sb_2Te_3 can be viewed as a stacking of distorted cubes (here, Sb_2Te_3).

9.2 Diffraction experiments

Measurements on liquids were performed at 930 K for Sb_2Te (T_m = 811 K [169]) and 950 K for Sb_2Te_3 (T_m = 889 K [169]), during 5 hours each, using a wavelength $\lambda = 0.6950$ Å. The empty quartz cell (6 mm internal/ 8 mm external diameter, cut from the same tube as for the samples) signal was measured at 930 K during the same counting time.

The diffraction experiments on amorphous Sb_2Te were performed within the framework of a collaboration with the group of Prof. M. Wuttig from the RWTH Aachen. The amorphous Sb_2Te_3 could not be measured, because of its propensity to recrystallize.

The amorphous samples were obtained by sputtering from compound targets (one target with the desired composition) onto glass substrates and afterwards scratched from the glass into a quartz container. The thickness of the films was in the μm range (2-3 μm). The container had a $\sim$ 2 mm diameter and a wall thickness of 10 μm. The amorphous material being difficult to obtain in quantity (here, a mass of $\sim$ 150 mg was used for the diffraction experiment), such particular quartz cells were necessary to maximize the sample / quartz ratio inside the beam. Because this ratio was about 15, only short counting times for the empty container were required, compared to the experiments on liquids for which the quantity of quartz is close to the quantity of sample, needing equivalent (or even longer)

counting times.

We used an incident neutron wavelength $\lambda = 0.4959$ Å, which, together with a 2θ angular range extended from 1.47° to 138.15°, permits to reach neutron scattering vectors $q = 4\pi \sin\theta/\lambda$ up to 23.7 Å^{-1}. Measurements were performed at room temperature, with counting times of 12 hours. The empty quartz cell (cut from the same tube as for the samples) signal was measured for 2 hours. These counting times give a ratio of the container+sample / empty container signals equal to ~ 8.

9.3 FPMD simulations

We simulated 210 atoms systems (140 Sb + 70 Te for Sb_2Te and 84 Sb + 126 Te for Sb_2Te_3) at the experimental liquid densities [170] ($\rho = 0.0303$ Å^{-3} for Sb_2Te and $\rho = 0.0283$ Å^{-3} for Sb_2Te_3). We first heated the liquid at 3000 K for 10 ps and then cooled it to the desired temperatures (930 K and 950 K) in 10 ps. After that, we thermalized the liquids for 15 ps each.

We then quenched the systems onto amorphous state at the experimental densities ($\rho = 0.0289$ Å^{-3} for Sb_2Te in amorphous state [171], as no data is available for the amorphous density of Sb_2Te_3, we kept the same density as for the liquid). We gradually decreased the temperature down to 200 K in 30 ps.

Finally, we took configurations of the quench as starting point for thermalization of 40 ps at 600 K, 400 K and 200 K. We performed such long runs in the quenched phase in order to obtain information on the dynamics of the systems (i. e. the dynamic structure factors, see section 9.6).

We included Sb and Te ($5s$ and $5p$) valence electrons in the calculations and used a 175 eV plane waves cutoff energy. Calculations were performed at the Γ point only.

9.4 Comparison between experimental and FPMD results

9.4.1 Structure factors $S(q)$

Liquid phase In the liquid (see Fig. 9.2), the structure factors (red markers) look similar for both compounds, and oscillate up to q values of 12 Å^{-1}. For both compounds, the first peak is predominant and followed by a small second peak and a higher third peak. Calculated structure factors from FPMD trajectories are plotted on the same graph for comparison (black lines). The agreement with the experiment is excellent, in particular on the two first peaks, with a small discrepancy in frequency at high q. This systematic distances overestimate has been reported for many, if not all, Te-based compounds studied by FPMD [9, 70] and has already been observed in Chapter 6 for liquid $GeTe_6$. This induces a slight interatomic distances overestimate in calculated pair correlation functions.

Amorphous phase The $S(q)$ of amorphous Sb_2Te shows oscillations of higher amplitude than the one of the liquid phase, up to much larger q vectors of 18 $Å^{-1}$. Despite this strong evolution, the peaks are situated at almost the same q in liquid and amorphous $S(q)$. This indicates that, despite the better defined structure of the amorphous, both phases probably present many similarities. Some evolutions in the general shape are observed:

- The ratio between first and second peaks heights decreases from liquid to amorphous phase (from 1.56 to 1.37).
- The asymmetric shape of the $S(q)$ third peak has a maximum position that evolves from the low-q side in the liquid phase to the high-q side in the amorphous. The same change is observed for the fourth peak.

These $S(q)$ evolutions from the liquid to the amorphous are very well reproduced by our calculations:

- The oscillations height is increasing and these are also observed up to much larger q values. At low q, we nevertheless observe slightly smaller amplitudes by FPMD than in the experimental $S(q)$ ($\sim$ 7 % and $\sim$ 13 % lower for the first and second peak respectively).
- The change in the ratio between the two first peaks (from 1.68 in liquid phase to 1.48 in amorphous phase) is of the same magnitude (~ -12 % in experiments and simulations).
- The evolution of the third and fourth peak shape is also reproduced by FPMD simulations, with a clear change in the asymmetry of both peaks upon quenching.

This good agreement could again be explained if the liquid and amorphous phase structures are relatively close to each other.

9.4.2 Comparison with AIST compounds

We have seen in subsection 9.1 (see also Chapter 1) that some PCM are build from doped Sb_2Te, for example with Ag or In (called $AIST$). It is thus interesting to compare the Sb_2Te and this doped compound. At the same time as the D4 experiment on amorphous Sb_2Te, we measured the structure factor of amorphous $AIST$ (the exact composition was $Ag_4In_3Sb_{67}Te_{26}$). We plotted it together with the $S(q)$ of Sb_2Te in Fig. 9.3. They are almost identical. We also plotted in this graph the $S(q)$ from FPMD simulations on $AIST$ ($Ag_{3.5}In_{3.8}Sb_{75.0}Te_{17.7}$) in liquid phase from Akola and Jones [47]. We see that their result is very close to our liquid Sb_2Te $S(q)$.

This similarity between Sb_2Te and $AIST$ confirms that the experimental or theoretical study of amorphous Sb_2Te structure and dynamics could give interesting data about one of the most promising PCM.

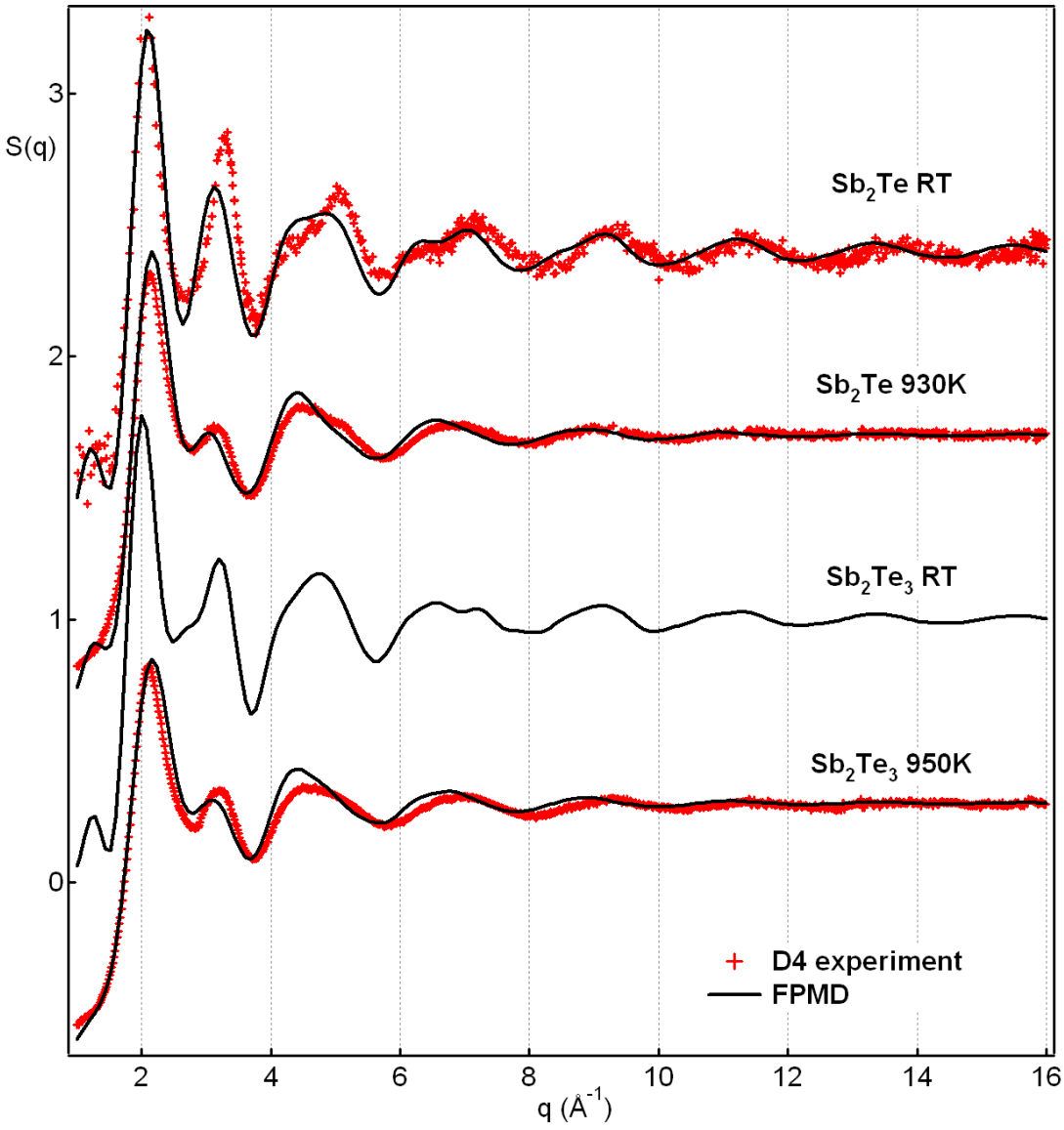

Figure 9.2: Structure factors from the experiments (red markers) and the FPMD simulations (black lines) in liquid and amorphous Sb_2Te and Sb_2Te_3.

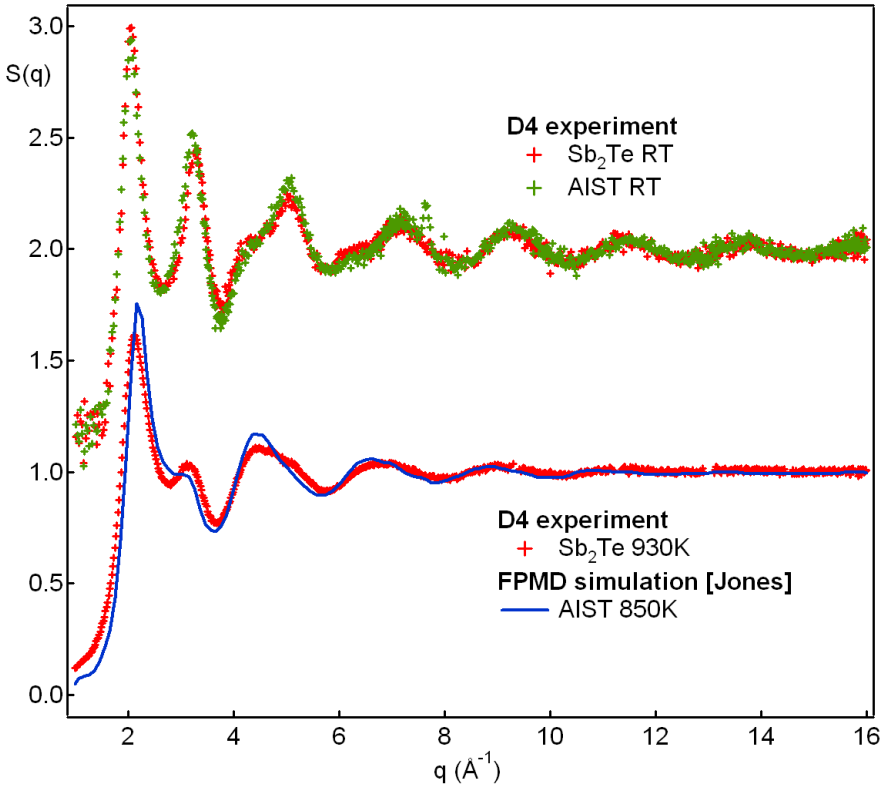

Figure 9.3: Upper curves : Structure factors from D4 experiment for Sb_2Te (red markers) and $AIST$ (green markers) compounds in amorphous phase. Lower curves : Structure factors of Sb_2Te in liquid phase (red markers) together with calculated $S(q)$ of $AIST$ from Akola and Jones [47](blue lines).

9.4.3 Pair correlation functions $g(r)$

Liquid phase The first $g(r)$ peaks positions are at slightly larger distances (by ~ 0.1 Å) in the FPMD curve than in the experiment (see Fig. 9.4), and the second peak is smaller, but except these small differences, the agreement is very good.

The first peak position, r_1, first minimum, r_{min}, and total coordination numbers N_c from both the experiment and the FPMD are indicated in Table 9.1. Coordination numbers were calculated by integration of $4\pi r^2 \rho g(r)$ from a fixed distance equal to 2.4 Å to a cutoff distance equal to r_{min}^{exp} for experiment and r_{min}^{FPMD} for calculations. Because of the interatomic distances overestimate mentioned before, we observe coordination numbers from FPMD that are slightly larger (by 0.4 in average) than the experimental ones.

In their paper, Caravati et al. [70] report total coordination numbers smaller than us in liquid Sb_2Te_3 phase (equal to 3.383). Their structure factor being similar to ours, this difference can be explained by the different cutoff distance chosen only.

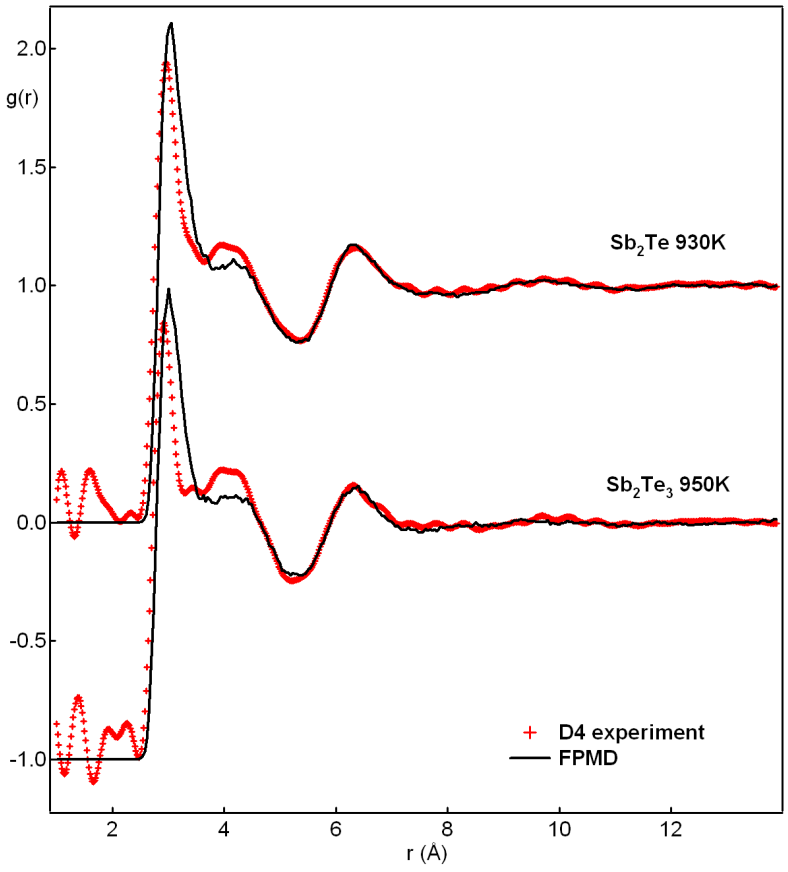

Figure 9.4: Pair correlation functions from the experiment (red markers) and the FPMD simulations (black lines) in liquid Sb_2Te and Sb_2Te_3.

Compound	T (K)	ρ (at/Å^{-3})	r_1^{exp}	r_{min}^{exp}	N_c^{exp}	r_1^{fpmd}	r_{min}^{fpmd}	N_c^{fpmd}
Sb_2Te	930	0.0301	2.9(6)	3.5(4)	4.5(9)	3.0(6)	3.6(3)	4.8(6)
Sb_2Te_3	950	0.0283	2.9(2)	3.5(1)	3.9(4)	3.0(1)	3.5(9)	4.3(8)
Sb_2Te	RT	0.0289	2.8(7)	3.1(5)	2.5(2)	2.9(5)	3.1(8)	2.7(1)
Sb_2Te_3	RT	0.0283				2.9(3)	3.4(7)	3.7(5)

Table 9.1: Compounds and temperatures studied by neutron diffraction experiment and FPMD simulations. Densities [170], positions of the first maximum r_1, first minimum r_{min} and coordination number N_c from experimental and calculated pair correlation functions $g(r)$. The second decimal is indicated within parentheses. All distances are given in Å.

Amorphous phase We observe a good agreement between the $g(r)$ of the amorphous phase from experiment and simulations (see Fig. 9.5). The first peak position is still slightly larger (by $\sim$ 0.1 Å) by FPMD than in the experiment, but the overall $g(r)$'s shapes are very similar. Most of the differences between experiment and simulations can be attributed to the unavoidable cutoff oscillations that are present in the experimental $g(r)$. The calculated $g(r)$ for Sb_2Te_3 is also plotted, its overall shape is close to the $g(r)$ of Sb_2Te. The first peak position, r_1, first minimum, r_{min}, and total coordination numbers N_c from experiment and FPMD are indicated in Table 9.1.

9.4.4 Evolution of partial pair correlation functions $g_{\alpha\beta}(r)$ upon quenching

Neutron diffraction experiments do not give access to the partial pair correlation functions $g_{\alpha\beta}(r)$, and, in particular, to their thermal evolution. These quantities can nevertheless be obtained from the FPMD trajectories.

The calculated $g_{\alpha\beta}(r)$, for $SbSb$, $SbTe$ and $TeTe$ pairs of atoms, in Sb_2Te and Sb_2Te_3 FPMD structures are plotted in Fig. 9.6 at 200 K, 400 K and 600 K and in the liquid state. For both compounds, the main evolution between liquid and amorphous is observed on the two first peaks of each partial, correlated with a short-range order evolution with temperature.

In Sb_2Te, for $SbSb$ and $SbTe$ partials, the first peak becomes sharper and higher with quenching, while, in comparison, the first peak height is almost constant for $TeTe$ correlations.

In Sb_2Te_3, the behavior with temperature of the $SbTe$ partial is identical to the Sb_2Te case. The $SbSb$ partial completely changes with T, the ratio between the two first peaks being larger than unity in liquid phase and smaller in the quenched phase. The $TeTe$ first peak of partial pair correlation function in liquid phase, which is very broad, separates into two peaks upon quenching.

The partial coordination numbers for Sb and Te in the quenched phase are indicated in Table 9.2. We observe, for both compouds, a decrease of the partial coordination numbers

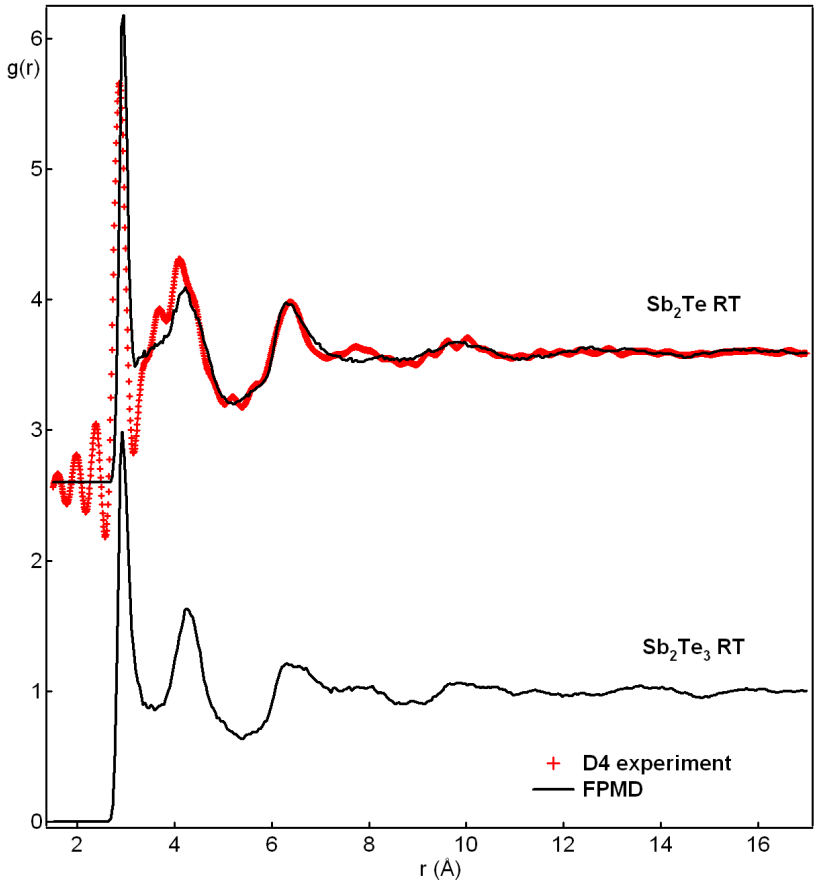

Figure 9.5: Pair correlation functions from the experiment (red markers) and the FPMD simulations (black lines) in amorphous Sb_2Te and Sb_2Te_3.

when the temperature decreases. This effect is much larger in Sb_2Te. There is a very low rate of homopolar bonds in both structures (exept for $Sb-Sb$ bonds in Sb_2Te). Again, the differences with results reported in [70] (see last line of the Table 9.2) are most probably due to the different cutoff distances chosen.

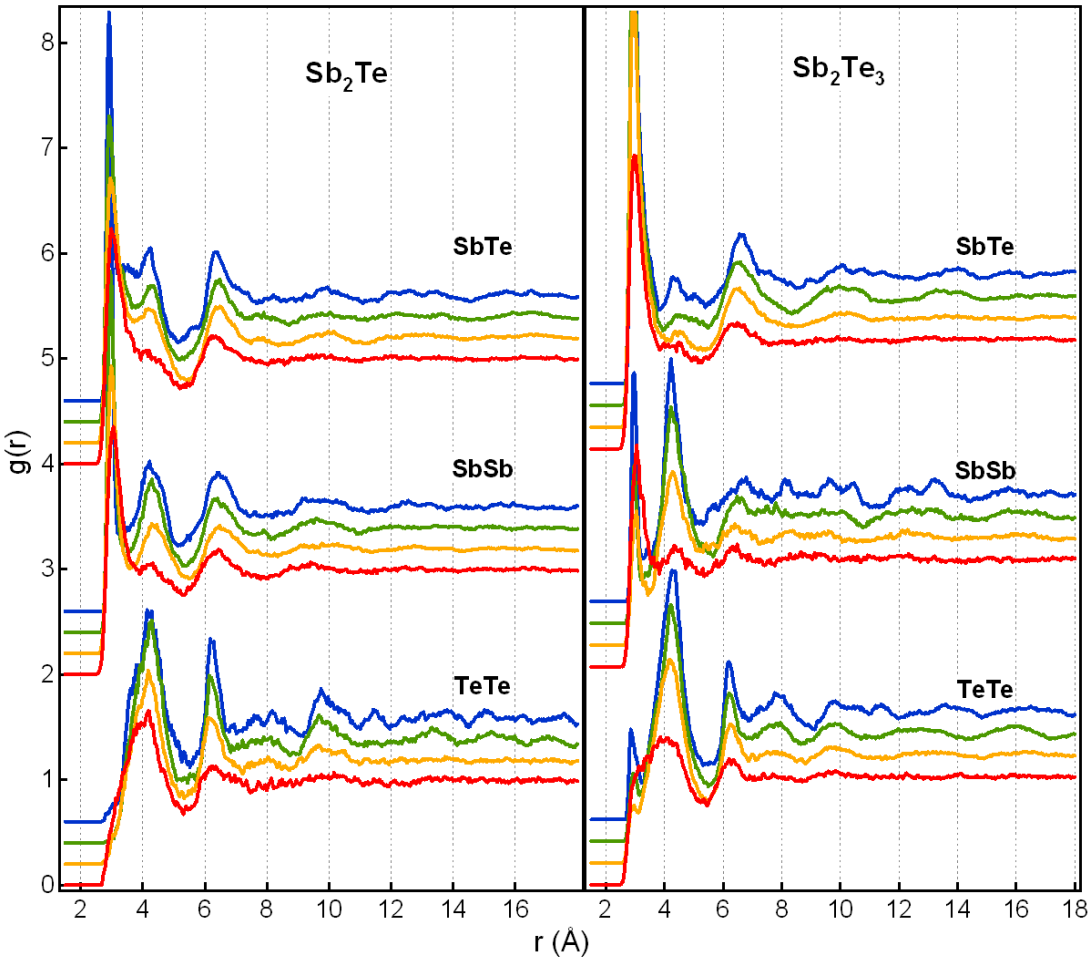

Figure 9.6: Temperature evolution of partial pair correlation functions calculated from FPMD trajectories, for Sb_2Te (left panel) and Sb_2Te_3 (right panel). Red lines : 930 K (Sb_2Te) / 950 K (Sb_2Te_3), orange : 600 K, green : 400 K and blue : 200 K.

Compound	T (K)	r_{min}^{fpmd}	N_c^{SbSb}	N_c^{SbTe}	N_c^{TeSb}	N_c^{TeTe}	N_c^{Sb}	N_c^{Te}
Sb_2Te	600	3.5(2)	1.7(8)	3.1(1)	2.0(7)	0.7(3)	4.8(9)	2.8(0)
	400	3.3(7)	1.5(6)	2.6(9)	1.8(0)	0.2(3)	4.2(5)	2.0(3)
	200	3.1(8)	1.2(9)	1.9(2)	1.2(8)	0.1(2)	3.2(1)	1.4(0)
Sb_2Te_3	600	3.5(1)	0.7(7)	3.8(7)	2.5(8)	0.9(8)	4.6(4)	3.5(6)
	400	3.5(1)	0.6(8)	3.9(7)	2.6(4)	0.9(0)	4.6(5)	3.5(4)
	200	3.4(7)	0.7(9)	3.7(2)	2.4(8)	0.7(8)	4.5(1)	3.2(6)
Sb_2Te_3 [70]	300	3.15-3.38	0.458	3.635	2.424	0.319	4.093	2.743

Table 9.2: Positions of the first minimum r_{min}^{fpmd} in total pair correlation functions, $g(r)$, from FPMD (taken as the cutoff distance for integration), partial coordination numbers from partial pair correlation functions, $g_{\alpha\beta}(r)$, and total coordination numbers for Sb and Te atoms. The second decimal is indicated within parentheses. The results [70] are from Caravati. All distances are given in Å.

9.5 Structural properties

9.5.1 Total angle distributions

The total angle distributions around Sb or Te atoms were obtained by summing the angles $\widehat{i0j}$ between one atom in the structure and its neigbors i and j, and including the 6 first neighbors in the calculations.

Total angle distributions, averaged on all Sb (Te) atoms and over the FPMD trajectories are plotted in solid (dotted) lines in Fig. 9.7. For both compounds, at each T and around each element, the total angle distributions are peaked around 90° and 180° : the local order remains mostly octahedral (the peaks become higher and thinner upon quenching but keep the same position).

This is in agreement with the results of Caravati et al. on liquid and amorphous Sb_2Te_3 [70], and with the FPMD study of Akola and Jones [47] on the parent liquid $Ag_{3.5}In_{3.8}Sb_{75.0}Te_{17.7}$.

9.5.2 Distance distributions

The interatomic distances are computed for the 6 first neighbors of all the atoms in the simulation box and averaged over the FPMD trajectories. We calculated these distributions around Sb or Te atom separately, and on average (see Fig. 9.8). It is relevant to include the 6 first neighbors because the total angle distributions indicate an octahedral local order.

For both compounds, the distributions in the liquid phase consist of six large peaks with average values comprised between ~ 2.8 Å and ~ 3.8 Å. The sum of these 6 distributions produces the total distance distribution of the 6 first neighbors (also plotted in Fig. 9.8)

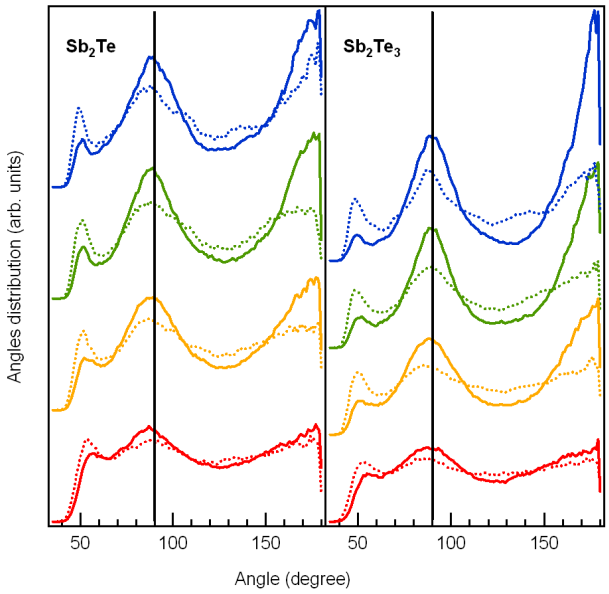

Figure 9.7: Evolution with T of total angles distribution around Sb (solid lines) or Te (dotted lines) atoms, in Sb_2Te (left) and Sb_2Te3 (right). Red lines : 930 K (Sb_2Te) / 950 K (Sb_2Te_3), orange : 600 K, green : 400 K and blue : 200 K.

which consists of a unique wide peak : the first neighbors shell in the liquid state doesn't show any particular profile but distribution broadens due to temperature.

In Sb_2Te, when the temperature decreases, this broad peak of 6 distances separates clearly in two sub-shells, of 3 distances each for Sb and 2+4 distances for Te[1]. The peaks corresponding to the 3 shortest distances become thinner (the full width at half maximum, FWHM, is divided by two between 930 K and 200 K), while the others keep the same FWHM.

In Sb_2Te_3, around Sb, the 3 first distances peaks become sharper (FWHM is divided by two between 950 K and 200 K) at low T, and the 3 other keep more or less the same width, but the separation between these peaks is less obvious than in the Sb_2Te case. Around Te, if we look at the sum of the 6 distributions, the 6 regularly spaced peaks of the liquid state evolve to form a $2+1+3$ peak structure.

From the distributions average on Sb and Te atoms, we see that the average coordination number is larger in Sb_2Te_3 (between 3 and 4) than in Sb_2Te (around 3) at lowest T, as already showed in Table 9.2 with the coordination numbers N_c obtained from the partial pair correlation functions $g_{\alpha\beta}(r)$.

To examine more carefully the local order evolution with T, we plotted in Fig. 9.9 the averages of the six first distances distributions around Sb and Te atoms.

[1] At 200 K, the octet rule is thus verified for the Sb and Te elements separately.

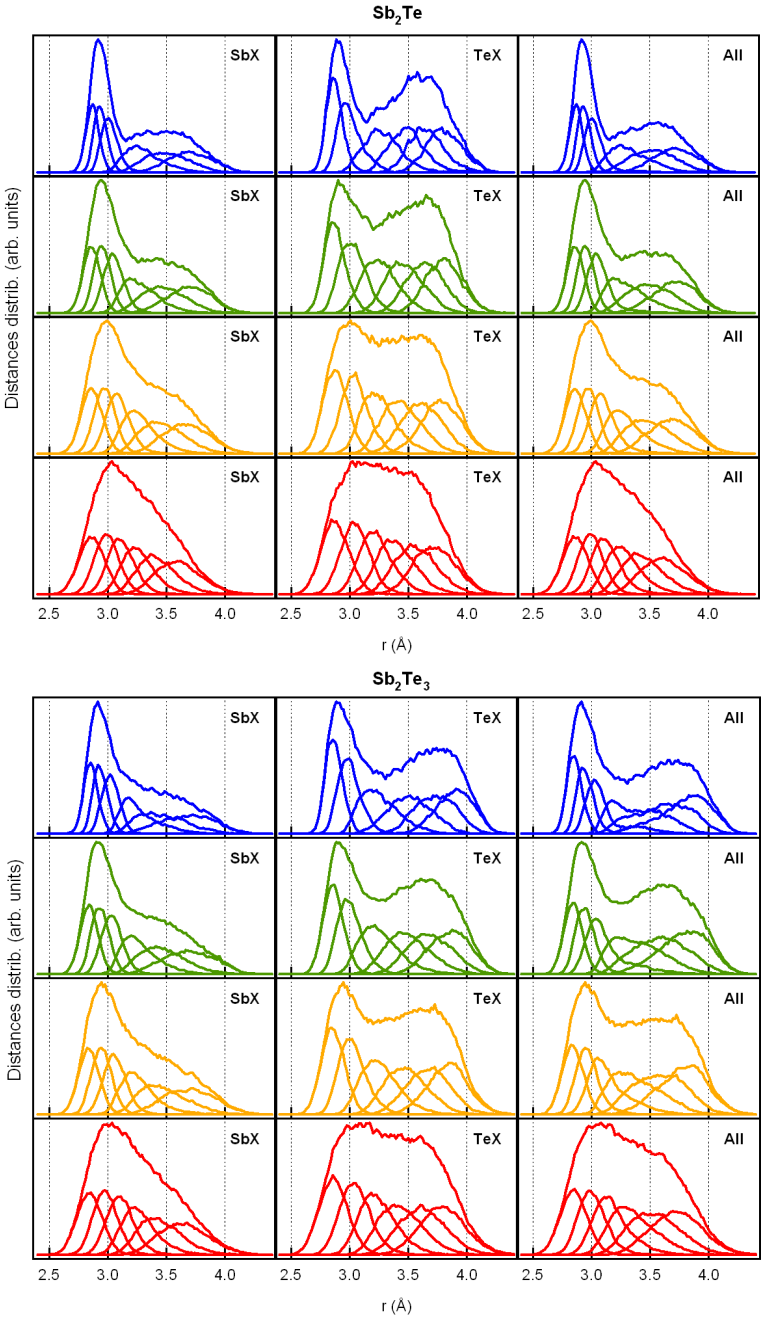

Figure 9.8: Six first interatomic distance distributions around Sb or Te atoms, and average on both, for Sb_2Te (top) and Sb_2Te3 (bottom), at different temperatures. Red lines : 930 K (Sb_2Te) / 950 K (Sb_2Te_3), orange : 600 K, green : 400 K and blue : 200 K.

In the liquid phase, the situation is similar for both compounds and around each element : the distances are equally distributed between ~ 2.9 Å and ~ 3.6 Å (~ 3.7 Å in Sb_2Te and ~ 3.8 Å in Sb_2Te_3) around Sb (Te) respectively.

In Sb_2Te, as soon as the compound is quenched, we observe a separation of the first neighbors shell in two sub-shells made of 3 'shorter' + 3 'longer' distances (around Sb) or 2 'shorter' + 4 'longer' distances (around Te). The shortest (first) distance remains constant for Sb and Te, the second (and third for Te) decreases while, on the other hand, the 'longer' distances increase.

In amorphous Sb_2Te_3, around Sb atoms, the 3 shortest distances decrease when T decreases while the 3 other remain constant, which tends to create two sub-shells, as in Sb_2Te. Around Te, the first and third distances remain constant with T, the second is decreasing and the 3 longest are increasing, which leads to a 2+1+3 environment at lowest T, as evidenced from the distances distributions in Fig. 9.8 (b).

9.5.3 Three Body Correlation function

In the liquid phase, the TBC probabilities around Sb and Te in both compounds are very low and the distances r_1 and r_2 corresponding to maxima are equal within ~ 0.2 Å (see Fig. 9.10 and 9.11). This is coherent with the 6 first distance distributions plotted in Fig. 9.8, which show the disordered neighborhood around each element.

In Sb_2Te, when T decreases, the values of the TBC functions maxima increase (both around Sb and Te), and their positions evolve to more distinct pairs of distances, expressing the appearance of a distorsion, coherently with the distances distributions. It is also interesting to note that, if we can observe such distinct maxima, it means that the shorter and longer bonds are not distributed randomly around atoms but preferentially face each other.

In Sb_2Te_3, the TBC maxima for Sb atoms do not shift with quenching, but their heights increase. This agrees with the average distances evolution depicted in Fig. 9.9, which shows the splitting of the first coordination shell between 2 sub-shells only because of the second and third bonds decrease (the other bonds remaining constant). Around Te, two well defined maxima appear with quenching, corresponding to 2 inequivalent distances.

Conclusion These three analysis of interatomic distances in our amorphous $SbTe$ structures lead to the picture of a *distorted octahedral local environment* around atoms, in which the type of sub-shells of first neighbors depends on the element and the nature of the alloys. This local environment is similar to what is found in the crystalline phase.

9.5.4 Local chemical order

To go further in the understanding of the local order and to compare it carefully to the crystals, we studied the chemical environment of Sb or Te atoms, by calculating the Warren-Cowley short-range order parameter [161, 162] for both elements, $\alpha^{(i)}$ (defined in

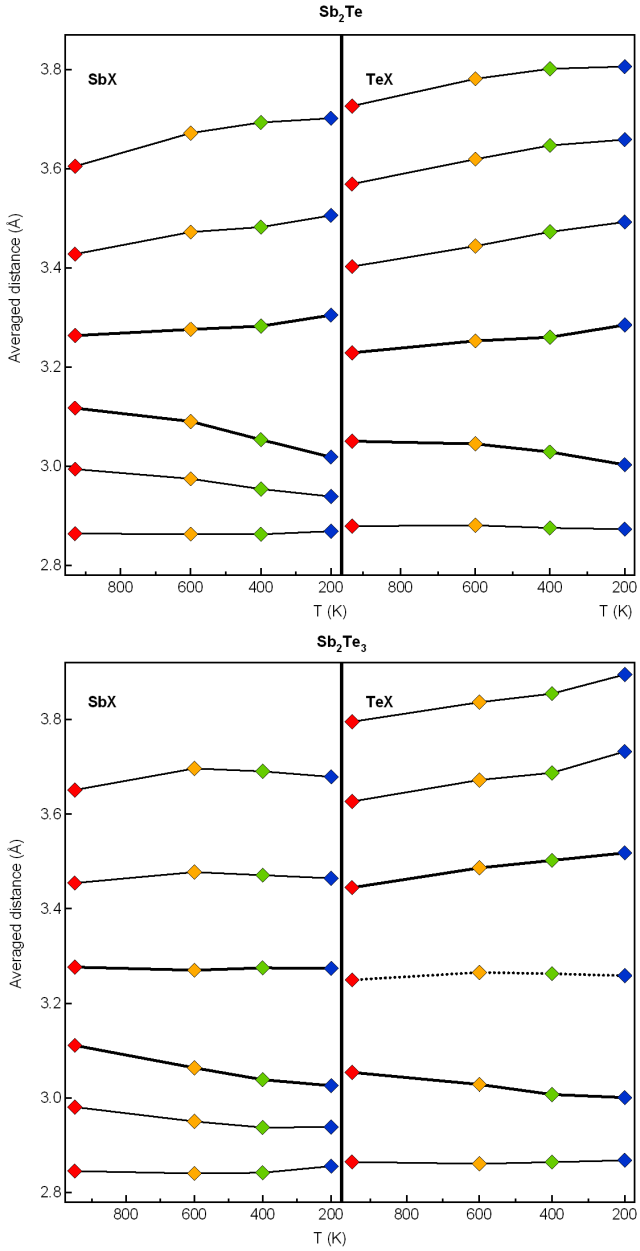

Figure 9.9: The evolution of average interatomic distances with T in Sb_2Te (top) and Sb_2Te_3 (bottom), around Sb and Te atoms (top and bottom panel respectively).

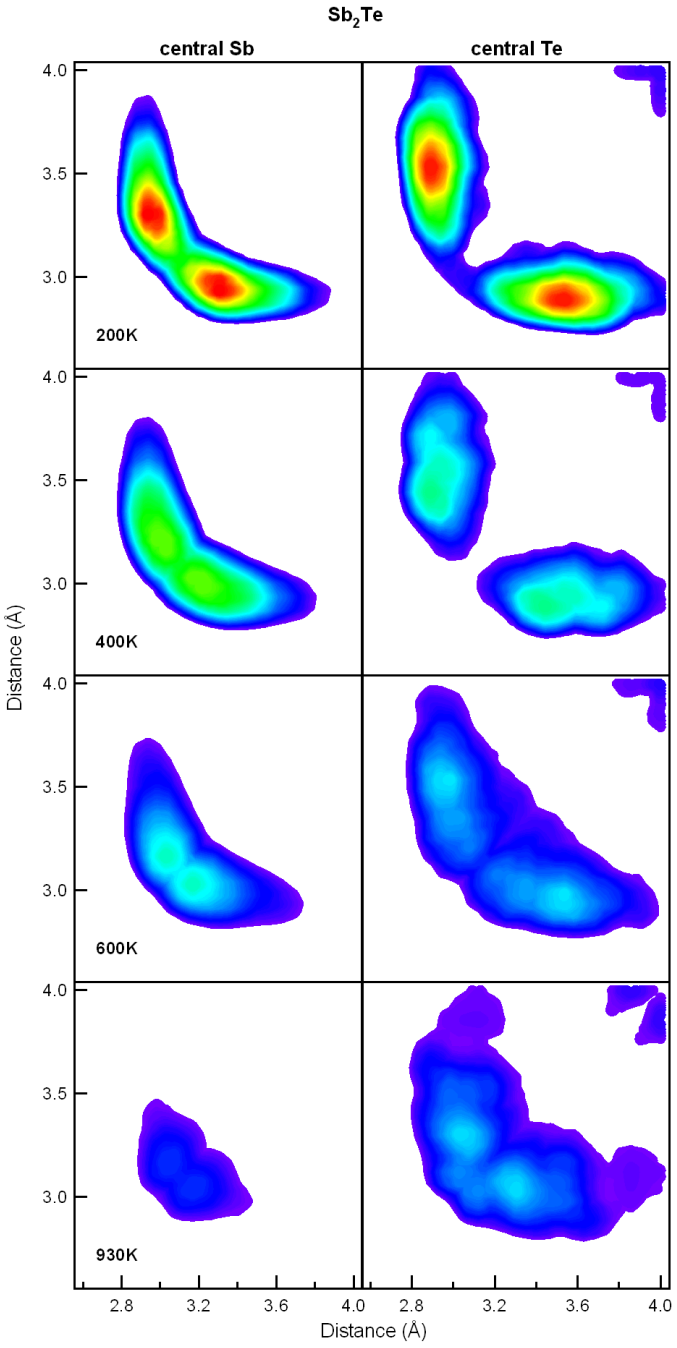

Figure 9.10: Evolution with T of TBC functions around central Sb (left panel) or Te (right panel) atom, for Sb_2Te. The three atoms considered are aligned within 15°. Colors go from blue (25 % of the maximum) to red (maximum).

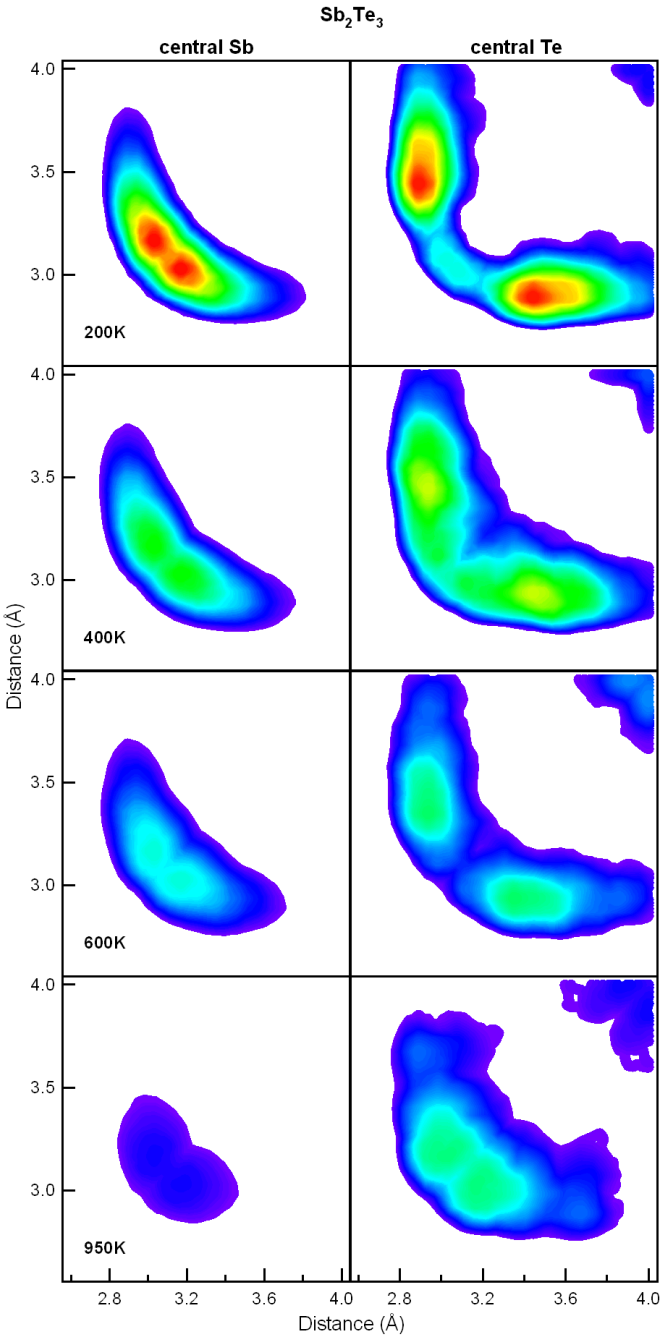

Figure 9.11: Evolution with T of TBC functions around central Sb (left panel) or Te (right panel) atom, for Sb_2Te_3. The three atoms considered are aligned within 15°. Colors go from blue (25 % of the maximum) to red (maximum).

Chapter 8 section 8.4). We averaged $\alpha^{(i)}$ on all Sb or Te atoms over the FPMD trajectories. Results are plotted in Fig. 9.12 for both elements in our structures. The chemical order is very different depending on the compound.

In Sb_2Te, the value of $\alpha^{(Sb)}$, around 0 for all temperatures, indicates a random arrangement of the chemical species, whether we consider only the 3 first or the 6 first neighbors. Around Te, in the amorphous phase, a perfect alternation is found if we consider the 2 closest neighbors, the maximal negative value of $\alpha^{(Te)}$ being -0.5, but this alternation is completely lost for the 4 other neighbors. In the crystal [59], three Sb sites are presents, with either Sb or Te as nearest neighbors, and two Te sites, which only have Sb atoms as 6 nearest neighbors (not the case in amorphous).

In amorphous Sb_2Te_3, around Sb, we observe a strong tendency to alternation, whether on the 3 first or on the 6 first neighbors, the value of $\alpha^{(Sb)}$ being close to -0.4 (compared to the maximum negative value of $-2/3$). Around Te, we computed $\alpha^{(Te)}$ values both with the 2 or 3 first neighbors because the average distances in quench has shown a 2+1+3 environment. The parameter $\alpha^{(Te)}$ is around -1 if we take into account the 2 or 3 first neighbors (the lowest possible negative value is -1.5) : an alternation is thus clearly present. Looking at $\alpha^{(Te)}$ for 6 neighbors, we can say that there is a strong disorder on the 3 more distant neighbors. These tendencies to alternate with the nearest neighbors are weaker in the liquid, which means that, despite the short quenching times compared to experiment, the chemical order in the system evolves a lot between liquid and amorphous states. Once at $T < T_m$, we do not observe any further significant evolution, the diffusion being very slow at these temperatures (see section 9.6). Actually, the chemical local order in amorphous Sb_2Te_3 is very close to the one found in the crystal [60], where the Sb atoms (one site) have 6 Te neighbors in the first neighbors shell, and the Te atoms (two sites) have 3 Sb atoms as nearest neighbors (bonds smaller than 3 Å) while they have either Sb or Te neighbors at longer distances.

With these results, we conclude that Sb_2Te_3 *chemical* local order in the amorphous is very close to the one of the crystal phase, while it is not the case for Sb_2Te.

9.5.5 Partial angle distributions

As seen in the section 9.1.2, the crystalline structure of both Sb_2Te and Sb_2Te_3 are Peierls distorted and can be viewed as a stacking of distorted cubes, with angles close to 90° between the 3 closest neighbors and smaller between the 3 others. Both crystals consist of a succession of layers, each one containing a unique chemical species.

We evidenced some similarities between the amorphous structures and crystals by looking at the local environment (total angles, distances and chemical order) around atoms. To go further in the comparison with crystals, we calculated the angles between the shortest or longest bonds in liquid and quenched structures (at 200 K) obtained by FPMD. For

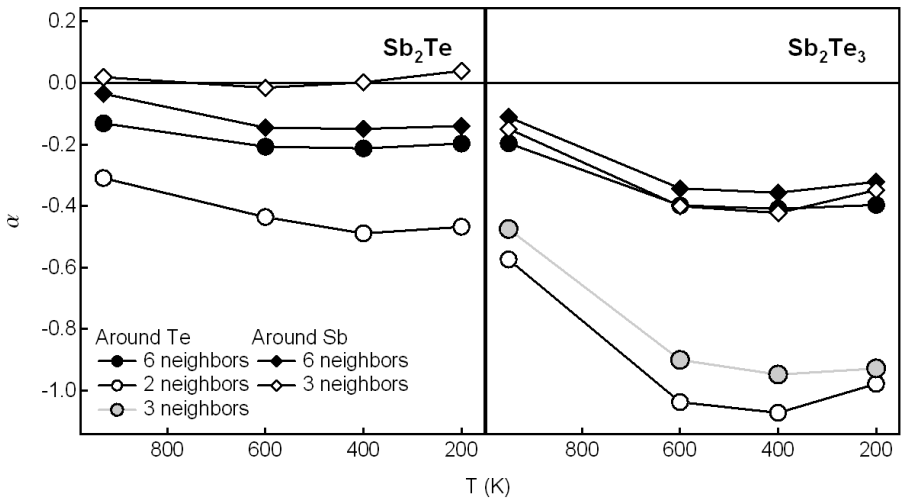

Figure 9.12: Evolution with temperature of the Warren-Cowley parameter $\alpha^{(i)}$ (see Eq. 8.1) for Sb (diamonds) and Te (circles) atoms. Different numbers of neighbors are taken for calculation.

this purpose, after having computed all the a_{ij} angles between r_i and r_j bonds ($i \neq j$) (plotted at 200 K in Fig. 9.13 and 9.14), we averaged a_{ij} for $i, j = 1, 2, 3$ or $4, 5, 6$ around Sb or Te, and a_{ij} for $i, j = 1, 2$ or $3, 4, 5, 6$ around Te only. Again, because of the 2+1+3 neighborhood of Te atoms at 200K, we tested two sets of 'shortest distances' around Te. Results are plotted in Fig. 9.15.

First, we note that, in the liquid phase, compounds behave in the same way : around Sb and Te, the angle distributions between shortest bonds are peaked around 90°, while they are really flattened for angles between the 3 longest bonds.

The amorphous phase has different distributions for both compounds. In Sb_2Te, around Sb (Te), in (a) ((c)), the angles between the 3 (2) shortest bonds are peaked around 90°, and no contribution is observed around 180°. Around Sb, the angle distributions between the 3 longest bonds is peaked around 70°, which is smaller that the average on the 3 Sb sites in the crystal phase ($\sim$ 80°), while around Te they are comparable to the liquid's case. In Sb_2Te_3, the angle distributions between shortest bonds (3 around Sb, 2 or 3 around Te) are peaked around 90°, as in the crystal. The Sb angle distribution between the 3 longest bonds (d) has evolved a lot from the liquid to amorphous, where it is peaked around 87°, a value that is very close to that of $\sim$ 84.8° found in the crystal. Around Te (e, f), this distribution is flatter (as in the Sb_2Te case), nevertheless a peak at $\sim$ 70° is present. We can make the correspondence with angles at 70.2° between Te (site 1) and its three second neighbors in crystal.

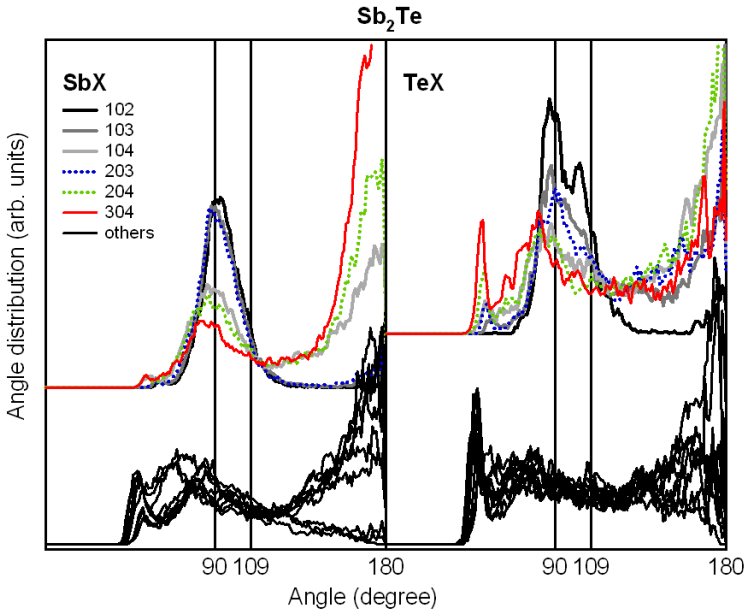

Figure 9.13: Partial bond angle distributions around Sb and Te atoms in amorphous Sb_2Te at 200 K.

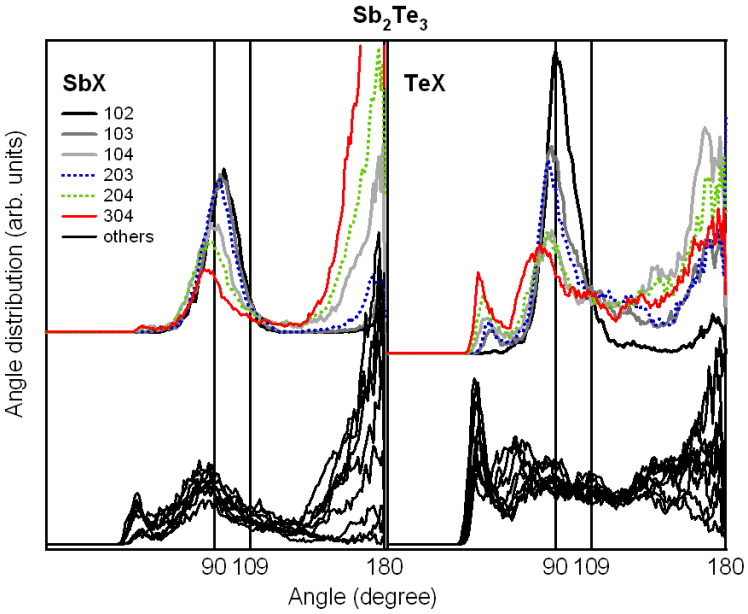

Figure 9.14: Partial bond angle distributions around Sb and Te atoms in amorphous Sb_2Te3 at 200 K.

Surprisingly, we found some partial angles in amorphous Sb_2Te_3 that are very close to what is found in the crystal, which is not observed in Sb_2Te. These distributions also help to refine the environment of Te atoms in Sb_2Te_3. Indeed, if we consider 3 shortest bonds instead of two, the peak at 70° is higher in the angle distributions between longest bonds, and the angle distributions between shortest bonds are almost unmodified. On the contrary, if we do the same comparison in Sb_2Te, we see that the angle distribution between the 3 shortest bonds has a much higher 180° peak than with 2 shortest bonds only. This let us think that, in Sb_2Te_3, the Te neighborhood is closer to 3+3, as in the crystal phase, than 2+4.

9.5.6 Medium-Range order

Up to now, we have checked the order in FPMD structures by looking at only the first shell of neighbors. Similarities between our amorphous structures and the crystals have been found in the local order around atoms. These similarities were found stronger in Sb_2Te_3. We wanted to check a possible order on more distant neighbors shells. For this, we developped a new analysis tool : we calculated the correlations between one triplet of atoms (one central atom and its 2 first neighbors) and atoms included in the complementary space of 2 cones (with an opening of 140°) perpendicular to the plane formed by the triplet. We project these correlations on the plane defined by the triplet of atoms. This is illustrated in Fig. 9.16.

Results are plotted in Fig. 9.17 and 9.18 for Sb_2Te and Sb_2Te_3 respectively. The spot drawn at origin (0,0) represents the central atom (either Sb or Te). The red spots at $\sim (|\vec{r}_1|, 0)$ and $(|\vec{r}_2 \cdot \vec{r}_1|, |\vec{r}_2 - \vec{r}_2 \cdot \vec{r}_1|)$ represent the two first neighbors at $\vec{r}_1$ and $\vec{r}_2$. The other marks in color represent the correlations between this triplet of atoms and atoms out of the cones drawn in Fig. 9.16, within the limits of our box length.

In both liquids (lower panels), we observe three well defined marks (in red) corresponding to the triplet of atoms considered (we observe again the octahedral *local* order). The second and further neighbors shells appear as larger marks, and it is difficult to distinguish correlations. This agrees with the range of visible oscillations in total pair correlation functions that extends up to ~ 9 Å (see Fig. 9.4).

When quenching to 200 K, we see that some marks corresponding to second and third neighbors shell grow or appear. In the surrounding circle, we see that some well defined marks are also appearing. The coordinations at 400 K and 200 K are, in both compounds studied, remarkably well defined, and extend up to more than 9 Å for some neighbors (i.e. up to the simulations box limits). For comparison, we plotted in Fig. 9.19 the correlations in plane for an octahedral crystal at finite temperature, where we clearly see the crystalline ordering.

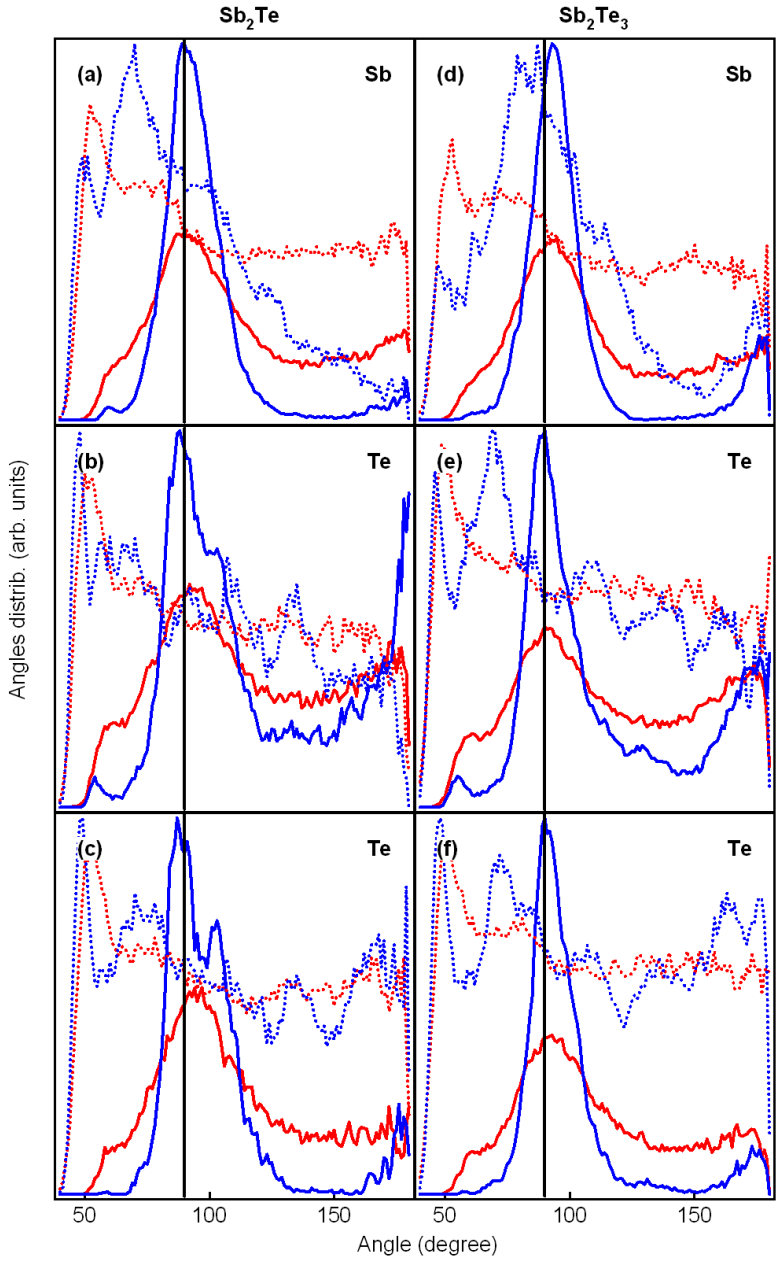

Figure 9.15: Partial angle distributions in liquid phase (red lines) and at 200K (blue lines), in Sb_2Te (left panels) and Sb_2Te_3 (right panels). (a) and (d) : Around Sb atoms, between the 3 shortest distances (solid lines) and the 3 longest distances (dotted lines). (b) and (e) : Around Te atoms, between the 3 shortest distances (solid lines) and the 3 longest distances (dotted lines). (c) and (f) : Around Te atoms, between the 2 shortest distances (solid lines) and the 4 longest distances (dotted lines). The vertical black lines are positioned at 90°.

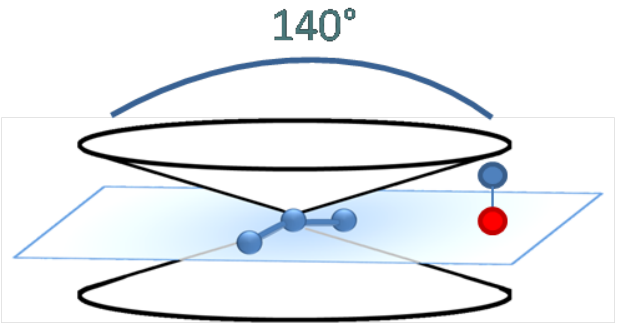

Figure 9.16: Sketch of the way to calculate the correlations between one triplet of atoms (one central atom and its 2 closest neighbors) and atoms of the box which are included in the complementary space of 2 cones (with an opening of 140 °) perpendicular to the plane formed by the triplet of atoms. We project these correlations in the plane defined by the triplet of atoms.

9.6 Dynamical properties

9.6.1 Diffusion

Using Eq. 6.2, we extracted the thermal evolution of the diffusion coefficient D (see Table 9.3) from the mean square displacements (MSD) of atoms in Sb_2Te and Sb_2Te_3 (plotted in Fig. 9.20). Using the Stokes-Einstein relation (see Eq. 6.3), with an atomic radius r_0 equal[2] to 1.6 Å, we obtain an estimation of the viscosity, η, from the diffusion coefficient (see Table 9.3). The diffusion coefficient obtained for the liquid Sb_2Te is similar to the result of Akola and Jones on the PCM $AIST$ [47]. As expected, the viscosity increases a lot when the temperature decreases below T_m (this phenomenon is slightly faster in Sb_2Te_3).

T (K)	Sb_2Te		Sb_2Te_3	
	D	η	D	η
930/950	3.88	1.1	4.62	0.9
600	1.14	2.4	0.47	5.8
400	0.15	12.2	0.13	14.1
200	0.04	22.9	0.04	22.9

Table 9.3: Evolution with temperature of the average diffusion coefficient D (in 10^{-5} cm^2/s) and the viscosity η (in cP) for Sb_2Te and Sb_2Te_3.

[2]We took $r_0 = \rho^{-1/3}/2$, where ρ is the liquid density.

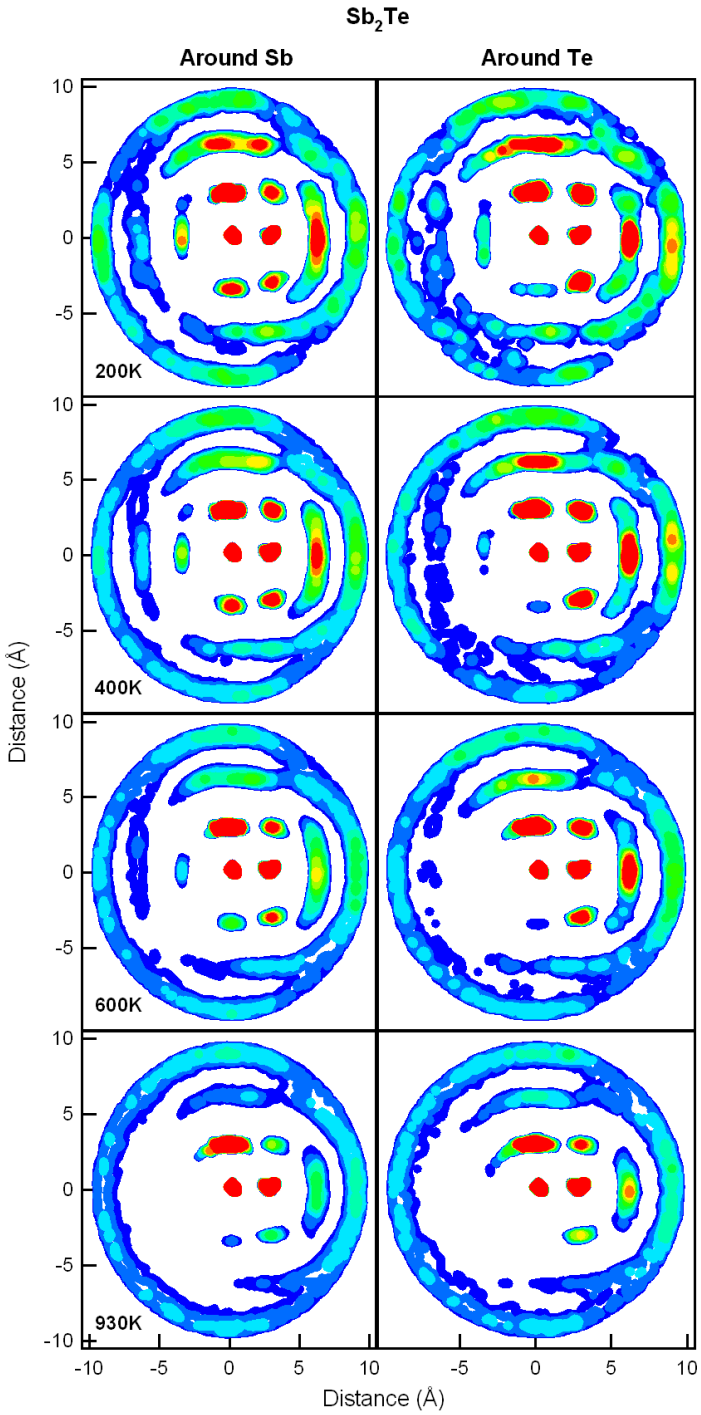

Figure 9.17: Evolution with T of the correlations, in Sb_2Te, between one triplet of atoms and atoms of the box which are included in the complementary space of 2 cones (with an opening of 140 °) perpendicular to the plane formed by the triplet of atoms. Colors go from blue to red (10 % to 50 % of maximum correlation).

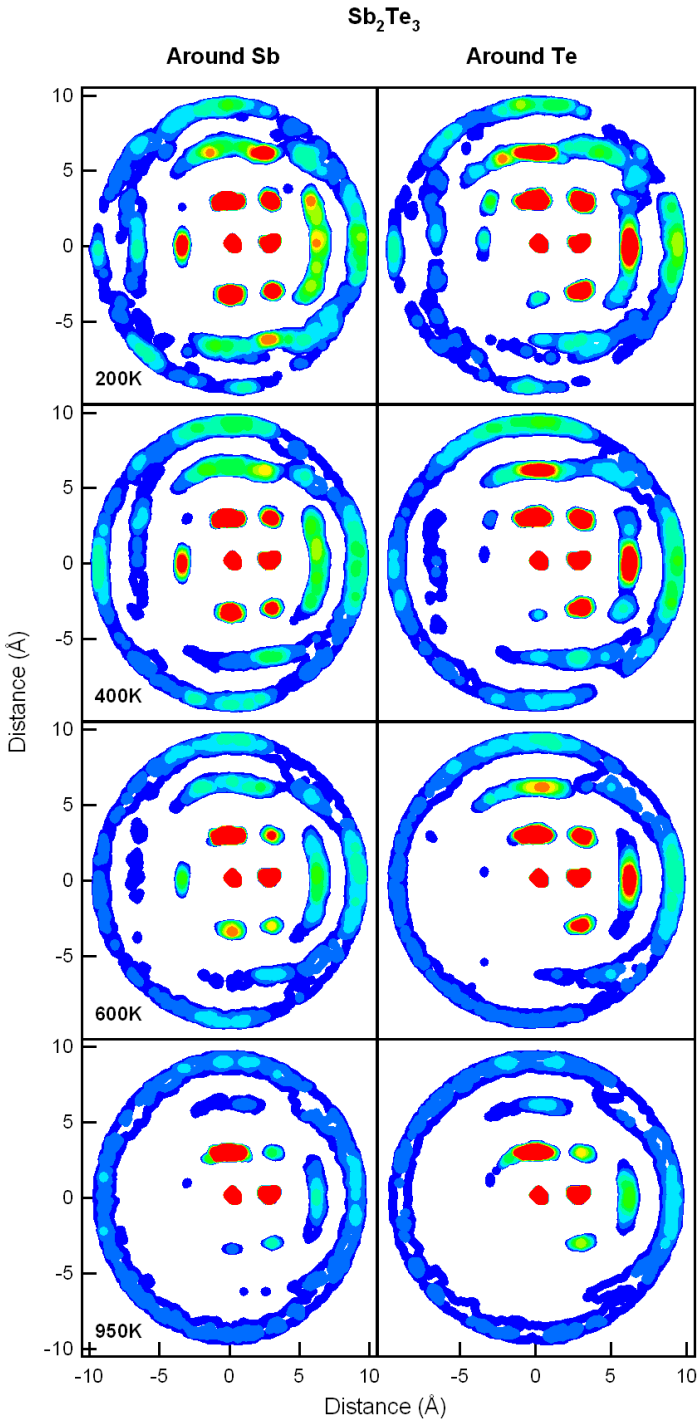

Figure 9.18: Evolution with T of the correlations, in Sb_2Te_3, between one triplet of atoms and atoms of the box which are included in the complementary space of 2 cones (with an opening of 140 °) perpendicular to the plane formed by the triplet of atoms. Colors go from blue to red (10 % to 50 % of maximum correlation).

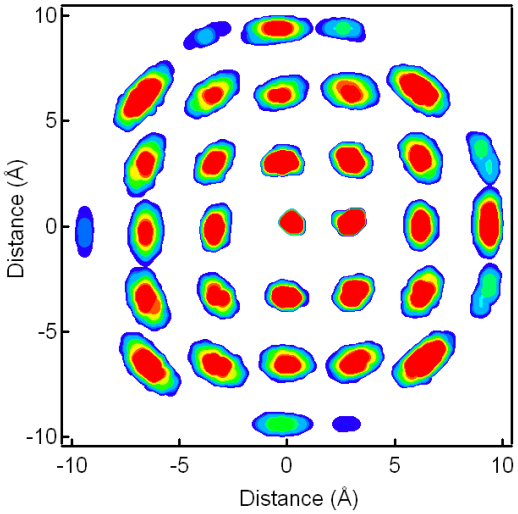

Figure 9.19: Correlations in plane for an octahedral crystal at finite temperature.

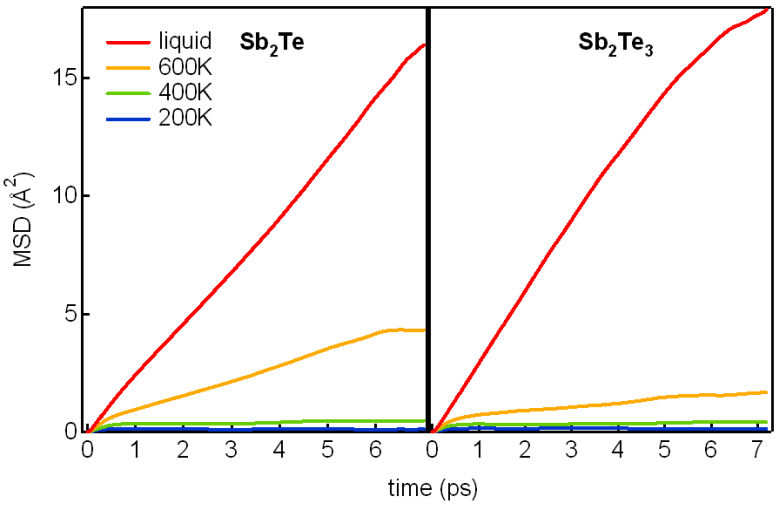

Figure 9.20: Evolution with temperature of the Mean Square atomic Displacement in Sb_2Te (left) and Sb_2Te_3 (right).

9.6.2 Dynamic structure factor

In the previous sections, we have seen that the local order present in the amorphous Sb_2Te_3 is very close to the local order found in the crystal, to the contrary of the Sb_2Te case. This difference must not hide the fact that we measured strong structural correlations (medium-range order) in *both* amorphous structures (see Fig. 9.18).

The coherent intermediate scattering function, $F(\mathbf{q}, t)$, as well as its frequency Fourier transform, the dynamic structure factor $S(q, \omega)$ (both defined in Chapter 4 section 4.6), can give information about collective motions in the systems.

If we want to look at the medium distances dynamics correlations that could appear in the FPMD amorphous structures (at $r \sim 8 - 10$ Å, as seen with the medium-range order analysis in Fig. 9.17 and 9.18), we basically have to look at $q = 2\pi/r \sim 0.6 - 0.8$ Å^{-1}. As these possible correlations would involve long distances, their contribution is expected at low energy. Our simulation times being equal to 40 ps, we have to access to energies down to ~ 0.10 meV.

We plotted in Fig. 9.21, 9.22 and 9.23 the $S(q, E)$ of Sb_2Te and Sb_2Te_3 at 600 K, 400 K and 200 K, in the low q (0.3 - 1 Å^{-1}) and small E (0 - 2.5 meV) region. At 600 K, the $S(q, E)$ of both compounds have close values, and low intensity. At 400 K, the spectra increase around 0.7 - 0.8 Å^{-1} in both cases. At the lowest $T = 200$ K, the $S(q, E)$ intensity has increased a lot for both compounds in this (low q, low E) zone. Moreover, a difference between both $SbTe$ alloys is clearly visible : we observe a larger density of *soft (low energy) / long wavelength* modes in Sb_2Te_3 than in Sb_2Te. This indicates that the medium-range order dynamics correlations are stronger in Sb_2Te_3.

These $S(q, E)$ high values in the (q, E) low-range, together with the medium-range order observed in the entire simulation boxes and the local order close to the crystal one, could explain the instability of amorphous Sb_2Te_3 against crystallization observed experimentally.

A complete determination of the stability of the amorphous against recrystallization would require the computation of the activation energy, which can not be directly accessed from our simulations.

9.7 Electrical properties

Phase-change materials can be used as memories thanks to their pronounced differences in conductivity between the crystalline and amorphous phases. The lowest conductivity is found in the amorphous phase.

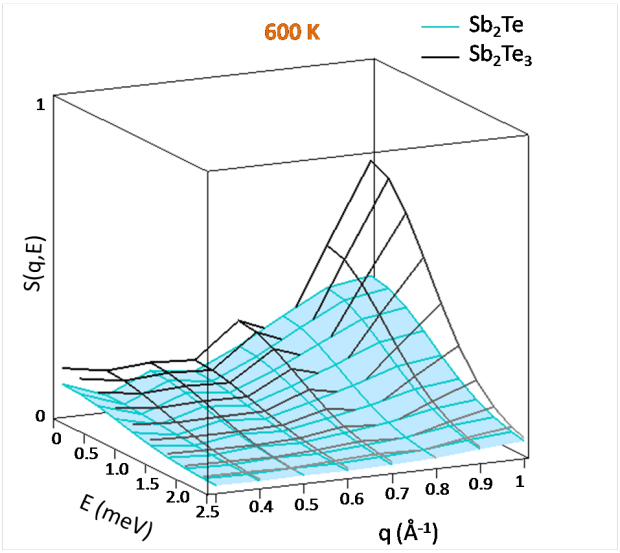

Figure 9.21: Dynamics structure factor $S(q, E)$ calculated at 600 K for Sb_2Te and Sb_2Te_3 alloys.

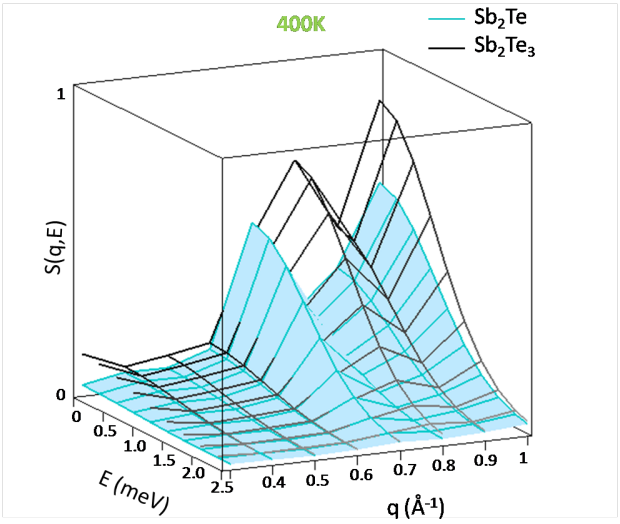

Figure 9.22: Dynamics structure factor $S(q, E)$ calculated at 400 K for Sb_2Te and Sb_2Te_3 alloys.

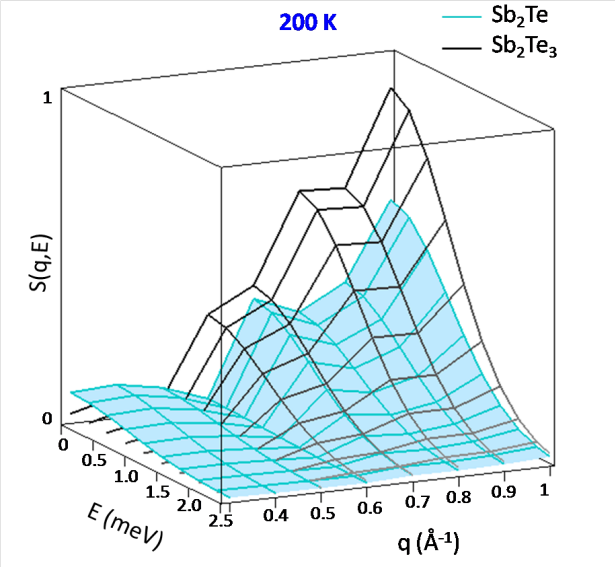

Figure 9.23: Dynamics structure factor $S(q, E)$ calculated at 200 K for Sb_2Te and Sb_2Te_3 alloys.

We plotted on Fig. 9.24 the thermal evolution of the partial electronic densities of states (EDOS), for the s-states and p-states of Sb and Te atoms, in both compounds. In the liquid, the EDOS at the Fermi level is relatively high, which is characteristic of a metallic behavior (see Fig. 9.25), as in the AIST [47]. When T decreases, the EDOS at the Fermi level is becoming lower, ultimately creating a gap at ambient T, both around Sb and Te atoms : this happens immediately below the melting temperature in Sb_2Te_3, while it appears continuously with quenching in Sb_2Te.

We computed the optical conductivities from our simulated structures by the Kubo-Greenwood formula [163, 164] (see Fig. 9.25). The electrical conductivity evolution with T is obtained by linear extrapolation to zero energy. The EDOS evolution described above is clearly translated into a metal-semiconductor transition (as computed by Caravati for Sb_2Te_3 [70]).

9.8 Conclusion

With this experimental and theoretical study of liquid and amorphous Sb_2Te and Sb_2Te_3 compounds, we obtained the following results :

– The local order around atoms in both amorphous compounds is similar to what is found in the crystalline phase, and is thus globally octahedral with distortions, and chemically ordered.

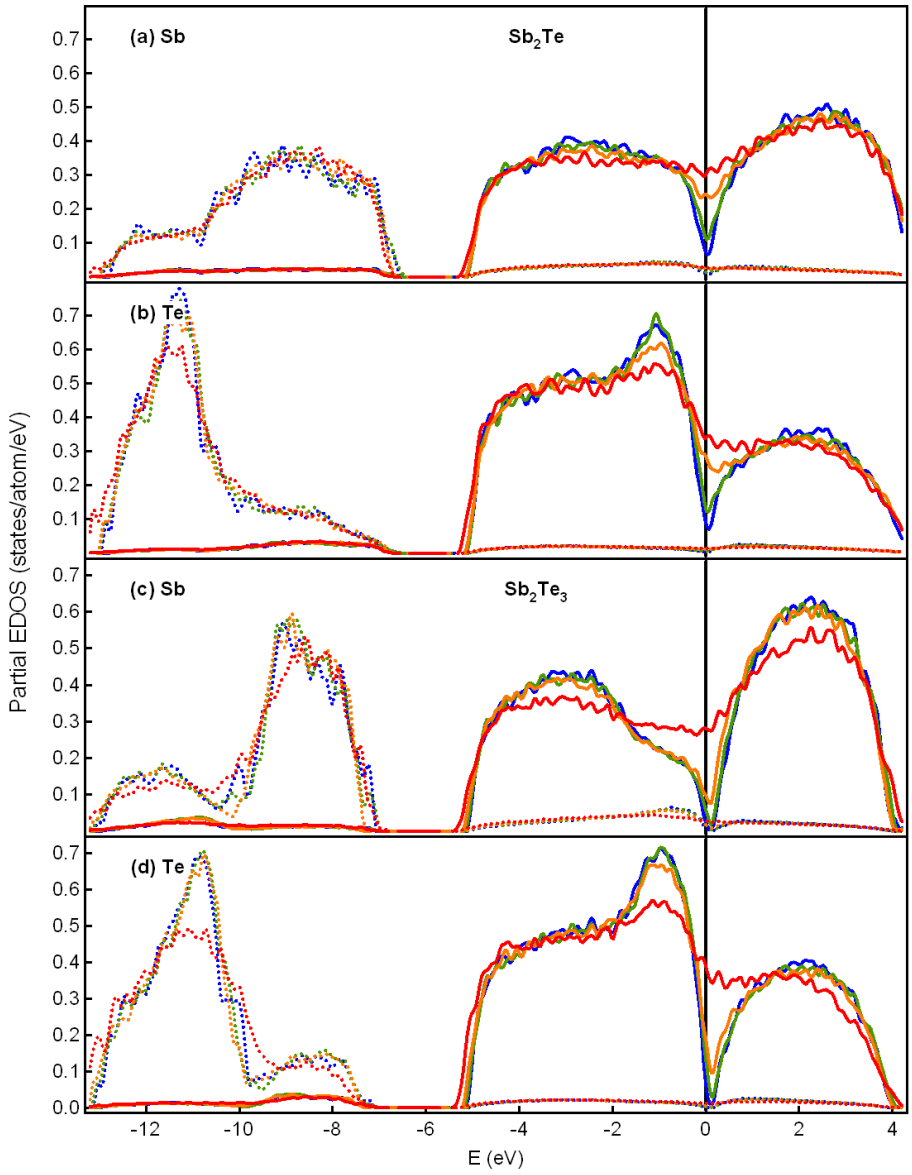

Figure 9.24: Evolution with T of partial electronic densities of states (EDOS), for the s-states (dotted lines) and p-states (solid lines) of Sb (a, c) and Te (b, d) atoms, in both compounds. Red lines : 930 K (Sb_2Te) / 950 K (Sb_2Te_3), orange : 600 K, green : 400 K and blue : 200 K.

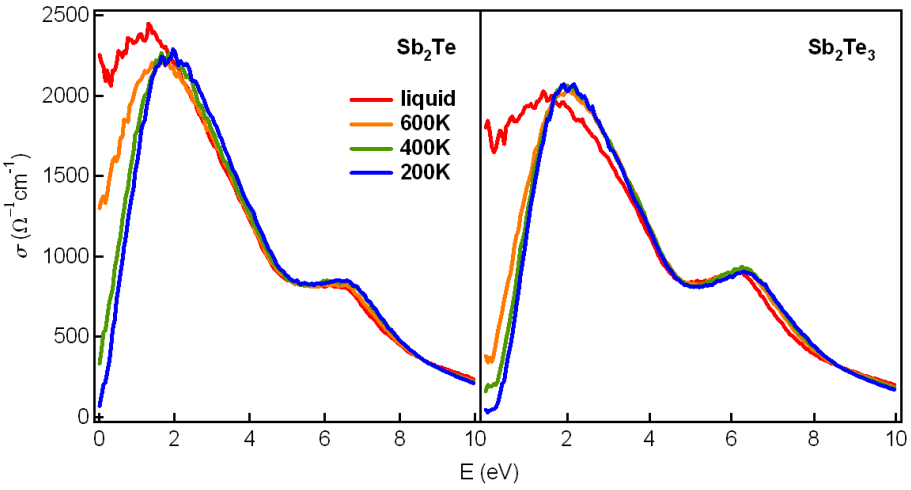

Figure 9.25: Evolution with T of dc conductivities for Sb_2Te (left panel) and Sb_2Te3 (right panel), at different temperatures. Red lines: 930 K (Sb_2Te) / 950 K (Sb_2Te_3), orange: 600 K, green: 400 K and blue: 200 K.

- The study of the correlations in space in the entire simulation boxes revealed a strong medium range order in both amorphous.
- The dynamical correlations show an increase of the long wavelength / low energy modes upon quenching.

These similarities between the amorphous and crystalline phases can to some extent explain the rapidity of the switching in compounds such as $AIST$, used as PCM, which was found similar in structure to the Sb_2Te alloy[3].

The detailed analysis of the local order (chemical order, partial angles) showed that in Sb_2Te_3, despite of its more complicated crystalline structure (15 layers in the cell instead of 9 in the Sb_2Te), some additional similarities between amorphous and crystalline phases exist. Moreover, the dynamical correlations at the medium distance range were found to be stronger for Sb_2Te_3 than for Sb_2Te. These two points could explain the experimentally observed instability of amorphous Sb_2Te_3 against crystallization (T_g lower than for Sb_2Te, which made the obtention of amorphous sample for diffraction experiment impossible). The amorphous Sb_2Te_3 local order is so close to that of the crystal that we expect the activation energy of recrystallization to be low, which would eventually not permit the obtention of a amorphous phase suitable for PCM use. According to this picture, a simple doping would probably not be sufficient to improve the stability, and the Sb_2Te_3 need to be associated with $GeTe$ units to be usable as PCM.

[3]The doping does not seem to influence the structure and affect only the optical and electrical properties.

Chapter 10

GeSbTe alloys

Phase change materials (PCMs), and among them the $GeSbTe$ (GST) alloys, are the components of current rewritable DVD's and are expected to be part of upcoming non-volatile memories. They display several unique properties: large contrast in optical and electrical properties between crystalline and amorphous phases, and rapid re-crystallization kinetics of the amorphous phase [172, 173]. Despite a growing application range and intense researchs these last decades, the atomic scale structure and mechanisms underlying the properties of these materials are still unclear (see Chapter 1).

Similarly to other GST alloys, $Ge_2Sb_2Te_5$ and $Ge_1Sb_2Te_4$ lie along the 'ternary line' between the stable $GeTe$ and Sb_2Te_3 compounds (see Chapter 1 Fig. 1.3), and display two possible crystalline structures: a stable hexagonal phase and a metastable close packed cubic one, the latter being used for data storage applications. In this metastable rocksalt structure, Te atoms occupy one of the fcc sublattices while Ge and Sb atoms share the remaining sites [64]. Depending on the GST composition, a large proportion of vacancies (which induce local distortions) is present, their concentration reaching for example 20 % in the $Ge_2Sb_2Te_5$ alloy [63, 64]. The role of these vacancies in the stabilization of the crystalline structure [37] and fast recrystallization [39, 174] has been highlighted.

Fingerprints of the amorphous structures were obtained via X-ray and neutron diffraction [72, 151], photoemission spectroscopy [45] and EXAFS measurements [36, 42]. Based on the latter, Kolobov et al. [36] designed a structural model that assigns the difference between the crystal and amorphous structures to a switching from octahedral to tetrahedral local order around Ge atoms (called *umbrella flipping*). Recently, Robertson [77] presented an alternative description to the Kolobov's model (see Fig. 1.8 in Chapter 1) : during the transition from the crystalline to the amorphous phase, the Ge atoms are displaced along the (110) direction rather than along the (111). In addition to this change in local order, the medium range order is totally lost in the amorphous structure (no order at the second-neighbor level). This hypothesis is in contradiction with our results on the $SbTe$ alloys (see the previous chapter). They evidenced a large difference in the optical properties of crystalline and amorphous phases of different compounds (Se, Te and $GeTe$)

and attributed it to the loss of the resonant bonding present in the crystalline phase due to the alignement of the p-orbitals.

In this chapter, we analyze a model for the amorphous phase of $Ge_1Sb_2Te_4$ and $Ge_2Sb_2Te_5$ alloys, obtained from ab initio molecular dynamics simulations. We show that the contrast in optical and electrical properties of phase-change alloys are caused by slight modifications in the first coordination shell of atoms, keeping an overall octahedral coordination, characteristic of p-bonded systems.

10.1 Method

10.1.1 Neutron diffraction experiment

The diffraction experiments on amorphous $Ge_2Sb_2Te_5$ and $Ge_1Sb_2Te_4$ (and a serie of other alloys) were performed within the framework of a collaboration with the group of Prof. M. Wuttig, from the RWTH Aachen.

The amorphous samples were obtained by sputtering from compound targets (one target with the desired composition) onto glass substrates and afterwards scratched from the glass into a quartz container. The thickness of the films was in the μm range (2-3 μm). A first diffraction experiment was performed with samples contained in quartz tubes of 2.3 mm internal /4 mm external diameter. Such quartz cells, in regards of the quantity of sample inside (the amorphous material being difficult to obtain in large quantity), led to a poor sample / quartz ratio, and consequently to very noisy results. A second experiment was thus performed with quartz cells of $\sim$ 2 mm diameter and a wall thickness of 10 μm, containing a mass of $\sim$ 150 mg of sample. Such particular quartz cells maximized the ratio sample / quartz in the beam. Because this ratio was about 15, only short counting times for the empty container were required, compared to the previous experiment, or to experiments on liquids (see previous chapters) for which the amount of quartz is close to that of the sample, requiring equivalent counting times. The $Ge_2Sb_2Te_5$ sample was not measured during this second experiment, which explains the poor statistics compared to the $Ge_1Sb_2Te_4$ results.

We used an incident neutron wavelength $\lambda = 0.4959$ Å, which, together with a 2θ angular range extended from 1.47° to 138.15° permits to reach neutron scattering vectors $q = 4\pi \sin\theta/\lambda$ up to large values of 23.7 Å^{-1}. Measurements were performed at room temperature, with counting times of 12 hours. The empty quartz cell (cut from the same tube as for the samples) signal was measured for 2 hours.

The results are presented together with FPMD results in the following.

10.1.2 FPMD simulations

We used Density Functional Theory as implemented in the VASP [134] and PWSCF [175] packages to obtain atomic trajectories and electronic structures of 168 and 162 atoms systems (24 Ge, 48 Sb, 96 Te for $Ge_1Sb_2Te_4$ and 36 Ge, 36 Sb, 90 Te for $Ge_2Sb_2Te_5$). The systems were first molten and equilibrated at the amorphous densities [176, 177] ($\rho = 0.0274$ Å^{-3} for $Ge_1Sb_2Te_4$, which is a slight underestimate of the experimental density equal to 0.0300 Å^{-3}, and $\rho = 0.0305$ Å^{-3} for $Ge_2Sb_2Te_5$) for 10 ps, then progressively cooled down from 1200 K to 100 K in 30 ps. This quenching rate is orders of magnitude faster than the experiment, as already discussed for $SbTe$ systems in the previous chapter, thus leaving the possibility for some remnants of the liquid local order in the amorphous structure. Nevertheless, both liquid and amorphous structure factors are in satisfactory agreement with the experiments. The atomic positions were then fully relaxed.

The Ge, Sb and Te valence s and p electrons are treated explicitly, while core electrons are represented by pseudopotentials. In VASP, ultrasofts pseudopotentials [133] are used, and normconserving Troullier-Martins pseudopotentials are used in PWSCF [178], which is only used for the DOS projections onto atomic orbitals for a fixed configuration. The exchange-correlation used is the Generalised Gradient Approximation PW91 in VASP [128] and the Local Density Approximation (LDA) in PWSCF [121]. In both codes, the electronic wavefunctions are represented on a plane waves basis, with a 210 eV cutoff in VASP and a 270 eV cutoff in PWSCF. Differences between PWSCF-LDA and VASP-GGA DOS are negligible (same gap value). Calculations were performed at the Γ point only.

10.2 Structure

10.2.1 Structure factors S(q)

The experimental and computed $S(q)$ for amorphous $Ge_1Sb_2Te_4$ and $Ge_2Sb_2Te_5$ are shown in Fig. 10.1. The $S(q)$ of both GST compounds are similar (as mentioned before the $Ge_2Sb_2Te_5$ signal is very noisy compared to $Ge_1Sb_2Te_4$). Prominent peaks are observed, as expected for amorphous compounds. At the low q-values, both calculated structure factors are in agreement with experiment for the positions, but are too small in amplitude. At high q-values, as for the Te-based compounds studied in the previous chapters, we observe a shift of the peaks of computed $S(q)$ towards smaller q values, which corresponds to an overestimate of the distances in our structures (as it was also noted in [41]). In Fig. 10.2, we compare our results with previously published calculations by Akola and Jones [39] on large size system (460 atoms) : the structure factors are almost similar, except that the first peak's heigth is slightly smaller in our calculations.

Evolution from the liquid to the amorphous phase It is interesting to examine the structure factor evolution when going from the liquid to the amorphous phase. The $S(q)$ for the amorphous is represented in Fig. 10.3 together with $S(q)$ at 1123 and 913 K from [69]. The peak heights are strongly increasing from liquid to amorphous phase, as

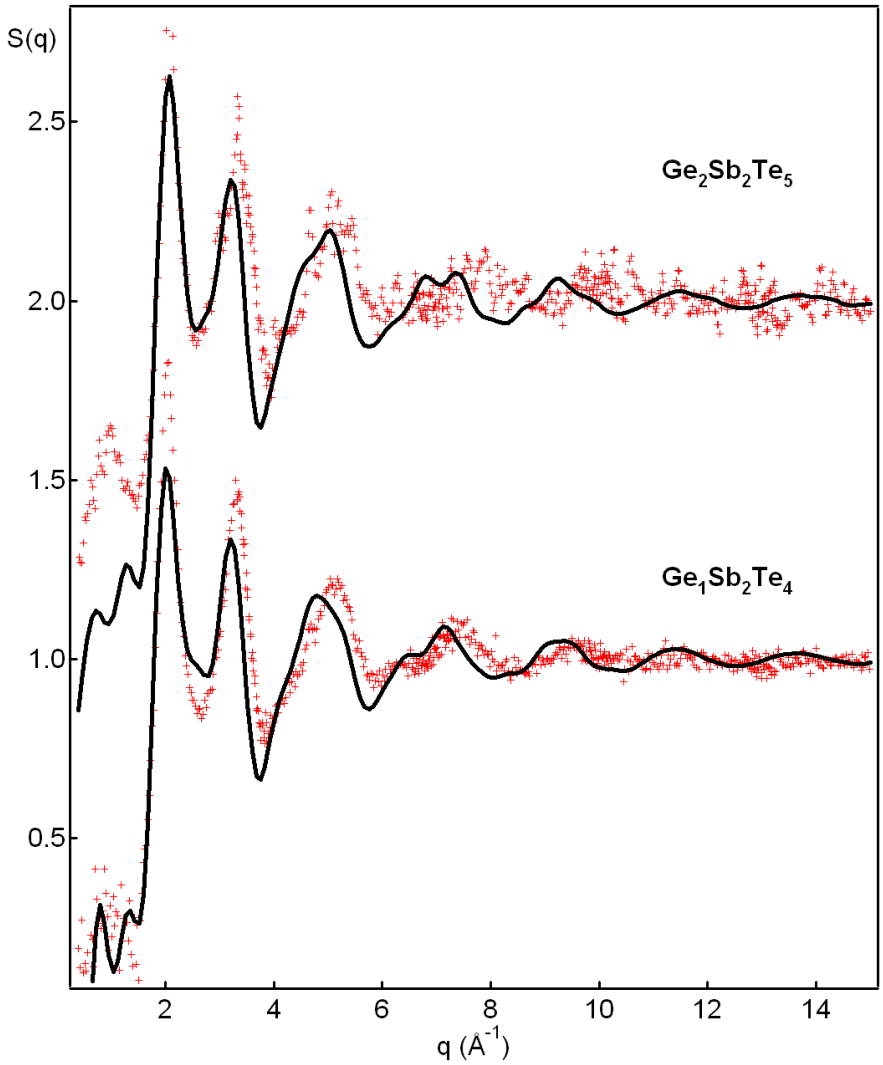

Figure 10.1: Experimental (red markers) and FPMD (black lines) neutron structure factors of amorphous $Ge_1Sb_2Te_4$ and $Ge_2Sb_2Te_5$.

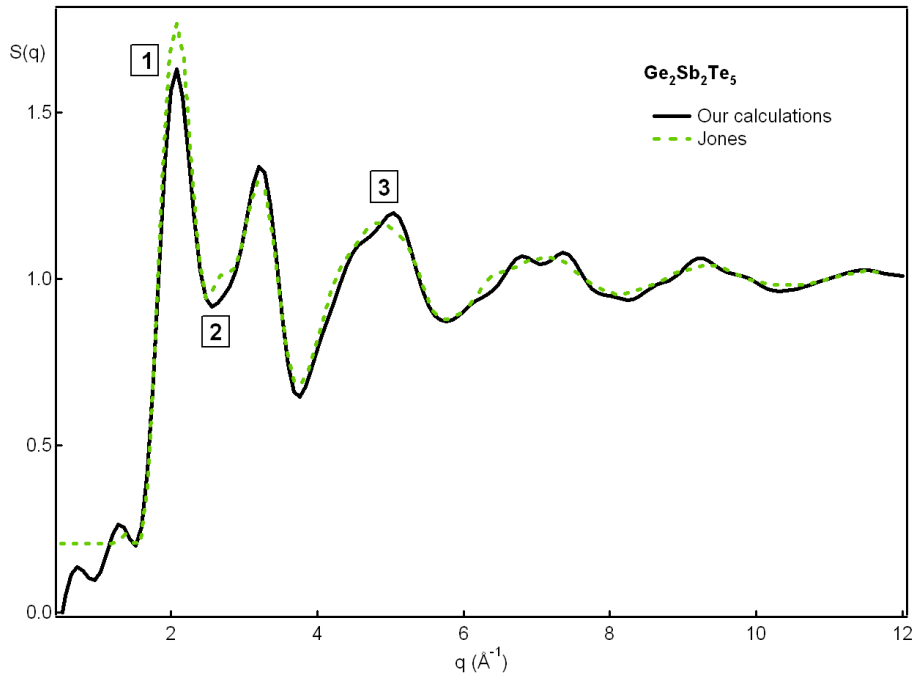

Figure 10.2: Structure factors from FPMD on $Ge_2Sb_2Te_5$ in amorphous phase. Our calculations: black lines. Jones' study [39]: green dotted line. If the first peak (1) is closer to the experiment in Jones' simulations, the absence of peak (2) and the asymmetry of peak (3) in our simulation are improvements over Jones' model.

expected. In particular, the first peak shoulder present at the higher temperature becomes a true peak in the amorphous. The peaks positions are also slightly evolving between both phases.

10.2.2 Pair correlation functions g(r)

The experimental and computed pair correlation functions, $g(r)$, are presented in Fig. 10.4 for both amorphous compounds. The positions of the first peaks are slightly larger in the simulation (2.89 and 2.86 Å for $Ge_1Sb_2Te_4$ and $Ge_2Sb_2Te_5$ respectively) than in the experiment (2.78 and 2.66 Å), especially in the $Ge_2Sb_2Te_5$ case, as predicted with $S(q)$ observation. The height of the first peak is larger in the computed $g(r)$ compared to the experiment, this could be at least partly explained by the noise encountered at high q values in the experiment. Despite these discrepancies on the first peak, the computed $g(r)$ are in relatively good agreement with the experimental ones (compared with results [39]).

10.2.3 Partial structure factors from FPMD simulations

The $GeTe$, $SbTe$ and $TeTe$ partial structure factors from FPMD simulations are plotted in Fig. 10.5 for $Ge_2Sb_2Te_5$, in the liquid and amorphous phases. We clearly observe a stronger ordering on the Te substructure of the amorphous phase in comparison with the liquid. This $Te-Te$ partial is responsible for the large first two peaks of the total S(q).

10.2.4 Partial coordination numbers

The partial pair correlation functions $g_{\alpha\beta}(r)$ (with $\alpha, \beta = Ge, Sb$ or Te) from the simulations are plotted for both compounds in Fig. 10.6. The main contributions to the first peak of total $g(r)$ come from the $GeTe$ and $SbTe$ partials. A non-negligible contribution is also arising from the $SbSb$ and, in a lower extent, $GeSb$ and $GeGe$ (at the shortest distances) partials. A few homopolar $TeTe$ bonds are also present. The second peak of total $g(r)$ is made of $GeGe$, $SbSb$, $GeSb$ and $TeTe$ contributions. From this, we can say that the structures we obtained for GST alloys in the amorphous state present strong similarities in local order (two first coordination shells) with the crystals, the heteropolar bonds being largely majority in the first coordination shell, with a few miscoordinated atoms (compared to the crystalline structures). The $GeTe$ and $SbTe$ bonds lengths (first maxima in the corresponding $g_{\alpha\beta}(r)$) are equal to 2.78 Å and 2.90 Å in the $Ge_1Sb_2Te_4$ and to 2.79 Å and 2.93 Å in the $Ge_2Sb_2Te_5$. They are similar to what was found in other FPMD studies [39, 47] and slightly larger than the distances measured by EXAFS (2.63 Å and 2.83 Å in $Ge_2Sb_2Te_5$ [42]).

The partial coordination numbers obtained from $g_{\alpha\beta}(r)$'s first peak integration (up to a cutoff distance equal to the minimum of total $g(r)$, i. e. 3.3 Å in $Ge_1Sb_2Te_4$ and 3.2 Å in $Ge_2Sb_2Te_5$, see Fig. 10.6) are listed, for both compound, in Table 10.1, in comparison with different experimental and simulations results.

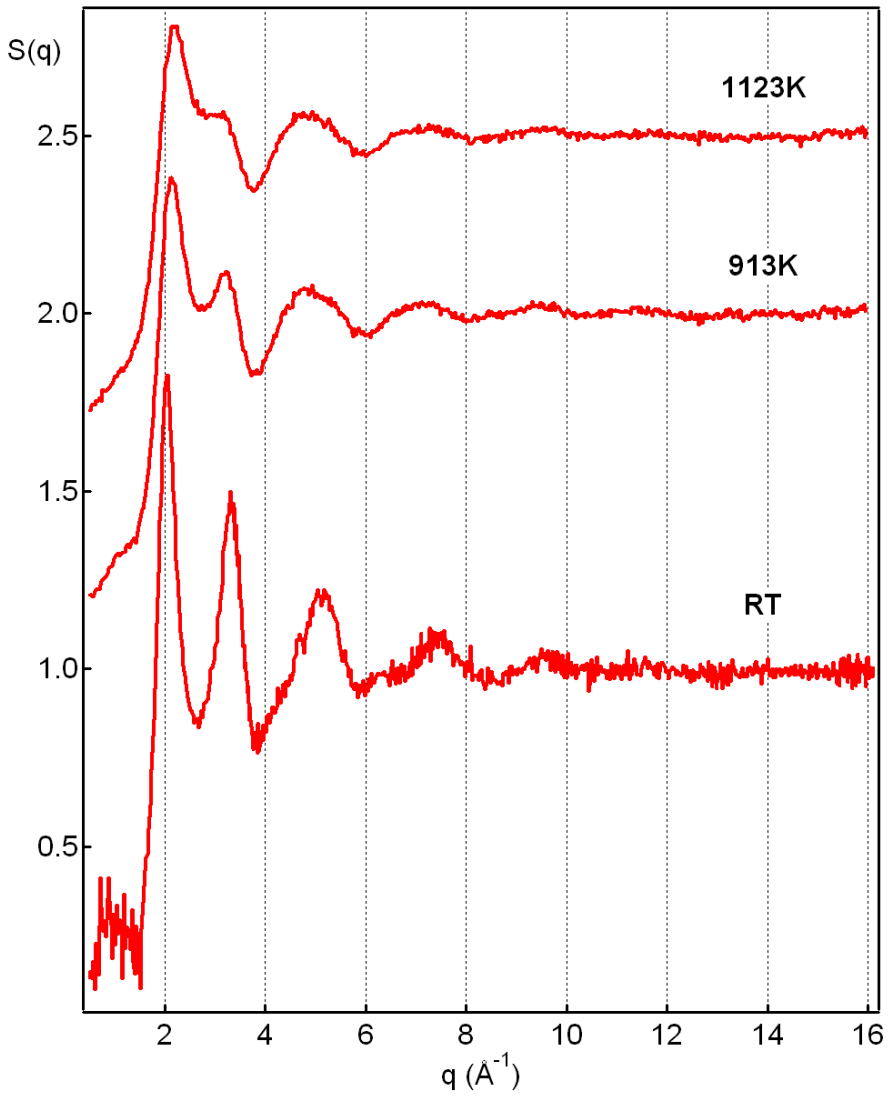

Figure 10.3: Experimental structure factors for the $Ge_1Sb_2Te_4$ compound (liquid phase : [69], amorphous phase : this study).

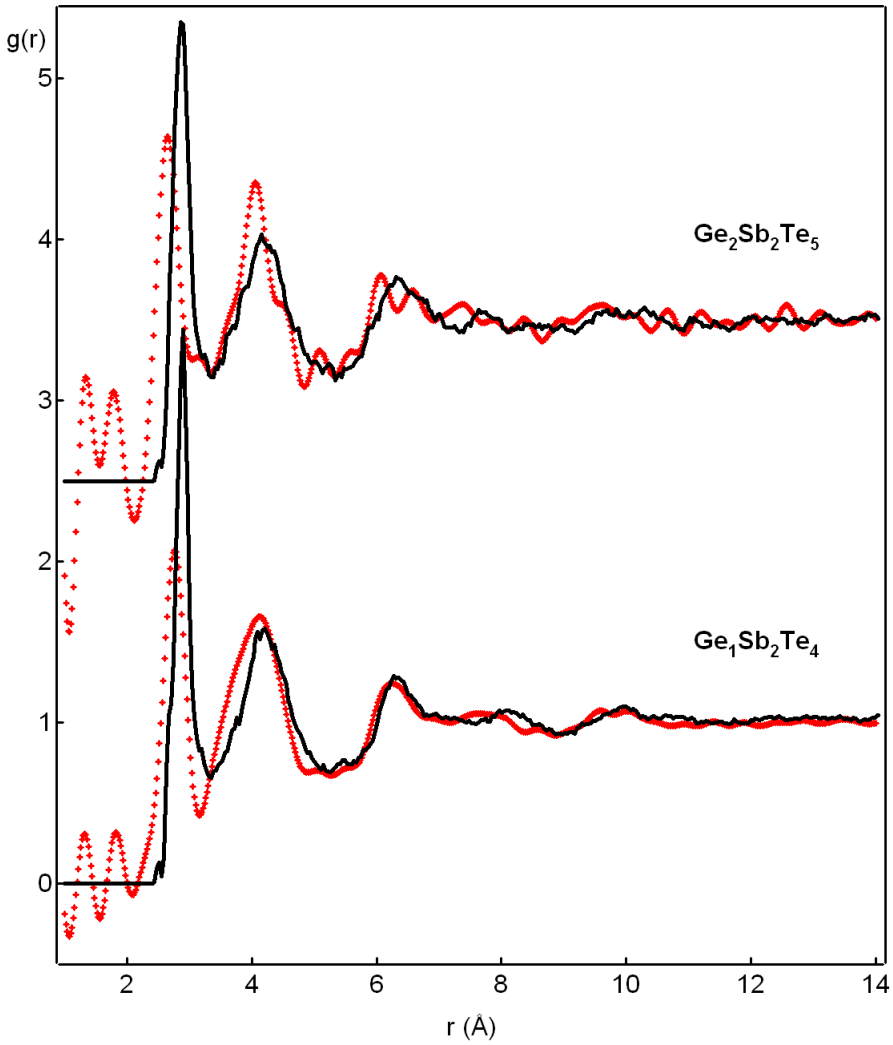

Figure 10.4: Pair correlation functions from experiment (red markers) and FPMD (black lines) in amorphous $Ge_1Sb_2Te_4$ and $Ge_2Sb_2Te_5$.

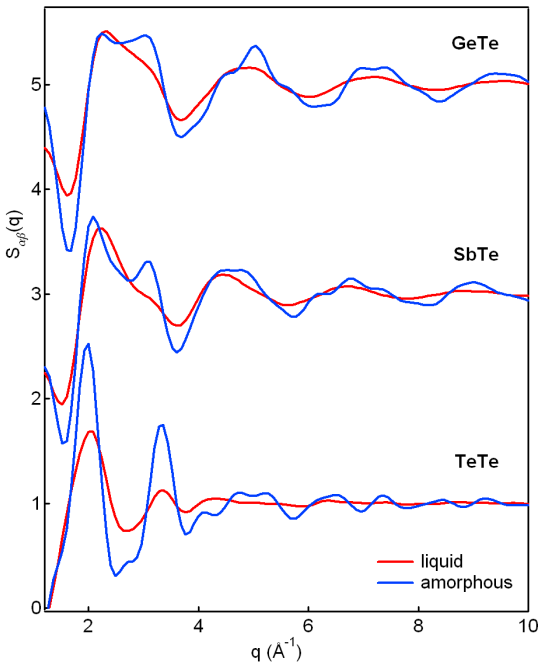

Figure 10.5: Partial structure factors from FPMD on $Ge_2Sb_2Te_5$ in liquid and amorphous phases (shifted by 3 for $SbTe$ and by 5 for $GeTe$). The $GeGe$, $GeSb$ and $SbSb$ structure factors are negligible.

$Ge_1Sb_2Te_4$											
Cent. atom	Ge	Sb	Te	Total	[73]		2 %	3 %	4 %	5 %	6 %
Ge	0.1(1)	0.2(4)	3.5(1)	3.8(6)	3.91		0	32	48	17	3
Sb	0.1(2)	0.7(2)	2.9(1)	3.7(5)	2.91		0	63	27	9	1
Te	0.8(8)	1.4(6)	0.4(2)	2.7(6)	1.98		47	46	7	0	0
$Ge_2Sb_2Te_5$											
Cent. atom	Ge	Sb	Te	Total	[42]	[39]	2 %	3 %	4 %	5 %	6 %
Ge	0.3(9)	0.3(5)	3.3(3)	4.0(7)	3.9±0.8	4.2	0	13	66	16	4
Sb	0.3(5)	0.6(1)	2.4(8)	3.4(4)	2.8±0.5	3.7	0	57	35	8	0
Te	1.3(3)	0.9(9)	0.3(2)	2.6(4)	2.4±0.8	2.9	37	55	8	0	0

Table 10.1: Partial and total coordination numbers compared with previously published data and analysis of the coordination distributions around each type of atom. Neighbors are defined by cutoff distance of 3.3 Å in $Ge_1Sb_2Te_4$ and 3.2 Å in $Ge_2Sb_2Te_5$.

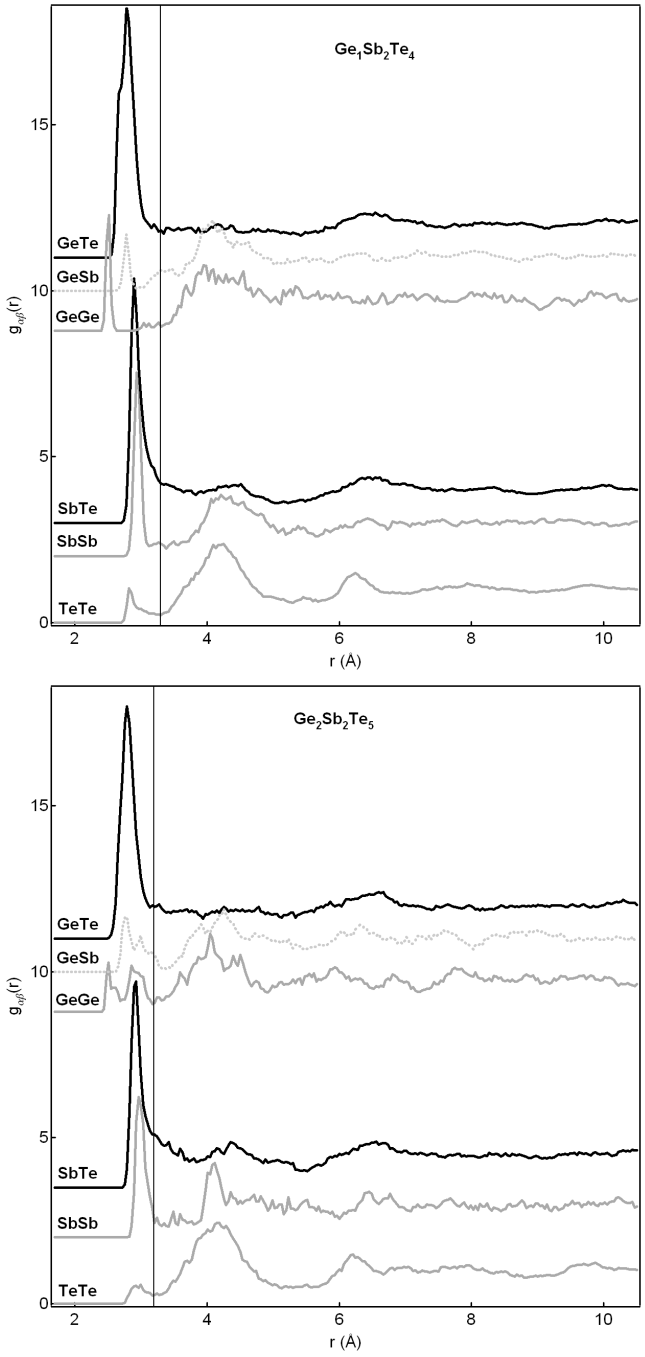

Figure 10.6: Partial pair correlation functions calculated from FPMD trajectories, for $Ge_1Sb_2Te_4$ (top) and $Ge_2Sb_2Te_5$ (bottom), shifted for clarity. The vertical black lines indicate the cutoff distances taken for the partial coordination numbers calculation.

The partial coordination numbers generally agree with those from [42], except for the partial coordination numbers that were not taken into account in the EXAFS analysis (since too small) and that are reported here. It is interesting to notice that Ge atoms are on average bonded to 3.4 Te atoms. The other neighbors consisting in almost equal proportions (~ 0.4) of Ge and Sb atoms in $Ge_2Sb_2Te_5$ and in 0.1(1) Ge and 0.2(4) Sb in $Ge_1Sb_2Te_4$. This total coordination, close to 4, is in agreement with the *umbrella flipping* model [36] and all previous computer simulations [39, 40]. However, a closer look at the atomic configurations will lead us to a different conclusion.

10.2.5 Distance distributions in FPMD structures

We calculated the distances distributions around each type of atom (see section 6.3.4 in Chapter 6 for definition) and averaged it over at least 4 ps of the run. (see Fig.10.7). These distance distributions confirm what was found previously with the partial coordination numbers : a splitting of the Ge ans Sb first neighbors shell into 3 shorter (well peaked), one intermediate (with a larger standard deviation) and 2 longer distances. The Te shell splits into 2 shorter, one intermediate and 3 longer distances.

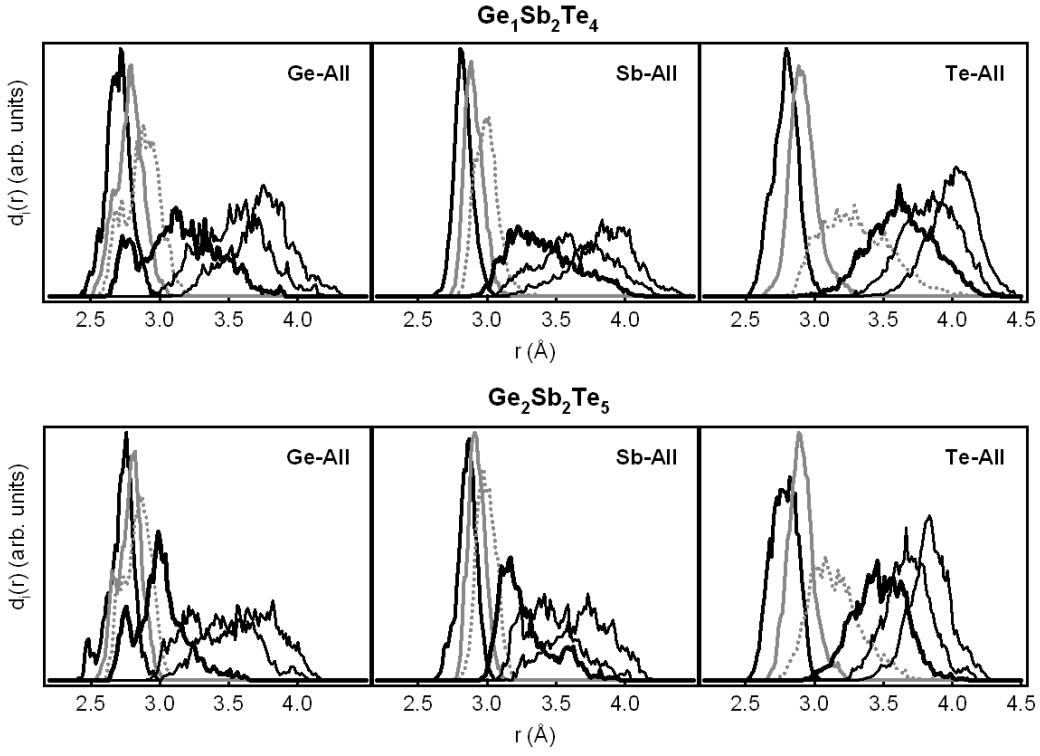

Figure 10.7: Six first distances distributions around Ge, Sb or Te atoms (*All* means no chemical discrimination of the neighbors) for amorphous $Ge_1Sb_2Te_4$ and $Ge_2Sb_2Te_5$.

Distance distribution around Ge atoms The $d_4(r)$ distribution of neighbors around Ge atoms is very unusual : it is, for both compounds, split in two parts (two distinct peaks are present). This could indicate the existence of two different types of Ge atoms environments.

To test this hypothesis, we decompose the population of Ge atoms by counting the number of neighbors at distances smaller than 2.85 Å in $Ge_1Sb_2Te_4$ and 2.81 Å in $Ge_2Sb_2Te_5$, which are the locations of the minima that separate the two peaks in distribution $d_4(r)$. It appears clearly in Fig. 10.8 that the 4 first neighbors' distributions around Ge atoms consist of two independent components (peaks). The short-distance sub-peak belongs to 4-fold bonded atoms (respectively 17 % and 16 % of the Ge atoms in the $Ge_1Sb_2Te_4$ and $Ge_2Sb_2Te_5$ structures are in this case) and the second sub-peak belongs to atoms with a coordination number of 3 (the remaining Ge atoms). These two types of Ge atoms will be referred to as Ge^3 and Ge^4 in the following.

10.2.6 Bond angle distributions

Partial bond angle distributions around each kind of atom in the amorphous structures are displayed in Fig. 10.9. They were calculated including the six first neighbors around each atom. For clarity, we plotted separately the 6 angles between the 4 first neighbors (that are well peaked) and the remaining angles (more flat). Around Te atoms, in both alloys, the angles between first neighbors (named 102, 103, 203) are peaked around the value of 90°(for some, a second peak is present, at 180°). The other angles (104, 204, 304 and others) are more flat but still exhibit a peak around 180°, which is an indication of an octahedral local order. Around Sb and Ge, the situation is very similar, the angles between first neighbors being however peaked around larger angle (around 95°), particularly in the case of $Ge_1Sb_2Te_4$.

Since the *umbrella flipping* model assumes a change of the first coordination shell of Ge atoms from octahedral to tetrahedral upon switching from crystalline to amorphous phase, we focused on Ge atoms and analyzed in details the Ge bonds angles. Because of the differences observed in the distances distributions, we made a separate analysis of the 3-fold and the 4-fold bonded Ge atoms, for both compounds (see Fig. 10.10).

In both compounds, for the 3-fold bonded Ge, we found bond angle distribution peaked around 95°, close to what found around Sb atoms (90-95°). It appears that the 4-fould Ge show very different bond angle distribution, with a maximum around 109°.

Moreover, in the bond angle distributions related to the 3-fold Ge atoms in both compounds, although the 4th neighbour is more loosely defined (broader 4th distribution), its bond angles with the first 3 neighbors is also peaked around 90°(plus some contributions in the large angle range, i.e. 130-180°).

Table 10.1 shows that most of the Ge atoms from the first coordination shell are four-fold coordinated in our structures (respectively 48 % and 66 % in $Ge_1Sb_2Te_4$ and $Ge_2Sb_2Te_5$).

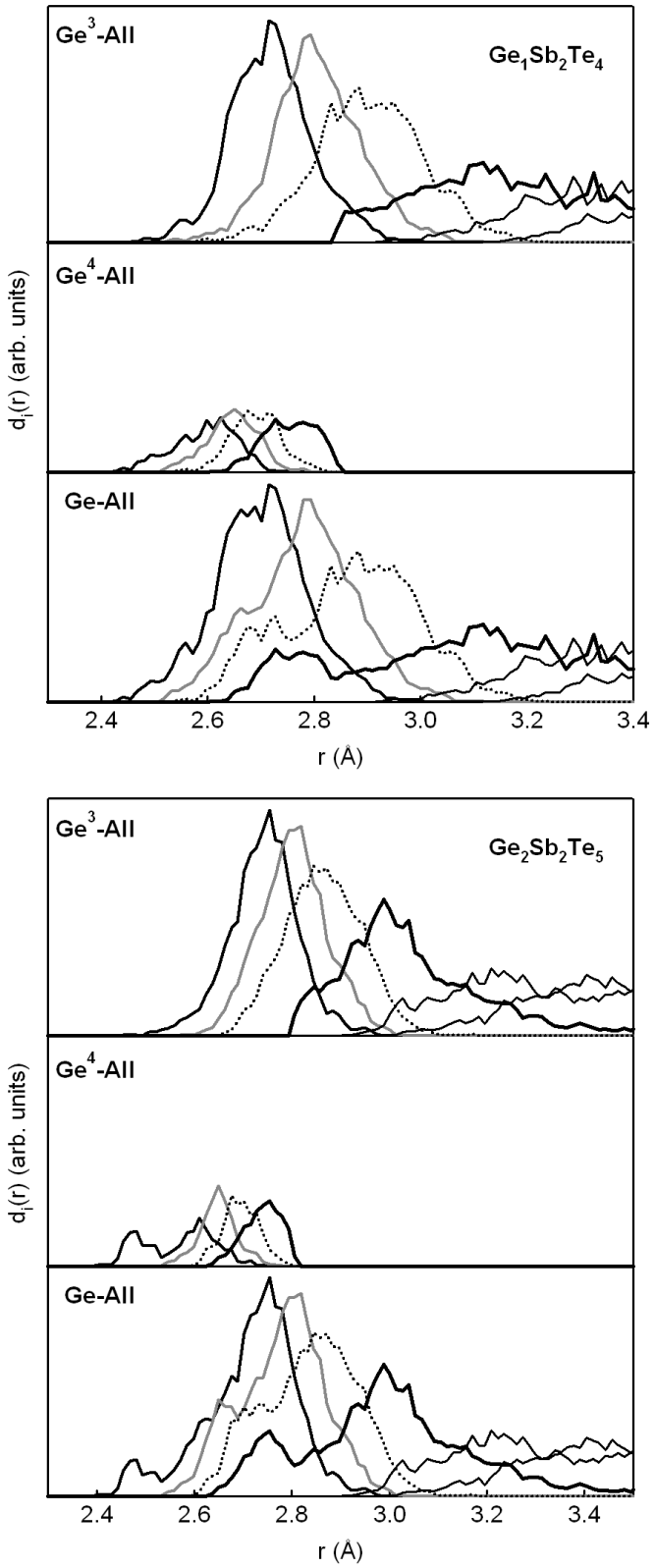

Figure 10.8: Six first distributions of neighbors around Ge atoms in amorphous $Ge_1Sb_2Te_4$ and $Ge_2Sb_2Te_5$. Decomposition into contributions due to the four-fold coordinated Ge (Ge^4) and the three-fold coordinated Ge (Ge^3).

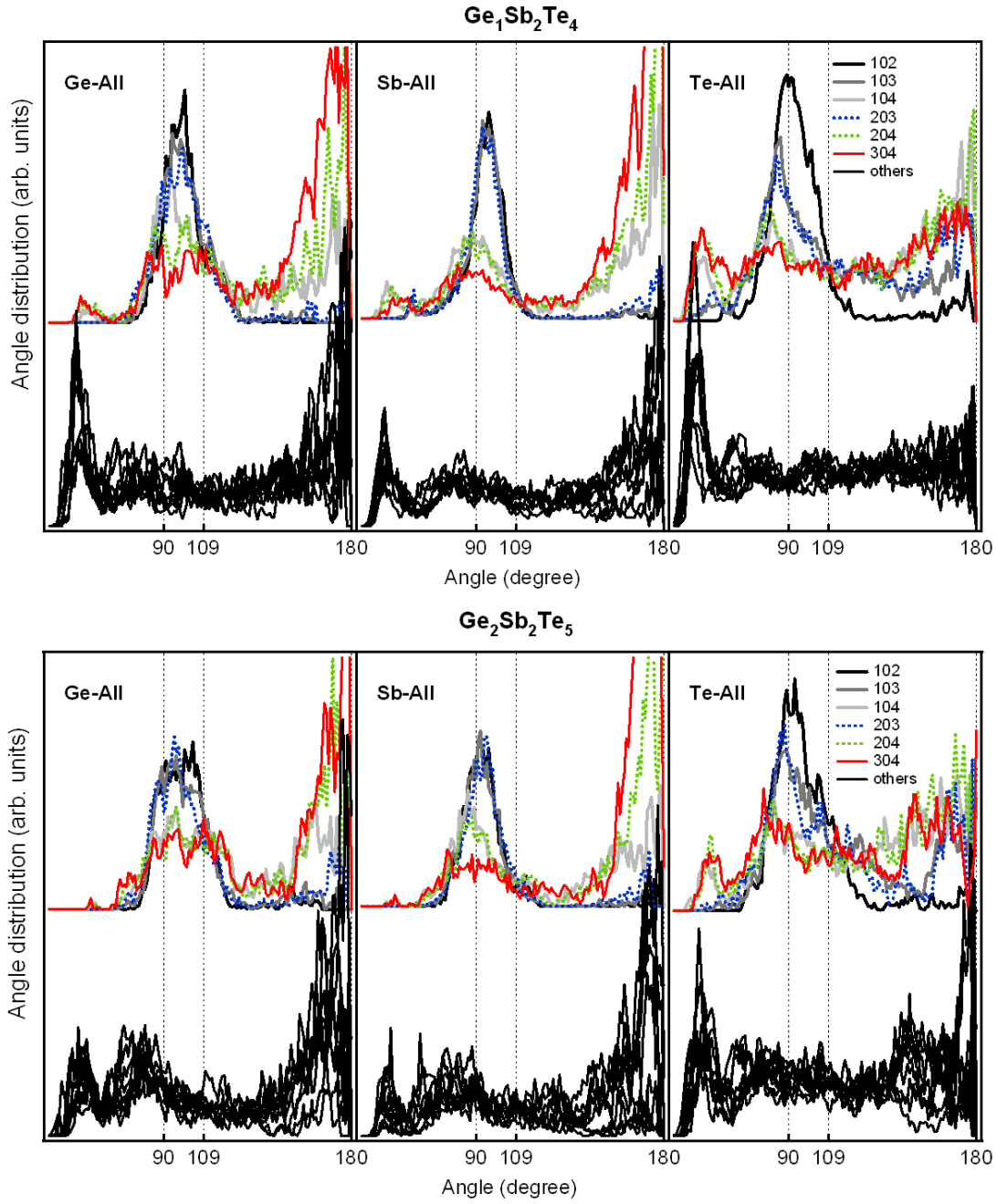

Figure 10.9: Partial bond angles distributions around Ge, Sb and Te atoms in amorphous $Ge_1Sb_2Te_4$ and $Ge_2Sb_2Te_5$.

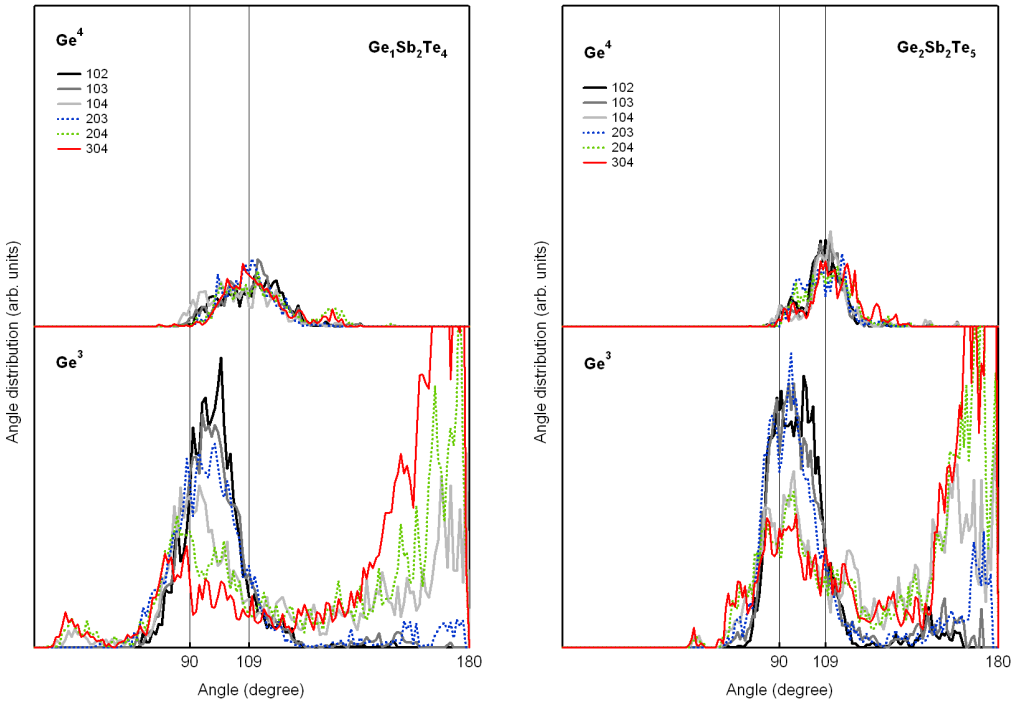

Figure 10.10: Partial bond angles distributions around Ge, for Ge^3 and Ge^4 type of atoms separately, in amorphous $Ge_1Sb_2Te_4$ and $Ge_2Sb_2Te_5$.

Only a small fraction of these four-fold coordinated Ge are tetrahedrally coordinated, the remaining atoms having four neighbors forming a local structure close to that of high pressure monoclinic crystalline Se or Te [179, 180] (see Fig. 10.11).

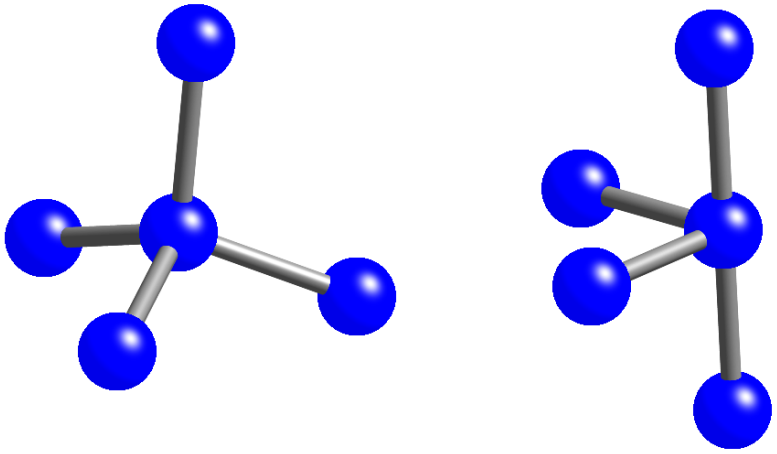

Figure 10.11: The two observed environment for Ge atoms in our amorphous : tetrahedral, in a small fraction (left), and similar to high pressure Te (right).

We also analyzed the bond angle distribution around Ge atoms by discriminating their chemical environment. Considering the six first neighbors of a central Ge atom, we displayed in Fig. 10.12 the statistics of $X\widehat{GeX}$ and $X\widehat{GeTe}$ angles ($X = Ge$ or Sb), the miscoordinated atoms compared to the crystalline structures, and $Te\widehat{GeTe}$. In each case, we discriminated between the Ge^3 and Ge^4 type of atom.

In both compounds, we see that the contribution of the $Te\widehat{GeTe}$ angles is, as expected, largely dominant. The Ge^3 atoms distributions are centered around 90-95° and 180°, while the Ge^4 atoms contribution is centered on 109°. This is also true for the $X\widehat{GeTe}$ angle distribution in the $Ge_2Sb_2Te_5$ (in the other distributions, it is difficult to conclude because of the lack of statistic). About 50 % of the tetrahedrally bonded Ge atoms exhibit wrong bonds in $Ge_2Sb_2Te_5$.

Our model amorphous $Ge_1Sb_2Te_4$ and $Ge_2Sb_2Te_5$ structures are rather similar to those obtained for the other studies on the $Ge_2Sb_2Te_5$, although the tetrahedrally bonded Ge atoms are present in a proportion of 17 % and 16 % here (for $Ge_1Sb_2Te_4$ and $Ge_2Sb_2Te_5$ respectively), against 33 % and 34 % in [40, 39]. There is a high degree of chemical ordering, the main defects being due to $SbSb$ bonds which are not present in the crystal.

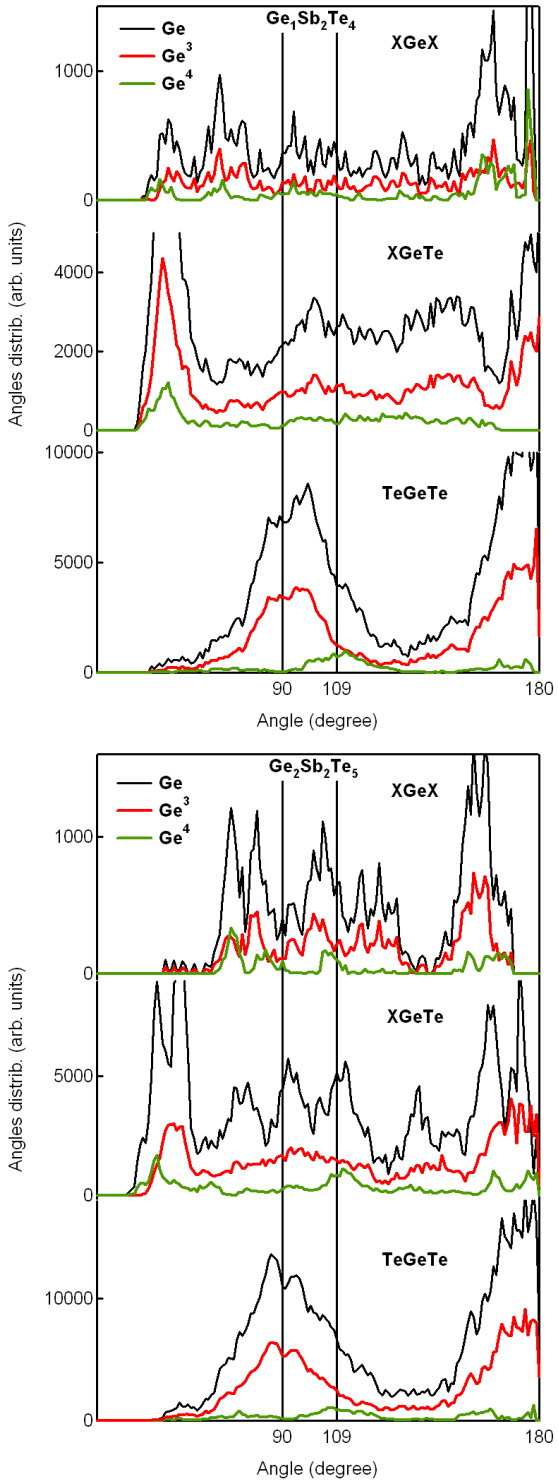

Figure 10.12: Partial bond angles distributions around Ge, for Ge^3 and Ge^4 type of atoms separately, in amorphous $Ge_1Sb_2Te_4$ and $Ge_2Sb_2Te_5$.

Except for the small amount of tetrahedral Ge, the bond angle distributions in amorphous $Ge_1Sb_2Te_4$ and $Ge_2Sb_2Te_5$ display characteristics of a covalently $p-$bonded system, with coordination numbers between 3 and 4 for Ge and Sb and between 2 and 3 for Te.

10.2.7 Three-Body Correlations

In our model, the connectivity of the Ge^3 atoms, as well as that of Sb atoms, is very similar to the GST cubic crystal case, and to the $GeTe$ A7 structure [86], with 3 first neighbors bonded at $\sim 90°$ angles. In this structure, however, the coordination is rather 3+3, as the first shell can be viewed as a distorted octahedron, with three first neighbors at 2.84 Å and three others at 3.15 Å (at 300 K, [83]). It is well know that this structure is, as in the case of the elemental As counterpart, stabilized by a Peierls distortion, which opens a gap at the Fermi level by breaking the cubic symmetry and doubling the periodicity of the cell (see Chapter 2). It has been shown [24] that a similar Peierls distortion can stabilise non-crystalline structures, amorphous and even liquids [23, 94], by locally doubling the periodicity and thus locally alternating shorter and longer bonds.

This hypothesis can be verified from the three body correlation functions analysis (see Fig. 10.13 and 10.14).

Depending on the angle between the bonds, the type of correlation differs. For tetrahedrally bonded Ge atoms (Ge^4 type), correlations have been checked for angle values in the range of $109 \pm 10°$ and are maximal for bonds of equal length 2.67 ± 0.05 Å. For 3-fold bonded atoms (Ge^3 type), the correlation is maximal for a succession of bonds with lengths 2.94 Å and 3.20 Å in $Ge_1Sb_2Te_4$ (2.88 Å and 3.04 Å in $Ge_2Sb_2Te_5$), which are close to the $GeTe$ crystal bond lengths (2.84 Å and 3.15 Å, respectively). The structure can thus be seen as a mix of almost perfectly tetrahedral Ge atoms and of Ge atoms that are bonded as in the $GeTe$ crystal, with some short-long alternation.

This differs from the results of Akola and Jones [39], in which no short-long correlation exist in their amorphous $Ge_2Sb_2Te_5$ model, with a dominant correlation between bonds of equal length (~ 2.8 Å), but this is in line with the recent model proposed by Robertson [77] for the amorphous PCM.

10.3 Electronic properties of the *GeSbTe* alloys

In the case of phase-change material, it is important to determine how the structural features translate into the electronic properties, as different explanations have been stated in previous works [36, 181, 40, 39, 77] (see Chapter 1).

10.3.1 Electronic densities of states EDOS

The total electronic densities of states (EDOS) and the projections onto the different kinds of atoms (calculated at the Γ point only) are plotted in Fig. 10.15. The gap is 0.45

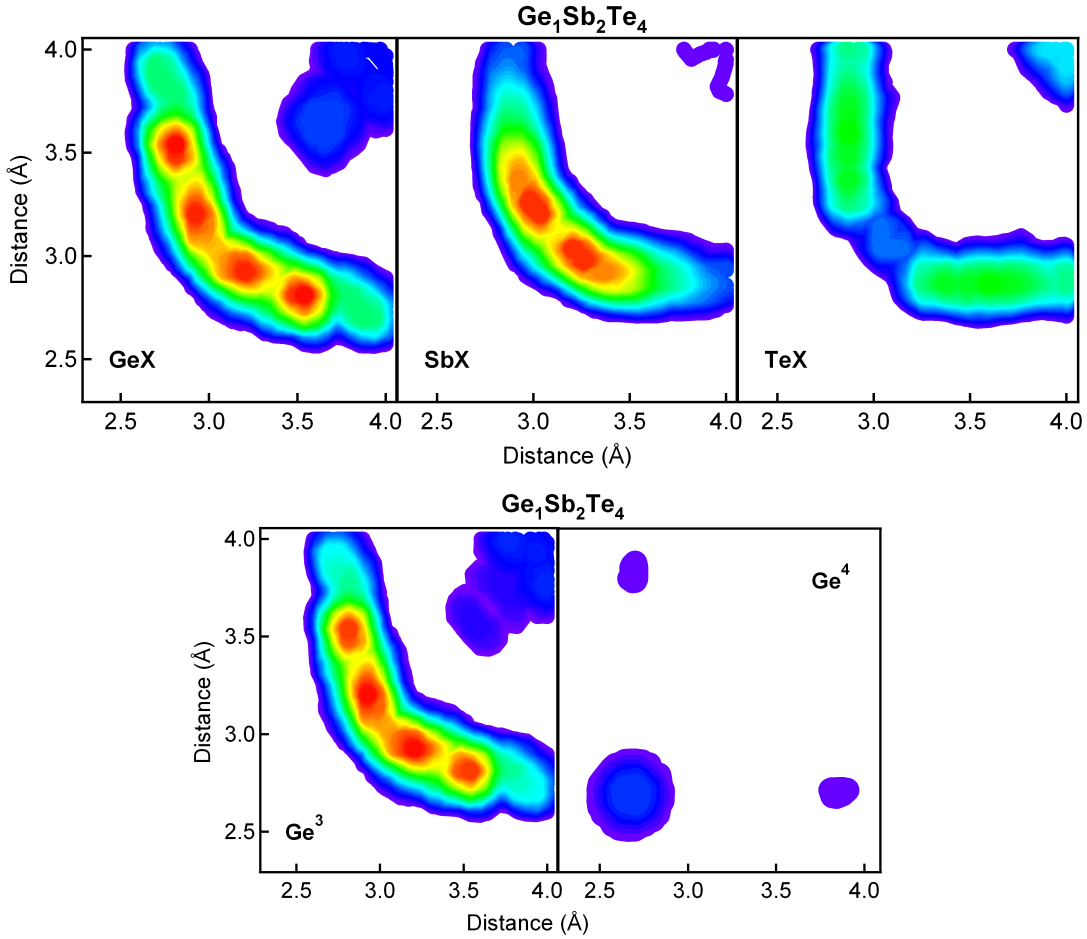

Figure 10.13: Three bodies correlation functions for central Ge, Sb or Te (top panel) and for Ge^3 and Ge^4 type of atoms separately (bottom panel), in amorphous $Ge_1Sb_2Te_4$.

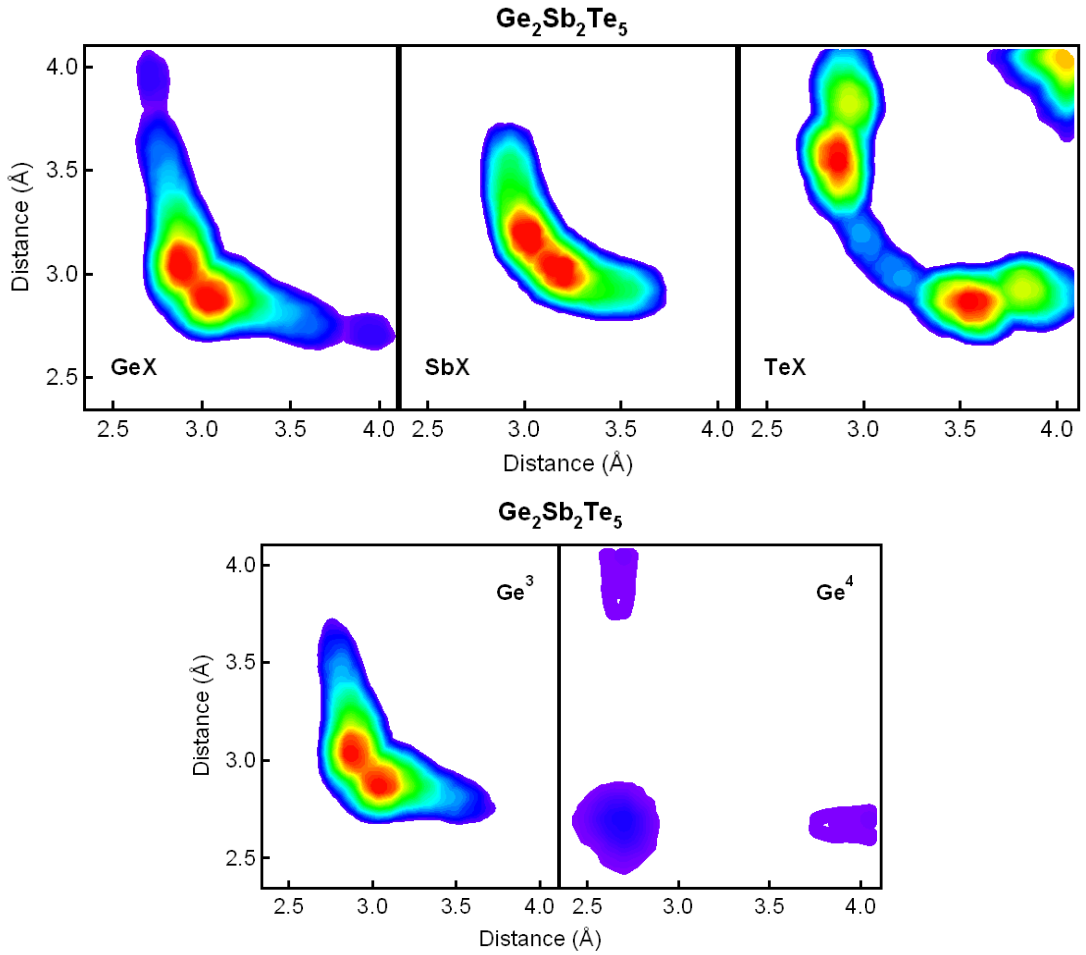

Figure 10.14: Three bodies correlation functions for central Ge, Sb or Te (top panel) and for Ge^3 and Ge^4 type of atoms separately (bottom panel), in amorphous $Ge_2Sb_2Te_5$.

eV (0.25 eV) wide in the amorphous $Ge_1Sb_2Te_4$ ($Ge_2Sb_2Te_5$). The gap value was found to be 0.19 eV for the amorphous $Ge_2Sb_2Te_5$ in the simulations [39]. These values are smaller than the experimental value (0.7 eV in $Ge_2Sb_2Te_5$ [173]) as expected for DFT-GGA calculations.

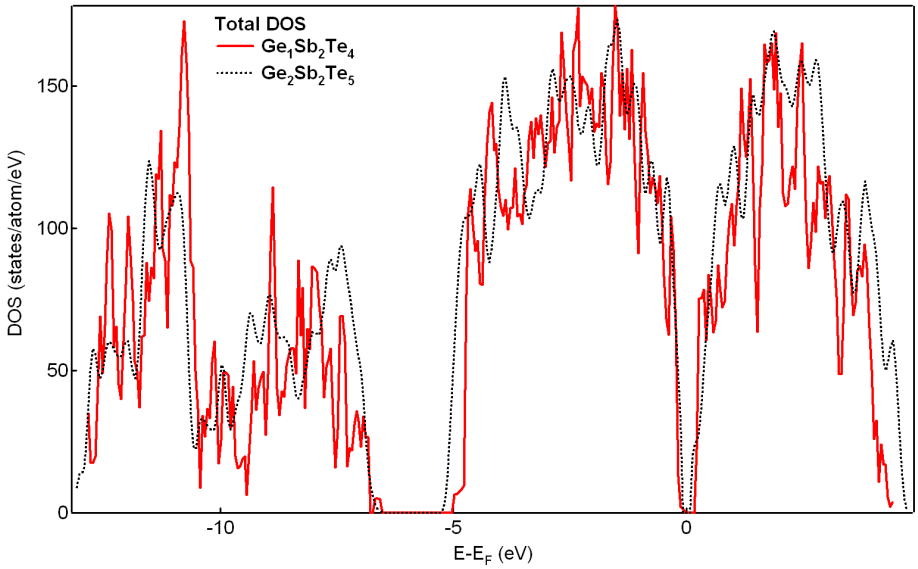

Figure 10.15: Total electronic densities of states in amorphous $Ge_1Sb_2Te_4$ and $Ge_2Sb_2Te_5$.

As the Ge atoms can be sorted in tetrahedral and octahedral environments, we projected separately the density of states onto the two kinds of atoms and present the partial DOS in Fig. 10.16. We first observe that both kind of Ge atoms have local DOSs with the same gap width. The global shape of the valence DOS is however modified for the Ge^4 type of atoms, as there is a depletion in the p-DOS in a 2 eV range below the Fermi level. We also note a transfer from a portion of s-states above the Fermi level for these atoms, as it is a consequence of a shift towards a sp^3 hybridization. So we cannot conclude that the sp^3 hybridization is the reason for the increase of the gap in the amorphous in comparison with the p-bonded crystal.

10.3.2 Conductivities

Coherently with the electronic DOS here above, the d.c. conductivities computed through the Kubo-Greenwood formula [163, 164] have a zero value (see Fig. 10.17), comparable to the experimental measurements [37]. The maximal conductivity is reached between 2.5 and 3 eV, vs $\sim$ 2.8 eV for the experiment in [181], which ensures a proper optical contrast.

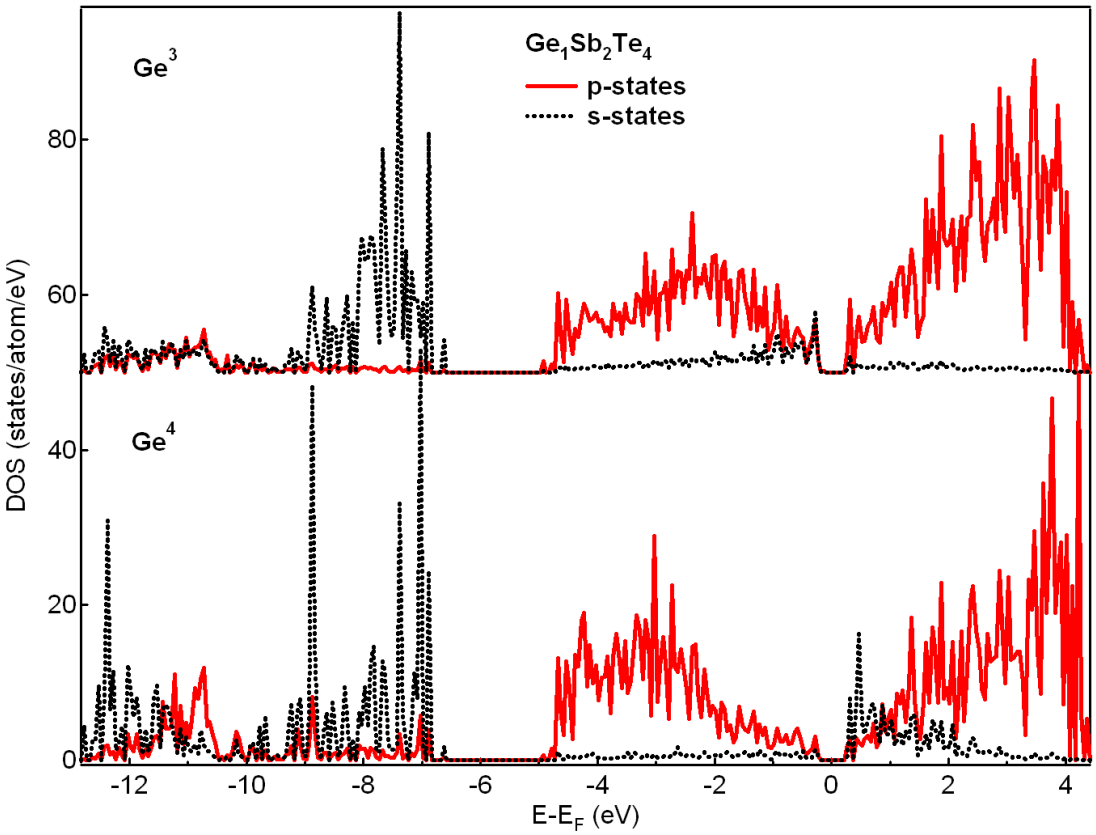

Figure 10.16: Partial electronic densities of states in amorphous $Ge_1Sb_2Te_4$: p-PDOS (solid red lines) and s-PDOS (dotted black line), calculated on the Ge^3 (octahedral, shifted by 50 for clarity) and Ge^4 (tetrahedral) sites.

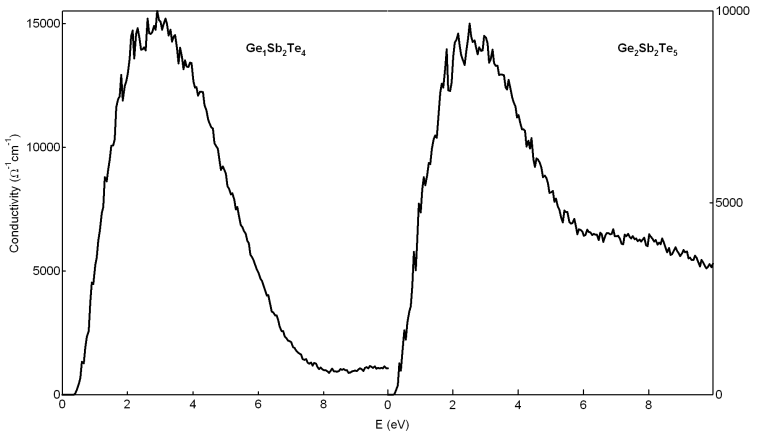

Figure 10.17: Optical conductivity curves for amorphous $Ge_1Sb_2Te_4$ and $Ge_2Sb_2Te_5$. The zero energy value gives the electrical conductivity.

10.4 Conclusion

Using ab initio molecular dynamics simulations, we have constructed a model for two phase change materials in the amorphous phase. Their structures have a generally cubic topology, as in the amorphous $Ge_2Sb_2Te_5$ from FPMD in [39, 74], but include only around 16 % of perfectly tetrahedrally bonded Ge atoms. The remaining atoms belong to Peierls distorted octahedral environments, as in crystalline and liquid $GeTe$, in agreement with the model suggested recently by Huang and Robertson [77]. The sp^3 hybridization of the tetrahedrally bonded atoms has no effect on the electronic gap, which is intrinsic to the system and is rather ionic in nature.

Chapter 11

The amorphous Phase-Change Materials from the view point of Maxwell rigidity

In this thesis, we have described the structural and electronic properties of several $GeSbTe$ PCM, and evidenced many common features. However, these are not compatible with the belief, used among else for guiding the EXAFS analysis from Baker et al. [42], that GST's are perfect glasses. In the following, we will establish a new method to unambiguously count the constraints in a material and make used of the Maxwell rigidity theory to quantify the GST amorphous glassy nature via their mechanical properties.

The rigidity theory offers a practical computational scheme using topology, namely the Maxwell counting procedure, and has been central to many contemporary investigations on non-crystalline solids, such as sulphur and selenium based amorphous networks [32, 33]. It has led to the recognition of a rigidity transition [34, 35] which separates *flexible glasses*, having internal degrees of freedom that allow for local deformations, from *stressed rigid glasses* which are 'locked' by their high bond connectivity. Mathematically, this transition is reached when the number of mechanical constraints per atom equals the number of degrees of freedom, that is 3 in three dimensions. What happens with heavier elements, such as tellurium, which would lead to more complicated local structures, as highlighted both from experiments [36, 37] and simulations [38, 39, 40, 41] ? Does the counting procedure still hold ? Attempts in this direction have been made on the basis of EXAFS measurements [42] but they seem to contrast with experimental findings and observations. A firm ground for the Maxwell constraint counting is therefore very much desirable. In this section, a precise enumeration of the constraints arising from bond-stretching (BS) and bond-bending (BB) interactions is developped, based on the analysis of atomic scale trajectories from First Principles Molecular Dynamics Simulations (FPMD). Combined with rigidity theory, this opens an interesting perspective to study amorphous phase change materials in much the same way as network glasses.

11.1 Estimate of constraints : General setting

At the heart of the rigidity concept is the identification of relevant interatomic forces between atoms in a manner similar to what Maxwell pioneered for trusses and macroscopic structures [182]. In mechanical engineering, the stability of such structures depends on the balance between forces acting on the node of a truss (i.e. the number of bar tensions connecting the node, that is the number of Lagrangian constraints [183]) and its number of degrees of freedom. When applied to covalent amorphous networks and once the forces acting as constraints are identified (BS and BB forces), a similar analysis can be performed leading to the Phillips-Thorpe rigidity transition [34], which separates flexible (underconstrained) networks from stressed rigid (overconstrained) networks [32, 33]. At the transition, the low frequency (floppy) modes, which represent the internal degrees of freedom permitting local deformations of the network, vanish [34].

As in standard mechanics however, instead of treating forces and querying about motion, one can ask the opposite question and try to relate motion to the absence of a restoring force. We apply this structural analysis in relation with rigidity theory on the FPMD structure obtained in the previous chapters of this work.

11.1.1 Neighbor distributions

In the compounds studied during this thesis, we are dealing with octahedral and tetrahedral environments around each atom in a given structure. We will thus consider the six first neighbors i, that are sorted according to their distance, and analyze the distribution $d_i(r)$ of these distances (see Chapter 6 section 6.3.4 for definition), the sum of which yields the pair correlation function $g(r)$.

The actual number of neighbors N_c, and hence the number of BS constraints, is calculated here by integrating the radial distribution function up to its first minimum (see Eq. 4.28 in Chapter 4). According to the constraint enumeration, one has $N_c/2$ BS constraints for a N_c-coordinated atom [34].

11.1.2 Partial bond angle distributions

To estimate the number of BB constraints we analyze the partial bond angle distributions, $\mathrm{P}(\theta_{ij})$, as defined in the Chapter 6 section 6.3.5. For each type of central atom 0, we have partial bond angle distributions for each of the 15 angles $\widehat{i0j}$ corresponding to the six first neighbors (with $i = 1, ..., 5$ and $j = 2, ..6$, $i \neq j$).

The standard deviation $\sigma_{\theta_{ij}}$ (or second moment) of $\mathrm{P}(\theta_{ij})$ provides a quantitative estimate of the angular excursion around the mean value $\bar{\theta}_{ij}$ of angle $\widehat{i0j}$, thus measuring the strength of the bond-bending restoring force. An angle displaying a wide $\sigma_{\theta_{ij}}$ corresponds to a broken BB constraint as there is a weak interaction to maintain the angle fixed. In an opposite way, sharp bond angle distributions lead to intact constraints. This way of

analyzing the results of FPMD simulations will provide a firm basis for the enumeration of BS and BB constraints in complex materials.

11.2 The simple case of $GeSe_2$

In order to check this method, we first apply it to the benchmark case $GeSe_2$, for which application of constraint counting algorithms is straightforward [34].

11.2.1 Constraints from experiment and rigidity theory

According to the Phillips-Thorpe enumeration [34, 35], one has for a N_c-coordinated atom:

- $C_{BS} = N_c/2$ bond stretching (BS) constraints.
- $C_{BB} = 2N_c - 3$ bond bending (BB) constraints.

Thus a four-fold Ge atom has 2 BS and 5 BB constraints whereas the two-fold selenium atom has 1 BS and 1 BB constraint leading to an overall number of constraints per atom equal to 3.67 [34, 35].

11.2.2 Constraints from FPMD structures

We have computed the Ge and Se centered pair distribution functions and the neighbor distributions (Fig. 11.1). These pair distribution functions reproduce very well the experimental data from Salmon and co-workers [184]. It can be clearly seen from Fig. 11.1 that Ge (Se) has 4 (2) neighbors contributing to the first peak, well separated from the other neighbors. Integration of the first peak up to the minimum at 2.75 Å (2.78 Å for Se) leads to similar values equal to 4.01 and 1.97 for Ge and Se respectively. Since the number of bond-stretching (BS) constraints is equal to $N_c/2$, it leads to a respective number of BS constraints of 2 and 1 for Ge and Se atoms.

We see in Fig. 11.2 that $\sigma_{\theta_{ij}}$ of $\mathrm{P}(\theta_{ij})$ vary between 10° and 40° around Ge or Se atoms, depending on the different angles $\widehat{i0j}$ considered. For the $Ge-$centered atoms, six standard deviations $\sigma_{\theta_{ij}}$ are found to be of the order of $10 - 15°$, clearly separated from all others for which $\sigma_{\theta_{ij}} \simeq 40°$. The gap between $10 - 15°$and 40° present in the $\sigma_{\theta_{ij}}$ allows to separate angles into those which are relevant for rigidity purposes (and act as rigid constraints), from those which are flexible (and lead to broken constraints). However there is one redundant constraint that needs to be removed because it can be determined from the five other angles. This leaves the estimate with 5 independent BB constraints for the Ge atom. For the Se atom, a single low $\sigma_{\theta_{ij}} = 12°$ (i.e. a single BB constraint) is found around the mean value $\bar{\theta}_{ij} = 100°$, in agreement with experiment [185].

We thus show that the constraints computation from FPMD matches exactly the direct counting from Ref. [34, 35].

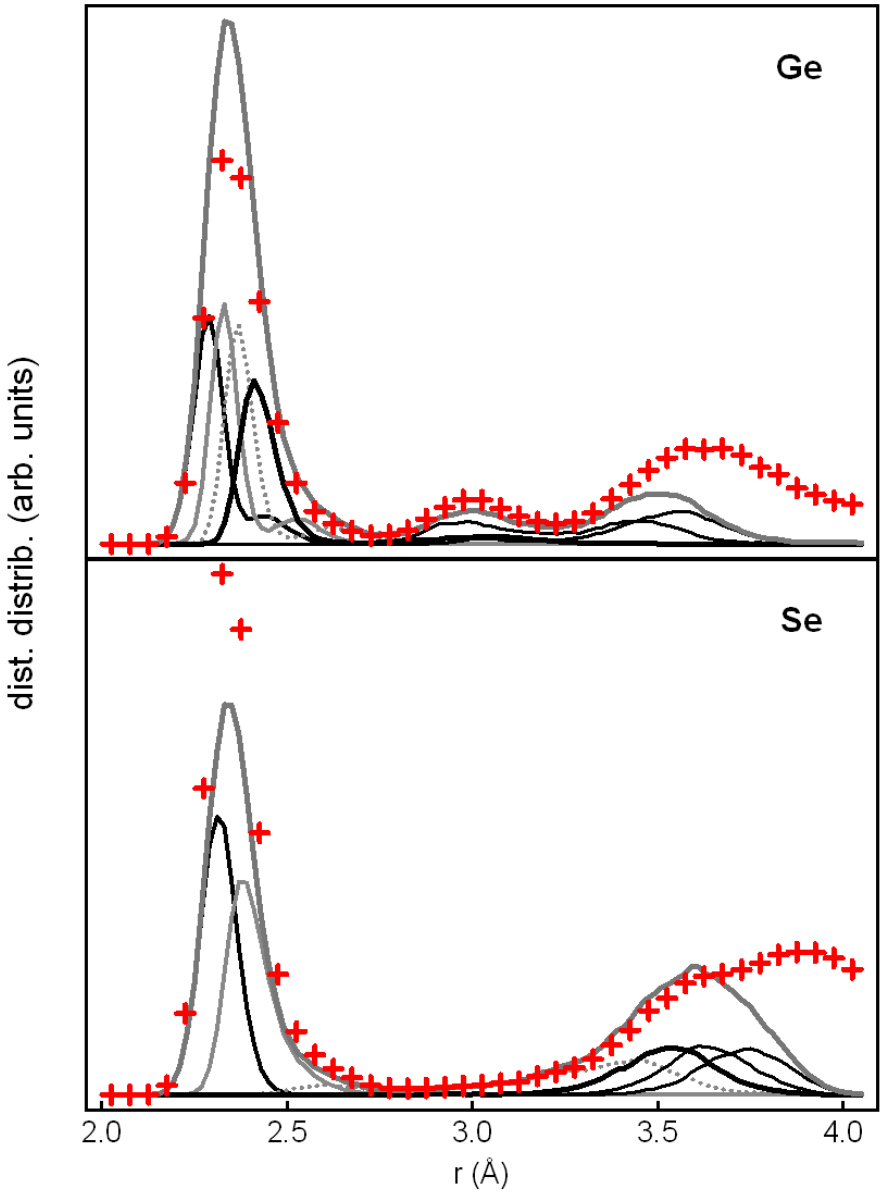

Figure 11.1: Experimental *Ge* and *Se*−centered (in top and bottom panel respectively) pair distribution function (red markers, data from Petri et al. [184]) together with the 6 first distributions of neighbors and total, around *Ge* and *Se* atoms, from FPMD.

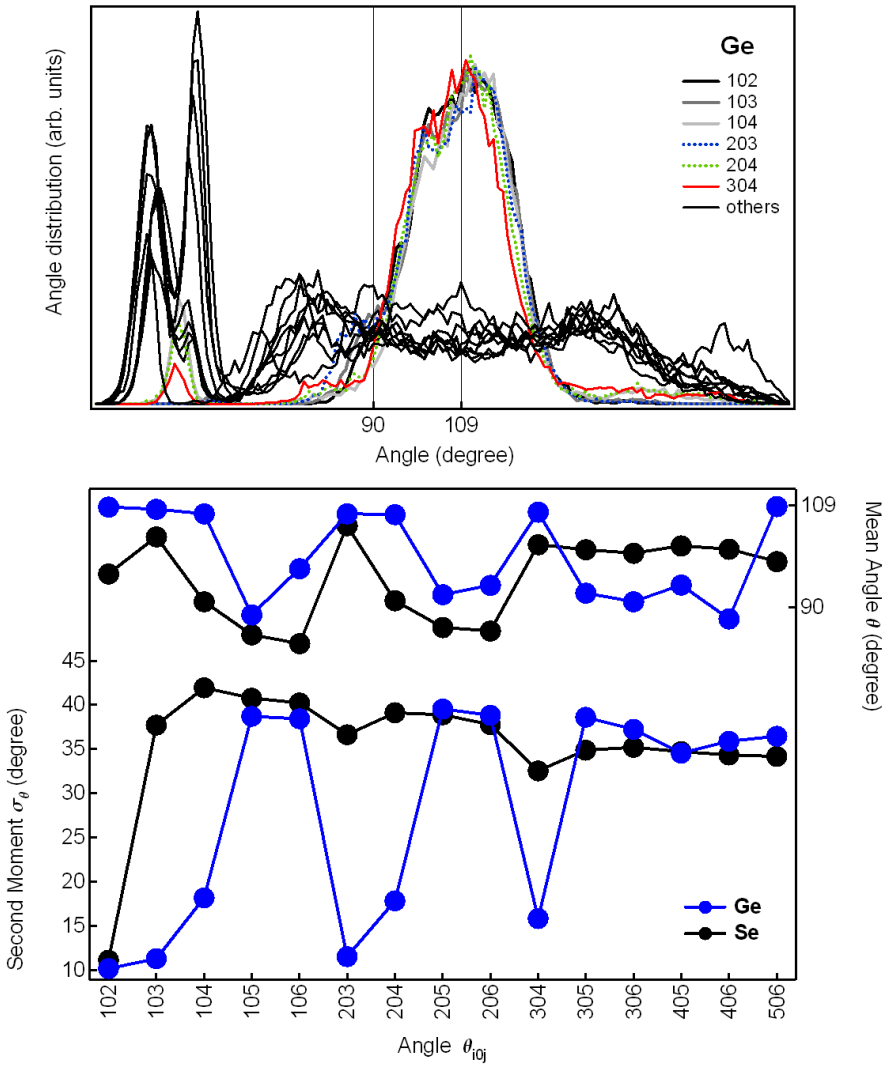

Figure 11.2: Top: $Ge-$centered partial bond angle bond angle distributions (PBADs, considering the 6 shortest neighbors) for the triplets of atoms $i0j$ ($i = 1, ..., 5$, $j = 2, ..., 6$) in amorphous $GeSe_2$. The six colored distributions have a low standard deviation (typically $10 - 20°$, see the bottom panel). Bottom: Standard deviation $\sigma_{\theta_{ij}}$ of the distributions (see the top panel for Ge) as a function of the angle $\widehat{i0j}$ in amorphous $GeSe_2$: Ge and $Se-$centered angles (blue and black respectively).

11.3 The constraints in amorphous *GeSbTe* alloys

11.3.1 Structures of amorphous *GeSbTe* alloys

Having validated the method with $GeSe_2$, we now turn to the amorphous $GeSbTe$ systems and focus on the constraint analysis of the five particular compositions we analyzed in this thesis, namely $GeTe_6$ (106), $GeSb_6$ (160) (the details of the FPMD simulations for these two compositions in the amorphous phase are given in the Appendix), Sb_2Te (021), Sb_2Te_3 (023), Ge_1Sb_2Te4 (124) and $Ge_2Sb_2Te_5$ (225).

We extend our study to another alloy comprised in the ternary diagram in Fig. 1.3 in Chapter 1 : $GeTe$ (101). The FPMD simulations details for this composition are given in the Appendix.

The structural properties for all these compounds, in particular the distances distributions and partial bond angle distributions, have been set out in details in the previous chapters or in the Appendix, and they will allow us to determine the BS and BB constraints. We resume the structural results obtained in the following subsections.

11.3.2 Distances distributions

If we compare the Ge environment in the amorphous materials studied in this work (except $GeSb_6$, see below) to $GeSe_2$, several differences are observed, such as the absence of a clear gap between the first and second shell of neighbors. Furthermore, the $GeTe$ (101), $GeTe_6$ (106), $Ge_1Sb_2Te_4$ (124) and $Ge_2Sb_2Te_5$ (225) display a bimodal distribution of the first four neighbors distances around Ge atoms. These two contributions arise from the mixture of (distorted) octahedral and tetrahedral environments (see the previous chapters, the Appendix and [186] for a detailed analysis).

These findings contrast with those found in absence of tellurium as in $GeSb_6$: around Ge atoms, a clear separation is found between the first four equivalent neighbors and the remaining fifth and sixth neighbor. These features are indicative of a tetrahedral environment also evidenced by the angular analysis.

In systems without germanium Sb_2Te and Sb_2Te_3 (see Chapter 9 Fig. 9.8), an intermediate fourth neighboring atom can be found between the first shell (i=1 to 3) and the second shell of neighbors (i=5 to 6) around a central Sb atom.

11.3.3 Coordination numbers and bond stretching constraints

By integrating the properly weighted partial radial distribution functions up to a cutoff distance taken equal to the first minimum of total $g(r)$, the average coordination number N_c around each atomic species has been obtained for the different amorphous alloys studied (see previous chapters). These coordination numbers will be used as input for the counting of BS constraints. We checked the influence of reasonable changes in the cutoff distance for integration, and the maximal error on N_c is ± 0.3, half of it being the error on the BS contribution to the constraint. The bond stretching constraints C_{BS} resulting from the coordination numbers N_c are given in Table 11.1.

11.3.4 Partial angle distributions and bond bending constraints

The Ge, Sb and Te centered partial bond angle distributions $\mathrm{P}(\theta_{ij})$ are plotted for each compound in the previous chapters. Some specific angles clearly display a limited motion around their mean value $\bar{\theta}_{ij}$. The Fig. 11.3, 11.4, 11.5, 11.6, 11.7 and 11.8 show the average $\bar{\theta}_{ij}$ of the 15 different bond angle distribution (first moments) and the standard deviations $\sigma_{\theta_{ij}}$, for all the compositions studied ((101), (106), (021), (023), (124), (225) and (160) respectively). This leads to the determination of the corresponding BB constraints for Ge, Sb and Te atoms, by counting the number of angles having a second moment of the order $\sigma_{\theta_{ij}} \simeq 10 - 15^{\circ}$. Compared to the benchmark system $GeSe_2$, we notice that $\sigma_{\theta_{ij}}$ is more scattered for large angle number n (i.e. $n > 6$), which suggests an increased orientational disorder when more distant neighbors are considered. In the ternary compositions (124) and (225), only three standard deviations are of the order of $\sigma_{\theta_{ij}} \simeq 10-15^{\circ}$ for the Ge and Sb atoms, associated with well-defined angles at $\bar{\theta}_{ij} = 90 - 100^{\circ}$ which are reminiscent of the distorted octahedral-like rocksalt cubic phase [36, 71]. The bond bending constraints C_{BB} are given in Table 11.1.

11.4 Total number of constraints

The present results contrast with the view that would follow the standard enumeration of BS and BB constraints, from coordination numbers obeying the $8-N_{sp}$ rule. Following this, a 3-fold Sb would give rise to 1.5 BS and 3 BB constraints [34, 35]. Here, in (124) and (225) for example, Sb has an additional neighbor that increases the number of BS constraints but it does not give rise to two additional BB constraints. In (124) and (225), only three Sb angles have a standard deviation of $10-15^{\circ}$ corresponding to average $\bar{\theta}_{ij}$=95° angles. The same holds for tellurium in the (021) alloy, that has around two neighbors, but only one angular constraint.

On the basis of the N_c and $\sigma_{\theta_{ij}}$ of $\mathrm{P}(\theta_{ij})$ calculated on FPMD structures, a Maxwell measure for the total number of constraints, C_{BS+BB}, of $\mathrm{Ge}_x\mathrm{Sb}_y\mathrm{Te}_{1-x-y}$ is given by :

$$\begin{aligned} C_{BS+BB} &= \left[x(C_{BS}^{Ge} - C_{BS}^{Te}) + y(C_{BS}^{Sb} - C_{BS}^{Te}) + C_{BS}^{Te}\right] \\ &+ \left[x(C_{BB}^{Ge} - C_{BB}^{Te}) + y(C_{BB}^{Sb} - C_{BB}^{Te}) + C_{BB}^{Te}\right] \end{aligned} \tag{11.1}$$

where the square brackets are used to separate BS from BB contributions. Resulting contraints are given in Table 11.1.

The case of a mixed environment In order to obtain a counting that takes into account different local topologies, a more subtle analysis is needed to compute the number of constraints in the alloys involving both germanium and tellurium atoms. In fact, two types of local environment can be clearly isolated for four-fold Ge in the presence of

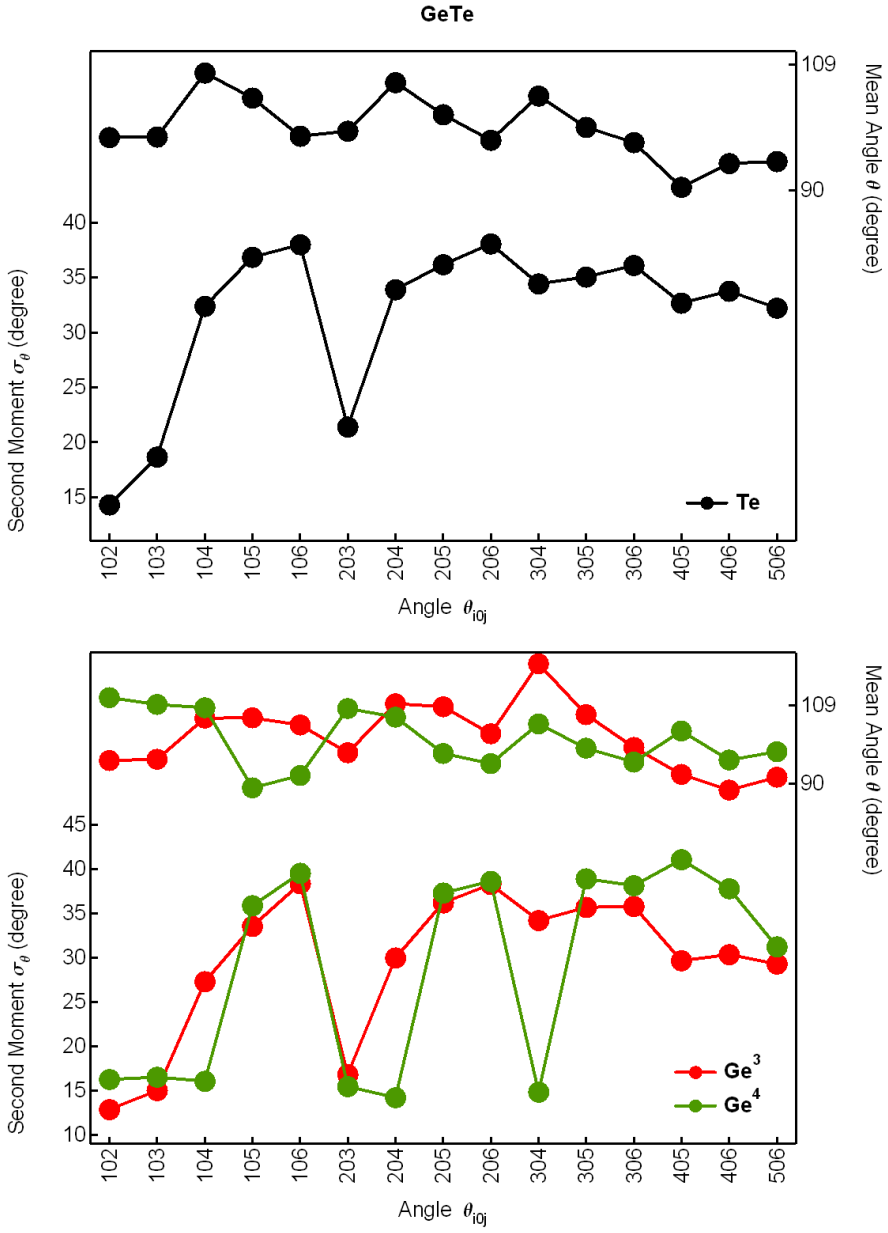

Figure 11.3: Average $\bar{\theta}_{ij}$ (first moments) of the 15 different bond angle distributions $\mathrm{P}(\theta_{ij})$ for angles $\widehat{i0j}$ (0 being the central atom) and the standard deviations $\sigma_{\theta_{ij}}$, for central Ge (discriminated between the Ge^3 and Ge^4 type) or Te atoms in amorphous $GeTe$.

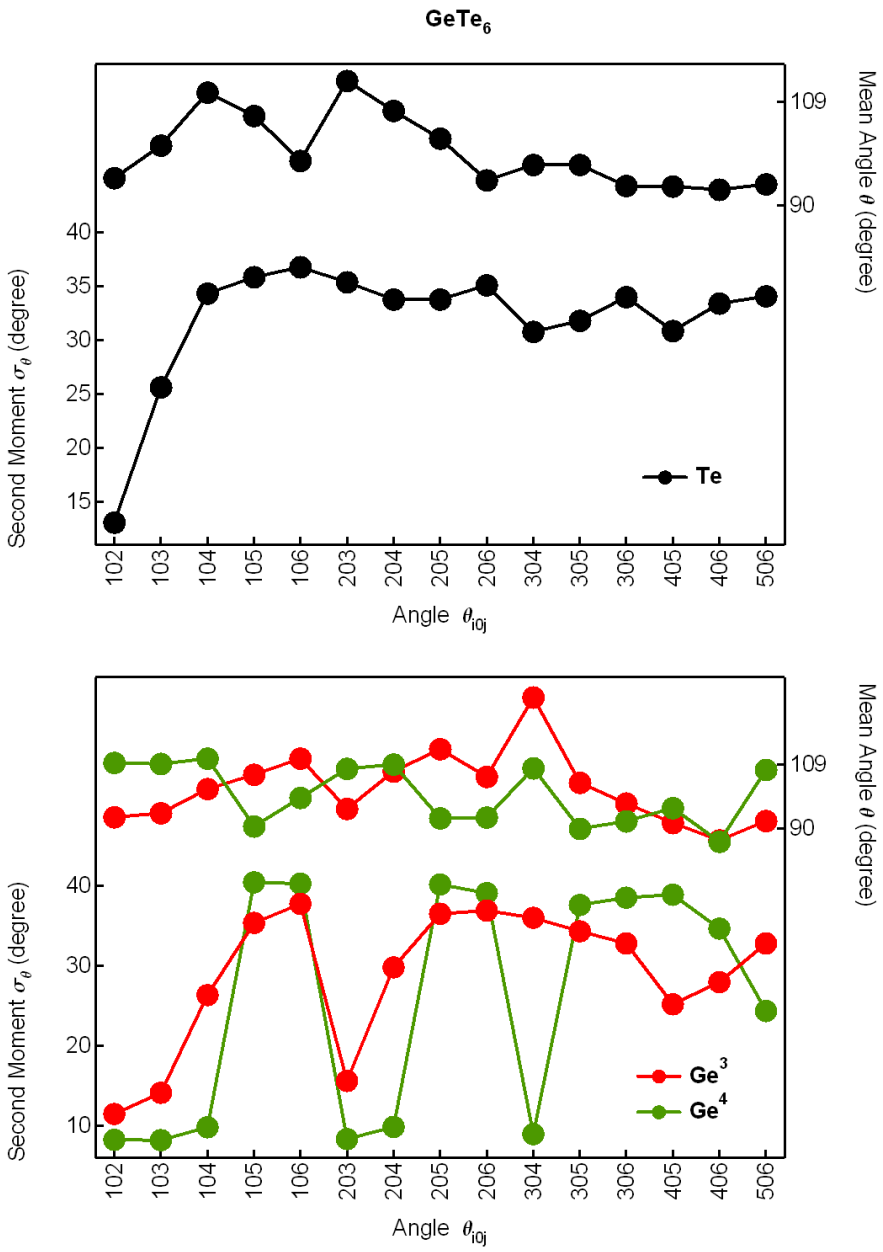

Figure 11.4: Average $\bar{\theta}_{ij}$ (first moments) of the 15 different bond angle distributions $\mathrm{P}(\theta_{ij})$ for angles $\widehat{i0j}$ (0 being the central atom) and the standard deviations $\sigma_{\theta_{ij}}$, for central Ge (discriminated between the Ge^3 and Ge^4 type) or Te atoms in amorphous $GeTe_6$.

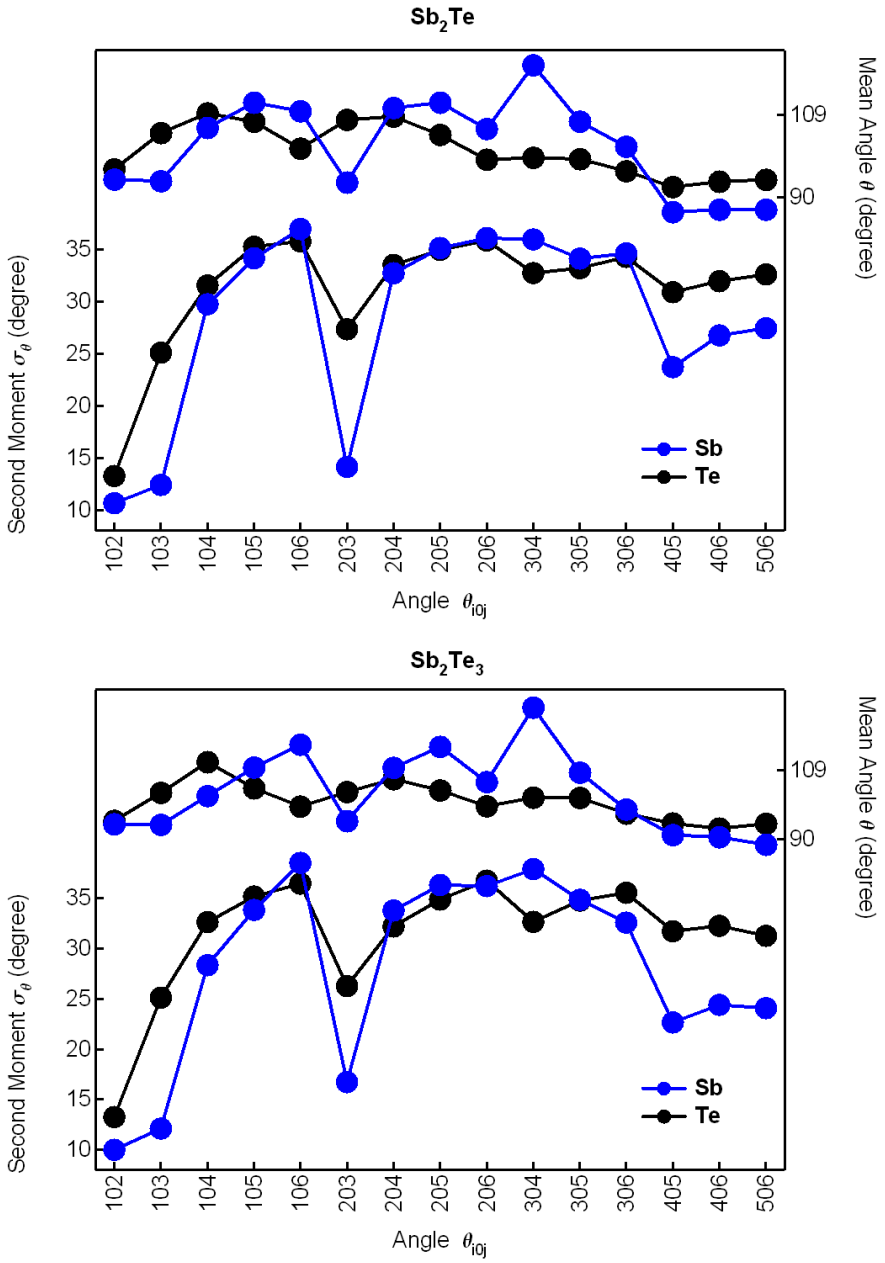

Figure 11.5: Average $\bar{\theta}_{ij}$ (first moments) of the 15 different bond angle distributions $\mathrm{P}(\theta_{ij})$ for angles $\widehat{i0j}$ (0 being the central atom) and the standard deviations $\sigma_{\theta_{ij}}$, for central Sb or Te atoms in amorphous Sb_2Te and Sb_2Te_3.

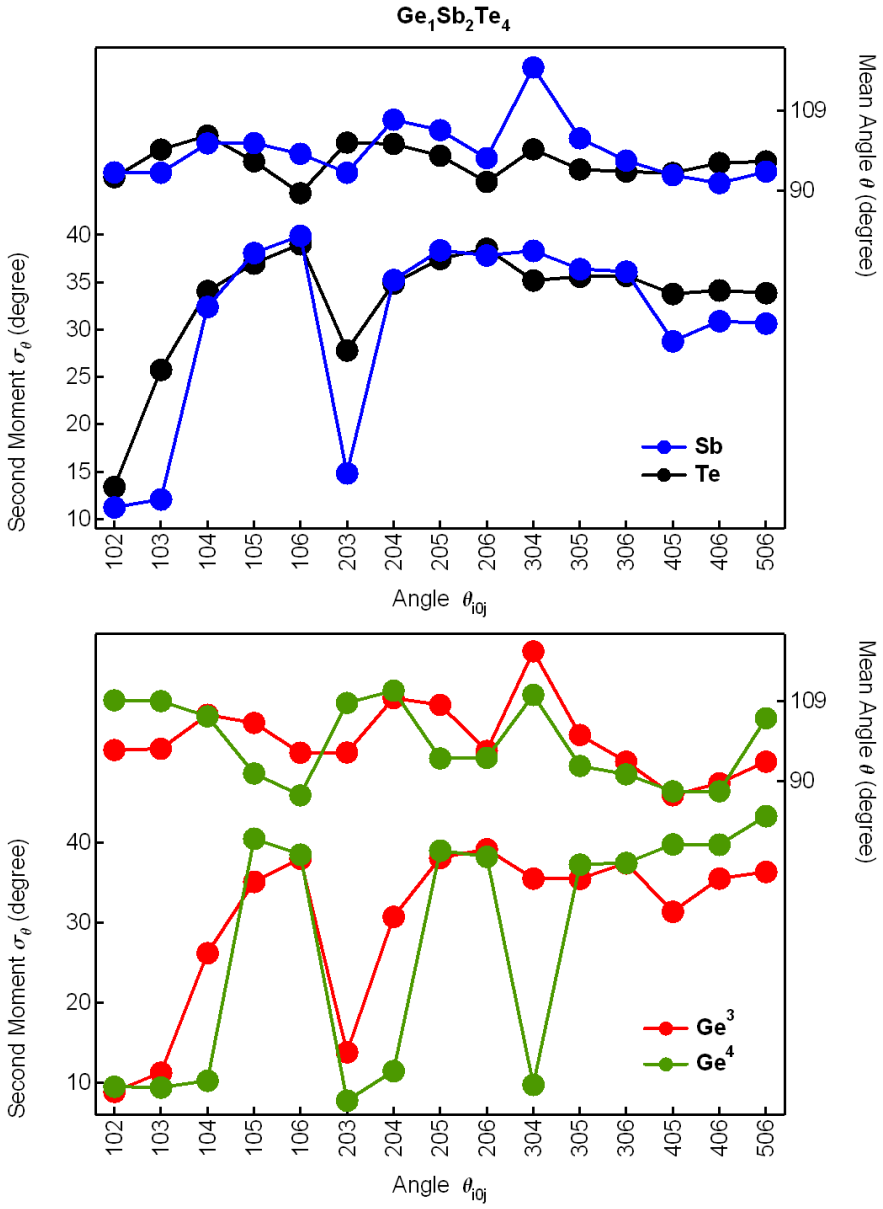

Figure 11.6: Average $\bar{\theta}_{ij}$ (first moments) of the 15 different bond angle distributions $\mathrm{P}(\theta_{ij})$ for angles $\widehat{i0j}$ (0 being the central atom) and the standard deviations $\sigma_{\theta_{ij}}$, for central Ge (discriminated between the Ge^3 and Ge^4 type), Sb or Te atoms in amorphous $Ge_1Sb_2Te_4$.

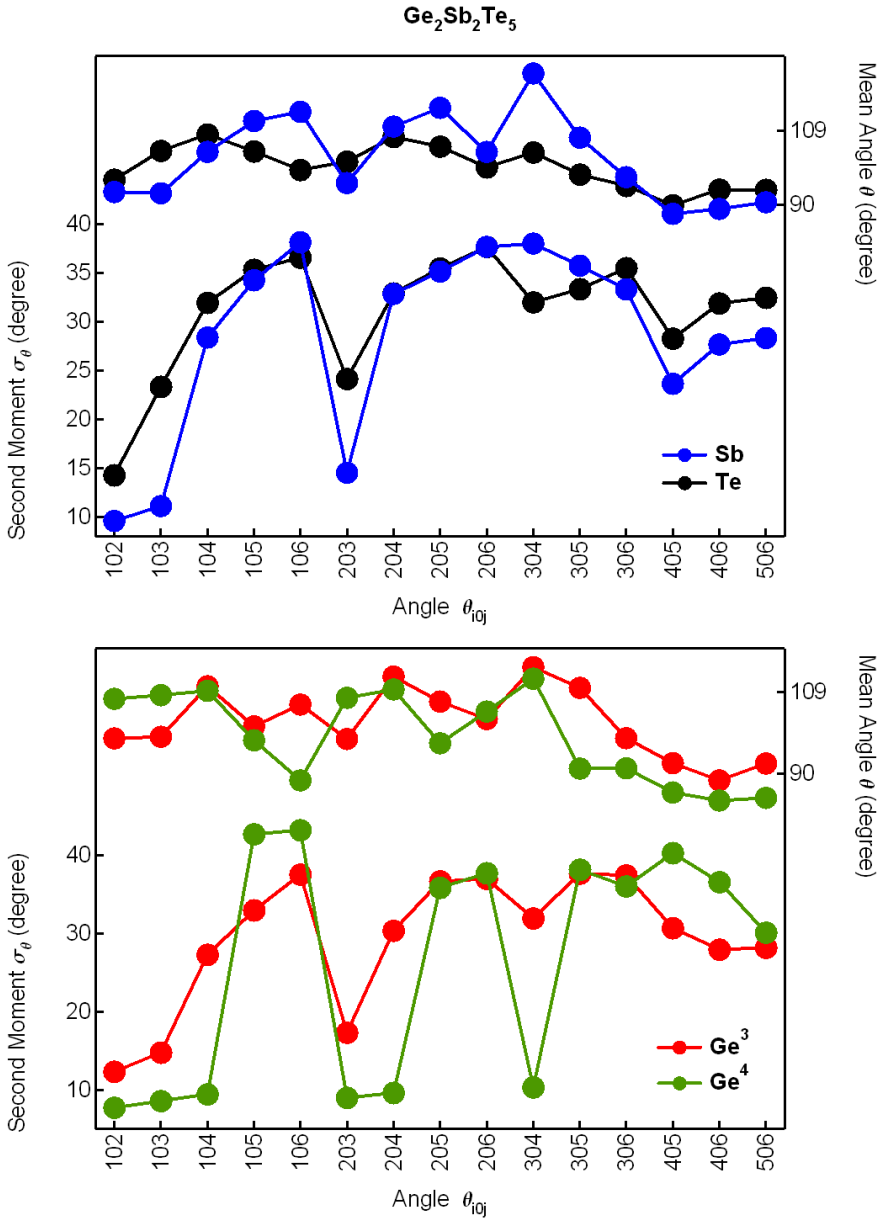

Figure 11.7: Average $\bar{\theta}_{ij}$ (first moments) of the 15 different bond angle distributions $\mathrm{P}(\theta_{ij})$ for angles $\widehat{i0j}$ (0 being the central atom) and the standard deviations $\sigma_{\theta_{ij}}$, for central Ge (discriminated between the Ge^3 and Ge^4 type), Sb or Te atoms in amorphous $Ge_2Sb_2Te_5$.

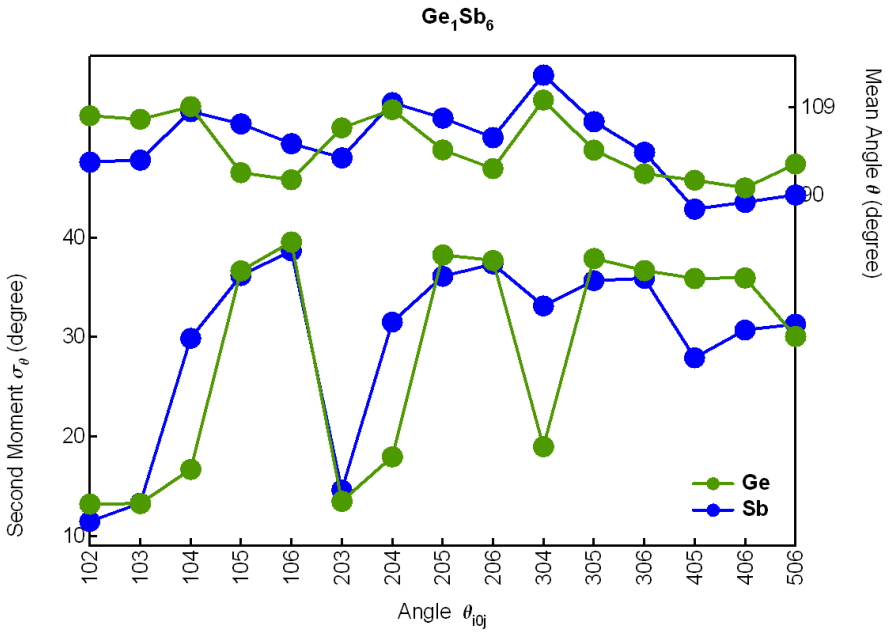

Figure 11.8: Average $\bar{\theta}_{ij}$ (first moments) of the 15 different bond angle distributions $\mathrm{P}(\theta_{ij})$ for angles $\widehat{i0j}$ (0 being the central atom) and the standard deviations $\sigma_{\theta_{ij}}$, for central Ge and Sb atoms in amorphous $GeSb_6$.

Compound	Atom	C^i_{BS}	C^i_{BB}	C_{BS+BB}
$GeTe_6$	Ge	2.0	3.3	
	Te	1.3	1.0	2.60± 0.16
GeTe	Ge	2.1	3.1	
	Te	1.55	1.0	4.1± 0.17
$Ge_1Sb_2Te_4$	Ge	1.85	3.3	
	Sb	1.85	3.0	
	Te	1.25	1.0	3.41± 0.14
$Ge_2Sb_2Te_5$	Ge	2.05	3.3	
	Sb	1.95	3.0	
	Te	1.35	1.0	3.60± 0.12
$GeSb_6$	Ge	2.1	5.0	
	Sb	1.95	3.0	5.26 ± 0.14
Sb_2Te	Sb	1.9	3.0	
	Te	1.2	1.0	4.00 ± 0.10
Sb_2Te_3	Sb	1.85	3.0	
	Te	1.15	1.0	3.23± 0.12

Table 11.1: Bond stretching constraints C^i_{BS} of the atomic species $i = Ge, Sb, Te$ (the maximum error on it is ±0.15), number of BB constraints C^i_{BB} computed from the standard deviations of the partial bond angle distributions (PBADs) $P_(\theta_{ij})$, and total number of constraints C_{BS+BB} in the six different $GeSbTe$ compounds studied. BB constraints, corresponding to a number of rigid angles, are integer values for Sb and Te. Since Ge may display two different environments, with 3 BB constraints for distorted octahedral, and 5 for tetrahedral, a weighted average is taken, with error bars of ±0.1 arising from the tetrahedral fraction of Ge (η_4) estimate.

tellurium, as seen in Chapter 10 for (124) and (225) and in the Appendix for (106) and (101):

- A majority of distorted octahedral sites having 3 constraints for the angles $\bar{\theta}_{ij} = 90 - 100°$.

- A minority (with fraction η_4) of tetrahedral Ge (calculated to be respectively η_4=0.16 and η_4 =0.17 in the (225) and (124), also found in Refs. [39, 40], and η_4=0.33 and η_4=0.25 in (106) and (101)) which have 5 BB constraints as in $GeSe_2$.

The determination of BB constraints can be generalized to mixed environments without any ambiguity as seen for $Ge_1Sb_2Te_4$ (Fig 11.6). For instance, after the identification of tetrahedra in $Ge_1Sb_2Te_4$, it is possible to obtain the standard deviation $\sigma_{\theta_{ij}}$ depending on the local structure, tetrahedral or octahedral. It appears clearly (Fig. 11.6) that the tetrahedral Ge sites have 6 rigid angles, corresponding to 5 BB constraints as in the $GeSe_2$ benchmark, while the distorted octahedral ones have only 3 rigid angles and BB constraints.

This means that the average number of germanium BB constraints is $C_{BB}^{Ge} = 5\eta_4 + 3(1-\eta_4) = 3 + 2\eta_4$ and gives for the Maxwell estimate:

$$\begin{aligned} C_{BS+BB} &= \left[x(C_{BS}^{Ge} - C_{BS}^{Te}) + y(C_{BS}^{Sb} - C_{BS}^{Te}) + C_{BS}^{Te}\right] \\ &+ \left[x(3+2\eta_4) + 3y + (1-x-y)\right] \end{aligned} \tag{11.2}$$

and finally to $C_{BS+BB}^{(124)}$=3.41 and $C_{BS+BB}^{(225)}$=3.60 (see Table 11.1). One can thus conclude that (124) and (225) are *stressed rigid*, i.e. they have more constraints than degrees of freedom (3 in 3D). The present results contrast with the assumption that GST are perfect glasses, assumption that was used to analyze EXAFS results in [42]. The present results agree with the observation that, apart the (106) alloy [187], which is found flexible, but close to the optimal $C_{BS+BB} = 3$, none of the alloys studied can form bulk glasses.

The case of $GeSb_6$ Again, we note that the $GeSb_6$ compound behaves very differently from tellurium containing alloys, as already emphasized in the previous chapter. The integration of the first peak of the pair distribution functions yields a coordination number of 4.15 and 3.70 for Ge and Sb respectively . However, the origin of a similar coordination number for both chemical species is quite different. One has indeed an octahedral distorted structure for the Sb atom (as manifested by three angles close to an average angle of 95° in Fig. 13 in the Appendix), whereas the closest angles for the Ge atom are indicative of a tetrahedral environment (109°). Corresponding partial angles show a low standard deviation, of the order of $15 - 20°$. In this respect, it appears that from the viewpoint of rigidity Sb is close to what is obtained for ternary telluride compounds while Ge is tetrahedral and behaves similarly to what is obtained for $GeSe_2$.

11.5 Rigidity transition in tellurides

Using these elements, we now determine an approximate *flexible to rigid transition composition* [34, 35] from the Maxwell estimate corresponding to $C_{BS+BB} = 3$. We plotted in Fig. 11.9 the numbers of constraints given in Table 11.1 for each compound studied, together with the level lines corresponding to number of constraints going from 2.6 to 6.6 by 0.2 step. The Maxwell line ($C_{BS+BB} = 3$), is found to be close to the compositional join $GeTe_4 - SbTe_4$ or e.g. to the $GeSbTe_8$ alloy on the $Ge_xSb_xTe_{1-2x}$ tie line and defines two regions in the GST triangle:

- In the tellurium-rich region the system has not enough Ge or Sb cross-links to ensure rigidity, and local deformations are allowed.
- In the second region, where usual PCMs are found, the amorphous phases are stressed rigid.

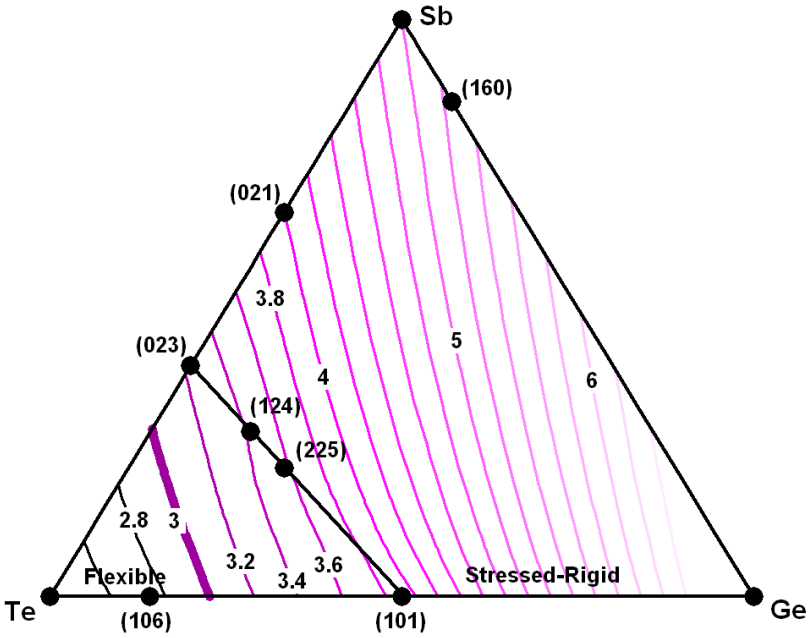

Figure 11.9: Contour map of the number of constraints C_{BS+BB} in the ternary $Ge_xSb_yTe_{1-x-y}$ phase diagram. The magenta and black lines correspond respectively to the stressed rigid and flexible phase. Black circles represent the compositions studied by FPMD in this thesis. The thick magenta line represents the rigidity transition line defined by $C_{BS+BB} = 3$, and separates the flexible (Te-rich) from the stressed rigid phase where most PCMs can be found, especially on the $GeTe - Sb_2Te_3$ tie line (black line).

Although the mechanical properties of the amorphous phase probably play a role in the recrystallization process, the most important direct application of the present analysis concerns the ageing of the amorphous structure, and consequently the drift of its electrical resistivity with time. As ageing has been found to be very small in optimally constrained glasses [33], we expect small drifts for alloy compositions yielding a number of constraints close to the rigidity transition ($C_{BS+BB} = 3$). Doping an established PC material with elements contributing to a lowering of the constraints should lead to improved properties as far as the ageing is concerned. This technologically important issue should obviously be addressed experimentally.

11.6 Conclusion

We have developed a new constraint counting algorithm applicable to tellurides for which a simple counting based on the $8 - N_{sp}$ (octet) rule does not apply in a straightforward manner [188]. We show that atomic-scale trajectories obtained from First Principles Molecular Dynamics simulations can be appropriately used for bond-stretching (BS) and bond-bending (BB) constraint counting and applied to the GST phase-change system, a family of huge technological interest. The results show that amorphous systems lying on the popular $Sb_2Te_3 - GeTe$ tie-line in the GST compositional triangle belong to a stressed rigid phase, whereas an isostatic stress-free Phillips-Thorpe rigidity transition line is obtained close to the $SbTe_4 - GeTe_4$ join.

Conclusion

A driving force to explain the Negative Thermal Expansion in liquid tellurides

Among the chalcogenides alloys we studied for their NTE, liquid $GeTe_6$ and As_2Te_3 showed, as expected, the most striking effects.

By means of neutron diffraction experiments, we evidenced a strong evolution of the structure factors with temperature, with, in particular, an increase of the ratio between the first and second peaks height. The extreme values of this ratio are a qualitative indicator of the importance of the structural changes related to a NTE. This evolution is correlated, for both alloys, with an increase of the coordination number.

First Principle Molecular Dynamics simulations reproduced the evolution of the measured quantities, and permitted to follow the structural changes at the microscopic scale. In all compounds studied, the local order remains clearly octahedral along the NTE. In the low temperature liquid (with the largest volume), a distortion, involving shorter and longer interatomic distances, was found. We showed that the distribution of shorter and longer bonds depends on the chemical element, the coordination numbers tending to follow the octet rule valid in the pure crystals. Moreover, the short and long bonds are not randomly distributed, and an alternation is preferred (at least, in $GeTe_6$, around the Ge atoms). Just above the melting point, the local order of these semi-conductors is thus governed by a Peierls-like distortion mechanism, which minimizes the energy by opening of a gap at the Fermi level. Along the NTE, our FPMD simulations revealed the gradual decrease of the Peierls distorsion, the local order becoming more symmetric with temperature, by an elongation of the shortest distances and a shortening of the longest ones. The longest distances decrease more than the shortest ones elongate, and the volume shrinks.

The most striking result of this thesis was probably the one obtained with inelastic neutron scattering, as we found that a strong evolution of the VDOS is associated with the NTE. We measured a *red-shift* (reproduced by our FPMD simulations) of the high-frequency part of the VDOS when the temperature *increases*. At the first sight, this observation is paradoxical, as it implies that the volume shrinking along the NTE is accompagnied by a *softening* of the vibrational modes. Nevertheless, this result further supported our model for the structural evolution. Moreover, the change in the VDOS

allowed for the calculation of the vibrational entropy variation along the NTE, and we showed that it represents the largest part of the total entropy thermal evolution, which is totally unusual.

With these experiments and computer simulations, we demonstrated that the gain of vibrational entropy is the *driving force* for the observed NTE in rich-Te Ge_xTe_{1-x} and As_xTe_{1-x} alloys [154]. We may expect this mechanism to apply to all Peierls distorted p-bonded elements and alloys, provided that the melting temperature is smaller than the distortion energy.

Another important result is that we reproduced, with FPMD simulations (for As_2Te_3), the semi-conductor to metal transition that occurs along the NTE. The alteration of the local Peierls distorsion is indeed responsible for a large increase in conductivity.

The Sb addition to Te-rich Ge_xTe_{1-x} alloys obscures the NTE effect in the liquid phase

When adding a quantity of Sb in Te-rich Ge_xTe_{1-x} alloys, a NTE is no longer observed, as in the case of the PCM $Ge_1Sb_2Te_4$ and $Ge_2Sb_2Te_5$. We studied this effect with experiments on liquid $Ge(Sb_{10}Te_{90})_6$ (i. e. $GeTe_6$ in which 10 % of Te has been replaced by Sb) and on $GeSb_6$ (which can be viewed as the extreme limit case). The latter was found to behave as a 'normal' liquid with temperature. The substitution of a small quantity of Te by Sb in $GeTe_6$ had considerable effects on the structural and dynamical characteristics of the compound. The structure factor still showed a slight thermal evolution, but the red-shift of the VDOS' high energy part when decreasing the temperature was no longer observed. The changes depend on the degree of Te substitution by Sb : in $Ge_1Sb_2Te_4$ (one third of the Te replaced by Sb compared to $GeTe_6$), the evolution of the VDOS as well as that of the $S(q)$ are totally canceled out. The addition of Sb to the eutectic $GeTe_6$, which presents a NTE just above the melting point, increases the T_m, and the anomaly is no longer observable in the thermodynamically stable liquid. From these results, we conjecture that these $GeSbTe$ alloys are on the high T range of the NTE (some still show an evolution), the lowest T range being unreachable (because located in the supercooled region). This is sustained by the $GeSbTe$ sound velocity behavior, which closely looks like the part comprised in the highest T range of the NTE of $GeTe_6$.

Structural and dynamical reasons for the ability of $SbTe$ alloys to switch easily from the amorphous to crystalline phase

The excellent agreement obtained between FPMD simulations results and neutron diffraction experiments on liquid and amorphous $SbTe$ alloys allowed a precise characterization of their structures. We found that the local order in amorphous Sb_2Te, and especially in Sb_2Te_3, is very close to what is found in their crystals (octahedral, with distortions, and

chemically ordered), and that a strong medium range order is present in both amorphous. Finally, the dynamical correlations showed an increase of the long wavelength and low energy modes upon quenching.

These similarities between the amorphous and crystalline phases can explain the rapidity of the switching in compounds such as $AIST$, used as PCM, which was found similar in structure to the Sb_2Te alloy. The amorphous Sb_2Te_3 local order is so close to that of the crystal that we expect the activation energy of recrystallization to be low, which does not permit the obtention of a amorphous phase suitable for PCM use.

Counting algorithm for the constraints in PCM

After the study of the $SbTe$ constituants of the most used PCM, we have constructed a model for the amorphous $Ge_2Sb_2Te_5$ and $Ge_1Sb_2Te_4$ alloys, using ab initio molecular dynamics simulations [186]. Their structures are shown to have a generally cubic topology, including around 16 % of perfectly tetrahedrally bonded Ge atoms. The remaining atoms belong to Peierls distorted octahedral environments, in agreement with models presented recently.

Finally, we have developed a new constraint counting algorithm applicable to tellurides for which a simple counting based on the octet rule does not apply in a straightforward manner, as in disordered phases [188]. We showed that atomic-scale trajectories obtained from FPMD simulations could be appropriately used for bond-stretching and bond-bending constraint counting. We applied the constraint counting algorithm to the different amorphous compounds studied during this thesis. The results show that amorphous systems lying on the $Sb_2Te_3 - GeTe$ tie-line in the GST compositional triangle belong to a *stressed rigid* (overconstrained) phase, whereas an isostatic stress-free Phillips-Thorpe rigidity transition line is obtained close to the $SbTe_4 - GeTe_4$ join. Since it has been found in amorphous selenides and sulphides that compositions around this transition line display some remarkable properties such as the absence of ageing, a stress-free character and space-filling tendencies [189], one may wonder to what extent these properties can be observed in tellurides as well, and how these properties, once being observed, could be used in close future to design phase-change materials with the corresponding functionality.

The obtention of the results summarized here would not have been possible without the combination of experimental methods and computer simulations. The quantities measured with experiments, especially on disordered systems, give a truncated (because of the experimental bias) and averaged view of what is happening in the sample. The ab initio simulations are useful to access directly to the atomic trajectories, which permit to obtain information about local order evolution, but the first step should always be to validate it by comparison with experiments.

Appendices

Ab initio simulations on the $GeSb_6$, $GeTe$ and $GeTe_6$ alloys in amorphous phase

We performed FPMD simulations with the VASP simulations package [134] to obtain atomic trajectories of 210 to 216 atoms systems ($GeTe$: 105 Ge + 105 Te, $GeSb/Te_6$: 31 Ge + 185 Sb/Te) at the experimental amorphous densities [171, 20] ($\rho = 0.0303$ Å^{-3} for $GeTe$, $\rho = 0.0303$ Å^{-3} for $GeTe_6$ and $\rho = 0.0283$ Å^{-3} for $GeSb_6$). In each case, we first heated the liquid at 3000 K for 10 ps and then gradually cooled it down to 300 K in 30 ps. After that, we thermalized the amorphous for at least 15 ps each. We used the PW91 exchange correlation functional [128], ultrasoft pseudo-potentials [133], Ge ($4s$ and $4p$), Sb and Te ($5s$ and $5p$) valence electrons and a 250 eV plane waves cutoff energy. Calculations were performed at Γ point only.

The structural results we obtained on these amorphous are detailed in the following, and in Chapter 11.

Amorphous $GeSb_6$

Comparison with neutron diffraction experiment

The neutron diffraction experiment on $GeSb_6$ in amorphous phase was performed on the two-axis diffractometer D4, in the same experimental conditions as the amorphous Sb_2Te and $Ge_1Sb_2Te_4$ (see Chapters 9 and 10 respectively).

We observe several changes of the overal shape of the $GeSb_6$ structure factor when going from the liquid to amorphous phase (see Fig. 10):

- The ratio of the first and second peak heights decreases strongly, from ~ 1.6 to ~ 1.1.
- The position of the first (second) peak is shifted by -0.14 Å^{-1} ($+0.2$ Å^{-1}).

– The asymmetry of the third peak evolves from the low-q side to the high-q side. The same change is observed for the fourth peak.

Our simulations reproduce the measured changes in $S(q)$ and $g(r)$ with a satisfactory agreement (see Fig. 10 and 11). Some discrepancies are however observed, as a lower height for the two first $S(q)$ peaks, and a slight overestimation of the distances in FPMD $g(r)$ (in which the three first peaks maxima are shifted by ~ 0.13 Å in average).

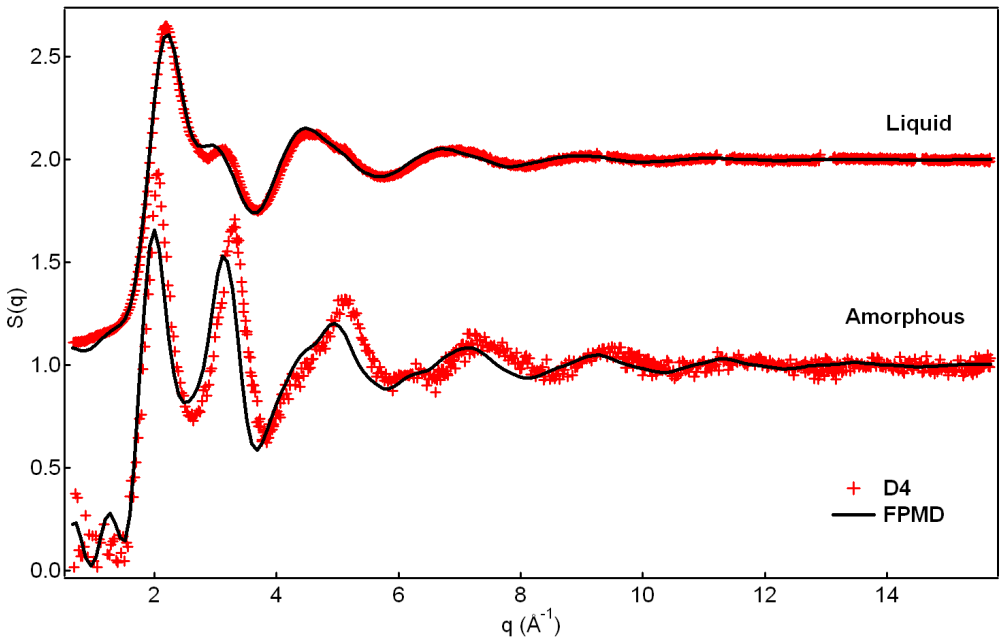

Figure 10: Structure factors from the experiment (red markers) and the FPMD simulations (black lines) in liquid and amorphous $GeSb_6$.

Structure of $GeSb_6$ in amorphous phase

The interatomic distances are computed for the 6 first neighbors of all the atoms in the box and averaged over the FPMD trajectories, around the Ge or Sb atom separately. In the distances distributions around Ge atoms (see Fig. 12), a clear separation is found between the first four equivalent neighbors and the remaining fifth and sixth neighbors.

This particular profile for the distances around the Ge atoms is indicative of a quasi-perfect tetrahedral order around Ge atoms, while Sb atoms have an octahedral neighborhood, as shown with the partial bond angle distributions of Fig. 13. It is actually quite unexpected to be able to reproduce such a large evolution of the Ge atoms neighborhood with the FPMD quench (from a perfect octahedral order in liquid, see Chapter 7, to a

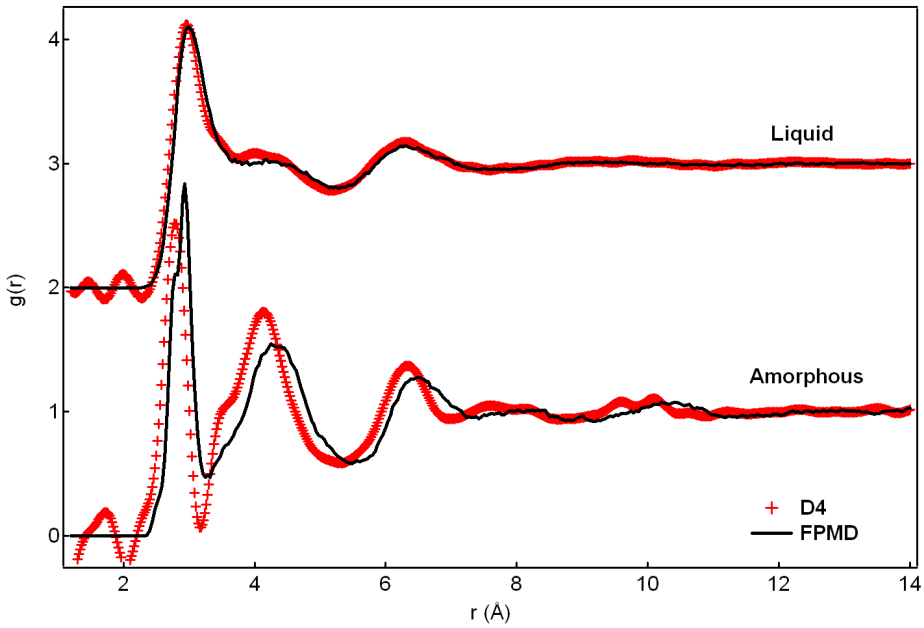

Figure 11: Pair correlation functions from the experiment (red markers) and the FPMD simulations (black lines) in liquid and amorphous $GeSb_6$.

perfect tetrahedral order in amorphous). These results are in agreement with previous results [55].

Amorphous $GeTe$

Comparison with X-ray diffraction experiment

As shown in Fig. 14, the structure factors obtained from the simulations on amorphous $GeTe$ compare favorably with the available experimental $S(q)$ obtained by X-ray scattering [72]. All peaks and especially the first ones found around 2, 3.4, and 5 $Å^{-1}$ are reasonably well reproduced in height and position.

We see in Fig. 15 that the 4 first distance distributions in amorphous $GeTe$ are split in two parts. As in the amorphous $Ge_1Sb_2Te_4$ and $Ge_2Sb_2Te_5$ compounds (see Chapter 10), it could be an indication of two distinct environments for the Ge atoms in the structure. We decompose the population of Ge atoms by counting their number of neighbors at distances smaller than 2.87 Å, which is the location of the minimum that separates the two peaks in the distribution $d_4(r)$. It appears (see Fig. 16) that the first 4 neighbors' distributions around Ge atoms consist of two independent components : the short-distance sub-peak belongs to 4-fold bonded atoms (25 % of the Ge atoms are in this case) and the

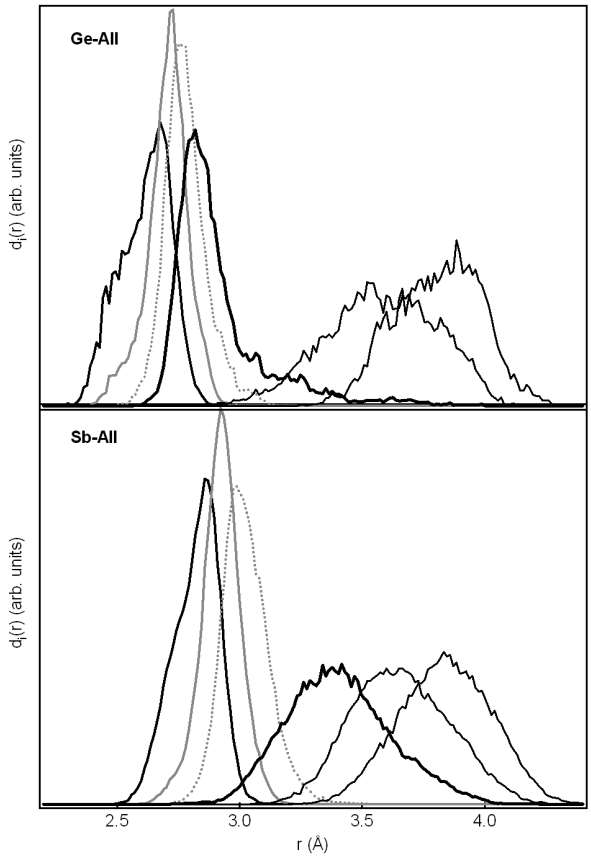

Figure 12: Six first interatomic distance distributions around Ge or Sb atoms in amorphous $GeSb_6$ from FPMD simulations.

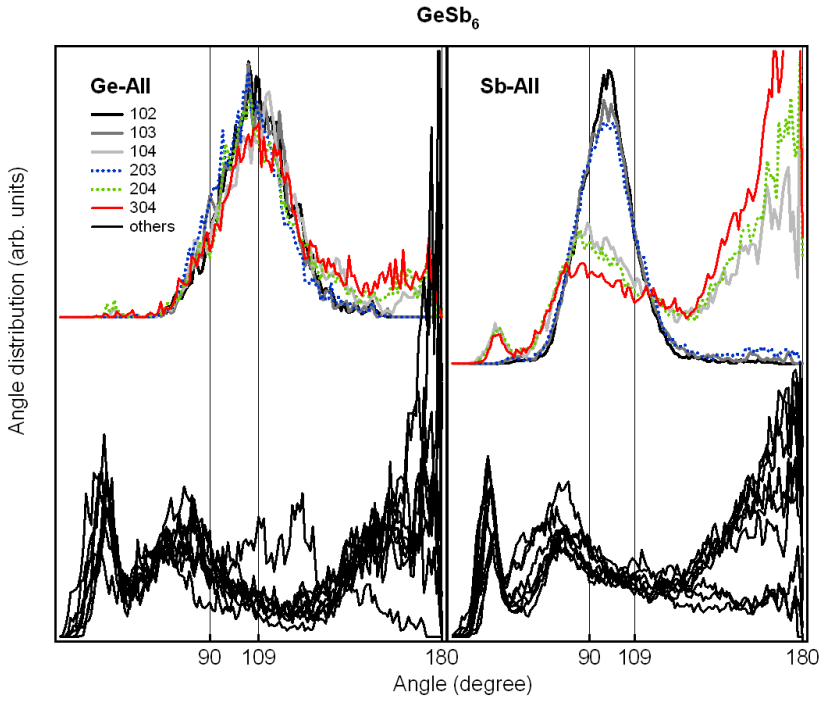

Figure 13: Partial bond angle distributions around Ge or Sb atoms in amorphous $GeSb_6$ from FPMD simulations.

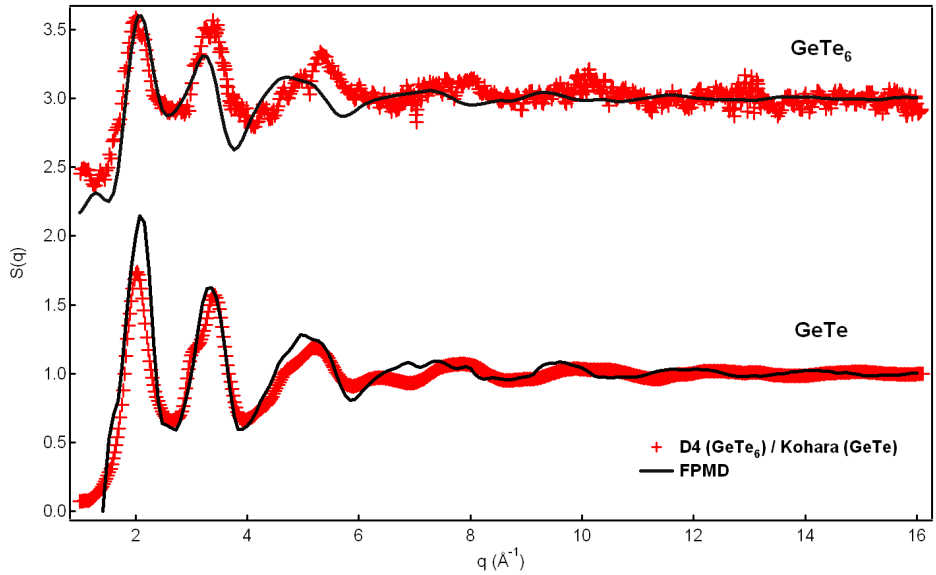

Figure 14: Structure factors from the experiments (red markers) and the FPMD simulations (black lines) in amorphous $GeTe_6$ and $GeTe$. The X-ray diffraction result on $GeTe$ is from Kohara et al. [72].

second sub-peak belongs to atoms with a coordination number of 3 (the remaining Ge atoms). These two types of Ge atoms are referred to as Ge^3 and Ge^4 respectively.

We analyze the bond angle distributions around Ge^3 and Ge^4 separatly (see the partial bond angle distributions in Fig. 17), and around Te (see the total bond angle distributions in Fig. 18). For the 3-fold bonded Ge, we found bond angle distribution peaked around 92°, close to what found around Te atoms ($\sim$ 87°). The 25 % of 4-fold Ge, as in $Ge_1Sb_2Te_4$ and $Ge_2Sb_2Te_5$, have very different bond angle distributions, with a maximum around 109°.

Amorphous $GeTe_6$

Comparison between experimental and FPMD results

The neutron diffraction experiment on $GeTe_6$ in amorphous phase was performed on the two-axis diffractometer D4, in the same experimental conditions as the amorphous $Ge_2Sb_2Te_5$ (see Chapter 10).

We observe a shift of the positions of the peaks between the experimental and FPMD $S(q)$ of amorphous $GeTe_6$ (see Fig. 14). This is linked with an overestimation of interatomic distances in the calculated pair correlation functions, as it was already noted in

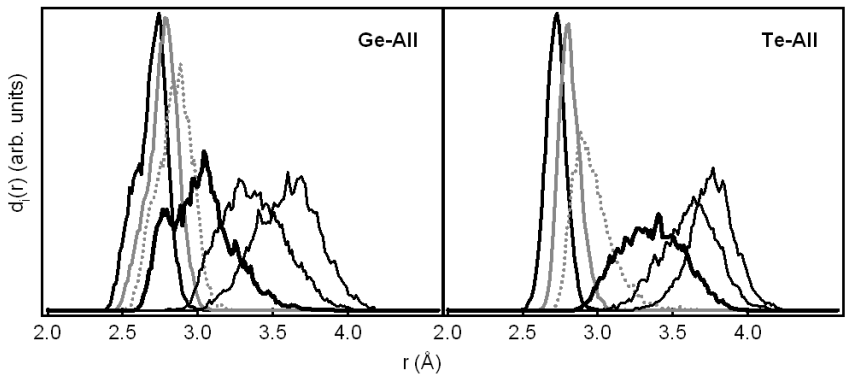

Figure 15: Six first interatomic distance distributions around Ge or Te atoms in amorphous $GeTe$ from FPMD simulations.

the study of the liquid $GeTe_6$ (see Chapter 6).

FPMD structure

As in amorphous $GeTe$ and $GeSbTe$ alloys, the 4 first distance ditributions in amorphous $GeTe_6$ are split in two parts (see Fig. 19). This is the compound in which the low-r sub-peaks are the most prominent. If we decompose the population of Ge atoms by counting their number of neighbours at distances smaller than 2.86 Å (locations of the minimum that separate the two peaks in distribution $d_4(r)$), we observe in Fig. 20, as previously noted in the phase-change alloys, that the short-distance sub-peak belongs to 4-fold bonded atoms (Ge^4) and the second sub-peak belongs to atoms with a coordination number of 3 (Ge^3). The proportion of Ge^4 is the most important in this compound (33 % of the Ge atoms are in this case). The study of the bond angle distributions show that the Ge^4 are tetrahedrally bonded, while the Ge^3 and Te atoms have a mostly octahedral environment (see Fig. 21 and 22).

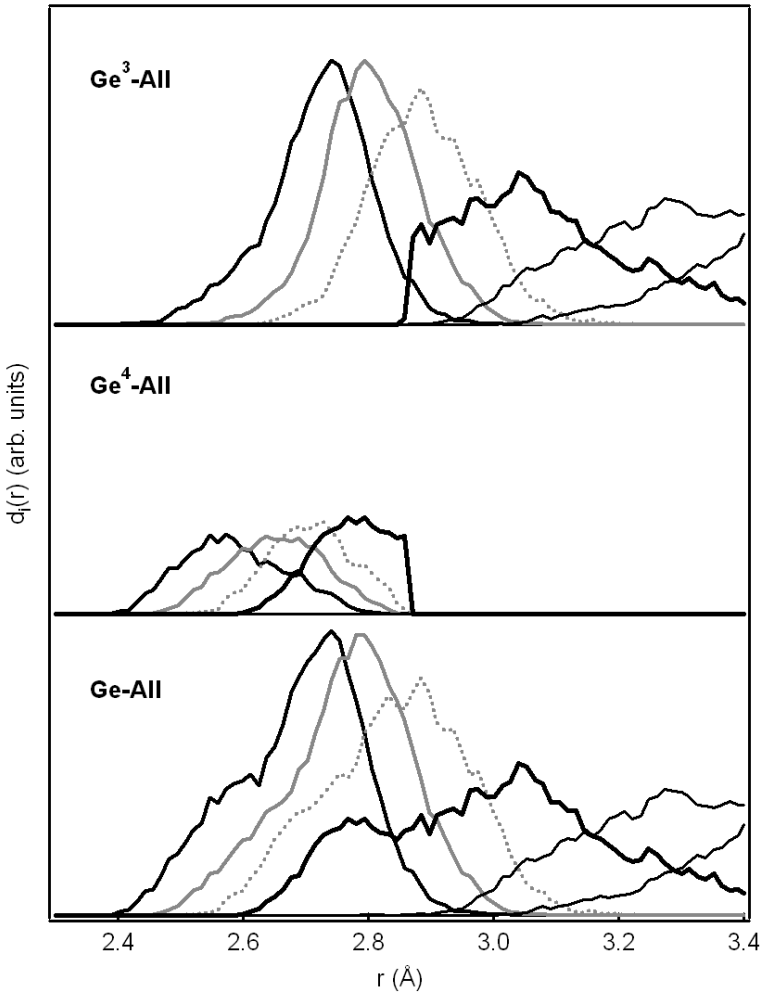

Figure 16: Six first interatomic distance distributions around Ge atoms in amorphous $GeTe$ from FPMD simulations, for the Ge^3 and Ge^4 type of atoms.

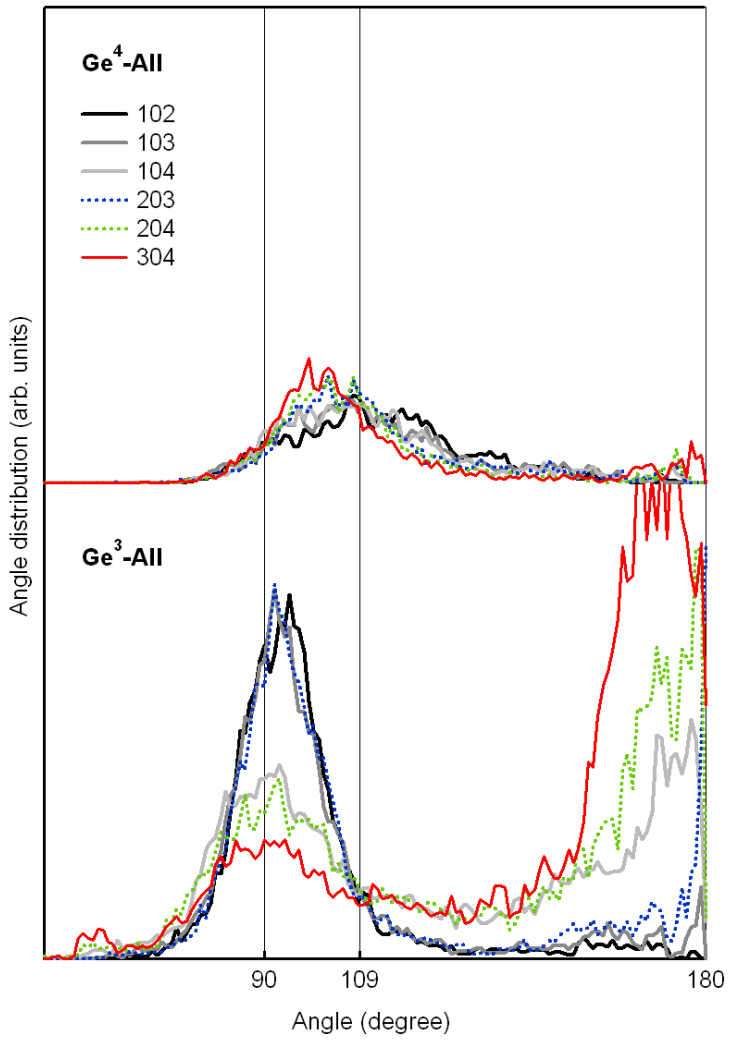

Figure 17: Partial bond angle distributions around Ge^3 and Ge^4 type of Ge atoms in amorphous $GeTe$ from FPMD simulations.

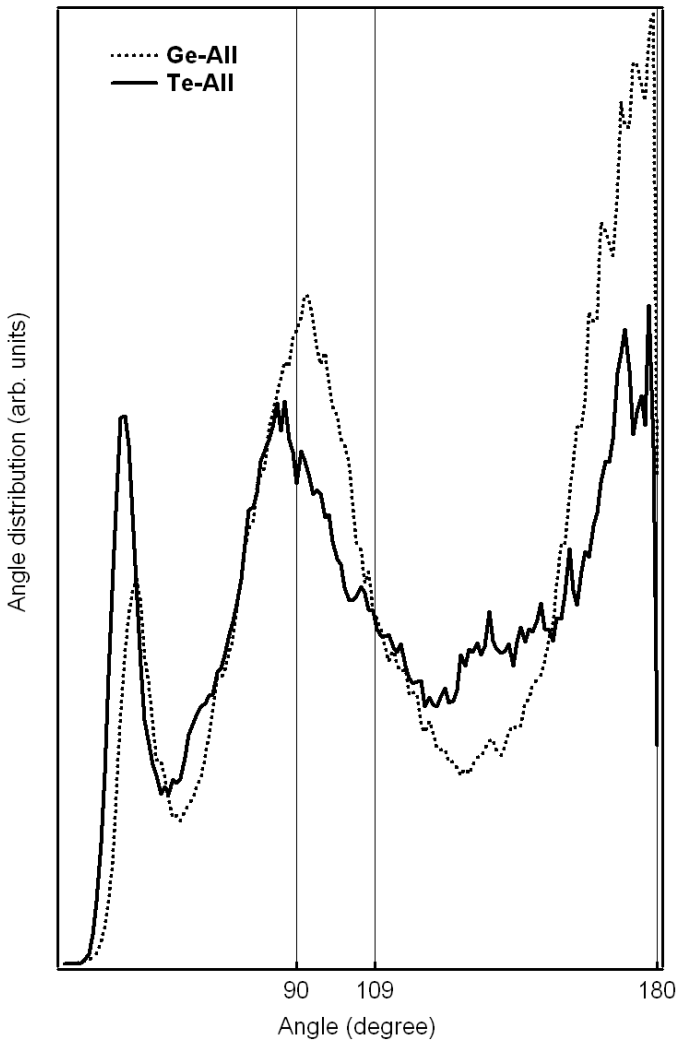

Figure 18: Total bond angle distributions around Ge and Te atoms in amorphous $GeTe$ from FPMD simulations.

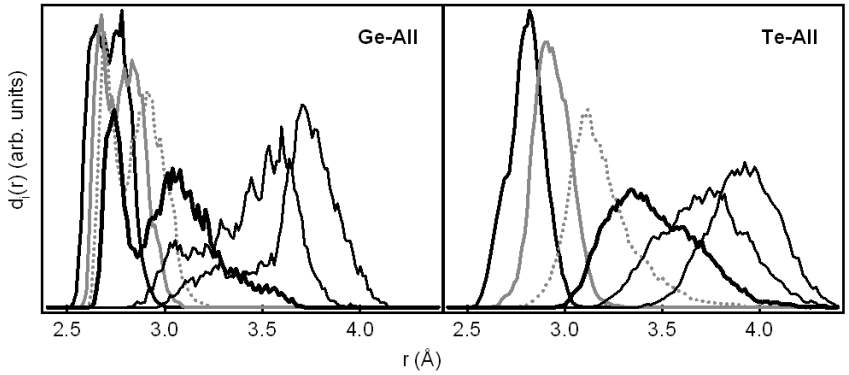

Figure 19: Six first interatomic distance distributions around Ge or Te atoms in amorphous $GeTe_6$ from FPMD simulations.

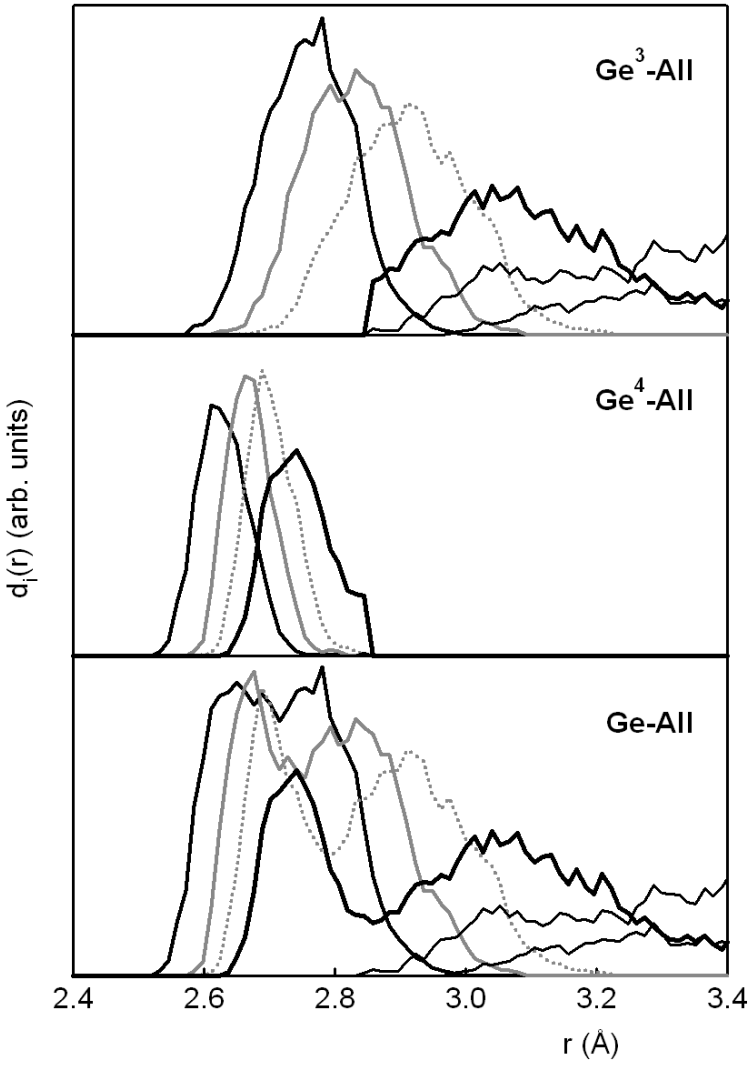

Figure 20: Six first interatomic distance distributions around Ge atoms in amorphous $GeTe_6$ from FPMD simulations, for the Ge^3 and Ge^4 type of atoms.

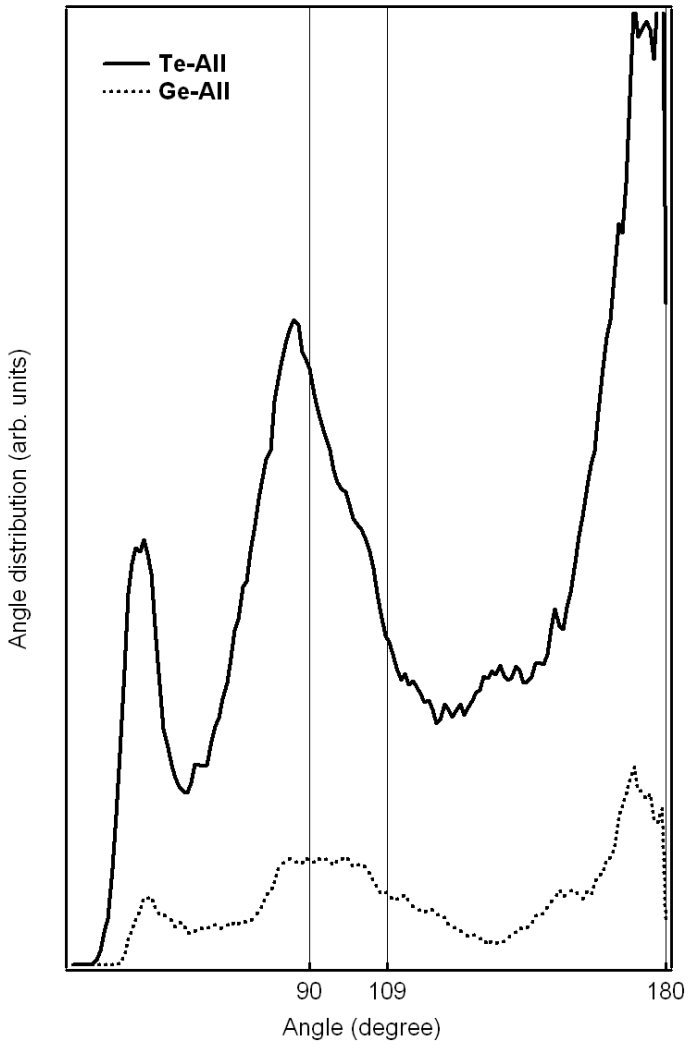

Figure 21: Bond angle distributions around Ge or Te atoms in amorphous $GeTe_6$ from FPMD simulations.

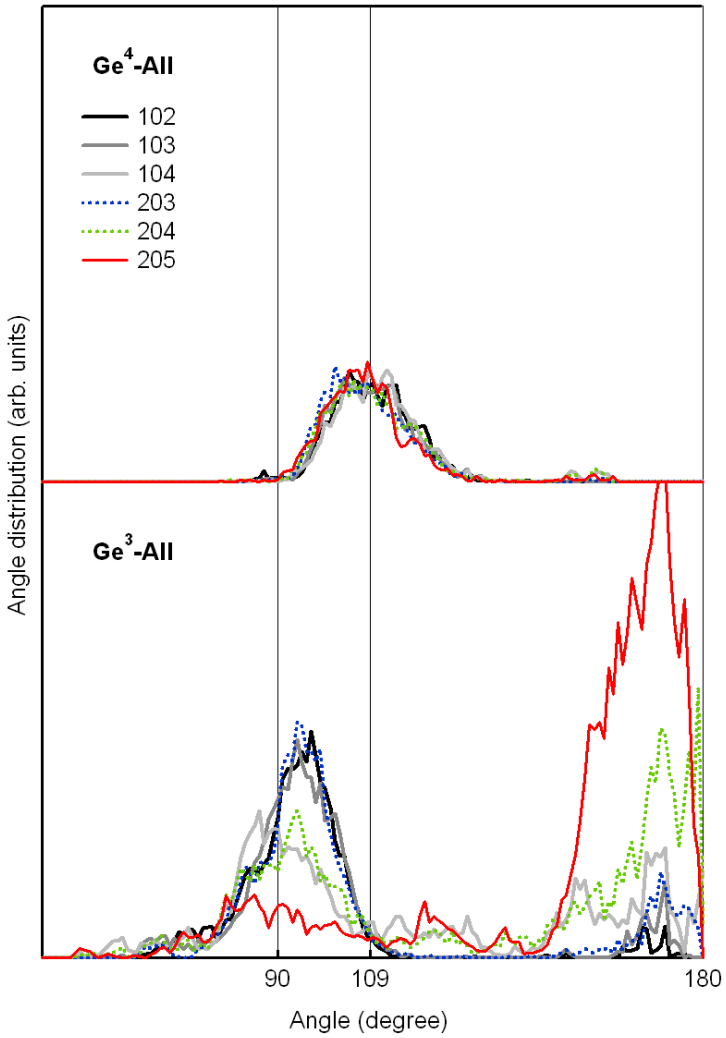

Figure 22: Bond angle distributions around Ge^3 or Ge^4 atoms in amorphous $GeTe_6$ from FPMD simulations.

Bibliography

[1] Y. Tsuchiya. *J. Phys. : Condens. Matter*, 3:3161, 1991.

[2] Y. Tsuchiya. *J. Non-Cryst. Solids*, 312-314:212–216, 2002.

[3] J. P. Perron. *Adv. Phys.*, 16:657, 1967.

[4] H. Ikemoto, H. Hoshino, T. Miyanaga, I. Yamamoto, and H. Endo. *J. of Non Cryst. Sol.*, 250-252:458–462, 1999.

[5] A. A. Oberafo. *J. Phys. C: Solid State Phys.*, 8, 1975.

[6] C. Bergman, C. Bichara, J.-P. Gaspard, and Y. Tsuchiya. *Phys. Rev. B*, 67:104202, 2003.

[7] M.-V. Coulet, D. Testemale, J.-L. Hazemann, J.-P. Gaspard, and C. Bichara. *Phys. Rev. B*, 72:174209, 2005.

[8] H. Endo, H. Hoshino, H. Ikemoto, and T. Miyanaga. *J. Phys.: Condens. Matter*, 12:6077–6099, 2000.

[9] C. Bichara, M. Johnson, and J.-Y. Raty. *Phys. Rev. Lett.*, 95:267801, 2005.

[10] N. A. Katcho, P. Zetterström, E. Lomba, L. G. Otero-Diaz, Y. D. Wang, Y. Ren, and S. Gruner. *Journal of Chem. Phys.*, 127:144707, 2007.

[11] N. Yamada, R. Kojima, M. Uno, T. Akiyama, H. Kitaura, K. Narumi, and K. Nishiuchi. *Proc. SPIE Vol. 4342 Optical Data Storage p. 55-63.* New York, 2001.

[12] M. Wuttig. *Nat. Mat.*, 4:265–266, 2005.

[13] M. Lankhorst, B. Ketelaars, and R. Wolters. *Nat. Mat.*, 4:347–352, 2005.

[14] G. Dolling and R. A. Cowley. *Proc. Phys. Soc.*, 88:463, 1966.

[15] G. D. Barrera, J.A.O. Bruno, T.H.K. Barron, and N.L. Allan. *J. Phys.: Condens. Matter*, 17:R217–R252, 2005.

[16] T. A. Mary, J. S. O. Evans, and A. W. Sleight. *Science*, 272:90, 1996.

[17] P. G. Debenedetti. *J. Phys. : Condens. Matter*, 15:R1669–1726, 2003.

[18] D. Chandra and L. R. Holland. *J. Vac. Sci. Technol. A*, 1 -3-:1620, 1983.

[19] V. M. Glazov, S. N. Chizhevskaya, and N. N. Glagoleva. *Liquid Semiconductors*. Plenum, New York, 1969.

[20] Y. Tsuchiya. *Private communication*.

[21] Y. Tsuchiya. *J. Phys. Soc. Jap.*, 60 -1-:227–234, 1991.

[22] R. Peierls. *Quantum Theory of Solids*. Pergamon, Oxford, 1955.

[23] R. Bellissent, C. Bergman, R. Ceolin, and J. P. Gaspard. *Phys. Rev. Lett.*, 59:661, 1987.

[24] J. P. Gaspard, A. Pellegatti, F. Marinelli, and C. Bichara. *Phil. Mag. B*, 77(3):727, 1998.

[25] A Chiba, Y. Ohmasa, and M. Yao. *Journal of Chem. Phys.*, 119-17:9047, 2003.

[26] H. Thurn and J. Ruska. *J. Non-Cryst. Solids*, 22:331, 1976.

[27] A. Menelle, R. Bellissent, and A. M. Frank. *Europhys. Lett.*, 4:705, 1987.

[28] K. Sato, M. Hanafusa, A. Noda, A. Arakawa, M. Uchida, T. Asahi, and O. Oda. *Journal of Crystal Growth*, 214-215:1080 – 1084, 2000.

[29] R. Sudhaesanan, G. D. Vakerlis, and N. H. Karam. *J. Elec. Mat.*, 26:745–749, 1997.

[30] C. B. Satterthwaite and R. W. Ure Jr. *Phys. Rev.*, 108:1164–1170, 1957.

[31] J. Britt and C. Ferekides. *Appl. Phys. Lett.*, 62:2851, 1993.

[32] M. F. Thorpe and P. M. Duxbury. *Rigidity theory and applications*. Kluwer Academic, Plenum Publishers, New-York, 1999.

[33] S. Chakravaty, D. G. Georgiev, P. Boolchand, and M. Micoulaut. *J. Phys. Cond. Matt.*, 17:L1, 2005.

[34] J. C. Phillips. *J. Non-Cryst. Solids*, 34:153, 1979.

[35] M. F. Thorpe. *J. Non-Cryst. Solids*, 57:355, 1983.

[36] A. Kolobov, P. Fons, A. Frenkel, A. Ankudinov, J. Tominaga, and T. Uruga. *Nat. Mat.*, 3:703–8, 2004.

[37] M. Wuttig, D. Lüsebrink, D. Wamwangi, W. Welnic, M. Gilleben, and R. Dronskowski. *Nat. Mat.*, 6:122, 2007.

[38] C. Bichara, J.-Y. Raty, and J.-P. Gaspard. *Phys. Rev. B*, 53:296, 1996.

[39] J. Akola and R. O. Jones. *Phys. Rev. B*, 76:235201, 2007.

[40] S. Caravati, M. Bernasconi, T. Kühne, M. Krack, and M. Parrinello. *Appl. Phys. Lett.*, 91:171906, 2007.

[41] C. Bichara, M. Johnson, and J.-P. Gaspard. *Phys. Rev. B*, 75:060201(R), 2007.

[42] D. Baker, M. Paesler, G. Lucowsky, S. Argawal, and P. Taylor. *Phys. Rev. Lett.*, 96:255501, 2006.

[43] S. R. Ovshinsky. *Phys. Rev. Lett.*, 21:1450, 1968.

[44] N. Yamada, O. Nishiuchi, N. Akahira, and M. Takao. *J. Appl. Phys.*, 69:5, 1991.

[45] A. Klein, H. Dieker, B. Späth, P. Fons, A. Kolobov, C. Steimer, and M. Wuttig. *Phys. Rev. Lett.*, 100:016402, 2008.

[46] J. A. Kalb, F. Spaepen, and M. Wuttig. *J. of Appl. Phys.*, 98:054910, 2005.

[47] J. Akola and R. O. Jones. *Phys. Rev. B*, 79:134118, 2009.

[48] J. Akola and R. O. Jones. *Appl. Phys. Lett.*, 94:251905, 2009.

[49] R. Zallen. *J. Non-Cryst. Solids*, 75:3–14, 1985.

[50] W. Welnic and M. Wuttig. *Materials Today*, 11:6, 2008.

[51] M. Libera and M. Chen. *J. Appl. Phys.*, 73:2272, 1993.

[52] N. Yamada, E. Ohno, K. Nishiuchi, and N. Akahira. *J. Appl. Phys.*, 69 (5):2849, 1990.

[53] E.R. Meinders, A. V. Mijiristkii, L. van Pieterson, and M. Wuttig. *Philips Research. Optical Data Storage. Theoretical aspects of phase-change alloys.* Eds Springer, Dordrecht, The Nederlands, 2006.

[54] H. Iwasaki, Ide Y., M. Harigaya, Y. Kageyama, and I. Fukimura. *Jpn. J. Appl. Phys.*, 31:461, 1992.

[55] D. Shakhvorostov, R. A. Nistor, L. Krusin-Elbaum, G. J. Martyna, D. M. Newns, B. G. Elmegreen, X.-H. Liu, Z. E. Hughes, S. Paul, C. Cabral, S. Raoux, D. B. Shrekenhamer, D. N. Basov, Y. Song, , and M. H. Müser. *PNAS*, 106-27:10907–10911, 2009.

[56] M. Wuttig and N. Yamada. *Nat. Mat.*, 6:824, 2007.

[57] A. Pirovano, A. Lacaita, F. Pellizzer, S. Kostylev, A. Benvenuti, and R. Bez. *IEEE Trans. Electron Devices*, 51, 5:714–719, 2004.

[58] J. P. Gaspard and R. Céolin. *Solid State Commun.*, 84:839, 1992.

[59] V. Aganfonov, N. Rodier, R. Céolin, R. Bellissent, C. Bergman, and J.-P. Gaspard. *Acta Cristallogr. C*, 47:1141, 1991.

[60] T. L. Anderson and H. B. Krause. *Acta Cristallogr. B*, 30:1307, 1974.

[61] K. Schubert and H. Fricke. *Z. Naturf. a*, 6:781, 1951.

[62] K. Schubert and H. Fricke. *Z. Metallk.*, 44:457, 1953.

[63] T. Matsunaga, N. Yamada, and Y. Kubota. *Acta Crystallogr. B*, 60:685–691, 2004.

[64] T. Matsunaga and N. Yamada. *Phys. Rev. B*, 69:104111, 2004.

[65] T. Matsunaga, H. Morita, R. Kojima, N. Yamada, K. Kifune, Y. Kubota, Y. Tabata, J.-J. Kim, M. Kobata, E. Ikenaga, and K. Kobayashi. *J. Appl. Phys.*, 103:093511, 2008.

[66] I. I. Petrov, R. M. Imamov, and Z. G. Pinsker. *Sov. Phys. Crystallogr.*, 13:339, 1968.

[67] S. Shamoto, N. Yamada, T. Matsunaga, Th. Proffen, J. W. Richardson Jr., J.-H. Chung, and T. Egami. *Appl. Phys. Lett.*, 86:081904, 2005.

[68] M. Luo and M. Wuttig. *Adv. Mat.*, 16:439, 2004.

[69] Ch. Steimer, V. Coulet, W. Welnic, H. Dieker, R. Detemple, C. Bichara, B. Beuneu, J.-P. Gaspard, and M. Wuttig. *Advanced Materials*, 20, 23:4535–4540, 2008.

[70] S. Caravati, M. Bernasconi, and M. Parinello. *Phys. Rev. B*, 81:014201, 2010.

[71] W. Welnic, A. Pamungkas, R. Detemple, C. Steimer, S. Blügel, and M. Wuttig. *Nat. Mat.*, 5:56–63, 2006.

[72] S. Kohara, K. Kato, S. Kimura, H. Tanaka, T. Usuki, K. Suzuya, H. Tanaka, Y. Morito, T. Matsunaga, N. Yamada, Y. Tanaka, H. Suematu, and M. Tanaka. *Appl. Phys. Lett.*, 89:201910, 2006.

[73] P. Jóvári, I. Kaban, J. Steiner, B. Beuneu, A. Schöps, and M. A. Webb. *Phys. Rev. B*, 77:035202, 2008.

[74] J. Hegedüs and S. R. Elliott. *Nat. Mat.*, 7:399–406, 2008.

[75] J. Akola, R. O. Jones, S. Kohara, S. Kimura, K. Kobayashi, M. Tanaka, T. Matsunaga, R. Kojima, and N. Yamada. *Phys. Rev. B*, 80:020201(R), 2009.

[76] K. Shportko, S. Kremers, M. Woda, D. Lencer, J. Robertson, and Matthias Wuttig. *Nat. Mat.*, 7:653 – 658, 2008.

[77] B. Huang and J. Robertson. *Phys. Rev. B*, 81:081204(R), 2010.

[78] J. Robertson, K. Xiong, and P. W. Peacock. *Thin Solid Films*, 515:7538, 2007.

[79] F. Gautier, M. Gerl, and P. Guyot éditeurs. *Electronic Structure of Crystal Defects and of Disordered Systems, Summer School Aussois*. Editions de la physique, France, 1980.

[80] G. Herzberg. *Atomic spectra and Atomic structure, 2nd. edition*. Dover, 1944.

[81] W. A. Harrison. *Electronic Structure and the Properties of Solids*. San Fransisco : W. H. Freeman, 1980.

[82] G. N. Lewis. *J. Am. Soc.*, 38:762, 1916.

[83] T. Chattopadhyay, JJ. X. Boucherle, and H. G. von Schnering. *J. Phys. C: Solid State Phys.*, 20:1431–1440, 1987.

[84] G. J. Carron. *Acta Crys.*, 16:338, 1963.

[85] J. E. Enderby. *Amorphous and Liquid Semiconductors*. Edt. J. Tauc, Plenum, New-York, 1974.

[86] R. Bellissent and G. Tourand. *J. de Phys.*, 37:1423, 1976.

[87] J.-P. Gaspard, R. Bellissent, A. Menelle, C. Bergman, and R. Ceolin. *Il Nuovo Cimento D*, 12:649, 1990.

[88] A. Chiba, M. Tomomasa, T. Hayakawa, M. Bennington, A. C. Hannon, and K. Tsuji. *Phys. Rev. B*, 80:060201, 2009.

[89] J.-Y. Raty, J.-P. Gaspard, M. Bioducci, R. Céolin, and R. Bellissent. *Journal of non-crystalline solids*, 250-252:277–280, 1999.

[90] M. Micoulaut, W. Welnic, and M. Wuttig. *Phys. Rev. B*, 78:224209, 2008.

[91] H. E. Stanley. *NATO Sciences Series A : Life Sciences*, 305:1–31, 1999.

[92] H. Tanaka. *Phys. Rev. Letters*, 80(26):5750, 1998.

[93] B. Zelezni. *Russ. J. Phys. Chem.*, 43:1331, 1969.

[94] C. Bichara, A. Pellegatti, and J. P. Gaspard. *Phys. Rev. B*, 47:5002, 1993.

[95] C. Bergman, A. Pellegatti, R. Bellissent, A. Mennelle, R. Ceolin, and J. P. Gaspard. *Physica B*, 156-57:158, 1989.

[96] X. P. Li, P. B. Allen, R. Car, M. Parinello, and J. Q. Broughton. *Phys. Rev. B*, 41(5):3260, 1990.

[97] Y. Tsuchiya. *J. Phys. : Condens. Matter*, 9:10087, 1997.

[98] Y. Tsuchiya. *J. of Non-Cryst. Solids*, 250-252:473–477, 1999.

[99] Y. Tsuchiya. *Z. Metallkd.*, 97:371, 2006.

[100] P. J. McGonial and A. V. Grosse. *J. Chem. Phys.*, 36:469, 1962.

[101] Y. Waseda. *Third International Conference on Liquid Metals 1976, IOP Conference Proceedings No. 30 pp. 230-240.* Eds R. Evans and D.A. Greenwood, Institute of Physics, Bristol and London, 1977.

[102] G. Tourand and M. Breuil. *J. Physique*, 32:813, 1971.

[103] B. Cabane and J. Friedel. *J. Physique*, 32:73, 1971.

[104] R. Stadler and M. J. Gillian. *J. Phys.: Condens. Matter*, 12:6053, 2000.

[105] R. Winter, C. Szornel, W. C. Pilgrim, W. S. Howells, P. A. Egeldtaff, and T. Bodensteiner. *J. Phys. : Condens. Matter*, 2:8427, 1990.

[106] K. Tamura. *J. NonCryst Solids*, 205-207:239, 1996.

[107] Y. Tsuchiya. *Thermochimica Acta*, 314:275–280, 1998.

[108] F. Kakinuma and Y. Tsuchiya. *J. of the Phys. Soc of Japan*, 70-10:2948, 2001.

[109] L. van Hove. *Phys. Rev.*, 95:249–262, 1954.

[110] H. E. Fischer, A. C. Barnes, and Ph. S. Salmon. *Rep. Prog. Phys.*, 69:233–299, 2006.

[111] G. L. Squires. *Introduction to the theory of thermal neutron scattering.* Dover Publications, INC., New-York, 1978.

[112] Institut Laue-Langevin. *Neutron Data Booklet.* Edts A-J Dianoux and G. Lander, Grenoble, 2001.

[113] H. H. Paalman and C. J. Pings. *J. Appl. Physics*, 33:2635, 1962.

[114] A. K. Soper. *Nucl. Instrum. Methods*, 212:337, 1983.

[115] G. Placzek. *Phys. Rev.*, 86:377, 1952.

[116] H. E. Fischer, G. J. Cuello, P. Palleau, D. Feltin, A. C. Barnes, Y. S. Badyal, and J. M. Simonson. *Appl. Phys. A*, 74:S160–S162, 2002.

[117] M. Bée. *J. Phys. IV France*, 111:259, 2003.

[118] ILL web site. *www.ill.eu.*

[119] R. Pick, M. H. Cohen, and R. M. Martin. *Phys. Rev. B*, 1:910–920, 1970.

[120] P. Hohenberg and W. Kohn. *Phys. Rev. B*, 136:864–871, 1964.

[121] W. Kohn and L. J. Sham. *Phys Rev. A*, 140:1133, 1965.

[122] D. Hartree. *Proc. Cambridge Philos. Soc.*, 89:24, 1928.

[123] V. Z. Fock. *Physik*, 61:126, 1930.

[124] D. G. Anderson. *Assoc. Comput. Match.*, 12:547, 1965.

[125] C. G. Broyden. *Math. Comput.*, 19:577–593, 1965.

[126] D. Ceperley and B. Alder. *Phys. Rev. Lett.*, 45:566–569, 1980.

[127] J.-P. Perdew and W. Yue. *Phys. Rev. B*, 33:8800–8802, 1986.

[128] J. P. Perdew, J. A. Chevary, S. H. Vosko, K. A. Jackson, M. R. Pederson, D. J. Singh, and C. Fiolhais. *Phys. Rev. B*, 46:6671, 1992.

[129] R. M. Martin. *Electronic structure. Basic theory and practical methods.* University press, Cambridge, United Kingdom, 2004.

[130] H. Hellmann. *Einfuhrung in die Quantumchemie.* Edt. Franz Duetsche, Leipzig, 1937.

[131] R. P. Feynman. *Phys. Rev.*, 56:340, 1939.

[132] W. Harrisson. *Pseudo-potentials in the theory of metals.* Benjamin/Cummings, Menlo Park, 1966.

[133] D. Vanderbilt. *Phys. Rev. B*, 41:7892, 1990.

[134] G. Kresse and J. Hafner. *Phys. Rev. B*, 47:558, 1993.

[135] S. Nose. *J. Chem. Phys.*, 81 (1):511, 1984.

[136] Y. Tsuchiya and H. Saitoh. *J. Phys. Soc. Jap.*, 62 -4-:1272–8, 1993.

[137] A. Schlieper, Y. Feutelais, S. G. Fries, B. Legendre, and R. Blachnik. *CALPHAD: Comput. Coupling Phase Diagrams Thermochem.*, 23:1, 1999.

[138] W. Klemm and G. Frischmuth. *Z. anorg. Chem.*, 218:249, 1934.

[139] *LAMP, the Large Array Manipulation Program. ILL web site: http : //wwwold.ill.fr/data_treat/lamp/lamp.html.*

[140] J. Akola and R. O. Jones. *Phys. Rev. Lett.*, 100:205502, 2008.

[141] J. Akola, R. O. Jones, S. Kohara, T. Usuki, and E. Bychkov. *Phys. Rev. B*, 81:094202, 2010.

[142] J. P. Perdew, K. Burke, and M. Ernzerhof. *Phys. Rev. Lett.*, 77:3865, 1996.

[143] J. Tao, J. P. Perdew, V. N. Staroverov, and G. E. Scuseria. *Phys. Rev. Lett.*, 91:146401, 2003.

[144] C. Wagner and H. Ruppersberg. *At. Energy Rev.*, 1:101, 1981.

[145] J.-P. Hansen and I. R. McDonald. *Theory of simple liquids*. Academic Press, London, 1976.

[146] F. Herwig and M. Wobst. *Z. Metallkde*, 82:917, 1991.

[147] G. R. Kneller, V. Keiner, M. Kneller, and M. Schiller. *Comp. Phys. Comm.*, 91:191–214, 1995.

[148] S. Yoshioka, Y. Kawakita, M. Kanehira, and S. Takeda. *Jpn. J. Appl. Phys.*, 38:468–71, 1999.

[149] R. H. Baughman, S. Stafstrom, C. Cui, and S. O. Dantas. *Science*, 279:1522–4, 1998.

[150] J.-Y. Raty, V. V. Godlevsky, J.-P. Gaspard, C. Bichara, M. Bionducci, R. Bellissent, R. Céolin, J. R. Chelikowsky, and P. Ghosez. *Phys. Rev. B*, 65:115205, 2002.

[151] M. Delheusy, J.-Y. Raty, R. Detemple, W. Welnic, M. Wuttig, and J.-P. Gaspard. *Physica B*, 350:1055–7, 2004.

[152] W. A. Phillips, U. Buchenau, N. Nücker, A.-J. Dianoux, and W. Petry. *Phys. Rev. Lett.*, 63:2381, 1989.

[153] E. L. Gjersing, S. Sen, and B. G. Aitken. *J. Non-Cryst. Solids*, 355:748, 2009.

[154] C. Otjacques, J.-Y. Raty, M.-V. Coulet, M. Johnson, H. Schober, C. Bichara, and J.-P. Gaspard. *Phys. Rev. Lett.*, 103:245901, 2009.

[155] J. C. Rouland, R. Ollitrault-Fichet, J. Flahaut, J. Rivet, and R. Ceolin. *Thermochim. Acta*, 161:189–200, 1990.

[156] O. Uemura, Y. Sagara, M. Tsushima, T. Kamikawa, and T. Satow. *J. of Non Cryst. Sol.*, 33:71–81, 1979.

[157] K. Maruyama, H. Hoshino, H. Ikemoto, and H. Endo. *J. of Phys. Soc. of Japan*, 73:380–387, 2004.

[158] F. Shimojo, K. Hoshino, and Y. Zempo. *J. of Non Cryst. Sol.*, 312-314:349–355, 2002.

[159] F. Shimojo, K. Hoshino, and Y. Zempo. *J. Phys.: Condens. Matter*, 14:8425–8433, 2002.

[160] X. F. Zhu and L. F. Chen. *J. Phys.: Condens. Matter*, 21:275602, 2009.

[161] B. E. Warren. *X-Ray Diffraction*. Addison-Wesley, Reading, MA, 1969.

[162] J. M. Cowley. *Phys. Rev.*, 77:667, 1950.

[163] R. Kubo. *J. Phys. Soc. Japan*, 12:570, 1957.

[164] D. A. Greenwood. *Proc. Phys. Soc.*, 715:585, 1958.

[165] J.-Y. Raty, J.-P. Gaspard, and C. Bichara. *J. Phys.: Condens. Matter*, 15:S167–S173, 2003.

[166] D. Lencer, M. Salinga, B. Grabowski, T. Hickel, J. Neugebauer, and M. Wuttig. *Nat. Mat.*, 7:972, 2008.

[167] A. Giani, A. Boulouz, F. Pascal-Delannoy, A. Foucaran, A. Boyer, B. Aboulfarah, and A. Mzerd. *J. Mat. SC. Lett.*, 18:541–543, 1999.

[168] J. W. Park, S. H. Eom, H. Lee, J. Da Silva, Y. S. Kang, T. Lee, and Y. H. Khang. *Phys. Rev. B*, 80:115209, 2009.

[169] N. Kh. Abrikosov, L. V. Poretskaya, and I. P. Ivanova. *Russ. J. Inorg. Chem.*, 4:1163–1166, 1959.

[170] K. Singh, R. Satoh, and Y. Tsuchiya. *J. Phys. Soc. Jpn.*, 72:2546–2550, 2003.

[171] P. Merkelbach. *Private communication.*

[172] A. L. Lacaita. *Sol. St. Electr.*, 50:24–31, 2006.

[173] B. S. Lee, J. R. Abelson, S. G. Bishop, D. H. Kang, B. K. Cheong, and K. B. Kim. *J. Appl. Phys.*, 97:093509, 2005.

[174] Z. Sun, J. Zhou J., and R. Ahuja. *Phys. Rev. Lett.*, 98:055505, 2007.

[175] P. Giannozzi et al. *J. Phys. cond. Matter*, 21:395502, 2009.

[176] T. Blachowicz, M. G. Beghi, G. Guntherodt, B. Beschoten, H. Dieker, and M. Wuttig. *J. Appl. Phys.*, 102:093519, 2007.

[177] W. K. Njoroge, H. Wöltgens, and M. Wuttig. *J. Vac. Sci. Technol. A*, 20:230, 2002.

[178] N. Troullier and J. L. Martins. *Phys. Rev. B*, 43:1993, 1991.

[179] K. Aoki, O. Shimomura, and S. Minomura. *J. Phys. Soc. Jpn*, 48:551–6, 1980.

[180] Y. Akahama, M. Kobayashi, and H. Kawamura. *Phys. Rev. B*, 47:20–6, 1993.

[181] W. Welnic, S. Botti, L. Reining, and M. Wuttig. *Phys. Rev. Lett.*, 98:236403, 2007.

[182] J. C. Maxwell. *Phil. Mag.*, 27:294, 1864.

[183] J. L. Lagrange. *Mécanique analytique.* Paris, 1788.

[184] I. Petri, P. S. Salmon, and H. E. Fisher. *Phys. Rev. Lett.*, 84:2413, 2000.

[185] B. Bureau, J. Troles, M. Le Floch, P. Guénot, F. Smektala, and J. Lucas. *J. Non-Cryst. Solids*, 319:145, 2003.

[186] J.-Y. Raty, C. Otjacques, J.-P. Gaspard, and C. Bichara. *Solid State Sc.*, 2:193, 2010.

[187] D. Selvanathan, R. N. Enzweiler, W. J. Bresser, and P. Boolchand. *Bull. Am. Phys. Soc.*, 42:249, 1997.

[188] M. Micoulaut, J.-Y. Raty, C. Otjacques, and C. Bichara. *Phys. Rev. B*, 81:174206, 2010.

[189] Editors M. Micoulaut and M. Popescu. *Rigidity and Boolchand Phases in Nanomaterials*. INOE Publishing House, Bucarest, 2009.